Sensory Mapping using High-Resolution 7 T fMRI

by

Michael Asghar, M. Sc

Thesis submitted to
The University of Nottingham
for the degree of
Doctor of Philosophy

November 2018

Abstract

One of the aims of medical physics and neuroscientific research is to non-invasively measure primary sensory human brain function with high spatial and temporal resolution. Imaging modalities such as functional magnetic resonance imaging (fMRI) have allowed a better understanding of broad neuronal properties. The Chapters in this thesis focus on high spatial resolution mapping in the visual and somatosensory system using ultra-high field (7 T) fMRI.

Functional MRI measures changes in the blood-oxygenation level that occurs in response to neural activity, eliciting a haemodynamic response function (HRF). This thesis develops novel fMRI paradigms for high spatial and temporal resolution retinotopic and somatotopic mapping. This includes population receptive field (pRF) mapping, to uncover the receptive fields in visual and somatosensory cortices. This is a phase-encoding, computational method that provides additional information beyond traditional retinotopic mapping. The dependency of the HRF on these computational models is also investigated. To accurately characterize the HRF in different sensory brain regions with good spatial coverage, the use of multiband imaging and short TRs are used in this work. It is suggested that pRF mapping is sensitive to model constraints, minimization algorithm and brain region. pRF development in somatosensory cortex requires the use of very careful experimental setups, which are discussed in this thesis. Finally, a battery involving quantitative sensory testing and fMRI paradigms are setup for patient studies. Specifically, future work in this area aims to consider whether there are any differences in Focal Hand Dystonia patients in the cortical representation of the digits, and/or departures from the norm in behavioural tasks.

Acknowledgements

Record scratch, freeze-frame

So, here's the thing. I'm not a physicist. At least, that's what I thought 3 years ago. Turns out, I'm more of a physicist than anything else.

So many people helped me. Without my supervisors (Sue and Denis), this thesis would be blank. Without help from post-docs (Rosa, Ayan, George), the data wouldn't have been analysed.

Without Jim, my code would consist of witty comments and nothing else. Without Ellie, I would have quit long ago. Jim, you got me through the final sprint to the end. And Ellie, well, you co-created Fireball.

Without my wife, Diana, my parents, and my daughter, Artemis, I wouldn't have been able to stay positive in the darkest times. They convinced me to start this endeavour and supported me at the end when stress levels were particularly high. Diana, you are the most amazing person in the universe for sticking by me through everything.

So, to the unlucky PhD student who might be reading this thesis (haha, no-one will ever read this); just know that you can get pretty damn far in life by working hard and being kind. Everything else will sort itself out in time.

drops mic

P.S. Special thanks to Sue for reading through every chapter at least 5 times and whipping this into shape.

P.P.S. Extra special thanks to Matt and Hollie for having to read this behemoth.

Contents

1 Introduction **1**

1.1 Overview of Thesis 1

2 Magnetic Resonance Imaging **4**

2.1 Overview of chapter 4

2.2 Magnetism 4

2.2.1 Fields and Phase 5

2.3 The NMR phenomenon 8

2.3.1 Spin 8

2.3.2 Energy and Equilibrium Magnetization 9

2.3.3 Precession 10

2.3.4 Resonance 13

2.3.5 Rotating Reference Frame 15

2.3.6 Relaxation 16

2.3.7 Free Induction Decay 20

2.4 Pulse Sequences 21

2.4.1 Gradient Echo 22

2.4.2 Image Contrast 22

2.4.3 Inversion Recovery 26

2.5 Image Acquisition 28

2.5.1 Effect of gradient and frequency encoding 28

2.5.2 Slice selection 29

2.5.3 Fourier Imaging 30

2.5.4 k-space 32

2.5.5 Phase Encoding 34
2.5.6 Resolution 35
2.6 Scanner hardware 37
2.6.1 Coils 37
2.7 Conclusion of Chapter 40

3 Advanced Imaging Techniques 41
3.1 Overview of chapter 41
3.2 Fast imaging 41
3.2.1 Partial Fourier Imaging 41
3.2.2 Echo Planar Imaging 43
3.2.3 Volume Acquisition 45
3.2.4 Parallel Imaging 46
3.2.5 SENSitivity Encoding 48
3.2.6 Simultanaeous Multi-Slice (SMS) 51
3.2.7 Controlled Aliasing In Parallel Imaging Results In Higher Acceleration (CAIPIRINHA) 52
3.3 Ultra High Field (UHF) Imaging 53
3.3.1 Field strength and Energy states 53
3.3.2 7 Tesla MRI 54
3.4 Functional Imaging 57
3.4.1 The BOLD effect in brief 57
3.4.2 Energy expenditure in the brain 59
3.4.3 BOLD and T_2^* 60
3.4.4 BOLD optimization 62
3.4.5 BOLD physiology 64

3.5 fMRI statistical analysis 67
3.6 Statistical analysis 68
3.7 Conclusion of Chapter 75

4 pRF Mapping in Visual Cortex 77
4.1 Overview of chapter 77
4.2 Introduction 78
4.3 Background 80
4.3.1 The Visual Cortex 80
4.3.2 Mapping Visual Cortex 81
4.3.3 Population Receptive Field Mapping of Visual Cortex 83
4.4 Methods: Data acquisition and paradigm optimisation . . . 86
4.4.1 Analysis pipeline 91
4.5 Results: Data acquisition and paradigm optimisation 92
4.5.1 Pilot visual HRF data 92
4.5.2 Optimising fMRI protocol: use of multiband acquisition 93
4.5.3 HRF spatial parameter maps 95
4.6 Methods: HRF fitting and separation 98
4.6.1 HRF fitting: pathway (i) 98
4.6.2 Modelling the HRF 98
4.6.3 Separating tissue versus vein signals 100
4.6.4 Vein masking 101
4.6.5 k-means clustering 103
4.7 Results: HRF fitting and separation 105
4.7.1 Vein-masking 105

4.7.2 k-means clustering 106
4.8 Methods: pRF mapping 112
4.8.1 pRF tests: pathway (ii) 112
4.8.2 Retinotopic mapping 112
4.8.3 pRF mapping 113
4.9 Results: pRF mapping 114
4.10 Methods: Comparing the pRF's and measured HRFs 121
4.10.1 Final protocol (C) 121
4.10.2 Comparison of the pRF derived HRF with the measured HRFs 121
4.11 Results: Comparing the pRF's and measured HRFs 122
4.11.1 HRF informed pRF fits 122
4.11.2 Comparing pRF HRFs to measured HRFs 122
4.12 Discussion 129
4.13 Conclusion of Chapter 132

5 pRF Mapping in Somatosensory Cortex 134

5.1 Overview of chapter 134
5.2 Introduction 135
5.3 Background 136
5.3.1 The Somatosensory Cortex 136
5.3.2 Mapping Somatosensory Cortex 139
5.4 Methods A: Data Acquisition and Paradigm Optimisation . 143
5.4.1 Development of pRF Models for somatosensory domain 149
5.4.2 HRF parameters 153

5.4.3 pRF Model outputs 153
5.4.4 Correlating pRF mapping results with TW results within subjects 155
5.4.5 Non-linear least squares algorithm choice 156
5.5 Results A: Data Acquisition and Paradigm Optimisation . . 156
5.6 Methods B: Optimising within-digit maps 162
5.7 Results B: Optimising within-digit maps 163
5.8 Methods C: Comparing TW and pRF analysis 167
5.9 Results C: Comparing TW and pRF analysis 168
5.10 Methods D: Data acq and Surface coil optimisation 182
5.11 Results D: Data acq and Surface coil optimisation 184
5.12 Discussion 191
5.13 Conclusion of Chapter 195

6 Behavioural and Clinical Studies 196
6.1 Overview of chapter 196
6.2 Background and Motivations 197
6.3 Focal Hand Dystonia 198
6.4 Behavioural measures 201
6.4.1 Literature review 201
6.4.2 Methods: Optimising behavioural measures 202
6.4.3 Results: Optimising behavioural measures 206
6.4.4 Results: Behavioural measures in patients 212
6.5 Methods: Optimising fMRI data acquisition and paradigms . 215
6.5.1 Pre-processing and Analysis 219
6.6 Results: Optimising fMRI data acquisition and paradigms . 222

6.7 Results: Patient fMRI data 232
6.8 Discussion 242
6.9 Conclusion of Chapter 244

7 Concluding Remarks 246

7.1 Future Directions 248

8 Appendix 249

8.1 Deeper Insights into pRF Mapping 249
8.1.1 Extending the pRF model 252
8.1.2 Modelling the HRF 255
8.1.3 Least Squares Approximation 257
8.1.4 Non-Linear Optimization 258
8.1.5 The Levenberg-Marquardt method 259
8.1.6 The Nelder-Mead method 260
8.2 Linear Least Squares 261
8.3 Dijkstra's distance 263
8.4 Psychophysics 264
8.5 Temporal SNR images 268
8.6 QST 271

CHAPTER 1

1 Introduction

1.1 Overview of Thesis

The work described in this thesis forms part of an international collaborative project known as 'TOUCHMAP': a Medical Research Council (MRC) grant utilizing neuroimaging procedures such as ultra-high field (7 T) functional magnetic resonance imaging (fMRI), magnetoencephalography (MEG) and intraneural microstimulation (INMS), in order to map the somatosensory cortex at high spatial and temporal resolution, record neural impulse traffic (and also stimulate individual mechanoreceptive afferents), and use this knowledge to investigate the neural basis of interventional treatments in specific patient populations. This thesis encompasses my progress from the inception of my doctorate candidacy in September 2015 to the completion of my research in November 2018.

The somatosensory system is a region in the brain that encodes the sensation of touch. This region is dynamic and its internal borders are susceptible to change. Reorganization of the somatosensory representation of our digits and hands in the brain can occur in response to external trauma (Kaas, 1991; Merzenich et al., 1983; Sur et al., 1980; Wall et al., 1986), unique usage (Elbert et al., 1995; Stavrinou et al., 2007; Sterr et al., 1998) and diseases, such as carpal tunnel syndrome (CTS) (Dhond et al., 2012; Maeda et al., 2014; Napadow et al., 2006) and focal hand dystonia (FHD) (Butterworth et al., 2003; Dresel et al., 2014; Nelson et al., 2009). These changes could be measured by receptive field mapping: identifying stimuli that most effectively drive responses at cortical locations. Accurate mapping in patients would

facilitate the development of diagnosis and novel treatments. The first step is to assess the brain's normal representation of our digits and henceforth be able to quantitatively measure differences from the norm.

This PhD thesis aims to develop techniques for improved cortical mapping of digits and assessment of changes in disease.

10 million people in the UK live with a neurological condition which has a significant impact on their lives (The Neurological Alliance, 2004). Approximately 38,000 of these people suffer from dystonia. Treatments for these illnesses are yet to be evaluated beyond a symptomatic basis. The application of a "travelling wave" (TW) paradigm and the development of a "population receptive field" (pRF) mapping technique will enable accurate measures of neuro-plastic changes that occur (if at all) with treatment and hence be used to eliminate fruitless therapies and guide fruitful interventions. This work aims to optimize the imaging techniques for attainment of high resolution functional data at ultra-high field (7 T). Sub-millimetre voxel sizes for functional data acquisition are now possible and receptive field mapping can take advantage of these advances.

Chapters 1-3 describe the theory behind Nuclear Magnetic Resonance (NMR) and its application to medical imaging known as Magnetic Resonance Imaging (MRI). More advanced acquisition techniques such as functional MRI, parallel and multiband imaging techniques and the use of these methods at 7 T are described.

Chapter 4 first tests the methodology of pRF mapping in the visual cortex, acting as a proxy for the pRF model in the somatosensory cortex. The visual cortex has high SNR compared to somatosensory cortex and thus provides an ideal domain for measuring haemodynamic response functions (HRFs) with high temporal resolution.

Chapter 5 describes the inception and development of a somatosensory pRF

method. This incorporates a description of imaging procedures, a variety of computational pRF models tested and how they compare to the TW paradigm. This chapter includes insights gained from Chapter 5, and how they can be used to improve or optimize the somatosensory pRF model.

Chapter 6 provides a tantalizing look at pilot behavioural and fMRI data acquired in a set of healthy controls and patients suffering from FHD. TW maps are measured in patients at high resolution for the first time, on an individual basis. The chapter concludes with a preliminary assessment of the differences between patients and controls, and how further development of the computational models presented in this report could be used to great benefit in this cohort.

The Appendix outlines functional imaging methods and expands upon the analysis of somatosensory and visual fMRI data. A review of retinotopic and somatotopic mapping is provided and the development of pRF mapping in visual cortex follows, providing a framework for its subsequent expansion into the somatosensory domain. Additional detail into analyses and quality assurance of data are also provided here.

CHAPTER 2

2 Magnetic Resonance Imaging

2.1 Overview of chapter

To reliably characterise sensory maps in humans using Magnetic Resonance Imaging (MRI), it is first important to understand the fundamental principles of Nuclear Magnetic Resonance (NMR), the process which gives rise to the MR signal which is spatially encoded in the form of images, which are analysed in functional MRI.

This chapter describes the principles that allow the study of a single proton in a magnetic field to structural and functional images of the human brain. First, the NMR phenomenon is discussed, this is followed by image acquisition, and the important concept of k-space. Following this, a summary of the hardware that encompasses an MRI scanner is presented, along with key modules that enable image acquisition. Finally, imaging techniques utilised in this project are discussed, as well as a description of common artifacts encountered. Throughout, each concept is linked to ultra-high field imaging, since the data shown in this thesis were acquired at 7 T.

2.2 Magnetism

In this section, some basic principles of magnetism are outlined. This sets out the crucial framework necessary for understanding NMR and subsequent theory.

2.2.1 Fields and Phase

A current carrying wire will produce a magnetic field, e.g. for a single wire, the field lines are perpendicular concentric circles. Bending the wire into a loop produces a rough approximation of a *magnetic dipole field*. Classically, we can picture an atomic nucleus as a spinning, charged sphere, or similarly as a stack of current loops. This *magnetic dipole* will possess a vector of magnetic moment, μ that describes the interaction effect of the dipole with the external magnetic field.

Converse to electrical currents producing magnetic fields, alternating (changing) magnetic fields will *induce* electrical currents. The phenomenon of electromagnetic induction is the basis for how a receiver coil picks up a signal in the MR scanner. If our spinning charged sphere is rotating about a perpendicular axis to its spin axis, the magnetic field produced will alternate in time; this dipole "sweep" will induce a current in a receiver coil placed near the dipole (Figure 2.1).

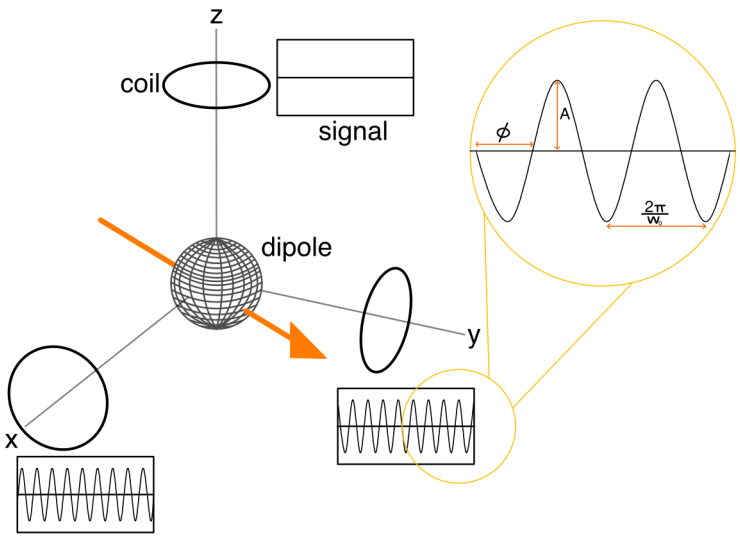


Figure 2.1: Signal induction in a coil caused by the sweep of a magnetic dipole field. Adapted from *Introduction to fMRI, 2nd Edition, Buxton, R., 2009.*

The induced current in the receiver coil(s) is proportional to the rate of change of the *flux* of the magnetic field. The key idea is that the rate of change of the *flux* or the "sweep" must pass through the coil, to produce a detectable signal. In Figure 2.1, the coil in the z-axis is in a parallel plane to the rotation of the dipole beneath. The flux here is constant and hence no signal is observed; not so in the x and y-axes, which are perpendicular. The keen observer will note that the sinusoidal waveforms in the x and y-direction are shifted with respect to one another; at this point, a definition of "phase" is appropriate.

A periodically oscillating sinusoidal wave possesses amplitude (A), angular frequency (ω_0) and phase (ϕ):

$$S(t) = A\sin(\omega_0 t - \phi) \tag{2.1}$$

where $S(t)$ is the signal detected.

The frequency is angular since the spinning dipole has an angular momentum, and phase is defined as an angular shift between the two sine waves. These terms are defined pictorially in Figure 2.1. In our example, the x and y-coil are shifted in time by 90° - an angular "phase shift". A complete period T of our periodic signal is $360° = 2\pi$ radians. One thing to note here is that two sine waves which are initially "in phase" but with differing angular frequencies will gain an accumulative phase shift: this is crucial for the later concept of how an image is spatially encoded. The themes of angular momentum and spinning nuclei are necessarily expanded later on, during an explanation of nuclear magnetic resonance, where *precession* is described; a fundamental concept in MRI.

One final principle to note in this section is that of *magnetic susceptibility*. This is simply a measure of the "degree of magnetization" of a material placed in a magnetic field. Materials may gain a polarization J, which op-

poses the main field (diamagnetism) or reinforces the field (paramagnetism, superparamagnetism or ferromagnetism), Figure 2.2. The polarization occurs due to the presence of magnetic dipoles in the material, i.e. unpaired electrons and nuclei aligning or opposing the main magnetic field.

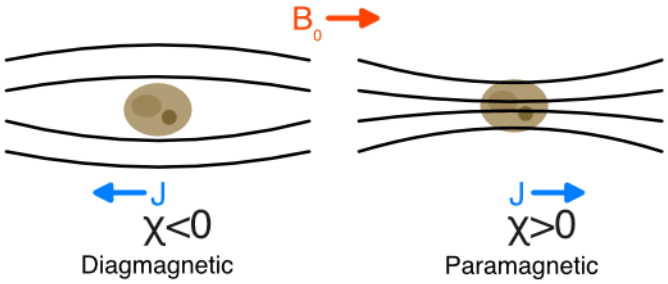


Figure 2.2: The distortion of magnetic field lines by diamagnetic and paramagnetic materials

We can define the magnetic susceptibility as:

$$\chi = \frac{J}{B_0} \tag{2.2}$$

where χ is the magnetic susceptibility and B_0 is the main magnetic field.

Susceptibility will be described further when endogenous contrasts such as the Blood Oxygen Level Dependent contrast (BOLD) used for functional MRI are discussed, since BOLD contrast depends on the diamagnetism and paramagnetism of oxy- and deoxyhaemoglobin, respectively.

Susceptibility effects are also a cause of certain MR artifacts: magnetic field distortions are produced by a magnetized body placed in a magnetic field; a heterogenous body, e.g. a human head, will have different internal susceptibilities (air, water, bone, tissue), and at these boundaries, field distortions will be exaggerated; this leads to distortions present in MR images. One method to alleviate distortions is the use of shim coils, which correct for the inhomogeneities of the main magnetic field and intrinsic inhomogeneities in

a body.

2.3 The NMR phenomenon

This section outlines the knowledge from the principle of NMR to how an MRI scanner works, to generate an image. First, a discussion of spin and precession is presented, followed by the excitation and relaxation of atomic nuclei; specifically this section outlines the use of ^{1}H for MRI, as this nucleus is used in this thesis.

2.3.1 Spin

In the previous section, the signal detected by a coil originated from a spinning, charged magnetic dipole. This notion provided a classical approximation of an atomic nucleus, however, the concept of "spin" is only correctly described by quantum mechanics. The linear momentum of an object is equal to:

$$p = mv \tag{2.3}$$

where p is momentum, m is mass and v is velocity. A spinning macroscopic object, e.g. a football, possesses angular momentum, which is proportional to the moment of inertia I and angular frequency of rotation ω:

$$L = I\omega \tag{2.4}$$

Angular momentum also takes into account the position of the rotation axis and the shape of the object.

Atomic/subatomic particles possess an intrinsic fundamental property called *spin*. This is similar to macroscopic angular momentum, but unlike our spinning football analogy, the classical notion of a spinning particle is inaccurate.

In fact, spin is a property with discrete values (it is *quantized*) that interacts with electromagnetic fields.

The most commonly utilised particle spin in MRI is the hydrogen nucleus, a proton, which possess nuclear spin I of $\frac{1}{2}$ (from here on, I defines nuclear spin, not inertia). I can be predicted from the number of nucleons in an atom, such that if a nuclei has an even number of protons and neutrons, then $I = 0$ and will not undergo NMR (e.g. ^{4}He); if nuclei have an odd number of protons and neutrons, then I is a positive integer, (e.g. ^{14}N, $I = 1$); all other nuclei spins are half integral, (e.g. ^{23}Na, $I = \frac{3}{2}$).

The total spin angular momentum is given:

$$S = \hbar\sqrt{I(I+1} \tag{2.5}$$

where $\hbar$ is Planck's constant divided by 2π. The spin quantum number (m_I) can take values of $-I, -I+1, ..., I-1, I$, the number of spin states for a proton is $2I + 1$. For ^{1}H, $I = \frac{1}{2}$, so the number of observable spin states is 2.

2.3.2 Energy and Equilibrium Magnetization

Returning to our magnetic dipole placed in a magnetic field, this possesses a magnetic moment μ and a spin angular momentum. We can mathematically describe the dipole interactions with B_0, with the energy E of the dipole in a magnetic field B given by:

$$E = -\boldsymbol{\mu}.\mathbf{B} = -\mu B\cos\theta \tag{2.6}$$

where θ is the angle between the magnetic dipole moment, $\boldsymbol{\mu}$ and the mag-

netic field, B_0 (and hence the energy depends on the dipole orientation). A torque τ will align the dipole with the field and is given by the cross product:

$$\boldsymbol{\tau} = \boldsymbol{\mu} \times \boldsymbol{B} \tag{2.7}$$

If we place a dipole in a uniform magnetic field such as B_0, then the dipole will tend to align with the uniform field (reducing θ to 0) - the dipole aligned with B_0 is in the lowest energy state. For an ensemble of spins an equilibrium distribution is set up. This is temperature dependent, since at higher energies, the degree of "energy equalization" is more pronounced, so more dipoles will be in a higher energy state. This is mathematically predicted by the *Boltzmann distribution*:

$$\frac{n_+}{n_-} = e^{\frac{-\Delta E}{kT}} \tag{2.8}$$

where n_+ and n_- define two population states of dipoles, which are either aligned (low energy n_+) or opposed (high energy n_-) to the magnetic field B_0. ΔE is the energy gap between the two states, k is the Boltzmann constant and T is temperature. On average, there is only a small number of spins in excess in the aligned (lower energy) state compared to a high energy state: approximately a 1 in 10000 difference. The net magnetic field of these spins gives rise to the equilibrium magnetization M_0.

2.3.3 Precession

A relationship exists between the magnetic moment μ and the spin angular momentum L of our nuclei. Both quantities are proportional to the speed of a spinning dipole (the angular speed ω), thus a constant known as the

gyromagnetic ratio can be defined as:

$$\gamma = \frac{\mu}{L} \tag{2.9}$$

where L is the angular momentum, and μ is the magnetic dipole moment. The units of γ are MHz/T. The gyromagnetic ratio is different for different atomic species, e.g. for a proton (^{1}H) it is 42.58 MHz/T. For a 7 T magnet, the precession frequency becomes $\approx$ 298 MHz.

Now we place our spinning dipole (possessing angular momentum) at some angle to the main magnetic field B_0. The angular momentum will be in the direction of the magnetic dipole moment μ, which is γL. The torque τ is defined to be the rate of change of angular momentum and is given by:

$$\tau = \frac{dL}{dt} = \gamma L \times B_0 \tag{2.10}$$

Equation 2.10 shows that in a short time dt, the change in angular momentum dL proceeds in the direction of the the torque τ. In other words, dL will be perpendicular to the original direction of L. This implies that L will rotate around the main field B_0 without changing the angle (or magnitude) it makes with the field. This is known as precession (Figure 2.3).

The number of observable spin states for a proton are known as the *spin-up* (+, $\uparrow$) and *spin-down* (-, $\downarrow$) states. It is incorrect to state that the spins of a proton reside exclusively in either of two states, in actuality, they exist in a superposition of both states until they are measured or observed (such as being placed in an external magnetic field). The splitting of energy states upon observation is known as the Zeeman effect (Figure 2.4), with the energy difference between the two states, given by:

$$\Delta E = \gamma h B_0 \tag{2.11}$$

where γ is the gyromagnetic ratio, and h is Planck's constant ($\approx 6.626 \times$

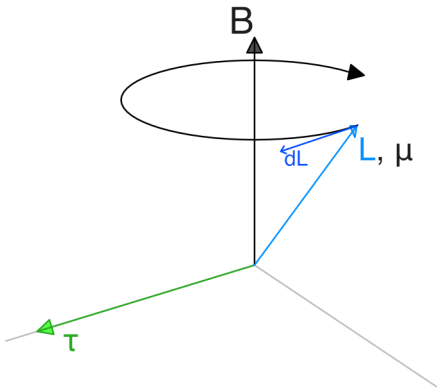


Figure 2.3: A classical depiction of a magnetic dipole precessing in a magnetic field. The change in angular momentum L is in the direction of the torque τ, thus the dipole precesses around the magnetic field, without any change in angle.

10^{-34} m^2 kg/s.

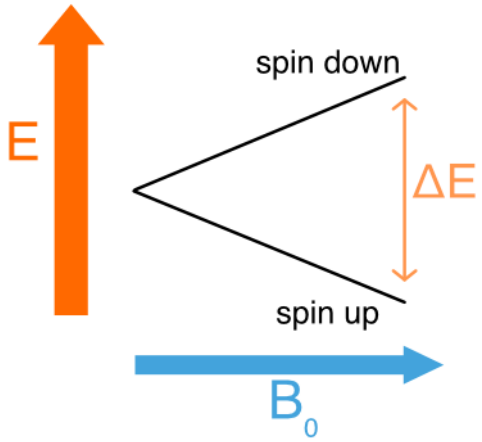


Figure 2.4: When nuclei with non-zero spin are placed in an external magnetic field, spins will tend to align or oppose the field, resulting in parallel (spin up) or anti-parallel (spin down) states. The energy difference between the two states is proportional to the magnetic field strength B_0. Hence, the stronger the magnetic field, the greater the energy gap will be (since more nuclei will be aligned to the magnetic field) and the net magnetization M_0 will be greater.

Planck's constant stems from the Planck relation:

$$\Delta E = hf_0 \tag{2.12}$$

where ΔE is the quantized energy change of a system following photonic emission of frequency f_0. In NMR, f_0 becomes ω_0, since we classically talk about nuclei as possessing an angular frequency measured in rad s^{-1}. Combining the two equations and we are left with the fundamental equation of MRI:

$$\omega_0 = \gamma B_0 \tag{2.13}$$

where ω_0 is the *Larmor frequency* associated with a precessing magnetic dipole in an external magnetic field.

2.3.4 Resonance

Outside the main magnetic field spins are randomly orientated. If we place a system of spins into a magnetic field B_0, all the nuclei will individually begin precessing at the same rate, but with random phase, with respect to the main field; the set up of an equilibrium magnetization however, takes a certain amount of time. Once placed into a magnetic field, there are two effects: spin precession and the set up of a net magnetization (M_0).

Application of a B_1 radiofrequency (RF) field perpendicular to B_0 at the resonant (Larmor) frequency (efficient energy transfer) serves to tip/rotate M_0 at a certain *flip angle*, depending on the RF field (Figure 2.6), e.g. a 90° pulse will tip M_0 into the transverse plane, where all the individual spins will come into phase (phase coherence).

After the B_1 field is switched off, M_0 will continue to precess and the transverse component of M_0 will induce a current in a nearby receiver coil (change in magnetic flux), thus detecting a measurable signal. However, the signal

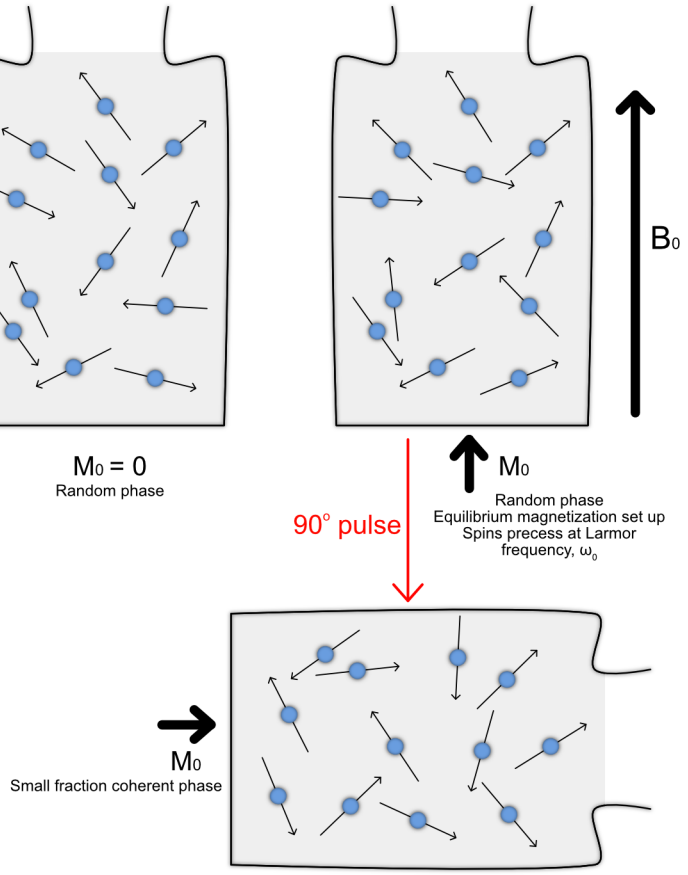


Figure 2.5: Equilibrium magnetization: Top left) Without any field, all spins in a sample are precessing with random phase and at random orientations. Top right) After being placed in a B_0 field, an equilibrium magnetization is set up with slightly more spins aligned with B_0 than opposed. This gives rise to a net magnetization, M_0. Spins are still in random phase, but precess at the Larmor frequency ω_0. Bottom) After a 90° pulse, all spins are tipped into the transverse plane. Spins are brought into phase and a resultant magnetization (phase coherence) occurs in xy plane.

does not last forever but decays with a given tissue relaxation time, coming both out of phase (reducing transverse magnetization) and returning to thermal equilibrium (gaining longitudinal magnetization).

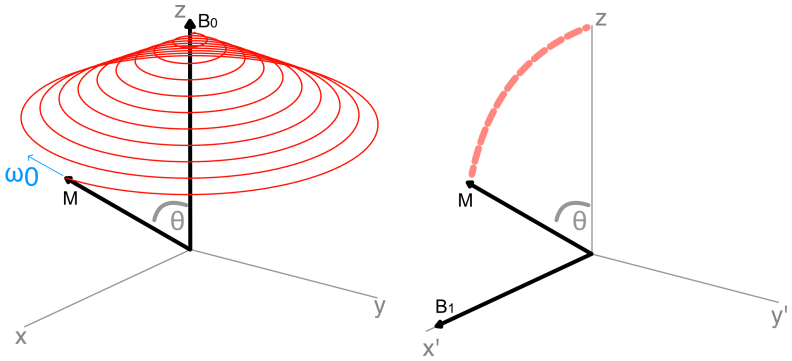


Figure 2.6: The net magnetization M_0 is tipped over (Left) following the application of a B_1 pulse, the degree of which depends on the flip angle θ. In a static (or laboratory x,y,z) reference frame, the net magnetization vector is seen to be precessing, whilst also being tipped, thus generating a widening spiral of motion downwards, by flip angle θ. Right) A B_1 pulse viewed from the rotating reference frame (x',y',z) serves to remove the precession about B_0, instead M_0 precesses about B_1 alone, moving downwards.

2.3.5 Rotating Reference Frame

The addition of a B_1 field to our system adds extra difficulty in visualizing how the net magnetization is affected in more complicated situations, e.g. during pulse sequences. The B_1 RF pulse is a weak magnetic field (μT) applied at the Larmor frequency for a short duration. This gives rise to a net field arising from both the B_0 and B_1 fields, which will tip slightly away from the original direction of B_0 (z-axis), and rotate too. Thus, M_0 is precessing about the net field and tipping downwards. It is much simpler to picture this if we (the observer) move into a rotating frame of reference that precesses at the Larmor frequency, and thus travel with M_0. In this reference frame, the net magnetization will be stationary - this concept is known as the *rotating frame of reference* (Figure 2.6).

In the rotating frame, it is as if the B_0 field has disappeared, hence M_0 no longer precesses about it. When a B_1 field at the Larmor frequency is applied, M_0 will precess about B_1 (which is also stationary along M_x, since

it is rotating at the Larmor frequency), and thus the widening spiral in the laboratory frame becomes a simplified precession of the net magnetization about B_1. The flip angle θ depends on how long the B_1 field is switched on for, as well as on the amplitude of B_1, and is given by:

$$\theta = \gamma B_1 t_p \tag{2.14}$$

where t_p is the duration of the B_1 pulse.

2.3.6 Relaxation

Before moving onto the nature of the signal that is detected following precession and resonance, we must first discuss relaxation, i.e. the evolution of the longitudinal and transverse components of the net magnetization and their recovery following a B_1 RF pulse. Felix Bloch described a set of differential equations (Bloch, 1946) that express mathematically the NMR phenomenon. The net magnetization possesses M_x, M_y and M_z components, given by:

$$\frac{\mathrm{d}M_x}{\mathrm{d}t} = \gamma B_0 M_y - \frac{M_x}{T_2} \tag{2.15}$$

$$\frac{\mathrm{d}M_y}{\mathrm{d}t} = -\gamma B_0 M_x - \frac{M_y}{T_2} \tag{2.16}$$

$$\frac{\mathrm{d}M_z}{\mathrm{d}t} = -\frac{M_z - M_0}{T_1} \tag{2.17}$$

Following a 90° pulse, the transverse (M_x and M_y) and longitudinal (M_z) components of the net magnetization will return to thermal equilibrium governed by two time constants: the time constant for the "regrowth" of longitudinal magnetization (T_1); and the time constant for the decay of transverse

magnetization in the xy plane (T_2). Solving the Bloch equations using appropriate boundary limits produces graphs of longitudinal and transverse decay as a function of time following a given B_1 RF pulse.

Longitudinal Magnetization (M_z)

Each proton in a sample experiences the main magnetic field, B_0, but also tiny, fluctuating magnetic fields that are produced by nearby protons, since they also have a magnetic moment and are rapidly tumbling due to Brownian (random, thermal) motion - these interactions are known as "dipole-dipole" interactions. Relaxation occurs due to the exchange of energy with surrounding molecules: the M_z component grows back towards M_0 (Figure 2.7).

The degree of relaxation for a given tissue is correlated with the frequency of fluctuations of protons in the tissue, i.e. the relaxation will be more efficient when the molecular motion of the protons matches the Larmor frequency. In a pure sample of water, molecular motion is unrestricted and rapid, leading to broad range of frequencies not well matched to ω_0, making relaxation inefficient leading to a very long T_1. If larger molecules (e.g. proteins) are present, water molecules (and hence the proton constituents) will tumble more slowly, leading to more molecules oscillating close to the Larmor frequency and more efficient relaxation resulting in a short T_1.

Transverse Magnetization (M_{xy})

Following a 90° pulse, spins are brought into phase coherence in the transverse (xy plane), such that the net equilibrium magnetization, M_0, is tipped into the transverse M_{xy} plane. The rate of loss of phase coherence, or "dephasing" is described by the time constant, T_2 (Figure 2.8). One can visualize this dephasing more clearly in the transverse plane, if one assumes a rotating reference frame (Figure 2.9).

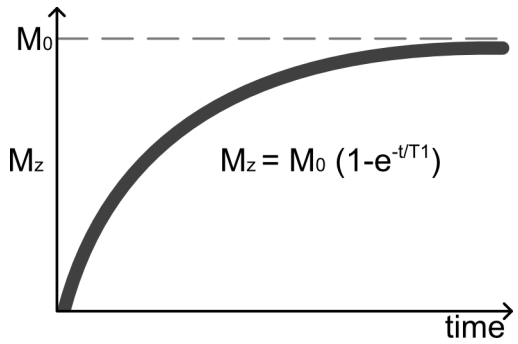


Figure 2.7: T_1 recovery describes the time it takes for the longitudinal component of the net magnetization to return to thermal equilibrium (return to lie along the z-axis), following a RF pulse, e.g. 90° pulse. The time constant of the longitudinal relaxation is given by a tissue-specific T_1 value.

This phase destruction is caused by time varying (dynamic) processes (T_2) and time-invariant (static) processes (T_2'). Dynamic processes include the slow molecular motions of nuclei in the sample, causing neighbouring nuclei to experience different fields; and the presence of macromolecules affects electron shielding from the applied field, so protons in macromolecules may feel a variety of different fields, leading to decoherence. Static processes include inhomogeneities in the main magnetic field (B_0); and magnetic susceptibility gradients in the sample, e.g. tissue/air/water interfaces. Together, these processes give rise to T_2^*:

$$\frac{1}{T_2^*} = \frac{1}{T_2} + \frac{1}{T_2'} \tag{2.18}$$

Since T_2^* includes static phase-destroying processes, it will always be shorter than T_2; the observed decay will be faster than expected. We can account for and refocus such static processes by way of a refocusing 180° RF pulse applied in the transverse plane, which serves to rephase the T_2' component and hence reflect "true" T_2. The is achieved by a *spin echo* pulse sequence (Hahn, 1950).

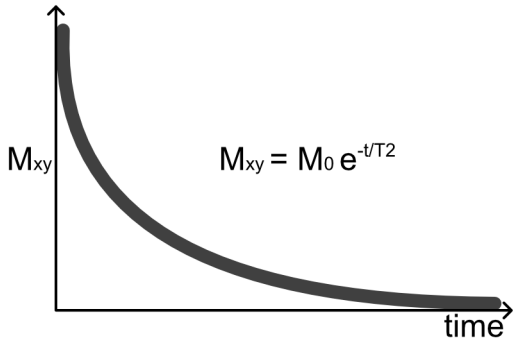


Figure 2.8: T_2 decay describes the time constant governing the transverse component of the net magnetisation (M_x, M_y) to de-phase, for example following a 90° pulse.

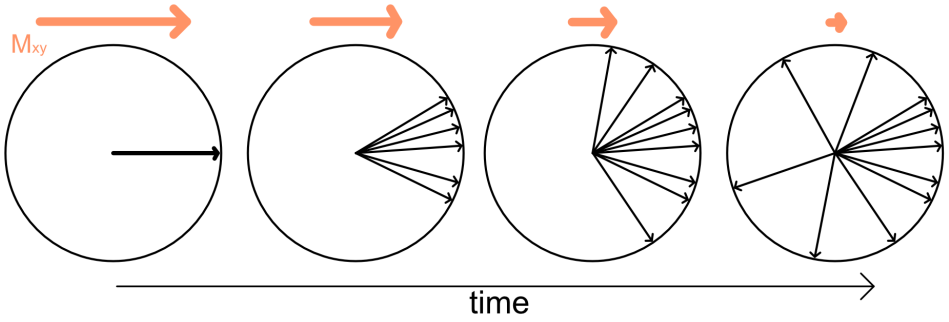


Figure 2.9: A top view of the transverse plane following RF excitation shown in the rotating frame of reference. Initially, spins (as dictated by the Boltzmann equation, though exaggerated here) have phase coherence. Dynamic and static processes result in de-phasing of individual spins, at different rates, i.e. some will be faster than the Larmor frequency, others slower. If viewed in the rotating frame of reference, where the rotation is equal to the Larmor frequency, then one can visualize the individual spins as "fanning out" in the xy plane. Note how the M_{xy} vector reduces in magnitude as more dephasing occurs.

2.3.6.1 Field strength and Relaxation times

The major mechanism for proton relaxation is the dipole-dipole interaction, e.g. two protons, with associated magnetic dipoles, that are near to each other will experience a through-space interaction effect. The strength of this mechanism is determined by the gyromagnetic ratio of the spins; the

distance of the spins to each other; the angle between the spins; and the degree of motion of the spin(s).

Increasing the field strength increases the Larmor frequency, and hence this will have an effect on relaxation rates of different molecules. The relaxation rates of spins attached to mobile molecules, e.g. free water, tend to be field-independent, whereas for slower, larger molecules, the amount of spins which are affected at the higher Larmor frequency is reduced, leading to a longer T_1.

Changing the Larmor frequency will not strongly affect T_2 relaxation resulting from relatively static fields. However, at field strengths of 7 T and above, T_2 drops; this may be due to microscopic susceptibility effects, which are emphasized at high fields. This occurs due to spins moving through local non-uniform fields, and losing phase coherence (de Graaf et al., 2006).

Typical values of T_1 at 7 T are 1130 ms for white matter, and 1940 ms for grey matter (Wright et al., 2008). For T_2, at 7 T, typical values are 55 ms for grey and 46 ms for white matter (Yacoub et al., 2003), while for T_2^*, typical values at 7 T are 33 ms for grey and 27 ms for white matter (Peters et al., 2007).

2.3.7 Free Induction Decay

We recall that the MR signal originates from a bulk net magnetisation vector (M_0) made up of protons precessing at the Larmor frequency, ω_0. The injection of a B_1 field and hence RF energy (oscillating at ω_0) into a spin system is on resonance. This tips M_0 into the transverse plane, producing phase coherence. Relaxation occurs, at rates according to longitudinal recovery (T_1) and transverse decay (T_2). The sweep of the relaxing net magnetization past a receiver coil induces a current. The form of the MR signal is known as the *free induction decay* (FID), i.e. the *free* precession of protons *induce* a

signal that *decays* with a time constant T_2^* (Figure 2.10).

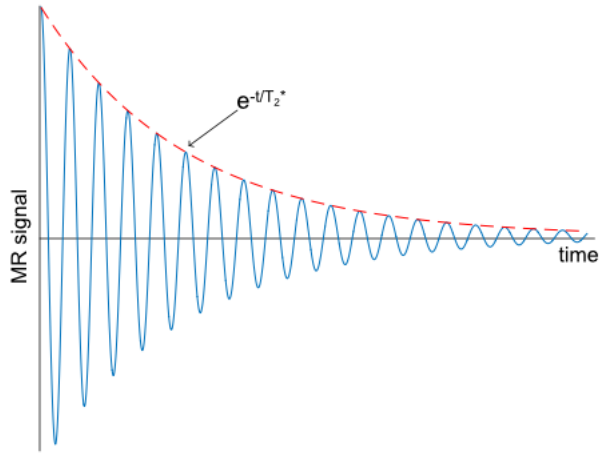


Figure 2.10: The Free Induction Decay (FID) signal. The signal is an oscillating sine wave, at the Larmor frequency. The signal is damped by a T_2^* decay envelope, which includes "true" T_2 decay and static processes arising from magnetic field inhomogeneties (T_2').

Receiver coils typically pass the signal to two phase-sensitive detectors (PSDs), allowing separation of frequencies precessing faster or slower than the Larmor frequency. The two detectors have a 90° phase shift between reference signals, creating real and imaginary components of the detected signal. This is known as quadrature phase detection.

2.4 Pulse Sequences

In this section, a discussion of how the application of different RF pulses can produce different detectable signals, sensitive to T_1, T_2 and T_2^* time constants, which in turn provides information about structure and function, is described.

2.4.1 Gradient Echo

The application of a gradient field across a sample can result in a signal "echo", through manipulation of the FID. Specifically, a dephasing gradient increases the rate of dephasing of a sample, then a rephasing gradient is applied with opposite polarity; rephasing the phase shifts caused by the dephasing, producing a *gradient recalled echo* (GRE). In the simplified GRE pulse sequence diagram (Figure 2.11), the first gradient "lobe" has negative polarity, creating a phase shift. The next lobe is twice the length of the first, and is of positive polarity, causing the peak of the echo to be placed at the centre of the lobe.

Typically, a train of RF pulses are switched on during a pulse sequence, so that after each pulse, a new echo is formed. The time from the RF pulse to the echo is known as the *echo time* (TE) and the time between subsequent RF pulses is the *repetition time* (TR).

2.4.2 Image Contrast

The aim of any pulse sequence is to optimize the image acquired to gain certain contrasts. Different image contrasts are governed by the repetition time (TR) and the echo time (TE) (see Table 1) and the flip angle θ. For a spin echo (SE) sequence, increasing the TE will allow more time for transverse T_2 decay, whereas changing the TR will affect the longitudinal recovery. The trends of these parameters is best described by Figure 2.12.

For example, if one wanted to maximize the contrast for T_1, then you would suppress the "weighting" towards T_2. Hence, use a short TR (maximize T_1 weighting) and a short TE (minimize T_2 weighting). The term weighting is a slight misnomer, in that, most images acquired will have a mixture of weighting from T_1, T_2 and pure proton density.

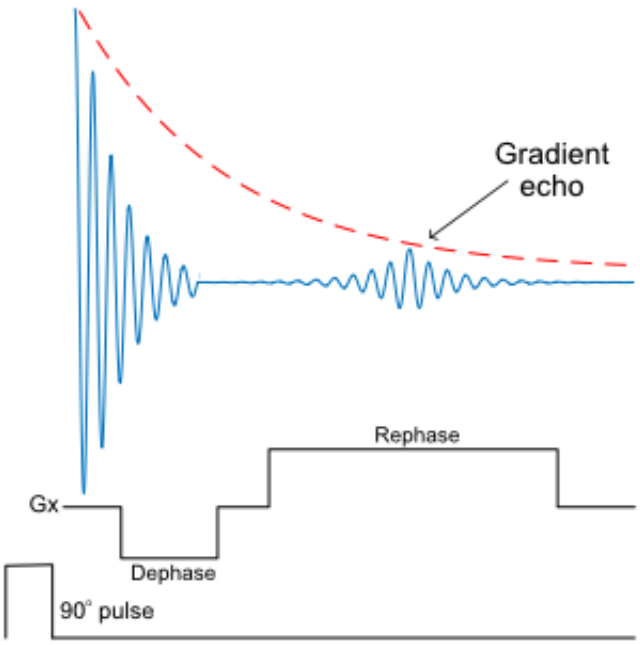


Figure 2.11: A gradient echo is formed by applying a dephasing gradient, followed by a rephasing gradient (which is twice as long) to the FID. Note that the signal is still decaying with respect to T_2^*.

Image Contrast		
	Short TR	Long TR
Short TE	T1	Proton Density
Long TE	Poor contrast	T2

Table 1: How TR and TE affect the image contrast with regards to T_1 and T_2 sensitivity.

As well as T_1 and T_2, another parameter modulating image contrast is the flip angle θ. Instead of using a 90° pulse, "partial flip angles" can be utilised which provide a higher signal at shorter TRs. Following a 90° pulse, the longitudinal magnetization M_0 (in the z-direction) has been destroyed, and now precesses in the transverse plane. If the TR is sufficiently long (of the order of $5 \times T_1$ of tissue) M_0 will fully recover prior to the next RF pulse, allowing subsequent RF pulses to be efficient. However, if a short TR is

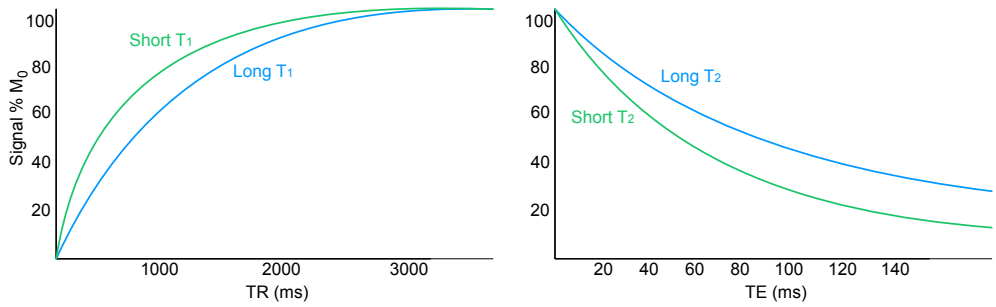


Figure 2.12: The dependence of tissue contrast on T_1 and T_2. Lines are drawn for two different tissue with long and short T_1/T_2. The intensity of the spin echo signal will increases as the TR increases, dependent on T_1, whilst the intensity will decrease as TE increases, dependent on T_2.

used, then the longitudinal recovery will not be fully recovered, and if RF energy is continuously injected into the system, preventing full longitudinal recovery, then the system will achieve a lower, "steady state" longitudinal magnetization M_{ss} (where $M_{ss} < M_0$). In this instance, the use of a lower flip angle, allows M_{ss} to retain high signal than if a larger θ was used.

The optimal flip angle to use to maximise the steady state signal is the *Ernst angle* α_E, which is given by:

$$\alpha_E = cos^{-1}(e^{-\frac{TR}{T_1}}) \tag{2.19}$$

Practically, in GRE pulse sequences, *spoiled* GRE sequences are used: this is where the cycle-to-cycle transverse coherences set up by successive RF pulses (at short TRs) are disrupted. If the TR is less than the T_2 of the imaged tissue, then the transverse magnetization of previous pulses (in a pulse train) will not have been destroyed completely, thus, "leftover" echoes will be present, meaning that the transverse magnetization never truly decays.

2.4.2.1 Spoiling

Spoiling removes the transverse magnetization from the steady state magnetization, i.e. M_{xy} is destroyed at the end of every cycle. There are three common methods of spoiling magnetization: 1) Long TR spoiling; 2) Gradient spoiling; and 3) RF spoiling.

Recall that a train of RF pulses will each generate an FID. Since these pulses are regular (governed by the TR), a pair of pulses will generate a spin echo, while a set of three pulses will produce a "stimulated echo". When the TR is much longer than the rate of T_2^* decay, natural spoiling occurs, since the transverse magnetization will decay anyway before the next RF pulse. The second method adds a spoiler gradient at the end of the cycle, with variable amplitude.

RF spoiling is superior to the previous two methods, since it will not vary spatially (unlike gradient spoiling, which can produce differences in the spoiling uniformity), and also won't generate eddy currents (currents that are induced by the rapidly changing magnetic fields). If the RF pulse phase is the same at every TR, and TR $< T_2^*$, then the transverse magnetization is not completely eliminated. If however, one varies the RF phase at each TR, then each magnetization component will acquire different phases, leading to possible cancellation. Optimum phase shifts that are incremented by a recursive formula starting at 117° provide good spoiling, without artifacts, and maintaining image contrast (Zur, 1991).

An example of a spoiled-GRE sequence is the Fast Low Angle SHot pulse sequence (FLASH) (Haase et al., 1986). The Philips vendor scan name is known as a T1-fast field echo (T1-FFE).

2.4.2.2 Flip angle and TR

If the TR is shorter than the longitudinal relaxation time (T_1), then M_z will not fully recover back to M_0 and thus after subsequent pulses, a new "steady-state" is achieved (M_{ss}). A small flip angle will push M_z shallower into the transverse plane, such that the magnetization will have less distance to travel to return back to M_0 (T_1 recovery). To maximize the MR signal, one must decide whether to fully tip M_z into the transverse plane, however this will reduce the magnitude of M_z, or use a smaller flip angle to increase M_{ss}, although less M_z is tipped into the transverse plane.

For quality assurance of shorter TR data compared to longer TR data, it is important to realise that there will be an intrinsic drop in SNR. For functional MRI, this is more appropriately measured using temporal SNR (tSNR) - see Chapter 4 for more detail.

2.4.3 Inversion Recovery

The application of a 180° inversion pulse prior to a GRE or SE sequence will invert M_0 so that the longitudinal magnetization opposes the main magnetic field B_0. T_1 relaxation will now occur, and the different tissue magnetizations will separate according to their T_1 values, the next 90° pulse will provide the detectable echo as before. This pulse sequence is known as an *Inversion Recovery* sequence. The delay between the 180° inversion pulse and the GRE or SE sequence is termed the *inversion time* (TI) (Figure 2.13).

If $TI > T_1$, then the preparatory 180° has no effect, since all the longitudinal magnetization will have recovered.

If $TI \approx T_1$, the signal will be T_1-weighted. Since the application of the inversion pulse means the the longitudinal magnetization recovers from $-M_0$

to M_0 rather than from 0 to M_0, doubling the dynamic range, therefore, the ability to discriminate between tissues with different T_1's is better.

Since the longitudinal magnetization is recovering from a negative magnetization, at some point it must pass through zero. If the TI is set to this value, then the signal will be 0 for a certain tissue magnetization passing through this point, i.e. no signal will be generated. This is known as the *null point* TI_{null}. Typically, $TR > T_1$, to allow recovery before the next pulse train, and $TI_{null} \approx 0.69 \times T_1$.

The disadvantage of using an IR sequence is the increase in scan time, as well as the additional specific absorption rate (energy deposition into the sample - usually a person).

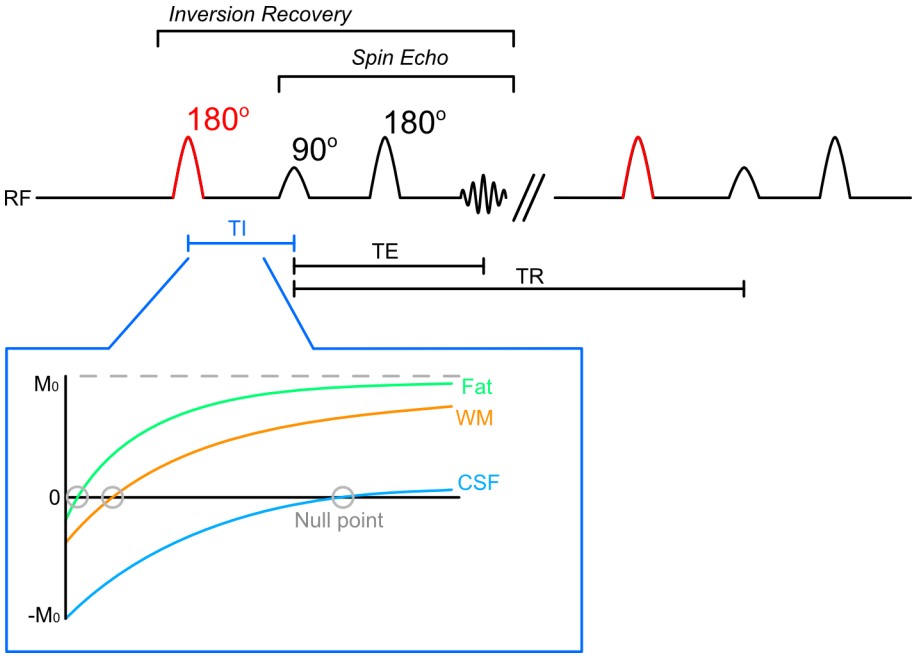


Figure 2.13: A simplified pulse sequence showing the RF pulses required for an Inversion Recovery (and a spin echo). The recovery of longitudinal magnetization M_z from $-M_0$ takes place during the inversion time TI.

2.5 Image Acquisition

In this section, the steps required in moving from a system of precessing protons to a two-dimensional image are outlined. Spatial encoding of signals is achieved by making the Larmor frequency spatially dependent using gradient coils.

2.5.1 Effect of gradient and frequency encoding

Frequency encoding can encode the frequency of the spins in a given plane of the sample (e.g. xy axes). For example, if a gradient field is switched on, such that as we move across a 2D image from left to right, the local field strength increases linearly. As a result, the resonant frequencies will change in a regular manner from left to right in the gradient plane. In this way, we have made one dimension of the image spatially dependent (Figure 2.16).

The gradient field adds to the main magnetic field, such that the local "effective" field experienced by spins at a point x will be:

$$B(x) = B_0 + x \times G_f \tag{2.20}$$

where B_0 is the main magnetic field and G_f is the frequency encoding gradient. From Equation 2.13, we can show that the resonant frequency will then vary linearly:

$$\begin{aligned} \omega_x &= \gamma B(x) \\ &= \gamma B_0 + \gamma x G_f \\ &= \omega_0 + \omega_g(x) \end{aligned} \tag{2.21}$$

where ω_0 is the Larmor frequency (in the main magnetic field), and $\omega_g(x)$ is the position-dependent frequency offset.

2.5.2 Slice selection

Initially, a *slice* or plane in the sample is chosen through slice-selection, which uses a slice-selective RF excitation and gradient. This is achieved by switching on a gradient field during an RF pulse, such that the resonant frequency of the spins in the selected slice are matched to the bandwidth of the RF pulse, respectively. In this way, *off-resonance* spins will experience no effect from the RF pulse. Since the slice select RF pulse tips the magnetization into the transverse plane (and hence begins to decay), an MR image can be thought of as a "frame" of said transverse magnetization.

The slice location and slice thickness are determined by the centre frequency of the excitation, ω, the RF bandwidth, $\Delta\omega$, and the gradient field strength G_z. The slice thickness, Δz is given by:

$$\Delta z = \frac{\Delta\omega}{\gamma G_z} \tag{2.22}$$

where γ is the gyromagnetic ratio.

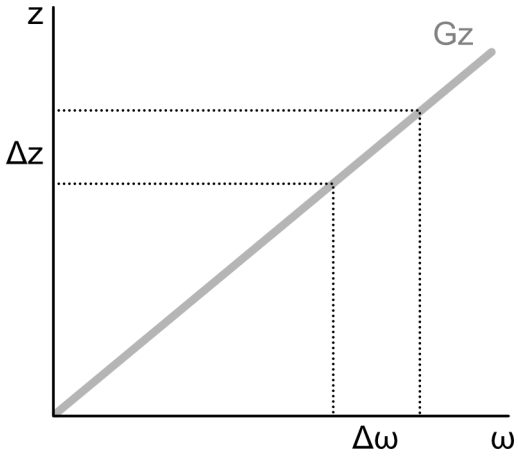


Figure 2.14: Slice selection. A gradient field is applied such that only spins within a slice of interest precess at the desired frequency. The frequency of excitation and frequency bandwidth determine slice location and slice thickness Δz.

In an ideal scenario, only the on-resonance spins would be tipped over by the RF pulse, however, those spins near to the slice "edge" will only be slightly off-resonance and will be tipped over slightly too. The optimum slice *profile* is a rectangular pulse, with a defined thickness and edge; this is mathematically described as a *sinc pulse* (Figure 2.15).

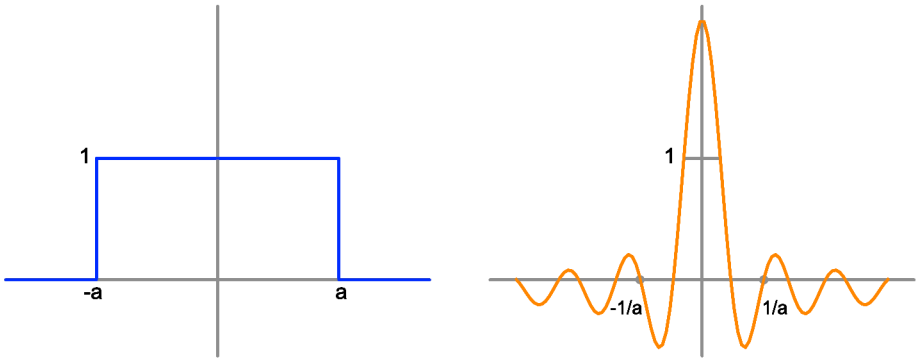


Figure 2.15: A rectangular shape in image space is described by a sinc function in "k-space". The rectangular pulse profile represents a function of position and can therefore be described as a sum of spatial frequencies, achieved by computing the inverse Fourier transform. Note that the sharp edges of the rectangle would be defined ideally by an infinite number of side lobes in the sinc function.

2.5.3 Fourier Imaging

Before we go beyond 1D spatial encoding, we must first discuss the nature of the MR signal, beyond the FID. Any periodic signal can be defined as a sum of sine waves, with amplitude, frequency and phase:

$$s(t) = a_0 + a_1 \sin(\omega t + \phi_1) + a_2 \sin(2\omega t + \phi_2) + ... \tag{2.23}$$

where a is amplitude, ω is the frequency, and ϕ is the phase shift. Note that this is exactly of the same form as Equation 2.1.

The power of the *Fourier transform* lies in its ability to convert a signal in

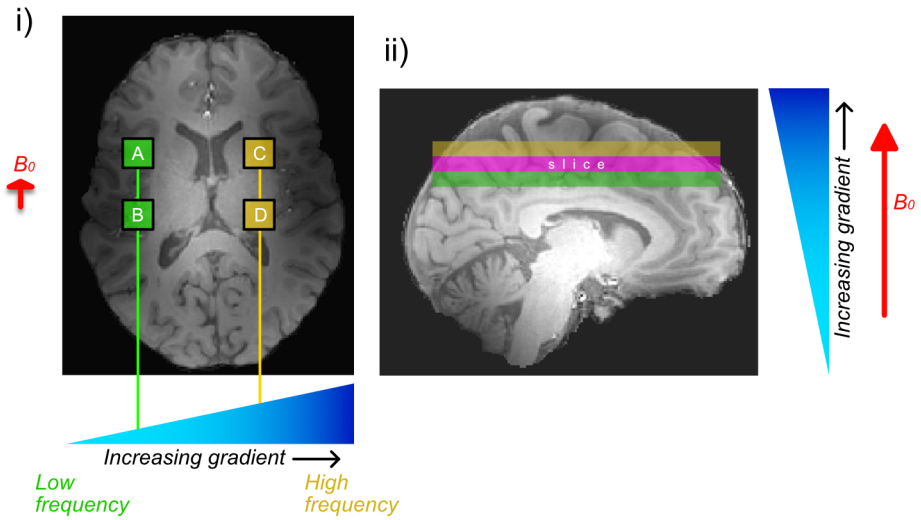


Figure 2.16: A visual description of frequency encoding in a plane and perpendicular to that plane. i) Application of a local gradient field alters the main magnetic field in a spatially dependent way. Here, the gradient field increases from left to right, with corresponding increase in resonant frequency, i.e. pixels A & B possess the same frequency, but a lower frequency than pixels C & D. Encoding in one direction in this plane means that A & B cannot be distinguished from each other. ii) Here, instead we are selecting an entire slice in the sagittal direction (pink), and it can be seen that slices above and below possess different frequencies, thus can be distinguished from each other.

the "time" domain to the "frequency" domain. Thus, a 1D signal can be decomposed into a sum of linear waves, whilst a 2D plane (or image) can be decomposed into a sum of planar waves, having different spatial frequencies. As described above, the ideal RF pulse profile is a rectangle. By taking the *inverse Fourier transform*, we can describe the shape in "image space" as a function in "k-space", where k is the inverse of the spatial wavelength (small values of k reflect low spatial frequencies and therefore long wavelengths).

2.5.4 k-space

We can express the inverse Fourier transform of a 2D image, $I(x, y)$ as $S(k_x, k_y)$, where S is the amplitude of the wave, and k the spatial frequency. These terms are related by the following:

$$S(k_x, k_y) = \int \int_{-\infty}^{\infty} I(x, y) e^{i2\pi k_x, k_y} dx dy \tag{2.24}$$

$$I(x, y) = \int \int_{-\infty}^{\infty} S(k_x, k_y) e^{-i2\pi k_x, k_y} dk_x dk_y \tag{2.25}$$

The simplicity of the above equations stems from the notion that we can describe the transverse magnetization as a complex number, where its magnitude is the signal amplitude, and its phase is the phase angle (due to precession), e.g. $Me^{i\theta}$. Equivalently, we can express the complex number as a combination of real and imaginary components. In this case, the magnetization would be described as a vector $M_{real} + iM_{imaginary}$.

It can be shown that the signal over time (following switching on the gradient and letting the phase evolve for a short amount of time) measures the spatial Fourier transform of the sample scanned. An assumption made is that whilst the spins being imaged may have different phase shifts, their frequency of precession is the same. If this is violated (off-resonance spins, field inhomogeneities), then artifacts will ensue.

k-space is a grid of raw data, i.e. the form of the data that the MR signal traces out during the decay of transverse magnetization. k-space describes the set of spatial frequencies that make up an object in image space, and can be transformed to and from it via the Fourier transform. Each point in k-space corresponds to every image point in the image, and vice versa - there is no one-to-one correspondence. Since k represents the inverse of spatial wavelength, high values of k correspond to short wavelengths, which

are present at the edges of k-space (details); and low spatial frequencies (basic contrast) appear at the centre of k-space.

The MR signal traces out the spatial Fourier transform of the image and this raw data *fills* k-space (see Figure 2.17 to see how this applies to frequency encoding). As discussed previously, each data point in the MR image describes the transverse magnetization as a complex number with magnitude and phase components (or real and imaginary components). In the simplest filling method, k-space is filled one line (or row) at a time. However, so far, we have only described how a single direction (one dimension) of the image can be spatially encoded (frequency encoding), and hence only one row can be encoded. The second dimension and the remaining rows of k-space are typically filled using *phase encoding*.

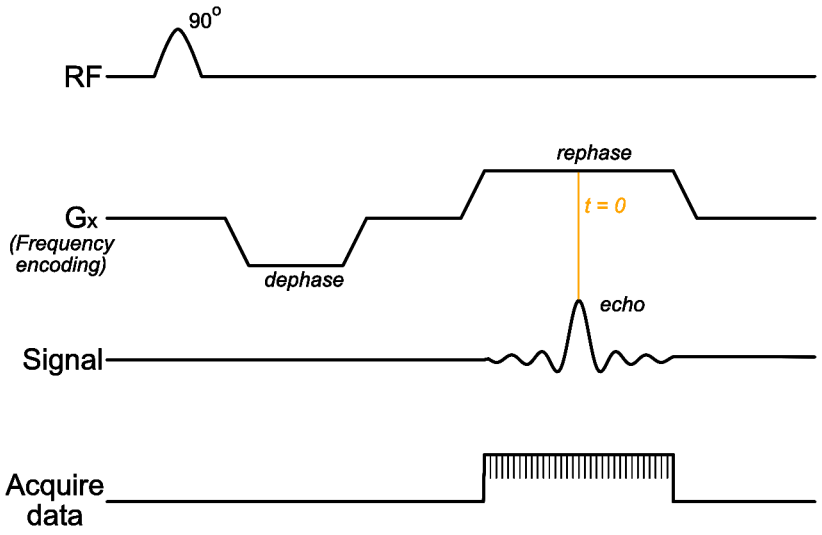


Figure 2.17: Following a 90° pulse, the frequency encoding gradient (G_x) is switched on (second line from the top). The effect of the preceding dephase lobe and doubled length rephase lobe is to ensure that the point where all excited spins are coherent (in phase) occurs at t = 0 (and k = 0). This point occurs at the centre of the data collection window, and becomes crucial when we explore deeper into "filling k-space".

2.5.5 Phase Encoding

When a gradient field is switched on in one direction, the frequencies of protons in one dimension will linearly change, but return back to their original precessional frequency (the Larmor frequency) once the gradient is switched off. The gradient field will also induce a phase shift for the selected protons, which accumulates, i.e. the phase shift does not revert back, but instead following subsequent gradient fields switching on, will continue to accumulate. This phase shift is proportional to the strength of the gradient field, and the time it is switched on for. In a pulse sequence diagram, the area underneath a lobe is proportional to the phase shift, since phase = frequency $\times$ time.

If we take two pixels which both lie along the same axis, e.g. pixel A & B in Figure 2.16, they will both possess the same frequency. If a second gradient is applied prior to and perpendicular to the first frequency encoding gradient, then the two pixels in question will have different phase shifts. If the signal is of the form of a sine wave in each pixel, then the addition of both waves will lead to a signal of the same frequency but an averaged phase (so impossible to discern individually in two dimensions). To locate the individual spins, the perpendicular gradient is applied again, and the difference is calculated between phase shifts in both phase encode steps.

Expanding on Figure 2.18, if we perform a single Fourier transform on the MR signal after one phase encode step, then we will delineate two lines in the frequency encode direction (sums of the frequency values for each pixel). For a two pixel example, knowledge of the accumulated phase differences is sufficient, however, for a typical MR image, which may be a 256×256 plane of pixels, a second Fourier transform is required - since the differences in phase between pixels are not simply multiples of 180°, but are variable. Successive rows are filled in k-space because as the MR signal evolves, phase shifts accumulate, where each time point corresponds to higher and higher spatial frequencies. This process is known as *spin-warp* imaging, and is

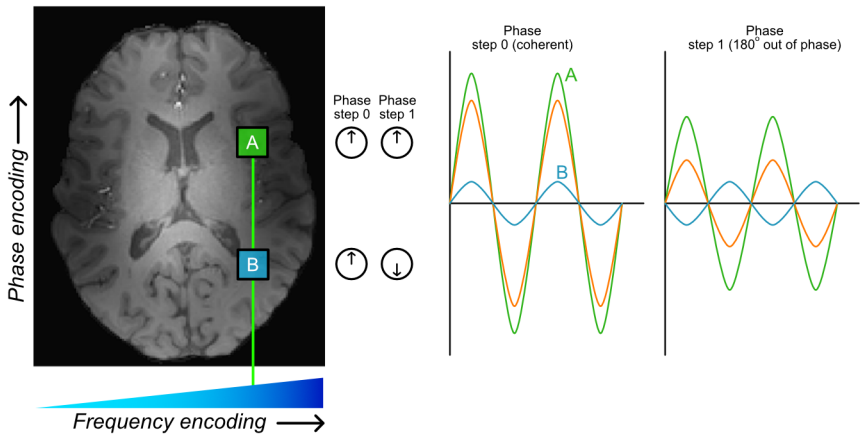


Figure 2.18: An example of phase encoding is given for two pixels. Left) Both pixels A and B in the image have the same resonant frequency, after a gradient field is switched on. At this point (phase step 0), both sets of spins in the pixels will be in phase with each other (since the RF pulse has tipped these spins into the transverse plane and set up phase coherence). A second gradient is switched on perpendicular (phase-encoding gradient) and this serves to add a phase shift along the perpendicular axis, such that both pixels now possess different phases (phase step 1). If the MR signal is acquired after each phase-encode step, the differences in accumulated phase between steps will allow each pixel to be located in the plane. Right) For a 180° phase shift, comparing the difference in phase shift across phase encode steps allows A and B to be determined.

the most common method for spatial localisation. The full GRE imaging sequence is depicted in Figure 2.19.

2.5.6 Resolution

There are a few important points remaining regarding the properties of k-space such as *field of view*(FOV) and *pixel width*(Δw). In the 2-dimensional case, the FOV refers to the area over which a single 2D image is acquired. The spacing between rows or columns in k-space is Δk and FOV in k-space is k_{FOV} or equivalently $2k_{max}$. The key equations are:

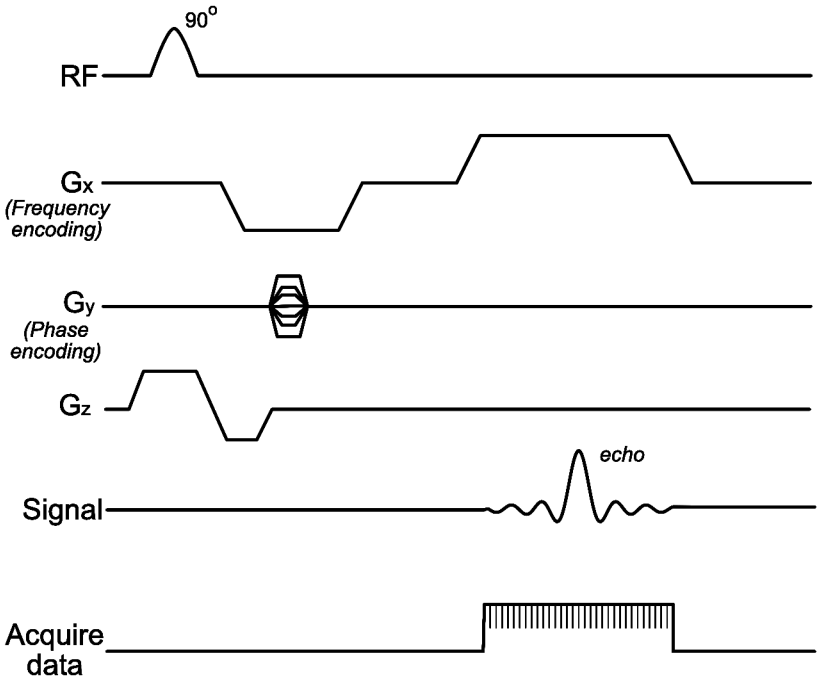


Figure 2.19: This pulse sequence is identical to Figure 2.17, except we have now added in the pulse sequence lines for phase encoding (G_y) and slice selection (G_z). First a slice is selected using an idealized rectangular RF slice profile. The frequency gradient is switched on in the x-direction, such that frequency projections of pixels in a single plane are encoded. The phase-encoding gradient is switched on in the y-direction, such that after one step, a single "row" in the image plane is visualized, via a 2-dimensional Fourier transform, utilising the accumulated phase differences between pixels along the y-direction, and then the entire sequence is repeated. At each repetition, the same frequency gradient is applied but the phase-encode gradient is incremented, so that the entirety of k-space is filled, row by row (this is simplified by showing some of the increments in a single line on G_y). Note: the downward lobe portion of G_z is used to correct for transverse phase decay, otherwise reducing the signal.

$$\Delta k = \frac{1}{FOV} \tag{2.26}$$

$$\Delta w = \frac{1}{2k_{max}} \tag{2.27}$$

These equations describe 1) the inverse relationship between spacing in k-space and image FOV, e.g. larger k-space sampling results in a smaller image FOV, resulting in image wraparound. Image wraparound occurs equivalently when the object to be imaged extends beyond the FOV; 2) the inverse relationship between the pixel width and k-space FOV, e.g. a smaller k-space FOV, centered around k_0, will negate measuring high spatial frequencies and hence the image will look blurry.

The process of acquiring signal values present in an image from the grid of raw data points in k-space is known as reconstruction. If one were to reconstruct a single point into image space, but reduce the "true" pixel size, then the single point will appear blurred or spread out across many pixels in the image (not a single pixel) - the shape of this spreading out is described by the *point spread function* (PSF). Ideally, to map the full snapshot of magnetization in our image, the k-space distribution would have to extend to infinite values of k. In reality, values of k_{max} and the spacing Δk make the sampling discrete and finite, respectively. Thus the reconstructed image is in fact a close approximation of the true object.

2.6 Scanner hardware

In this section, the hardware that is required to acquire and spatially encode the MR signal is described. In addition to the static magnetic field (B_0), a set of gradient coils and radiofrequency coils are required to produce and measure the NMR signal.

2.6.1 Coils

An MR scanner consists of multiple layers of coils of wire (Figure 2.20). The innermost coils are the main B_0 coil, which contains superconducting coils

to provide the internal field. Superconductivity is a phenomenon exhibited by certain materials whereby below a certain temperature (T_c), electrical resistance is 0. Typically, all materials show a decrease in resistance as the temperature decreases, since the scattering of free electrons due to thermal vibrations is reduced. Using superconducting wire loops is the basis for the construction of high field (1.5, 3, and 7 Tesla) magnets, which, if kept below a critical temperature (kept cold using liquid helium or nitrogen), the current loops should theoretically not dissipate and hence the magnetic field (B_0) will be constantly "on".

Next, are more shim coils to improve the inhomogeneity of the main magnetic field, and then the *gradient coils*, which are fundamental to image acquisition to encode the image in three dimensions. Within the gradient coils sits the receive and/or transmit (or combined) radiofrequency (RF) coils which are used to detect/transmit RF waves, to exploit the NMR phenomenon.

Gradient coils are typically large cylindrical loops of windings and/or etchings, that are used to distort the B_0 field in x, y or z directions. The additional fields add to B_0, which lies along the z-axis, thus linearly varying B_z along a chosen axis. Spatial encoding of atomic nuclei resonant frequencies allows images to be discerned.

The gradient coils are powered via external amplifiers, which are cooled by a chilling system. The gradient coils inside the scanner bore also heat up - this is caused by eddy currents and resistive heating as current is pulsed through the coils. Eddy currents are set up during scanning due to rapidly changing magnetic fields ("gradient switching") used to spatially encode the MR signal; these induced currents are predicted from the *Faraday-Lenz* law. Since the magnitude of the eddy currents is proportional to the rate of change of the magnetic field, the more rapid the pulsing on and off of the gradients, the greater the eddy currents, e.g. in fast imaging sequences such

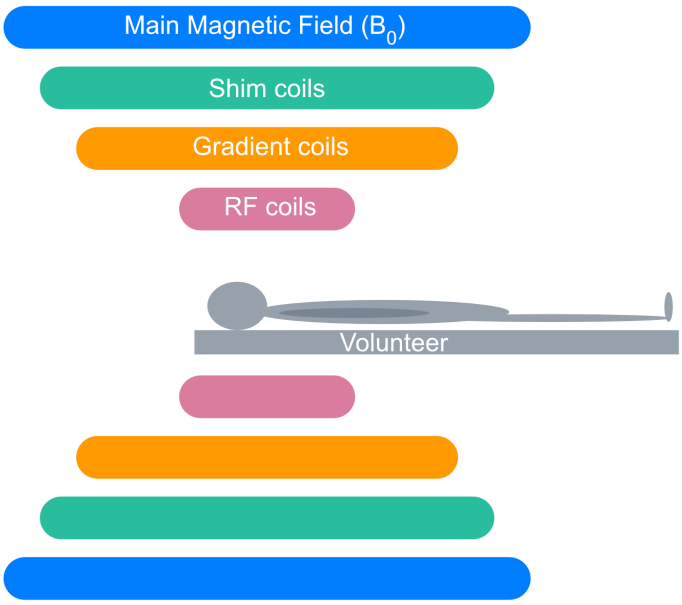


Figure 2.20: An MRI scanner is a coil within a coil within a coil within a coil. Working inwards, we proceed from the windings comprising B_0, the shim coils, gradient coils and finally the radiofrequency (RF) coil(s).

as Echo-Planar Imaging.

The RF coil transmits radiation at specific resonant frequencies into a system of spinning nuclei, and a second RF "receive" coils detects the MR signal produced. This detection is the induced current produced by the sweep of the net magnetization. The rate of energy deposition into the body by an RF pulse is known as the specific absorption rate (SAR). RF pulse energy $\propto$ (EM field amplitude)^2, and hence SAR $\propto$ (flip angle)^2.

The 7 T scanner in Nottingham uses a 32 channel Nova medical receive coil, shown in Figure 2.21.



Figure 2.21: A 32 channel Nova medical receive head coil, used in the Philips Achieva 7 T MRI in Nottingham.

2.7 Conclusion of Chapter

A system of protons placed in a magnetic field will undergo precession at a resonant frequency, the Larmor frequency, since each proton possess a magnetic moment and spin angular momentum. After a time, an equilibrium magnetization will be setup, such that a tiny proportion of protons preferentially align along the main magnetic field - this comprises a net bulk magnetization. Application of a radiofrequency pulse tips this "longitudinal" magnetization into a transverse plane, whereby relaxation occurs at rates determined by the sample's T_1 (longitudinal recovery) and T_2 (transverse decay). The sweep of the transverse net magnetization induces a current in a receiver coil, producing a detectable signal. Gradient fields are switched on during the RF pulse to manipulate the frequency of protons, and instil an accumulated phase, such that spatial localization can be achieved in two-dimensions, via a 2D-Fourier transform.

CHAPTER 3

3 Advanced Imaging Techniques

3.1 Overview of chapter

Chapter 2 described the fundamentals of NMR and MRI. We can now assess how the image acquisition can be optimized, and the use of functional MRI (fMRI) to investigate neural signals in the brain in a snapshot.

In this chapter, the more specialised imaging techniques utilised during the work presented in this thesis are described. This includes faster acquisition methods such as Simultanaeous Multi-Slice (SMS or *Multiband*), the advantage and limitations of ultra-high field imaging (7 Tesla), and fMRI with the use of the endogenous blood oxygenation level dependent (BOLD) contrast.

3.2 Fast imaging

Imaging speed can be increased through unique methods of traversing k-space, utilising multiple receive coils to better resolve the MR signal, and by implementing simultaneous multiple slice (SMS) or multiband (MB) excitation. These concepts are outlined in the following section.

3.2.1 Partial Fourier Imaging

Raw data is acquired in MRI through the filling of k-space. The *conjugate symmetry* of k-space can be taken advantage of to reduce imaging time. Each

data point in k-space has been previously described as a complex number, with real and imaginary components, of the form $a+ib$, where the conjugate of the same point is $a-ib$. If we define k-space as a square grid, and draw two lines representing the k_x and k_y axes, the complex conjugates of data points can be found by mirroring across the origins of k_x or k_y (Figure 3.1).

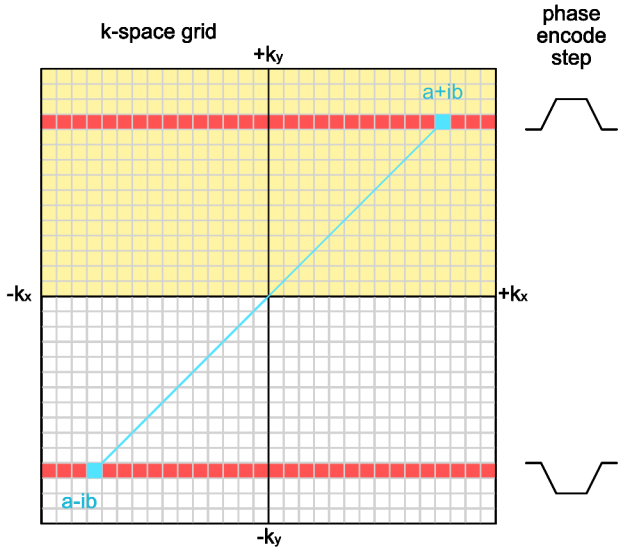


Figure 3.1: An example of k-space symmetry. The mirror of a point in k-space, passing through the origin possesses the same magnitude, but opposite phase. An extension of this idea is that one half of k-space can be made redundant. Only measuring half of k-space and estimating the remainder significantly reduces imaging time. The figure is a specific example of *phase-conjugate* symmetry, where the top (golden) half of k-space is measured, while the bottom half is estimated. In reality, the minimum k-space sampling is typically 65%.

The use of "half-Fourier" or *phase-conjugate* acquisition methods (Figure 3.1) allows many phase-encoding steps to be skipped, reducing the imaging time, but correspondingly this reduces SNR. This option of reducing k-space is defined as "halfscan" on Philips scanners.

3.2.2 Echo Planar Imaging

Echo Planar Imaging (EPI) is a method of sampling the entirety of k-space rapidly, following a single RF pulse: following excitation, gradient coils are switched back and forth, such that the trajectory of k-space traversal during image acquisition proceeds in a "raster" fashion (Figure 3.2). This is termed "single-shot EPI" (Mansfield, 1977).

For a given FOV and resolution, the rate of k-space traversal for the EPI method is determined by the strength of the gradient and the speed of switching. The rate of gradient switching is determined by the *slew rate* (maximum rate of change of the field) and the *rise time* (the time for the gradient to reach maximum strength from 0). Note that the slew rate = maximum gradient strength / rise time. The maximum gradient strength for a 7 T scanner is 40 mT/m, and a slew rate of 200 T/m/s, though often 33 mT/m and 166 T/m/s is used.

There are safety issues concerned with the rapid gradient switching in EPI. EPI can cause additional peripheral nerve stimulation (PNS), due to the rapid rate of change of the local magnetic field (hence the need to limit the slew rate). The changing magnetic field can induce currents in the body, since the gradient is reversed and powered up to its maximum negative or positive value at each switch. Furthermore, acoustic noise is exacerbated by the gradient switching: as the current is pulsed through a gradient coil, an associated magnetic force serves to move the coil against the epoxy/scanner, producing a tapping noise. This can be alleviated to a degree by adorning ear protection.

"Ghosting" in EPI refers to shifted, faint repeats of the object in the image, in the phase encoding direction. This effect occurs due to alternate sampled lines in k-space not being equivalent, i.e. there is a difference in even and odd lines in k-space. It is important to ensure that every even and odd echo

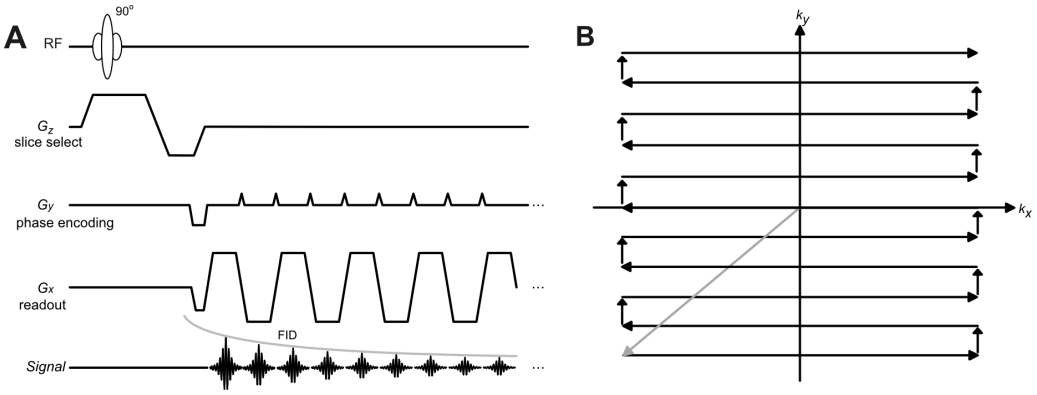


Figure 3.2: Echo Planar Imaging. A) The pulse sequence for a GRE-EPI acquisition: The frequency encoding gradient (or "read-out" gradient) switches back and forth between positive and negative, so that an echo occurs at the centre of each acquisition window. The sign determines the x-direction of traversal through k-space. The phase encoding gradient progresses through each line via small *blips*. B) k-space trajectory for an EPI acquisition. Initial negative lobes for G_x and G_y serve to move the start of k-space sampling to the bottom left of the grid $(-k{+}max)$, and then the rastering pattern follows moving back and forth through k-space.

are mirror images, otherwise small offsets will propagate into later echoes (peaks of even and odd will not line up after the FFT). This manifests as a phase error, and the ghost images are shifted N pixels / 2.

Distortions in EPI occur due to a violation of an assumption of MR theory: that all spins precess at the same rate in the absence of any gradient fields. This assumption falls down because there are multiple tissue types/borders in the brain, and hence field variations. One can correct for this by acquiring a B_0 field map, and correct distortions in post-processing - this is possible across the dynamic frames collected. The degree of distortion is proportional to the time it takes to acquire an image, which itself is inversely proportional to the SNR; hence there is a trade-off. Techniques such as parallel imaging also serve to reduce distortions in EPI, by reducing the acquisition time of k-space for an image (see Section 3.2.4).

3.2.2.1 Off-resonance effects

This effect occurs when there are spins precessing at different rates, without any gradient field switched on. One example of a resonance offset is the difference between ^{1}H in fat and in water: the fat protons have better electron shielding, and experience a weaker local magnetic field, resulting in a lower resonant frequency than water protons. This results in a mis-mapping of fat relative to water, along the frequency encoding direction.

In EPI, mis-localization of fat/water is evident in the phase-encoding direction, due to off-resonance effects. This occurs most dramatically using EPI because all of k-space is measured following a single excitation pulse, and hence phase shifts from off-resonance effects will accumulate in the y-direction. Smoother distortions also occur in EPI, due to smooth field variations. Distortions in EPI are proportional to the acquisition time, and also to B_0: one can reduce the acquisition time using parallel imaging, but this will reduce SNR, or one can raise the field strength (increasing amount of equilibrium magnetisation) and SNR, but this also increases magnetic susceptibility effects, and hence distortions.

3.2.3 Volume Acquisition

In the 2D situation, a single slice is excited and spatially resolved in a single plane, i.e. the x-direction is encoded using frequency encoding and the y-direction is encoded using phase-encoding, such that each line in k-space is measured sequentially, by incrementing the phase encode (y) gradient (raster), or, in the case of 2D EPI, the entire slice is excited at once, and rapid gradient switching (phase-encode blips) allows rapid zig-zag k-space traversal.

In the 3D situation, a secondary phase encoding process occurs to resolve

the z-direction, and the slice excited now becomes a thick "slab". Since the image space now contains a measurable z-component, so will k-space, and hence image acquisition proceeds to fill 3D k-space.

The acquisition time increases in proportion to the number of z-coordinate phase encoding steps, hence volume acquisition tends to take longer than 2D. However, there is a large improvement in SNR with volume imaging, since all voxels in the slab contribute to the overall image, whereas in 2D, voxels in different slices do not contribute to SNR in other slices. Acquisition time can be reduced by reducing the TR, which is possible with a gradient echo sequence. Furthermore, with 3D-EPI, it is possible to use parallel imaging (see Section 3.2.4) in both phase encoding directions, shortening the acquisition time of the 3D volume.

The Magnetization Prepared Rapid Gradient Echo (MPRAGE) pulse sequence is a common volume imaging technique used in MRI: an initial preparatory inversion pulse is followed by fast GRE acquisition; this leads to strong T_1 weighting (good difference between GM and WM) and can be used to collect high resolution images (Mugler and Brookeman, 1990).

3.2.4 Parallel Imaging

Parallel imaging (PI) refers to the use of multiple independent receive coils which localize the MR signal simultanaeously (in parallel). The receive coil in the 7 T in Nottingham has 32 receive channels. The signal recorded by each receive coil varies as a function of position. Typical MR imaging can use multiple coils (e.g. multiple surface coils), where the individual outputs are combined into a complex signal; PI on the other hand processes the individual signals from each separate coil at the same time. The benefits of PI arises in the reduced imaging time afforded by a fewer number of phase-encoding steps, i.e. undersampling of k-space (Deshmane et al., 2012;

Glockner et al., 2005; Larkman and Nunes, 2007). The reader will note that reducing the number of steps in the phase-encode direction will consequently reduce the FOV, and also lead to image wraparound - this artifact is also known as "aliasing". PI increases the width of the sampling interval, but then recovers the sampling required by the Nyquist theorem by measuring the coil sensitivities - this is the basis of increasing acquisition speed.

While PI delivers reduced acquisition time, e.g. R = 2 (halving the number of phase encode steps or equivalently, doubling the k-space sampling distance), the downside is a reduction in SNR, i.e. $\sqrt{R}$.

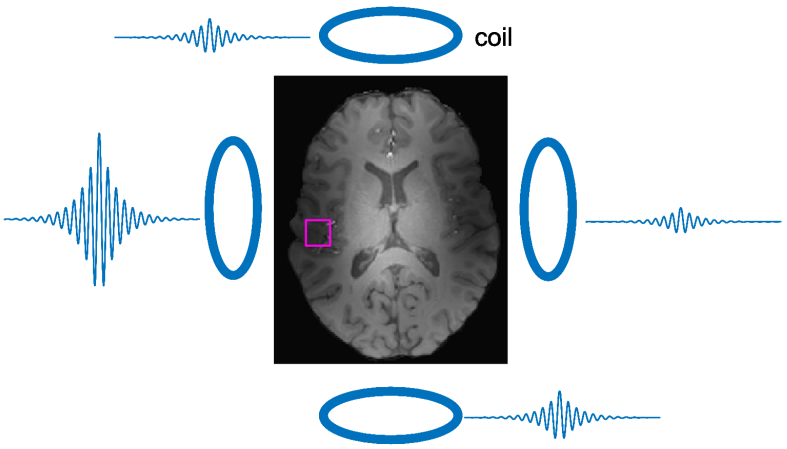


Figure 3.3: Multiple receive coils allow spatial localization of the MR signal. The unique coil sensitivities are used to reconstruct the image via anti-aliasing methods such as SENSE. Imaging time is reduced through reduction of phase encode steps.

Aliasing occurs due to the sampling rate of a signal being too low; thus its frequency is incorrectly determined. The *Nyquist sampling theorem* states that "the sampling rate must be at least twice the highest frequency in the signal" for a correct measurement. The MR specific explanation of this artifact relates to phase mismatch: an object being imaged exceeds the FOV; the phase cycle for a single phase-encode step is from 0°to 360°; parts of the object that exceed these values (e.g. from 361°to 450°), will be given

incorrect values of $360 - 1$ and $450 - 360°$; this is visible on the image as foldover or wraparound. The phase-encode direction chosen during scanning will affect which side of the image is wrapped on to another. The simplest method of alleviation is to increase the FOV (however this leads to a drop in spatial resolution, which can be corrected for by adding more phase-encode steps, which itself increases the imaging time).

"Unaliasing" or "unfolding" the aliased image is performed by techniques such as *SENSitivity Encoding* (SENSE) (Pruessmann et al., 1999), or GeneRalized Autocalibrating Partial Parallel Acquisition (GRAPPA) (Griswold et al., 2002). PI reconstruction on the Philips scanner as employed in the work in this thesis uses SENSE; a more detailed description of this technique is given below.

3.2.5 SENSitivity Encoding

All parallel imaging methods require that the sensitivity of each coil be measured to unalias the resulting image, acquired through undersampling k-space. SENSE gathers this information by collecting a pre-scan, and the subsequent reconstruction is performed in image space (unlike GRAPPA, where reconstruction is performed in k-space). In Chapter 2, we saw that $\Delta k = \frac{1}{FOV}$, hence, if we double the spacing between k-space lines, we will halve the FOV in image space. Generally, for a reduction factor (or acceleration factor), R, the individual coil FOV will be reduced by $\frac{1}{R}$. In image space, this reduction in FOV manifests as image wraparound or "foldover", a type of aliasing - one way to understand SENSE is as an unfolding reconstruction algorithm (Blaimer et al., 2004).

For example, if we have 2 coils detecting an object, each covering only one half of the FOV (in reality, there is no sharp boundary, rather a gradual signal reduction as a function of distance from the coil), we only have to

collect half of the usual phase encode steps. For a single coil covering the entire FOV, we would require the full phase encoding steps in k-space. The two coil (half FOV) images are collected simultaneously (independently), hence halving the imaging time, hence "parallel" imaging. Finally, the half FOV images can be combined, e.g. using sum of squares. In this example, the reduction factor is 2, and so the SNR will be reduced by $\sqrt{2}$. This example can be generalized to parallel MRI, rather than solely for SENSE.

To unfold the aliased images, there must be at least as many independent coils as R, the number of pixels to be separated (or in other words, the reduction factor). In addition to the SNR loss associated with skipping phase encoding lines, there is also a penalty incurred based on matrix inversion difficulty, known as the *g factor*. How easy it is to perform the matrix inversion depends on how different the rows are from one another (independence) in the sensitivity matrix $\hat{C}$, which in turn depends on coil geometry. This is depicted in Figure 3.4. Thus, the SNR loss is

$$SNR_{SENSE} = \frac{SNR_{full}}{\sqrt{R} \cdot g} \tag{3.1}$$

SENSE involves first generating coil sensitivity maps, then acquiring undersampled k-space data, reconstructing the partial FOV images from each coil, unfolding the aliased images via matrix inversion and finally combining them. The generation of the coil sensitivity maps are arguably the most important step in SENSE, since any errors at this step will cause residual aliasing in the final full FOV image, e.g. motion between calibration scan and functional scans will result in reconstruction artifacts.

Advantageously, pushing the acceleration factor higher with SENSE, with single shot EPI for example, can reduce blurring, signal loss (T_2^* related), and distortion from off-resonance spins. However, the reconstruction of EPI with SENSE can be difficult, since distortions will be different between the

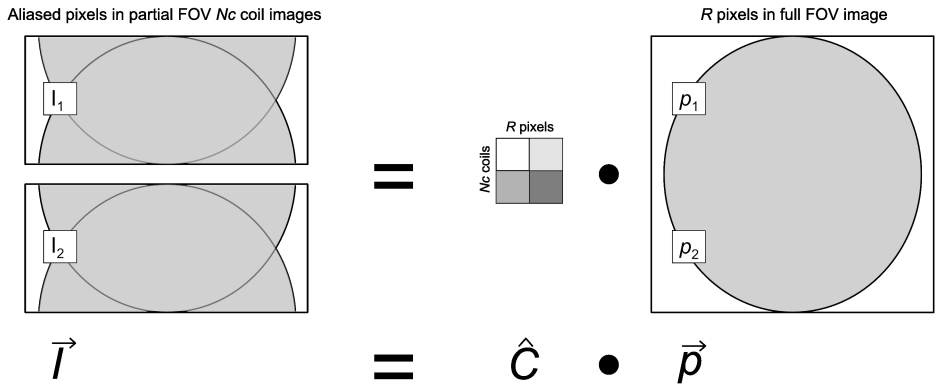


Figure 3.4: SENSE for 2 pixels, 2 coils. For the hypothetical situation of having two independent coils, imaging a sphere, we can select 1 pixel in each of the reduced FOV images (one from each coil). These aliased pixels **I** are the product of the sensitivity matrix $\hat{C}$, with N_c rows (number of coils) and R pixels (from the desired full FOV image, equivalent to the acceleration/reduction factor), and the vector ρ, full set of R pixels in desired full FOV image. Generalized matrix inversion (or Moore-Penrose pseudoinverse) is used to unfold the images and hence solve for ρ, per pixel. Note that the number of pixels to be separated (the acceleration factor) must not exceed the number of coils.

calibration scan and the EPI images.

There are several things to consider when using SENSE: SENSE requires that the FOV be greater than the object image, to prevent any additional aliasing (known as the "SENSE ghost"). Since the SENSE algorithm operates pixel by pixel, if the coil sensitivity maps are inaccurate, then local noise changes may manifest in the final image. Increasing acceleration factors result in higher g-factor related artifacts, which manifests as noise enhancement (graininess) in SENSE images. Typical SENSE factors used in this thesis are SENSE 1.5, 2 or 3.

3.2.6 Simultanaeous Multi-Slice (SMS)

In a typical MRI experiment, a slice-selective RF pulse is used to select a single slice with a given thickness. Thus, it is only in this particular slice that spatial encoding occurs until the next RF pulse excites a different slice. "Simultaneous Multi-Slice" (SMS), is an acquisition technique that uses a multi-radiofrequency (*Multiband*) spectrum excitation to selectively excite multiple slices and acquire them at once (Larkman et al., 2001). Since more slice are acquired during one excitation pulse, i.e. one TR, the imaging speed will be greater than usual single slice excitation. Additionally, there is no SNR loss due to undersampled data (as in parallel imaging), since each slice is excited identically, however, g-factor losses do appear due to image aliasing (Moeller et al., 2010). Slice images acquired are aliased, and separation is achieved using SENSE - exploiting different sensitivities of multiple coils, along the slice direction.

The total acceleration factor is defined as the SENSE factor (in-plane phase-encoding reduction factor) multiplied by the Multiband factor (number of slices excited / number of different bands in the RF pulse). For example, one such study demonstrated SMS-GRE-EPI at 7 Tesla, with 16-fold acceleration (multiband factor 4 $\times$ SENSE factor 4), using GRAPPA to unfold the aliased images (Moeller et al., 2010).

For functional imaging, EPI is the most common imaging readout, and is usually collected as a GRE scheme, and with the advent of parallel imaging and SMS, SMS-GRE-EPI with SENSE reconstruction is now a standard, albeit cutting-edge, imaging method to acquire high quality functional MRI data. SMS-EPI also has a shorter echo train length, reducing image blurring caused by T_2^* decay (reduced acquisition time, less effects from relaxation on the measured signal - this effect is equivalent to smoothing with an altered windowing function in k-space).

3.2.7 Controlled Aliasing In Parallel Imaging Results In Higher Acceleration (CAIPIRINHA)

Parallel imaging methods require knowledge of coil sensitivities to separate out aliased images, whether accrued through undersampling k-space or simultanaeous slice excitation (see Section 3.2.6). SENSE performs the unfolding by an iterative, pixel-wise matrix inversion algorithm, whereas GRAPPA "fills" in the missing k-space lines, prior to image reconstruction. The efficiency of the matrix inversion in SENSE is measured by the g-factor, and this is dependent on the coil independencies, i.e. if the spatial variation of the receive coils are too similar, e.g. over a small slice stack / small ROI, then the g-factor will rise, indicating a more difficult matrix inversion.

CAIPIRINHA eases the matrix inversion by introducing spatial shifts in aliasing patterns of multiple slices. The scheme of k-space undersampling is altered, such that the spatial distance between aliased voxels is increased. The premise of this technique is the fact that adding phase shifts or modulation to the phase-encode direction in k-space, shifts the Fourier-transformed image - this can be achieved via RF pulses with different phases. Thus, slices can be shifted in this way as well, by adding phase modulation to a multiband RF pulse (Breuer et al., 2005). Subsequently, the g-factor in CAIPIRINHA is affected by the phase modulations, as well as the coil arrangement.

$$SNR_{CAIPIRINHA} = \sqrt{NS} \cdot \frac{SNR}{g_{CAIPIRINHA} \cdot \sqrt{R}} \tag{3.2}$$

where NS is the number of simultaneously excited slices.

For CAIPIRINHA, SNR increases with the square root of NS and increases due to an improved g-factor.

In the extreme scenario, where two coil sensitivities will be the same at two slice locations, the SENSE algorithm would fail, the aliased pixels would have the exact same sensitivities and be inseparable, however, due to the spatial FOV shifts via CAIPIRINHA, the pixels can be separated since they will be guaranteed different sensitivities (since we can affect sensitivity in the slice encoding direction as well).

CAIPIRINHA has been shown to work with conventional FLASH, by using a multiband RF pulse with phase modulation, alternating the phase of every other line in k-space, resulting in FOV/2 image shift for the excited slice. This method is not suited to EPI, since readout in the phase-encode direction occurs after a single RF pulse. "Blipped"-CAIPIRINHA or just blipped-CAIPI, is a modification to the original method by adding phase cycling; short gradient blips in the slice-select direction, at the same time as the blips in the phase-encode direction of normal EPI. The slice-select direction blips are sign-reversed each time to avoid accruing phase variation in the through plane direction. Blipped-CAIPI thus adds a shift in the phase-encode direction, demonstrated to work with SMS-EPI (Setsompop et al., 2012).

3.3 Ultra High Field (UHF) Imaging

3.3.1 Field strength and Energy states

As well as advances in faster imaging, technological advances in hardware have motivated a push towards higher field strength (B_0). With increasing B_0, the energy difference between the spin-up and spin-down proton population states (occurring due to Zeeman splitting), increases, thus due to the dependence of field strength on the Boltzmann distribution, the number of spins in the lower (parallel) energy state will be slightly greater, leading to

increased signal in an NMR experiment.

3.3.2 7 Tesla MRI

A magnetic field strength of 7 T and above is considered "Ultra-High" and 9.4 T studies are now being used for human participants. At high field, the sensitivity and specificity of the Blood Oxygenation Level Dependent contrast (BOLD) is higher (Ugurbil et al., 2007; Yacoub et al., 2001), an indirect measure of neural activity which is explained in more detail in Section 3.4. This endogenous contrast is used in Functional MRI (fMRI) to identify regions of "activation" during some sort of task; this is the most simplified version of an fMRI experiment. Additionally, larger areas of activation are measurable at higher fields (Ugurbil et al., 2007).

The increased energy gap between spins leads to a linear increase in SNR at UHF. This higher SNR can be traded for increased spatial resolution, i.e. a smaller voxel will have less SNR than a larger one, however, at high fields, the SNR of a small voxel will be acceptable, relative to the same small voxel at a lower field, where the data SNR will be limited. At higher fields, the echo time must be reduced (TE $\approx T_2^*$), since T_2 drops. This is explained in more detail below.

Since functional MRI acquires a voxel timecourse, a measure of image quality, i.e. image signal-to-noise ratio, iSNR, is less appropriate than measuring the image quality across time, i.e. temporal signal-to-noise ratio (tSNR). This is the voxel-wise mean signal intensity divided by the voxel-wise noise in the image time-course. If physiological noise (cardiac, breathing, etc.) and thermal noise (random motion of electrons in the receive coil), are assumed to be independent, then the denominator becomes the standard deviation of the signal.

$$tSNR = \frac{\bar{S}}{\sqrt{\sigma_0^2 + \sigma_p^2}} \tag{3.3}$$

where $\bar{S}$ is the mean image signal intensity, σ_0^2 is the thermal noise component, and σ_p^2 is the physiological noise component.

Triantafyllou et al. (2005) compared physiological noise across field strengths, observing that this noise component was dominating at high flip angles, at high fields (3 T and 7 T). They also validated several findings: tSNR rose asymptotically with SNR; image SNR increased with voxel volume; and the ratio $\frac{\sigma_p^2}{\sigma_0^2}$ rose with voxel volume; as did tSNR, with the largest gains occurring at 7 T (Triantafyllou et al., 2005).

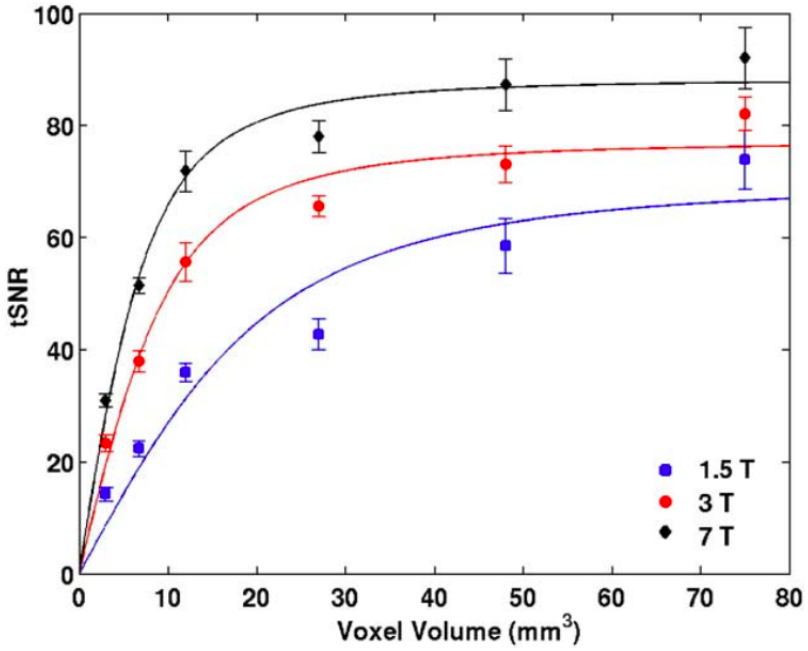


Figure 3.5: Time-course SNR (tSNR) as a function of voxel volume. Data are averaged over 5 subjects, at each field strength, derived from grey matter. Reproduced from Triantafyllou et al. 2005 (Triantafyllou et al., 2005).

At high field, blood-related contributions to the BOLD response, i.e. large

vessels, are diminished (Yacoub et al., 2001), while the microvascular contribution is enhanced, leading to greater specificity. Additionally, using a spin-echo sequence at high fields may be more advantageous than a gradient echo: the reduced T_2 of blood eliminates the extravascular BOLD effect from the veins, increasing specificity (Yacoub et al., 2003). Note that at higher fields, the reduced T_2 implies that a reduced field of view is limiting, since the usable echo time is shortened. A discussion of the mechanisms contributing to the BOLD effect is presented in more detail in Section 3.4.

The B_1 field is susceptible to greater inhomogeneity at higher field; the Larmor frequency increases, and hence the wavelength inside the head will decrease, such that strong electromagnetic interactions occur between the RF coil and the inhomogenous, asymmetric head (interference patterns (Keltner et al., 1991; Yang et al., 2002)). The wavelength is inversely proportional to the square root of the relative permittivity (Vaidya et al., 2016).

$$\lambda \propto \frac{1}{\sqrt{\epsilon_r}} \tag{3.4}$$

where λ is the wavelength inside the head, and ϵ_r is the relative permittivity (dielectric constant).

For a mean dielectric constant of 64 (grey matter), the wavelength of RF transmission inside the head is 12.5 cm at 300 MHz at 7 T, which is almost half the diameter of the largest head dimension (Ibrahim et al., 2001). In addition to the shortened wavelength at higher fields, RF power deposition increases, since a higher frequency is required to achieve the Larmor condition (field fluctuations are faster, more energy transmitted and absorbed by the tissue); this leads to an increase in tissue heating (Schick, 2005).

As well as the B_1 field, susceptibility effects caused by inhomogeneities in the static field (B_0) are worse at higher fields. This can be quantified by

measuring T_2^*, which is reduced at higher fields (Dietrich et al., 2008).

For EPI, the severity of artifacts is aggravated as field strength increases. Geometric distortions (caused by persistence of off-resonance effects in the phase encode direction) are worsened; signal dropouts occur by local dephasing due to inhomogeneity of B_0 (can be remedied by reducing voxel size); the number of slices per second is reduced due to SAR limitations at higher fields, however, this may be mitigated through parallel imaging / SMS techniques; and finally, the enduring acoustic noise caused by fast gradient switching, intrinsic to EPI (Speck et al., 2008).

With relevance to Multiband and PI techniques, at higher fields, the coil sensitivity profiles have better spatial variability (Wiesinger et al., 2004), making each coil more independent than another, allowing higher parallel imaging acceleration (Setsompop et al., 2016).

3.4 Functional Imaging

In this section, an overview of measuring functional brain responses using the blood oxygenation dependent contrast (BOLD), in response to neural activity is described. The BOLD effect is an indirect method of measuring neural activity, and its interpretation has many caveats - what follows is a concise outline, beginning with energy expenditure in the brain, and ending with the profile of the haemodynamic response function.

3.4.1 The BOLD effect in brief

In addition to measuring the static transverse magnetization to acquire T_1 / T_2-weighted images, etc., one can measure the functional activity of a voxel in response to a task. Functional MRI takes advantage of the magnetic

susceptibility difference of oxyhaemoglobin (HbO_2) to deoxyhaemoglobin (dHb): the endogenous deoxygenated version of haemoglobin, which is used for transporting oxygen within the blood, to tissues.

At rest, arterial oxygenated blood (containing diamagnetic HbO_2) reaches the brain, and approximately 40 % O_2 is extracted. The venous blood therefore contains a significant fraction of paramagnetic deoxyhaemoglobin, which has a positive magnetic susceptibility, and causes a decrease in the MR signal. Upon brain activation in response to a task, the rise of CBF and cerebral blood volume (CBV) is much greater than the cerebral metabolic rate of oxygen consumption ($CMRO_2$), causing increased venous blood oxygenation, flushing out the dHB in venous blood, and paradoxically causing a local increase in the MR signal in active voxels.

3.4.1.1 A brief history of BOLD fMRI

The origin of the BOLD contrast begins with the investigation of haemoglobin in the 1930s by Linus Pauling (Pauling and Coryell, 1936). Pauling elucidated deoxy-Hb's paramagnetic properties (unpaired electrons and a magnetic moment), that distort an external magnetic field.

Later, in the 1990s, researchers led by Seiji Ogawa scanned rodents at high MR field strengths to maximise the difference between transverse relaxation rates of HbO_2 and dHb. By changing the amount of oxygen the rodents breathed, the scientists could discern that deoxy-Hb (in normal air) reduces the MR signal, compared to oxy-Hb (pure oxygen) (Ogawa et al., 1990a,b, 1992). Further work on anaesthetised rats, combined with EEG, suggested that the BOLD contrast depended on oxygen demand caused by neural activity. The amount of deoxy-Hb depends on oxygen consumption (neural demands) and supply (blood flow).

The growth of fMRI stemmed from the development of echo-planar imaging

in the 1970s, which allowed images to be collected rapidly; as well as the ubiquity of clinical MR scanners, which rose in demand due to its non-ionising assessment of the body. In 1992, Kwong and colleagues used BOLD contrast to image brain activation to visual stimulation at 1.5 T (Kwong et al., 1992); these findings were confirmed by several other groups (Blamire et al., 1992; Frahm et al., 1992); as well as in motor cortex (Bandettini et al., 1992).

The studies described above were some of the first to investigate the BOLD signal, using simple, but very important paradigms. The remainder of this chapter explores in more detail the neural origins of the BOLD signal, optimization of pulse sequences and paradigms, and the physiology of the haemodynamic response function (HRF).

3.4.2 Energy expenditure in the brain

Blood flow delivers both O_2 and glucose to the brain: glucose moves to where it is needed by facilitated diffusion, and oxygen is transported to tissues by binding to haemoglobin. Early Positron Emission Tomography (PET) studies found that increased glucose metabolism in the brain (cerebral metabolic rate of glucose, CMRGlc) is linked to functional activity (Sokoloff, 1981). Using radioactive tracers, studies have also shown that the increase of CMRGlc is comparable to CBF change and hence similarly much greater than O_2 metabolism (Fox et al., 1988).

The larger increase of CBF compared to $CMRO_2$, in response to activation, results in less O_2 being removed from the blood, resulting in a drop in the oxygen extraction fraction (OEF). This is the basis for the BOLD effect.

3.4.3 BOLD and T_2^*

Haemoglobin (Hb) is an iron-containing protein present in red blood cells that serves to carry oxygen from the lungs to the tissues. The protein is made up of four globular units: each unit binds a heme group (an iron ion held in a porphyrin ring), with the protein attaching to the iron. Four other bonding sites on the iron are taken up by the nitrogen atoms in the ring, and the final (sixth) position can reversibly bind oxygen. *Oxy-haemoglobin* (HbO_2) forms when an O_2 molecule is bound to the iron, and *Deoxy-haemoglobin* (dHB) is the unbound form (Figure 3.6).

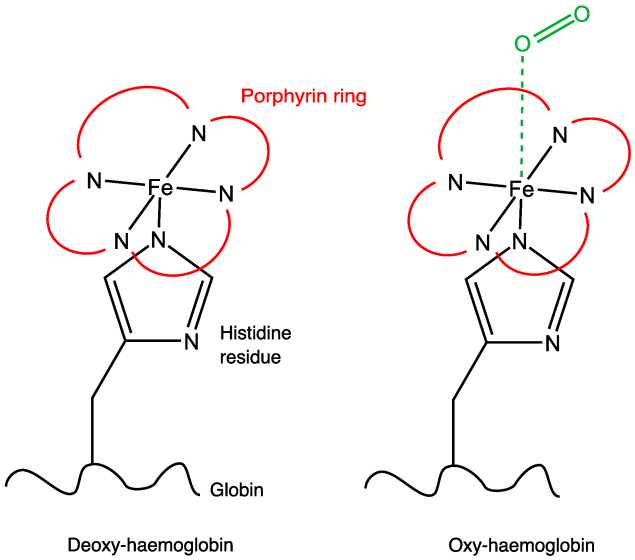


Figure 3.6: Simplified schematic of Haemoglobin. Left) Deoxy-haemoglobin (dHb). Right) Oxy-haemoglobin (HbO_2). The large alpha and beta subunits of the protein molecule have been omitted for clarity. It is the Iron-containing heme group that binds oxygen reversibly and undergoes a conformational change.

Deoxy-haemoglobin is paramagnetic, that is, it has unpaired electrons and will "concentrate" the magnetic field, setting up local magnetic field distortions (susceptibility gradients). Spins nearby (in the blood/vessels) will dephase, i.e. they will become out of phase with each other. While this occurs in the normal B_0 field due to static field inhomogeneities, the additional

dephasing caused by dHb will serve to shorten T_2^*: the MR signal will decay faster. This T_2^* shortening occurs at rest, most predominantly in veins (40 % dHb concentration).

Upon brain activation, there is a drop in OEF, the blood in veins/capillaries has a lower concentration of dHb, so the local field distortions are reduced; T_2^* becomes longer and the MR signal (using a pulse sequence sensitive to T_2^*) increases.

The field inhomogeneity ensures that spins will have a range of precession rates, leading to destructive interference. This is quite dissimilar to T_2 effects, which are brought about by (mainly) dipole-dipole forces from interacting spins (and within molecules): a tumbling molecule will experience fluctuating fields from surrounding dipoles, e.g. a proton, and these random fields may add or subtract from the tumbling molecule's rate of precession - across time, these random field patterns will cause the spins to become more and more out of phase with each other. On the other hand, the constant field offsets caused by T_2^* decay can be corrected by a spin echo pulse sequence.

In addition to molecular tumbling, and precession, extravascular spins will also be diffusing (translating) across space, which will have an effect on T_2^*. As a water molecule diffuses randomly through fields, which will vary in distortions, the precession rate will be different at each location, hence, it is not constant. This reduces the BOLD magnitude. The size of this effect is dependent on diffusion distance: if the distance moved is much smaller than the vessel radius, e.g. a vein, then the field variation felt by the spin will be minimal, whereas, if the distance moved is greater, e.g. a capillary, then there will be large field variations, and so T_2^* will shorten due to the averaging caused by diffusion.

The above implies that the extravascular BOLD effect is dominated by the veins, where diffusion effects are small, and there are large variations in

haemoglobin concentration. The intravascular component of the tissue comprises only $\approx 4\%$, however, due to higher dynamic range of signal change (at rest, the venous blood signal can change by approximately 50 %), the intravascular signal can be comparable to the extravascular signal.

3.4.3.1 T_2^* artifacts

Increasing acquisition time increases SNR, however, this factor is limited by relaxation effects: the signal will have decayed according to T_2^* and the values at high spatial frequencies of k-space will be zero - this occurs if acquisition time is much longer than T_2^*. T_2^* is a value that combines both relaxation due to T_2 decay, and field inhomogeneities, the latter of which is affected by voxel size: the larger the voxel volume, the greater the range of field offsets, the greater the variety of spin precession frequencies, and hence the faster they will come out of phase with each other, shortening T_2^*. This also occurs when one selects a thick slice, versus a thin slice. T_2^* effects are visible in the image as signal dropouts (areas with a very short T_2^*) and blurring (dependent on acquisition time).

3.4.4 BOLD optimization

In addition to its magnetic field dependence certain acquisition parameters strongly affect the BOLD response.

The voxel size must be carefully chosen to maximize the SNR (large voxel size means more spins) and the spatial resolution (for specificity and to reduce signal dropout - since a larger size will include a larger range of field variations).

Altering TE affects the sensitivity of the MR signal to the BOLD effect: too short a TE and the signal is insensitive; too long and the T_2^* signal has

decayed. The maximum signal change occurs at an echo time equal to the T_2^* of grey matter, which is approximately 25-30 ms at 7 T. This is specific to GRE pulse sequences; for SE, the TE is chosen to be longer, to maximize the signal change from TE $\approx T_2$.

For any TR, there is an optimal flip angle to maximize SNR, given by the Ernst angle. Additionally, the shorter the TR, the higher the sampling of the signal within the same amount of time (the total experiment time), and statistically, this will improve power; since SNR is proportional to $\sqrt{N}$.

3.4.4.1 Motion artifacts due to head movement

In addition to optimising the pulse sequence to maximise the BOLD signal, one must also take care to avoid/prevent image artifacts and distortions. A major issue, unrelated to any specific parameter or sequence is head motion. Since the positions of voxels are assumed to be the same during the scan, any movement relative to the coil will cause signals to be misplaced (since the coil is not fixed to the subject's head). This becomes very apparent at the edges of the brain, where there are sudden jumps in image intensity (GM/CSF/skull), and voxels here may appear to have different amounts of GM volume across time, due to movement. Motion can be corrected retrospectively via realignment of the images.

3.4.4.2 Physiological artifacts

In functional imaging, we measure a dynamic set of images, and hence the timecourse will include physiological motion (such as head motion). This problem is extremely problematic with BOLD fMRI, which usually involves a long scan (several minutes), including task and rest periods. Additionally, the signal change associated with dHb is small, relative to baseline, and head

motion can cause voxels to produce a comparable signal change (especially at the edge of the brain / at air boundaries), increasing the difficulty in separating signal from noise.

Motion correction during post-processing corrects small translations/rotations to some degree, but not fully. Other sources of physiological noise include cardiac and respiratory effects. This can be corrected using an image based method for retrospective correction, RETROICOR (Glover et al., 2000). This method fits low order Fourier series to images, based on the phase cycles of respiratory and cardiac motion, which must be monitored via a respiratory belt and photoplethysmogram (PPG).

Periodic/regular motion, such as blood flow or the heart beating will cause discrete ghosts in the image. This is dependent on the periodic rate compared to the TR, e.g. this can be thought of as aliasing: a high frequency signal appears to be low frequency because the sampling rate is too low (Nyquist frequency). The degree of displacement (shift) is defined by N $\times$ TR / T, where N are the number of phase encoding steps, and T is the period of motion.

3.4.5 BOLD physiology

Upon activation, the BOLD response becomes dependent on three factors: the increase in CBF; the ratio of CBF change to $CMRO_2$ change; and a scale factor depending on local Hb concentration. The larger the ratio, i.e. the bigger the CBF change relative to $CMRO_2$ change, the larger the BOLD response. The scale factor determines the upper limit of any BOLD signal change (since the BOLD effect is determined by a drop in dHb concentration).

Transients in the BOLD response profile include the "initial dip" and the "post-stimulus undershoot": these can be explained by investigating the

interplay of CBV, CBF and $CMRO_2$. A simplified view of how a stimulus leads the BOLD response is shown in Figure 3.7.

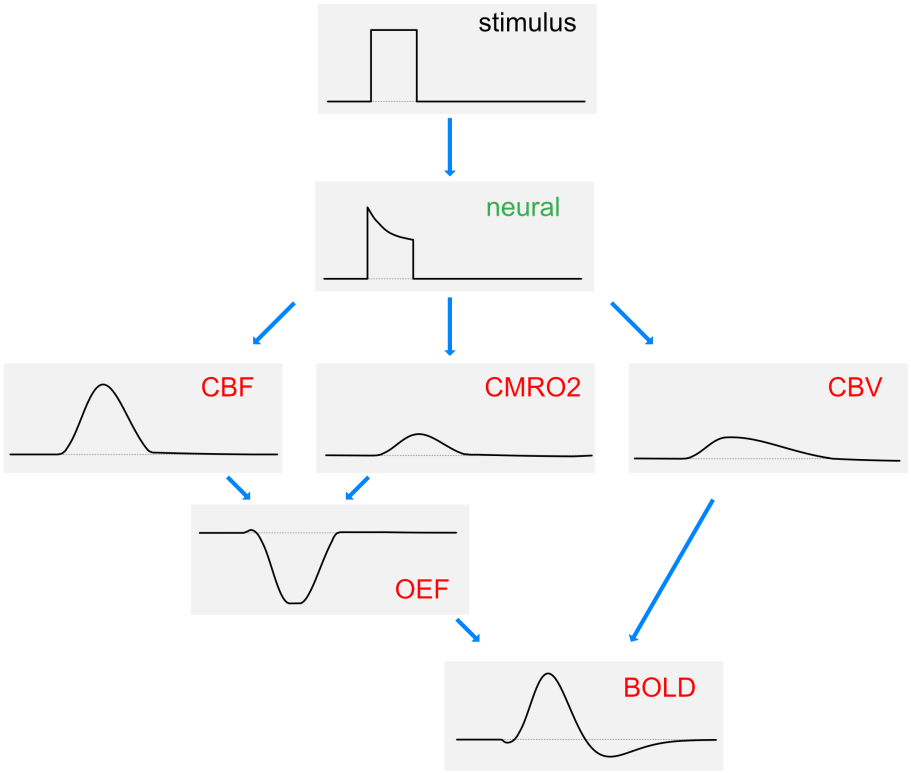


Figure 3.7: From stimulus to the BOLD response. Following stimulation, neural activity causes a large rise in CBF and smaller rises in $CMRO_2$ and CBV. The large difference in CBF/$CMRO_2$ causes the drop in OEF. The orchestrated changes in CBF, CBV and $CMRO_2$ all serve to produce the BOLD response.

The BOLD response has a characteristic shape termed the *haemodynamic response function* (HRF), defined by a slow ramp following activation, at about 5-6 s post-stimulus, then sustained activation and a rapid drop, which falls below baseline, known as the post-stimulus undershoot. An example experiment presenting a visual checkerboard for 5 s ON and then 40 s OFF, acquiring data using GRE-EPI, with a TR of 1 s to fully sample the HRF (see Chapter 4), will yield a time-averaged HRF across 6 cycles from a single voxel, as shown in Figure 3.8.

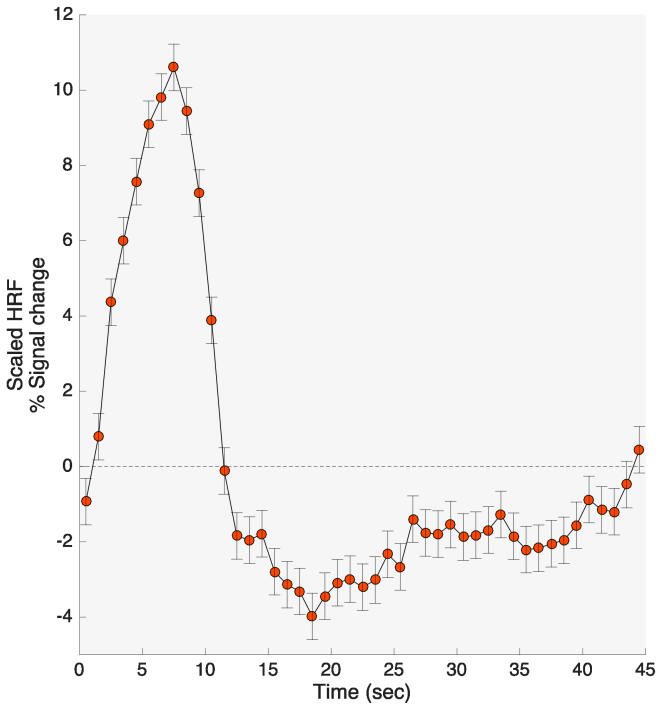


Figure 3.8: An example haemodynamic response function from a single voxel, in response to a full field flashing checkerboard stimulus, on for 5 s, off for 40 s. Data acquired on a Philips Achieva 7 T, TR 1 s, 1.5 isotropic voxels, GRE-EPI. This output is following a deconvolution GLM analysis, where the input file was when the stimulus was on across 270 dynamics. The characteristic slow rise, plateau, and long undershoot are visible here.

It was stated above that the rise in CBF serves to deliver O_2 to the tissue upon activation, however, it was not made clear that this is not a feedback response, in fact, it is more likely a feedforward model, i.e. the CBF is not waiting for a message from metabolism - CBF changes rise in parallel with neural activity, e.g. neurotransmitter release.

The BOLD response is variable - one example of modulation is caffeine: a vasoconstrictor that increases the concentration of dHb and reduces the baseline BOLD resting signal, which can lead to a larger increase in the BOLD contrast upon activation (Mulderink et al., 2002). Other studies have shown that the BOLD response varies significantly between subjects,

with some variation within subjects (on the same day, and on different days) (Aguirre et al., 1998).

The neural activity that gives rise to the BOLD response is in fact made up of a complex process of excitatory, inhibitory, synaptic and spiking activity, even within a single voxel. The fMRI signal may not be able to distinguish across hierarchical signals, or function-specific processing vs. neuromodulation, and is sensitive to the neural population size. A key study found that local field potentials (low frequency extracellular potentials, reflecting synaptic activity) correlated more strongly with and better predicted, BOLD activity, as compared to multi-unit activity (reflecting spiking) (Logothetis, 2008; Logothetis et al., 2001).

Roughly, the BOLD response sums linearly, e.g. in an event-related task where multiple presentations of a fast stimulus occur. While there are non-linearities present, the linear approximation does not produce large errors for many applications (unless one is trying to separate overlapping responses) (Buckner, 1998; Dale and Buckner, 1997).

3.5 fMRI statistical analysis

In this section, some statistical analysis procedures for discerning activation are described. The ideas behind the General Linear Model (GLM) are described. The measurement of the goodness of fit between a model and data, and a few specific analyses that are used in this thesis such as *deconvolution* and *coherence* are outlined.

3.6 Statistical analysis

Following sensory stimulation, e.g. tapping fingers, a haemodynamic response will be generated in a voxel timeseries in the motor cortex. Performing this task multiple times should lead to multiple HRFs; the profile of which will depend on the "ON-OFF" duration in this simple example. fMRI researchers aim to tease apart the signal from the noise, by identifying statistically relevant BOLD activity.

The simplest method to identify signals is to average the ON trials, and compare them to the OFF trials, more generally, task versus rest. However, the noise across different voxels will be non-uniform. The source of this "noise" is thermal and physiological: the former originating from currents in the body inducing random voltages in the receiver coil, and the latter resulting from various bodily processes such as respiratory fluctuations and cardiac pulsations, which in turn cause cerebral spinal fluid (CSF) pulsations. The residual difference following signal averaging of two noisy signals, e.g. task and rest signal, may be so large that it may mask "real" activity, and the signals which show the largest fluctuations, e.g. breathing artifacts, will produce large spikes in the signal - taking the Fourier transform of the difference signal would show spatial structure probably dominated by artifacts.

3.6.0.1 Student's *t*

A simple statistical test is the *t-test*. For example, consider a rest and task condition. For a single voxel, we can then calculate the two separate means for the two populations: task and rest. We can calculate a value for "t"; this value is compared to a continuous probability distribution, known as the "t-distribution". For large degrees of freedom, this distribution is comparable to the normal distribution:

$$f(\nu, \mu, \sigma) = \frac{1}{\sigma\sqrt{2\pi}} e^{-\frac{(\nu-\mu)^2}{2\sigma^2}} \tag{3.5}$$

where f is the normal probability density function plotted for a variable, ν, with mean, μ and standard deviation, σ.

Once you have your t-statistic, you then choose a threshold probability (p), e.g. 0.05, above which the t-statistic is not significant and hence may be due to chance.

There is an issue that arises when performing many t-tests, which will occur since BOLD responses are evaluated across thousands of voxels in the brain, i.e. for p = 0.05, and 10,000 voxels, there will be approximately 500 voxels activated by chance (5 %). This is based on the *familywise error rate* (FWE), e.g. for p = 0.05:

$$FWE = 1 - 0.95^n \tag{3.6}$$

where n is the number of tests performed. The FWE gives the chance for making a Type 1 error, also known as a false positive. For a single test at p = 0.05, this is 5 %, but increases for every additional test performed, e.g. searching for significant activity across multiple voxels in the brain.

One common method to correct for this *multiple comparisons problem* is to use "Bonferroni correction": the p-value is divided by the number of measurements (voxels), and this new, conservative value of p is used to define significance.

While FWE correction minimises the number of false positives, another, less stringent method controls for the number of false positives given the reported positive results - this is known as *False Discovery Rate* correction. The alpha value calculated in FDR correction depends on the distribution of

significance values (Benjamini and Hochberg, 1995). This approach means that the more voxels that are active, the lower the significance threshold - this improves experimental power, at the cost of including a higher risk of false positives as compared to FWE.

3.6.0.2 The General Linear Model

The univariate General Linear Model (GLM) refers to simple linear regression. For a single predictor variable (independent variable), there will be a relationship between it and an outcome variable (dependent variable). Regression describes the set of processes which serve to quantify that relationship. The GLM is based on the following equation:

$$\begin{aligned} outcome_i &= (b_0 + b_1 X_i) + error \\ Y_i &= (b_0 + b_1 X_i) + \epsilon_i \end{aligned} \tag{3.7}$$

where X denotes the predictor variables across measurements (voxels) i. Y is the outcome variable, and b_1, called a "beta weight" quantifies the relationship between X and Y. b_0 gives the value of Y when $X = 0$.

The GLM can also be expressed in matrix form:

$$Y = X\beta + \epsilon \tag{3.8}$$

where Y is a vector containing the data, β is a vector of the regression coefficients/model parameters, X is the design matrix, and ϵ is the unknown error.

To find the beta weights, first the differences between the observed data and

the predicted value (model values) are calculated. From these "residuals" the sum of squared residuals is calculated, giving an estimate of the error in our model. For a more detailed explanation see Appendix 8.2.

3.6.0.3 Fourier analysis

In Fourier analysis, the BOLD timecourse can be decomposed into its frequency components, using the Fourier transform (FT). The component at the fundamental frequency of the stimulus sequence, e.g. for 10 cycles, the frequency at $\frac{1}{10}$ Hz, should show a strong spike in the FT spectrum.

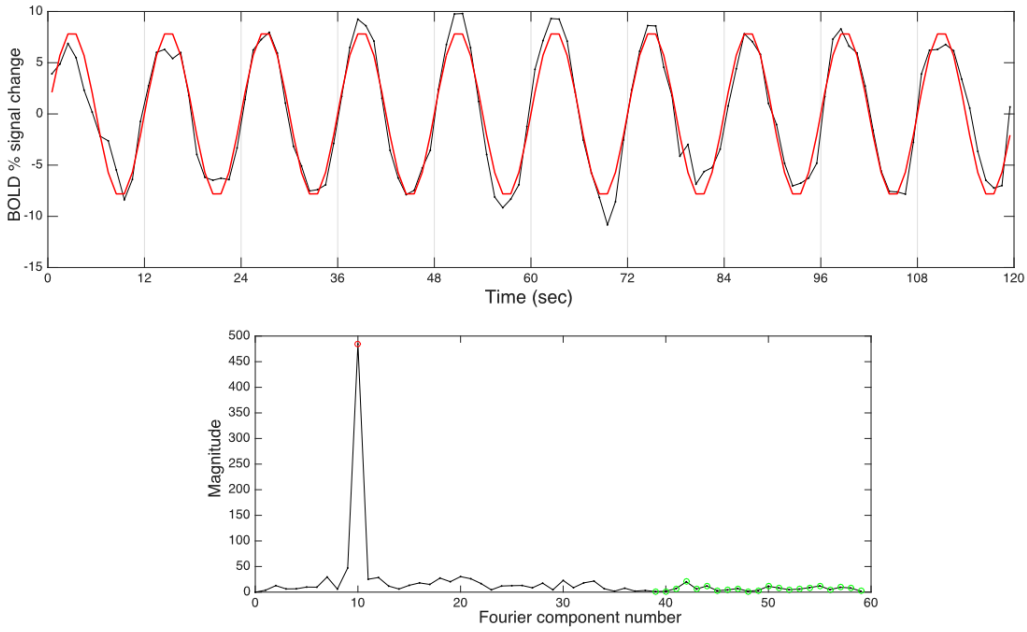


Figure 3.9: Top) Example fMRI timecourse from a single voxel, in response to 10 cycles of travelling wave visual stimulation. Bottom) The Fourier spectrum components of the fMRI timecourse.

Fourier analysis is the basis of the retinotopy and somatotopic travelling wave analyses described in detail in Appendix 8. Coherence is defined as

the correlation in Fourier space, between signals, e.g. a predicted timecourse such as a sinusoid (usually the best correlated harmonic at the stimulus frequency) and an observed timecourse (Engel et al., 1997).

Specifically, it can be shown that the maximum correlation between the harmonic (sinusoid) with the timecourse is:

$$c(h(F, \phi_f), d) = \frac{a_F}{\sqrt{\sum_{f=0}^{N-1} a_f^2}} \tag{3.9}$$

where the coherence is c, as a function of the sampled harmonic function $h(F, \phi)$, at a stimulus frequency, F. d is the timecourse data a single voxel. a_F is the amplitude of the timecourse's Fourier component at F. $\sum_{f=0}^{N-1} a_f^2$ represents the timecourse power (Besle et al., 2013).

The phase of the response measures the delay of the activity relative to the stimulus sequence, thus giving a spatial map of stimulus position across time, across multiple voxels. It can be shown that the correlation in Fourier space (the coherence) will be maximized when the phase of the two signals are the same. A high coherence can also be achieved even if there is a phase offset between signals, as long as the offset is constant.

3.6.0.4 fMRI design

A well-designed paradigm should elicit suitably powerful activation, which can be detected by statistical analyses described later.

In general, there are two broad categories that fMRI designs fall into: a *block* design, or an *event-related* (ER) design. A block design comprises sequential blocks of ON periods followed by OFF periods. A simple example would be to present images of houses for 5 seconds, followed by 30 seconds rest,

repeated multiple times over a scan. By comparing the weak signal change at "activation" verus "rest" conditions, one could find a BOLD fMRI response (hopefully in visual cortex). An event-related experiment is much more flexible and allows multiple stimuli to be presented in random order - this feature provides more complex experiments to be devised.

The type of design requires a subtle difference during analysis using a linear model (GLM). In the GLM, as described above, the data is compared to a model, the *design matrix*, e.g. when a stimulus was ON or OFF, and predictions are made from the model parameters. fMRI analysis requires an additional step due to the haemodynamic lag relative to neural activity, specifically, the model response must be convolved with a haemodynamic response function (HRF) - thus smoothing the model response. One can use a *canonical* HRF for the convolution, or perform trial-triggered averaging to extract the data-specific HRF.

In block designs, for a sufficiently long OFF period, the HRF will decay back to rest, thus allowing comparison with a relative baseline. In a fast ER design, subsequent trials may not allow the HRF to decay to baseline, and hence separation of the specific HRF to a specific trial becomes more difficult. Here, the use of a complex design matrix in a GLM can be used to regress the trial-specific responses.

If one wants to find the shape of the HRF, a slightly different analysis method to the GLM, known as *deconvolution* produces the inverse of convolution, i.e. division in the Fourier domain. If the neural response can be estimated, and the voxel response is known, one can perform the division and pull out the HRF (in other words, the smoothing filter on the assumed instantaneous neural response). Note that deconvolution is extremely susceptible to noise, insofar that alternatives to "regular" deconvolution have been devised, e.g. Weiner deconvolution, as used in (Glover, 1999) and in this thesis (Chapter 4).

3.6.0.5 Wiener Deconvolution

One way to imagine a simple ON-OFF paradigm, in terms of the BOLD functional timeseries, is that of a series of instantaneous neural responses smoothed with a filter; in this case, the haemodynamic response. In the Fourier domain, this "smoothing" is simply a multiplication by a sliding window. In image space, this is known as *convolution*.

If one can assume the neural boxcar, e.g. a 5 second ON period, and one has the convolved timeseries, then to determine the HRF shape, one simply has to perform a division in Fourier space, otherwise known as *deconvolution* in image space.

The difficulty in performing a deconvolution is that any noise introduced into the system, e.g. thermal/physiological noise in an MRI scan, severely deteriorates the deconvolution. One way to remedy this is to use *Wiener* deconvolution. This is a method that utilises an estimate of the noise within the system. This is performed by using a Wiener filter (Papoulis, 1977), as described in (Glover, 1999).

For a linear system, we can define $h(t)$ as the HRF, $s(t)$ as the neural response and thus $m(t)$, the measured signal response, can be defined as

$$m(t) = s(t) * h(t) + n(t) \tag{3.10}$$

where $n(t)$ is a measurement of noise. The neural approximation s' can be obtained using a Wiener filter, $d(t)$

$$s'(t) = d(t) * m(t) \tag{3.11}$$

Equation 3.11 can be altered to find the impulse response approximation

$h'(t)$, i.e. the HRF, instead of the neural response. In Chapter 4, we will find out why it is the HRF we are trying to tease out of the deconvolution, rather than the neural response, which we can assume here.

Next, we can define $S(\omega)$, $M(\omega)$, $N(\omega)$, and $D(\omega)$ as the Fourier transforms of $s(t)$, $m(t)$, $n(t)$, and $d(t)$, respectively. And so

$$D(\omega) = \frac{S^*(\omega)}{|S(\omega)|^2 + |N(\omega)|^2} \tag{3.12}$$

where $S^*(\omega)$ here represents the complex conjugate of $S(\omega)$. The estimate neural response is then

$$h'(t) = \mathfrak{F}^{-1}[D(\omega)M(\omega)] \tag{3.13}$$

where $\mathfrak{F}^{-1}$ is the inverse Fourier transform. We now input a value for the noise, $N(\omega)$, which is acquired from a voxel in a non-activated cortical region. The final impulse response is then

$$h'(t) = \mathfrak{F}^{-1}\frac{S^*(\omega)M(\omega)}{|S(\omega)|^2 + N_0^2} \tag{3.14}$$

3.7 Conclusion of Chapter

This chapter has outlined the set of advanced fMRI methods used throughout this thesis. To acquire functional data with good coverage, spatial and temporal resolution, the relationship between TR, Multiband and SENSE factor must be optimized. For BOLD fMRI, the design and statistical analysis must be carefully chosen. A portion of each experimental chapter is dedicated to the development of an optimized protocol for the fMRI paradigms

used in this thesis.

CHAPTER 4

4 Population Receptive Field Mapping in Visual Cortex

4.1 Overview of chapter

In this experimental chapter, I develop an imaging protocol for population receptive field (pRF) mapping in the visual cortex using 7 T multiband (MB) or simultanaeous multislice (SMS) fMRI to collect data with high spatial and temporal resolution. Additionally, I measure the haemodynamic response function (HRF) shape in an independent experiment, such that it can be entered into the pRF model. The findings from these experiments serve to inform the use of the pRF method in the somatosensory cortex. The methods of retinotopy and pRF mapping are described, as well as insights gained into the development of unique procedures in somatosensory cortex.

This work was presented as an oral "power pitch" presentation and electronic poster at ISMRM 2018, Paris, entitled: *Using measured haemodynamic response functions in population receptive field mapping at 7 T*. Abstract #874.

4.2 Introduction

To validate assumptions in BOLD fMRI, using paradigms such as the travelling wave (TW) (Sanchez-Panchuelo et al., 2014) or more elaborate modelling approaches such as pRF mapping (Dumoulin and Wandell, 2008), one must be able to accurately measure, and model, the haemodynamic response function (HRF). The optimal data for such a study is an event-related experiment, with a long OFF period, so as to allow the HRF to fully recover back to baseline and be fully characterized.

There have been few studies that have measured the haemodynamic response function (HRF) at 7 T in sensory cortices. The first important contribution of the work here is therefore to provide new data investigating any alterations in model parameters or HRF shapes to those that have been measured at lower field strengths of 1.5 and 3 T (Lindquist et al., 2009; Lindquist and Wager, 2007). Here, HRFs are characterized at 7 T in the visual cortex.

At 7 T, increased sensitivity and BOLD contrast to noise ratio (CNR) allows the assessment of the HRF at high spatial resolution ((1.5 mm)^3 isotropic voxels) using few repeats of a stimulus cycle, in a single scan, in a single subject. Additionally, the use of multiband (MB) RF pulses enables faster scanning. The multiband factor, together with repetition time (TR), are variables which should be assessed to determine optimal image quality. Previous work (Sanchez-Panchuelo et al., 2012b) has demonstrated that (1.5 mm)^3 provides sufficient spatial resolution and good SNR for retinotopic mapping. One important first study was to assess and show that the quality of HRF measurements and retinotopy paradigms is consistent when moving to higher multiband factors of 2 and 3. This also relates to Chapter 5 and Chapter 6 where multiband is assessed for the study of somatosensory function.

General Linear Model (GLM) and pRF methods rely on an accurate descrip-

tion of the HRF, but previous literature has shown that there is substantial variability within and between subjects (Aguirre et al., 1998). Therefore, using a canonical model/HRF may be problematic, as this fails to capture individual spatial HRF differences (Handwerker et al., 2004). The idea is therefore to estimate voxelwise HRFs from sparse, event-related (ER) scans and apply these results to further analyses such as pRF mapping.

One disadvantage of pRF mapping is the number of free parameters that are used to fit the model. An increase in the degrees of freedom of the model may lead to overfitting. The simplest 2D-Gaussian pRF model used has 10 parameters, 7 of which are used to model the HRF (using a double gamma function).

In this Chapter, I describe how a robust, 'real' HRF measurement can be used to inform the pRF, i.e. instead of the pRF adding extra parameters to model the HRF shape, a subject-specific "true" HRF can be input, bypassing the HRF-fitting procedure. This would provide valuable insight into the sensitivity of the pRF to HRFs in sensory cortices. From the insights gained from these data, this chapter aims to allow the pRF model to take into account subject-specific HRFs.

One advantage of developing this method of using an individual subject measured HRF in the pRF model, in the visual cortex, is that there are strong BOLD responses to simple stimuli like a flashing checkerboard. There is also a firm foundation in producing robust pRF maps from the literature (Wandell and Winawer, 2015). These advantages are further enhanced at ultra-high-field (7 T) (De Martino et al., 2016). Thus, this domain provides a good testing ground, compared to for example the somatosensory cortex.

As well as measuring HRFs at high spatial resolution at 7 T, I will in this Chapter use a multiband acquisition to study the HRF with high temporal resolution (TR 1 s). As the field strength increases, the T_2 and T_2^* of

venous blood decreases. This implies that the intra-vascular BOLD component (from draining veins) is reduced (Duong et al., 2003; Yacoub et al., 2001), and hence there will be greater spatial specificity of the measured BOLD fMRI signal. The increased sensitivity of ultra-high field fMRI has been demonstrated (van der Zwaag et al., 2009), with a greater number of active voxels shown at 7 T compared to 3 and 1.5 T, as well as greater fractional change differences. Here, I utilise this increased spatial specificity and sensitivity to display HRF parameter maps on the visual cortex. I aim to address the following objectives:

1. Primary: To what extent can fMRI parameters be optimized to acquire robust individual subject HRF measurements?
2. Primary: Can a measured HRF be included in the pRF model to improve the statistical and physiological accuracy of the procedure?
3. Secondary: Can veins be separated from tissue in HRF scans based on high-resolution vein masking?
4. Secondary: In visual cortex, does multiband imaging improve the HRF measurement?

4.3 Background

4.3.1 The Visual Cortex

The visual cortex is located in the occipital lobe of the cerebral cortex, and is responsible for the processing of visual information. Visual information arrives at the retina, where the receptive field of a visual receptor is excited. Information is then passed along axons from the ganglion cells, crosses the optic chiasm, passes through the lateral geniculate nucleus in the thalamus, and finally arrives at primary visual cortex (V1). Axons at the retina maintain their topographic relationship to each other at V1, that is: neighbouring

portions of visual space are represented in neighbouring parts of visual cortex. Hence they are said to be *retinotopically organized*. This feature of topographic organization is not unique to visual cortex, but also exists in auditory and somatosensory cortex, and has been exploited for decades to map sensory cortices.

Visual cortex possesses functional organization by way of *cortical columns*: moving perpendicular to the surface of the cortex, neurons encountered possess similar response properties (Hubel and Wiesel, 1977). Additionally, moving tangentially across the cortical surface, the variation of orientation preference transitions smoothly. Both of these phenomena tie into the adjacent retinal topographic (retinotopic) maintenance of visual cortex, described above, and it is this architecture which has led to the mapping of visual cortex, also known as *retinotopy*.

4.3.2 Mapping Visual Cortex

The receptive field (RF) of a neuron is the area of sensory space that, when stimulated, produces a strong response in that neuron. It is a fundamental concept for understanding the mapping between sensory space and cortex. Receptive fields of neurons have been traditionally measured invasively on mammals via electrode recording, e.g. in the anesthetized cat, researchers identified mutually antagonistic excitatory and inhibitory RFs in visual cortex using a light stimulus; they identified specific arrangements/orientations of RFs; that the driving of an RF was stimulus specific; and observed binocularly activated units (Hubel, 1959).

The work performed by Hubel and Wiesel, among others in the field, provided a vivid insight into animal sensory cortices, however, as we come closer to the present day, the drive for non-invasive parallel measures in humans has grown in momentum; particularly with the advent of fMRI.

Retinotopic organization was observed using fMRI with a simple but very powerful visual experiment: a contrast-reversing (flickering) checkerboard ring (expanding/contracting rings and a rotating wedge) was presented to a volunteer in the scanner during fMRI acquisition. As the flickering ring expands, a "travelling wave" of activation moves from the part of cortex representing the fovea to the periphery; since the activity at the periphery will be delayed relative to the fovea, and the neural activity alternates periodically, one can measure the delay from measuring the phase and map out the activity. This 'phase-encoding' design is also used with the rotating flickering wedge to measure polar angle, i.e. neural activity is delayed at locations further along rotation direction relative to that near the beginning of the stimulus, and thus position dependent information can be computed by looking at the phase (Engel et al., 1994; Engel, 2012; Engel et al., 1997).

The travelling wave method can be used to delineate the visual cortex by visual area (e.g. V1/V2 boundary) by producing maps of retinotopy with respect to polar angle. Boundaries are defined by identification of reversals of response phase - a signature of the borders between visual field representation in early visual areas. By plotting visual field eccentricity against cortical distance, one can also identify retinotopy as a function of the expanding/contracting rings (Larsson and Heeger, 2006). An example of the output following retinotopy on data acquired for this thesis is shown in Figure 4.2, and a literature example is also shown for comparison in Figure 4.1.

Engel concluded that the fMRI signal is strong enough to measure stimulus dependent properties of neuronal populations; a step beyond simple localization experiments. By employing computational methods to explore the tuning properties of neurons, together with the sensitivity achieved by improved hardware, such as higher field magnets and the use of surface coils, retinotopic mapping is beginning to bridge the gap between single neuron RF measurements and the response tunings of groups of neurons. The voxel

encoding method known as 'population receptive field' (pRF) mapping aims to provide greater information than retinotopy, and has been successfully utilized in visual cortex over the past decade. It is this methodology we now turn to in more detail.

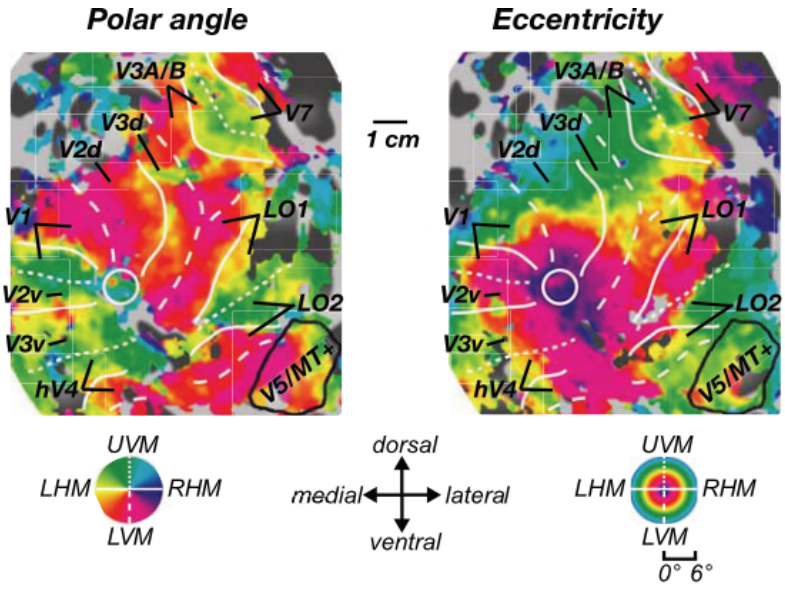


Figure 4.1: Visual polar angle and eccentricity maps are shown displayed on unfolded patches of cortex, for a single subject, in the right hemisphere. White circle indicates foveal representations of V1/V2/V3. Coherence is thresholded at 0.25. Adapted from (Larsson and Heeger, 2006).

4.3.3 Population Receptive Field Mapping of Visual Cortex

Retinotopy is a widely used method to measure visual field maps, by relating stimulus position to cortical response. The rings and wedge stimuli provide the 'most effective field position' (Wandell et al., 2015) per voxel, i.e. the most effective angle and eccentricity that drives the response of a given voxel. One limitation of the standard retinotopy analysis is that it is "blind" to the size of the visual field mapped by each voxel. To address

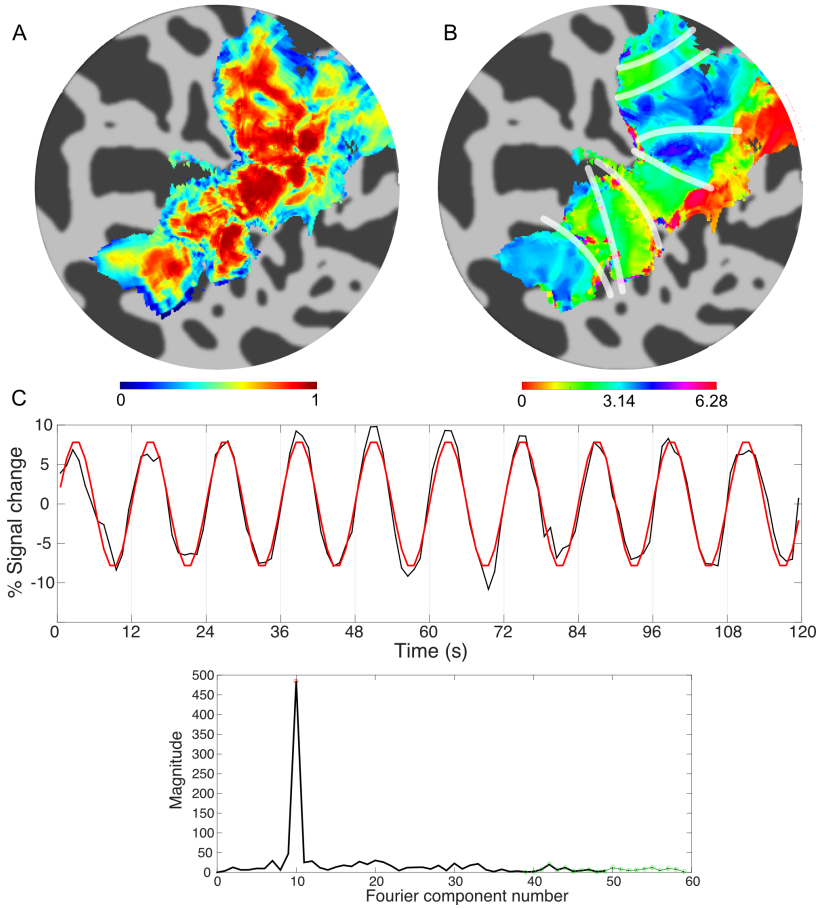


Figure 4.2: Coherence and phase maps from an example retinotopy experiment, for a single subject, on the right hemisphere, displayed on a flattened patch of cortex. A) Coherence measures the correlation between the best fitting sinusoid at the stimulus frequency and the voxel time series. B) The phase measures the relative delay of the stimulus at each voxel. Approximate phase reversals are indicated by white lines. C) In visual cortex, large BOLD signal changes can be observed: 10 cycles of rotating wedges are shown, with the Fourier component (frequency) displayed below.

this problem, a computational model of the fMRI response was developed, to determine the precise tunings of populations of neurons (Sereno et al., 1995; Victor et al., 1994) within a voxel. These models can be split up rather crudely into *decoding* or *encoding* models: whereby voxel activity is used to predict sensory or cognitive information, or the reverse, predict the

voxel activity given known sensory or cognitive information (Naselaris et al., 2011) - population receptive field (pRF) mapping is an example of a voxel based encoding model, where given known stimulus conditions, the model can predict the fMRI response.

Specifically, one can approximate a two-dimensional (2D) Gaussian model with centre coordinates (x,y) and spread (σ) i.e. this could be used to summarise the 'population' of neurons with a voxel. A model-based approach allows parameterization of voxel properties, as well as the development of novel outputs from voxel tunings (Dumoulin and Wandell, 2008).

Overlapping the Gaussian pRF model with the stimulus description (slowly translating bar), and convolving with a haemodynamic response function (to account for the sluggish blood response), produces a predicted fMRI timeseries, for a single voxel. By evaluating the errors between this predicted response and the actual data timeseries, one could find the optimum pRF model by non-linear least squares (more detail is given in a later section, for a flow chart describing this process see Figure 4.3). An approximation of pRF size can be derived from the standard deviation of the Gaussian model, for each voxel - a parameter unattainable with standard retinotopy. Current research into visual pRF is briefly described in subsection 8.1.1. Example pRF parameter maps are shown in Figure 4.4.

The code that is used to analyse retinotopy and pRF mapping in this thesis can be found online here: https://github.com/justingardner/mrTools/tree/master/mrLoadRet/Plugin/pRF.

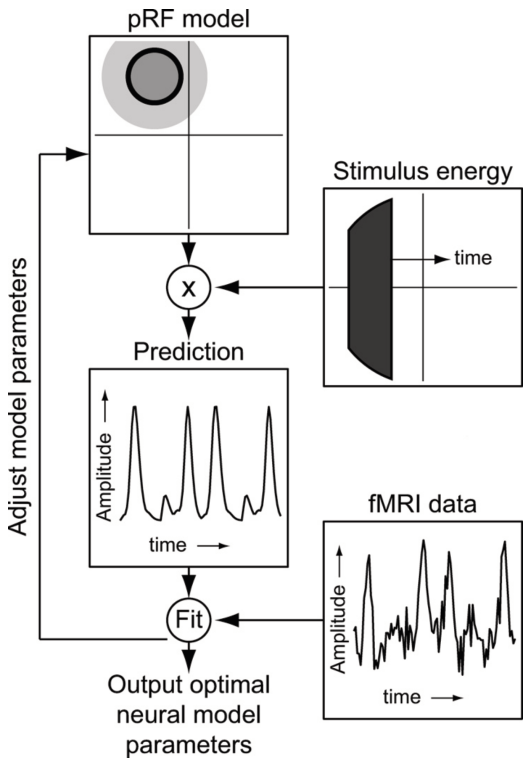


Figure 4.3: The pRF method. The pRF model is convolved with the stimulus sequence and HRF, producing a predicted fMRI timeseries. The errors between the modal and the timeseries are minimized by non-linear least squares. Adapted from (Dumoulin and Harvey, 2012)

4.4 Methods: Data acquisition and paradigm optimisation

Datasets were acquired on a 7 T Philips Achieva scanner, using a 32-channel Nova head coil (Nova Medical, Massachusetts). A series of experiments were conducted to establish the optimal fMRI acquisition protocol for HRF measures (A), pRF mapping (B) and combined assessment (C).

Figure 4.5 shows the wedge, bar and ring stimuli used for retinotopy and pRF mapping in this Chapter. The code can be downloaded here: https://github.

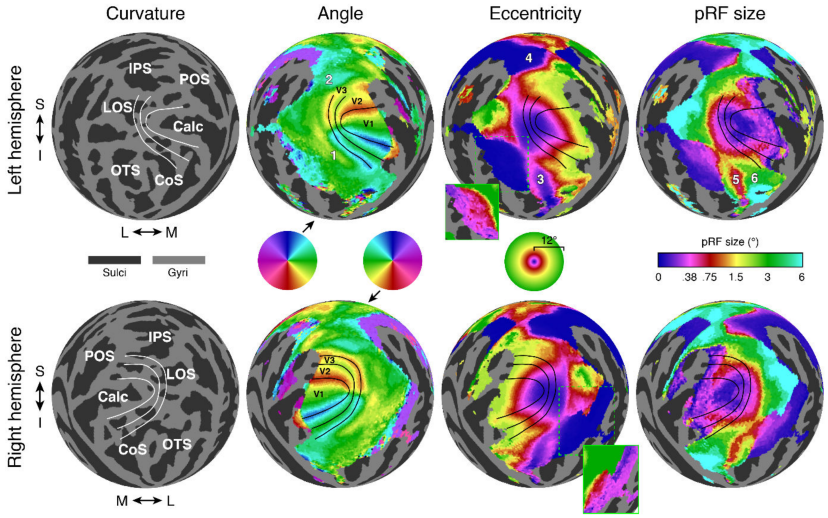


Figure 4.4: Visual cortex pRF parameter maps displayed on a spherical cortical surface. In addition to polar angle and eccentricity, maps of pRF size can be computed. Adapted from (Benson et al., 2018)

com/justingardner/mgl/blob/master/utils/mglRetinotopy.m. The default parameters were used and these are 24 s per cycle, with 24 steps (e.g. how many steps the wedge goes through to complete one cycle) per cycle, and 10 cycles.

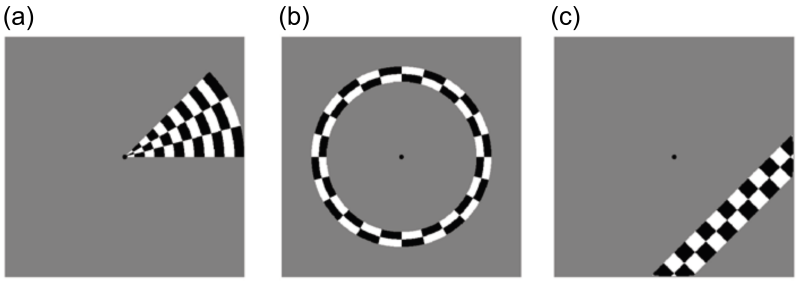


Figure 4.5: (a) Rotating wedges, and (b) an expanding/contracting ring are stimuli used in retinotopic mapping, to measure polar angle and eccentricity, respectively. For population receptive field mapping, (c) drifting bars provide sufficient continuous activity across visual cortex for mapping. Adapted from (Dumoulin and Wandell, 2008).

4.4.0.1 Pilot HRF protocols (A): optimising paradigm design

Initially, two datasets were obtained in the same individual, to ascertain the optimum ON-OFF paradigm to define a robust and high-SNR HRF. For these HRF scans, the subject viewed a full-field high-contrast flashing checkerboard using MR-compatible prism glasses. A 5 second ON period was chosen for the stimulus, with an OFF period of both 40 and 50 s assessed. There were 6 repeats of the checkerboard stimulus presentation, and during the OFF period, the subject fixated on a mid-grey background. At this stage, data were acquired without using multiband implementation. Details of these data are shown in Table 2.

HRF protocols (A)						
Dataset	Resolution mm^3	TR (s)	Dynamics	[ON OFF]	Runs	Slices
1	1.5	1	270	5 40	1	10
2	1.5	1	330	5 50	4	12

Table 2: fMRI parameters collected on a single subject during presentation of a full field flashing checkerboard. Both datasets had 6 cycles of ON-OFF stimulation and were acquired with no multiband.

Voxelwise HRFs were estimated using a General Linear Model (GLM) framework: for every voxel, the fMRI timeseries were scaled and meaned using trial-triggered averaging to determine the voxel-wise HRF shape. The HRF was fitted (non-linearly) using a double gamma function. Spatial maps defining HRF parameters of the time-to-peak (TTP), amplitude, and full-width-at-half-maximum (FWHM) were calculated across a visual region-of-interest (ROI). These activation maps were overlaid on a high-resolution (Phase Sensitive Inversion Recovery, $0.3\times0.3\times1mm^3$) flattened patch of cortex using Freesurfer. T_2^*-weighted FLASH images of spatial resolution $0.5\times0.5\times1.5mm^3$ were also acquired for co-registration.

4.4.0.2 Pilot HRF data and pRF protocols (B)

In a second set of fMRI experiments, a HRF scan followed by four retinotopy/pRF scans were performed in a single scan session. Visual stimuli commonly used for retinotopic mapping were used - rotating wedges (2 scans) and drifting bar apertures of high-contrast checkerboards (2 scans), in forward and reverse directions. Each stimulation cycle lasted 24 s (10 repeats per scan). A multiband factor of 2 allowed 30 slices to be acquired, covering all of early visual cortex. In one scan session, an additional HRF measurement scan was acquired with both a 1 s and 5 s checkerboard stimulus for comparison. Details of these datasets are shown in Table 3.

HRF and pRF protocols (B)				
Dataset	HRF or pRF type	TR (s)	multiband factor	Dynamics
1	HRF [5 50]	1	2	330
	Wedges (fwd)	2	1	126
	Wedges (rev)	2	1	126
	Bars (fwd)	2	1	126
	Bars (rev)	2	1	126
2	HRF [5 50]	1	2	330
	Wedges (fwd)	2	2	126
	Wedges (rev)	2	2	126
	Bars (fwd)	2	2	126
	Bars (rev)	2	2	126
	HRF [1 54]	1	2	330

Table 3: Data from pilot protocols (**B**). All scans acquired at spatial resolution 1.5 mm ^{3}. Initially, multiband (MB) factor 1 was used for the retinotopy. Later testing showed no substantial drop in tSNR with MB2 while providing a much improved spatial coverage, and hence MB2 was used to collect Dataset B2.

4.4.0.3 Final protocol assessment (C)

In a further set of experiments, the final protocol was collected on 5 subjects. This comprised the HRF scan of ON duration of both 1 s and 5 s and pRF scans (1 pair of bars, 1 pair of wedges) using the optimized fMRI acquisition parameters. All data were collected using multiband factor (MB) 3. For 2 datasets the pRF scans and the 1 s and 5 s HRF scans were collected at both MB2 and MB3; these were used to compare the effect of multiband acquisition within a single session. The overall acceleration was SENSE factor X MB. Details of these data are shown in Table 4.

(C) protocol: Matrix size: 128x128x30 slices, $(1.5\ mm)^3$ isotropic voxels, SENSE 1.5, Halfscan 0.7, Flip angle 80°(TR 2s), 57°(TR 1s).

Final protocol (C)				
Dataset	HRF or pRF type	TR (s)	multiband factor	Dynamics
1	HRF [5 50]	1	3	330
	HRF [1 54]	1	3	330
	Bars (fwd)	2	3	120
	Bars (rev)	2	3	120
	HRF [5 50]	1	2	330
	HRF [1 54]	1	2	330
	Bars (fwd)	2	2	120
	Bars (rev)	2	2	120
2	HRF [5 50]	1	3	330
	HRF [1 54]	1	3	330
	Bars (fwd)	2	3	126
	Bars (rev)	2	3	126
	HRF [5 50]	1	2	330
	HRF [1 54]	1	2	330
	Bars (fwd)	2	2	126

	Bars (rev)	2	2	126
3	HRF [5 50]	1	3	330
	HRF [1 54]	1	3	330
	Bars (fwd)	2	3	126
	Bars (rev)	2	3	126
	Wedges (fwd)	2	3	126
	Wedges (rev)	2	3	126
4	HRF [5 50]	1	3	330
	HRF [1 54]	1	3	330
	Bars (fwd)	2	3	126
	Bars (rev)	2	3	126
	Wedges (fwd)	2	3	126
	Wedges (rev)	2	3	126
5	HRF [5 50]	1	3	330
	HRF [1 54]	1	3	330
	Bars (fwd)	2	3	126
	Bars (rev)	2	3	126
	Wedges (fwd)	2	3	126
	Wedges (rev)	2	3	126

Table 4: Datasets acquired following optimization of the HRF and pRF paradigms. Scans were acquired at MB3, with all other parameters as in Table 3. Dataset 1 and 2 were additionally used to assess any differences between MB2 and MB3.

4.4.1 Analysis pipeline

In this section, the analysis performed on the HRF scans and the pRF scans is described with two analysis pathways performed. The development of the HRF fitting and GLM procedures were performed on the pilot protocols **A** and **B**.

For pilot protocol **B**, the 1 s HRF was compared with Wiener deconvolution of the 5 s HRF (pathway **i**). In addition, pRF analysis was performed on the bars and wedge scans here, along with the development of inserting voxelwise HRFs into the pRF mapping.

The final, optimized protocol **C** validated the HRF fitting, pRF and "HRF-informed" pRF models in 5 subjects (pathway **ii**). The analysis pipeline of each pathway is described in Figure 4.6.

4.5 Results: Data acquisition and paradigm optimisation

4.5.1 Pilot visual HRF data

BOLD responses from visual cortex were robust and showed large signal amplitudes. Figure 4.7 shows an example BOLD time course from an ROI, taken from the HRF scan in dataset A1. Note that the good CNR leading to a very high percentage signal change. This high CNR level was consistent across all datasets acquired.

Figure 4.8 shows the fitted HRF model using a GLM and *lsqcurvefit* for example 1 s and 5 s HRF scans, for dataset B2. The r^2 maps displayed on the flattened cortex are thresholded at 0.3 to highlight the difference in CNR between the 1 s and 5 s stimulation responses. As expected, the 5 s stimulation provides a much larger BOLD response than 1 s stimulation.

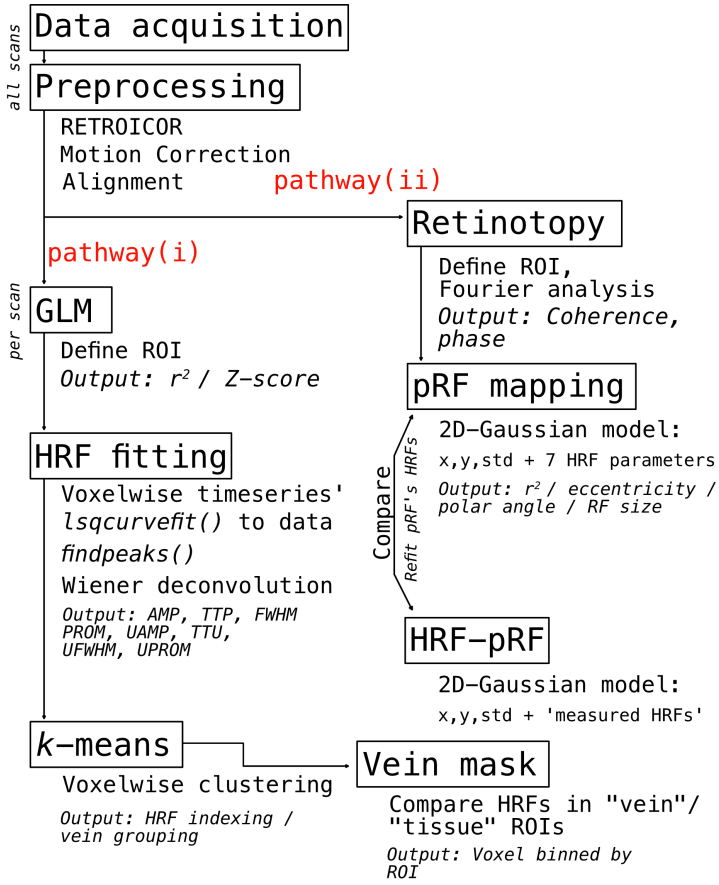


Figure 4.6: The analysis pipeline used in this chapter comprises exploring HRF fitting (pathway **i**) and retinotopy/pRF mapping (pathway **ii**). The pRF is performed by either fitting HRF parameters, or using measured HRFs input from the acquired HRF scan. Additional parameter maps and analyses can be derived from the HRF fitting scan, e.g. k-means clustering. For the HRF fitting, the *findpeaks()* function in MATLAB outputs 8 descriptive fit parameters: AMP (amplitude), TTP (time-to-peak), FWHM (full-width-at-half-maximum), PROM (peak prominence). The parameters for the undershoot peak are suffixed with U.

4.5.2 Optimising fMRI protocol: use of multiband acquisition

Figure 4.9 shows time-averaged HRFs collected from the 5 s HRF scan from a single dataset to compare MB factors for the fMRI acceleration. A higher

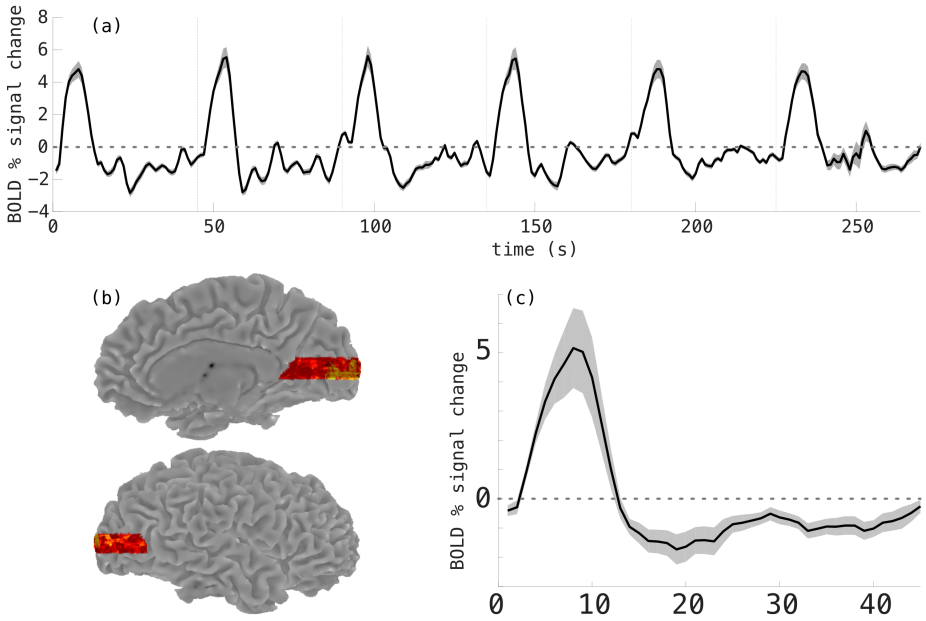


Figure 4.7: i) BOLD response timecourse for a 5 s ON 40 s OFF paradigm taken from an ROI in visual cortex (mean of 1000 voxels). The subject viewed a flickering checkerboard stimulus during the ON period and a mid-grey background for the OFFs. Black dotted vertical lines indicate the stimulus onset. The shaded grey background indicates standard error. The data for this region of interest timeseries were acquired at multiband 2. ii) ROI location taken from visual cortex. GLM r^2 is shown overlaid on the subject-specific surface. iii) Time averaged HRF of i).

MB factor provides greater spatial coverage within a TR. With no multiband, it was not possible to cover the entire visual cortex with a TR of 1 s. There is little difference between the two MB factors in terms of HRF response or tSNR of the data, while MB3 allows the whole of visual cortex to be sampled. This provides confidence that MB acquisition has little effect on the HRF measurement, which is complementary information to temporal SNR values. There were no large differences in temporal SNR (tSNR) between multiband acquisitions.

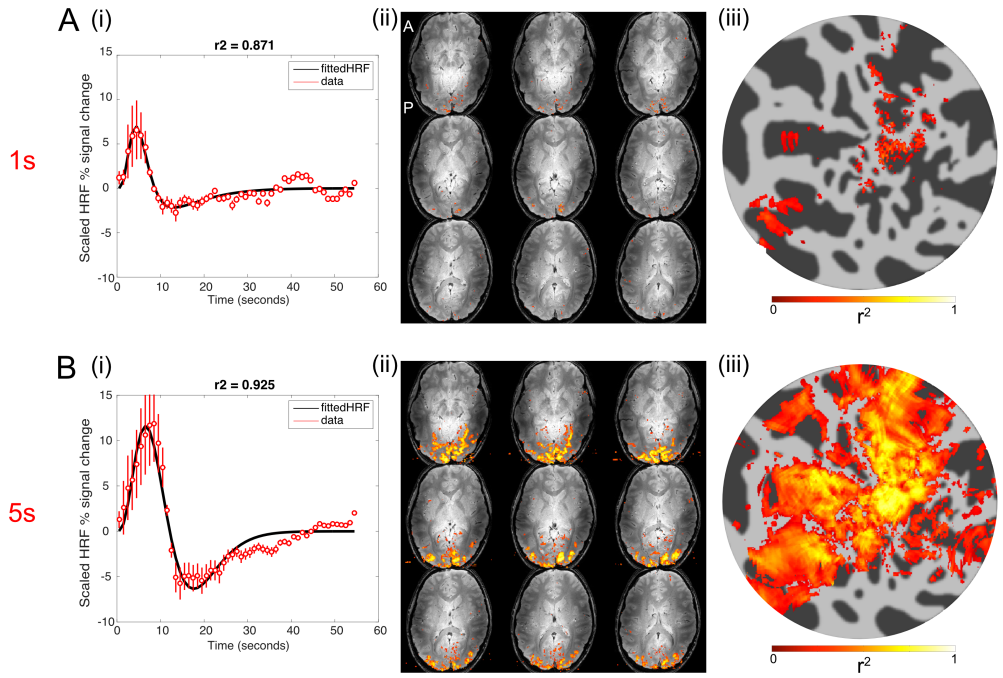


Figure 4.8: HRF to (A) 1 s ON and (B) 5 s ON visual stimulation for the HRF scan. (i) Single voxel timecourse showing the HRF fit to a double gamma function and associated r^2. (ii) GLM parameter map (threshold $r^2 = 0.3$) to the visual stimuli overlaid on subject-specific high-resolution T_2^* images. (iii) The corresponding parameter map overlaid on a flattened section of cortex, taken from Freesurfer. Data are taken from dataset B2.

4.5.3 HRF spatial parameter maps

For the 1 s and 5 s HRF scans, and the 5 s Wiener-deconvolved HRFs, the timeseries' were modelled with a double gamma function as described above (Section 4.6.2). Spatial parameter maps of amplitude, TTP and FWHM were calculated from *findpeaks()* (and also for the HRF undershoot) resulting in 6 maps. For further analyses, the prominence (PROM) parameter was not used (thus 6 maps instead of 8, from the 8 parameters described by *findpeaks()*). Figure 4.10 shows a representative example of the spatial maps,

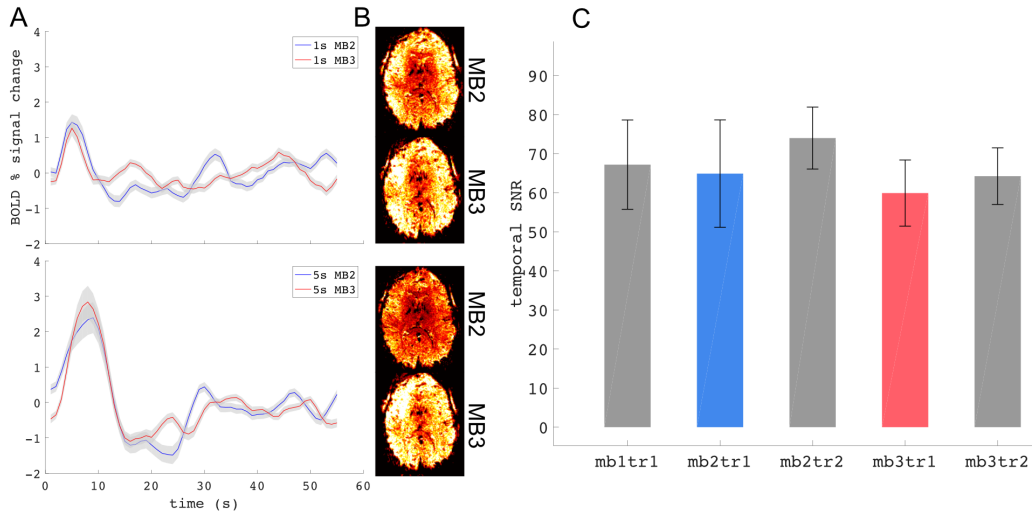


Figure 4.9: Mean HRFs for 1 s and 5 s HRF ON scans collected at MB2 and MB3 in the same scan session (dataset B2). A) There is no significant difference in BOLD signal percentage change between 1 s and 5 s HRFs at different multiband factors. As expected, tSNR is reduced as TR is reduced for a given MB factor (despite using the Ernst angle). This implies that MB acquisition has little effect on the HRF measurement quality and the increased spatial coverage provided by multiband should be used. Standard errors are indicated by grey shading. B) Temporal SNR (tSNR) is shown on a single slice taken from each of the 4 HRF scans. In visual cortex, there is little change in tSNR. Signal drops can be due to physiological noise or motion artifacts. C) Mean tSNR values from all visual datasets in this Chapter, comparing Multiband factor and TR. Black error bars are 95% confidence intervals.

for the 1 s and 5 s HRF scan, in a single subject.

It is difficult to discern any striking spatial patterns or borders separating groups of voxels that have similar HRF parameters, e.g. TTP. This example is representative of all subjects in the protocol **C** datasets.

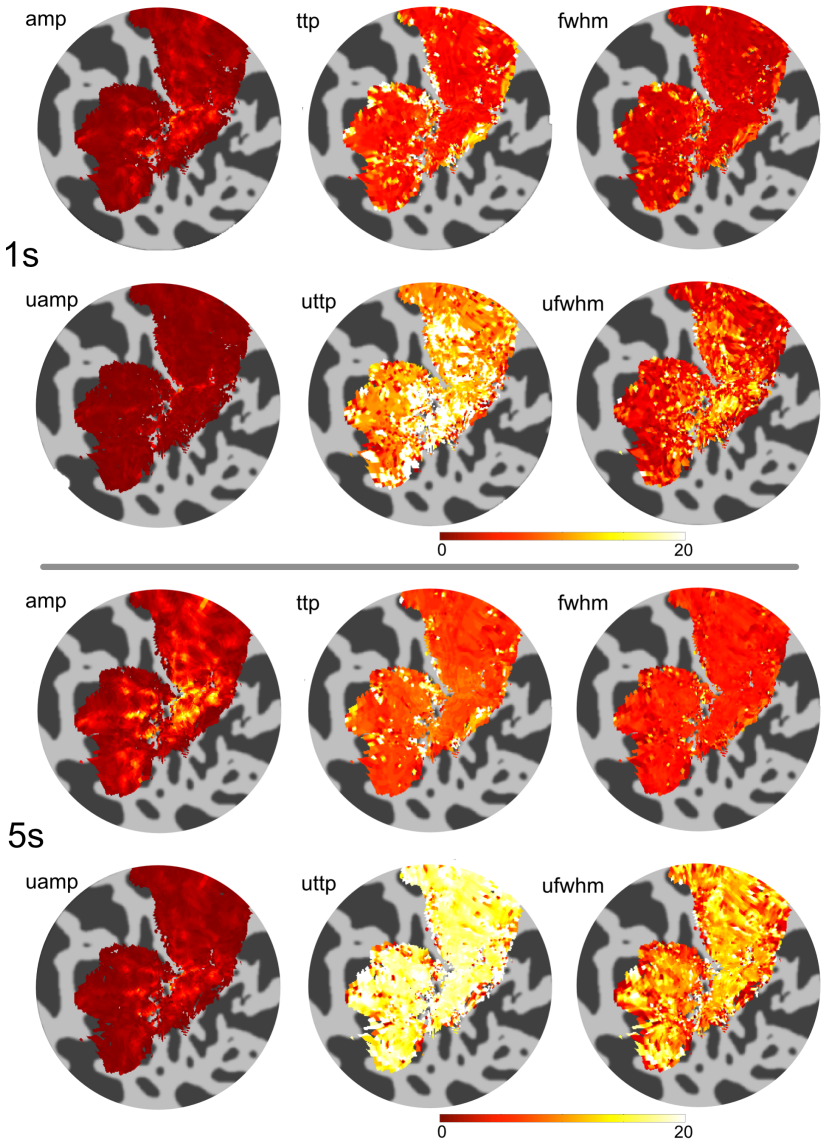


Figure 4.10: Maps of HRF-derived spatial parameters are displayed on a flattened patch of visual cortex, for a single hemisphere, from a single subject (dataset C2). These maps were generated from the 1 s (Top 6) and 5 s (Bottom 6) HRF scan and show the parameters for amplitude (amp, %), time to peak (ttp, s), full-width at half maximum (fwhm, s), undershoot amplitude (uamp, %), undershoot ttp (uttp, s) and the undershoot fwhm (ufwhm, s).

4.6 Methods: HRF fitting and separation

4.6.1 HRF fitting: pathway (i)

For the HRF protocols **A** and **B** (see Table 2), data were first preprocessed (motion correction, alignment and temporal filtering to remove drift). A GLM analysis was then performed to identify regions of activation in the visual cortex. From the GLM-defined ROI, the "raw" HRFs were extracted (avoiding any GLM scaling); curves were fit to each voxel's HRF using non-linear least squares fitting, as described in detail in Section 4.6.2.

To determine if there was any spatial structure, or clustering, of voxels with similar HRF fit parameters k-means clustering was performed and this is described in Section 4.6.5. Spatial maps of this cluster index were displayed to allow determination of whether voxels with similar HRF shapes also clustered in space.

Cortical depth must also be considered with regards to HRF variability, since it is known that there is a greater venous contribution on the more superior layers of grey matter compared to deeper layers (Duvernoy et al., 1981) which may result in different shaped HRFs. Typically, region-of-interest (ROI) drawing is performed at 0.2-0.8 mm on a flat patch of cortex, which will inherently reduce the contribution from veins in the top layer of the cortical patch. Thus, vein and tissue ROIs were taken across the entire cortical depth for k-means clustering.

4.6.2 Modelling the HRF

To derive a description of HRF shape, a curve can be fitted to the measured HRFs using *lsqcurvefit()* in MATLAB. In Appendix 8, the modelling of a

canonical HRF shape using a double gamma function is described. From the fMRI data collected, with a long OFF period, the trial-triggered average was computed for every voxel in the activated region-of-interest (ROI), producing a matrix consisting of x rows (length of HRF) by y columns (number of voxels).

A double gamma function (Worsley, 2001) - difference of two gamma functions - was used to fit the data-derived HRFs (on a voxelwise basis). The response function $h(t)$ over a series of timepoints t is given by,

$$h(t) = \left(\frac{t}{d_1}\right)^{a_1} e^{-\left(\frac{t-d_1}{b_1}\right)} - c\left(\frac{t}{d_2}\right)^{a_2} e^{-\left(\frac{t-d_2}{a_2}\right)} \tag{4.1}$$

where $d_j = a_j * b_j$ and is the time-to-peak, and a set of default (canonical) parameters (Glover, 1999) are used as a starting point of $a_1 = 6$, $a_2 = 12$, $b_1 = b_2 = 0.9$ seconds, and $c = 0.35$. The model function is minimized using a non-linear least squares solver (*lsqcurvefit*). From these modelled HRF curves, spatial parameter maps can be calculated; this allows the assessment of the spatial distribution of TTP, etc. across the cortex. For visualization purposes, these were overlaid on the high-resolution flattened cortical patch.

For each voxel's fitted HRF curve, 8 descriptive parameters were obtained using the *findpeaks()* function in MATLAB: time-to-peak (TTP), full-width-at-half-maximum (FWHM), peak amplitude (AMP) and the prominence, which measures the amount a peak stands out amongst its neighbours due to its intrinsic height (PROM) - for the peak and the undershoot (prefixed with U). Each voxel will thus produce a set of 8 parameters, and associated spatial maps of these parameters can be derived and displayed on subject-specific flattened cortices. An example of a HRF fit and associated parameters are shown in Figure 4.11.

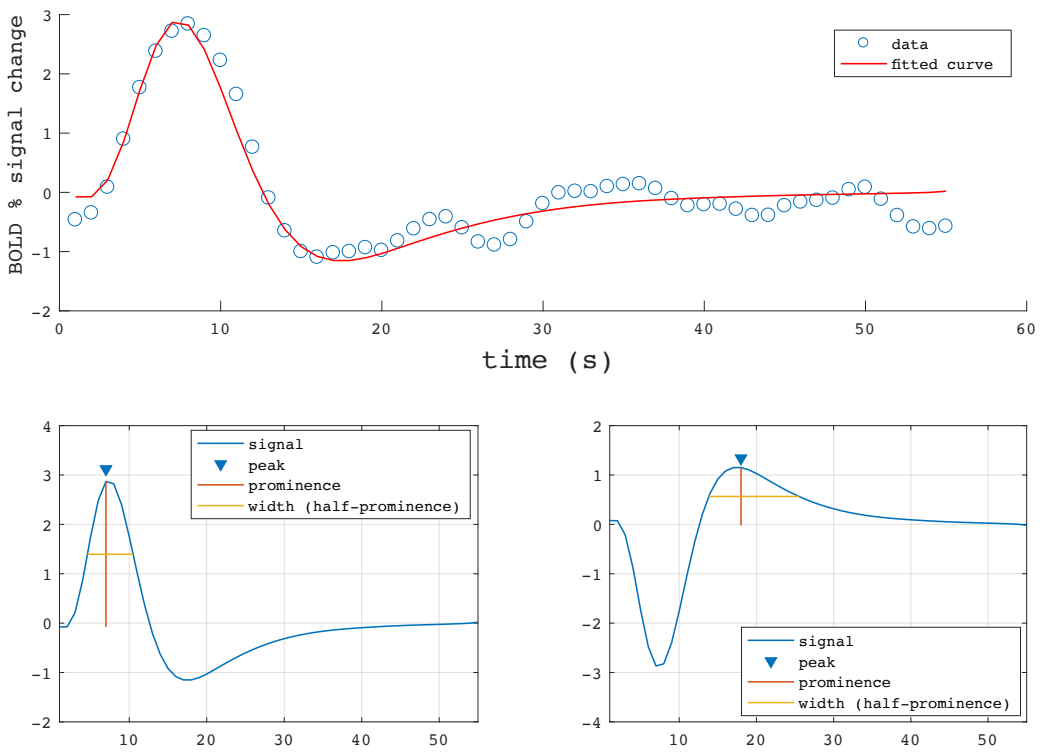


Figure 4.11: Top) Example HRF and fitted curve using *lsqcurvefit()* in MATLAB. Left) 8 descriptive parameters can be measured from a HRF using the *findpeaks()* function, 4 for the positive portion: Peak (AMP), width (FWHM), prominence (PROM), index of peak (TTP), and 4 for the corresponding parameters applied to the undershoot. Right) To find the corresponding parameters for the minima in the HRF shape, the curve is multiplied by -1.

4.6.3 Separating tissue versus vein signals

The acquisition of a high-resolution T_2^*-weighted scan allows veins to characterized as these have a short T_2^* compared to tissue. When resampled to a flattened space this scan can be used to mask veins from the functional data. To this end, it is of interest to assess whether there is a correspondence between the maps of the 8 HRF parameters and the location of veins in visual cortex.

Veins are not typically included in the statistical maps of pRF mapping. As a consequence of this being a phase-encoding method that cycles through all stimulations without a rest period and hence, it is a form of differential mapping in which any non-modulating components will be eliminated (Ugurbil et al., 2003). In contrast, the HRF scans are acquired in a block-design and thus are susceptible to transient signals from draining veins.

To address whether voxels can be segregated based on spatial proximity to vein or tissue, two complementary approaches were taken. 1) Using the vein-mask defined from the FLASH scan to separate and generate tissue and vein timecourse HRFs from two separate ROIs; 2) Using a model-free method to derive the voxels that lie preferentially in veins or tissue, based on their HRF shape and thus fitted parameters. It is of interest to determine whether certain values of the 8 parameters are more likely to reflect venous voxels, as opposed to tissue in grey matter. The latter method used the output from the k-means clustering (list of index values) to determine how much of each cluster belongs to either a venous or tissue voxel - which are known from the vein mask.

4.6.4 Vein masking

An additional analysis was performed across subjects to validate the registration of the vein mask derived from the high-resolution FLASH scan to the EPI data. Region-of-interests were derived from the FLASH scan, and the venous dilation and distribution thresholds are chosen individually. The registration from the functional EPI images to the structural FLASH scan were validated visually.

Here, the mean image intensity from the raw 5 s HRF EPI scan was calculated (in which the veins appear darker due to a higher deoxyhaemoglobin content). A second set of ROIs were then derived from this mean inten-

sity image by fitting a mixture of Gaussians (Gaussian mixture model) to the histogram of the intensities. The separation between the Gaussians was derived from the venous peak mean + 2 standard deviations (see Figure 4.12).

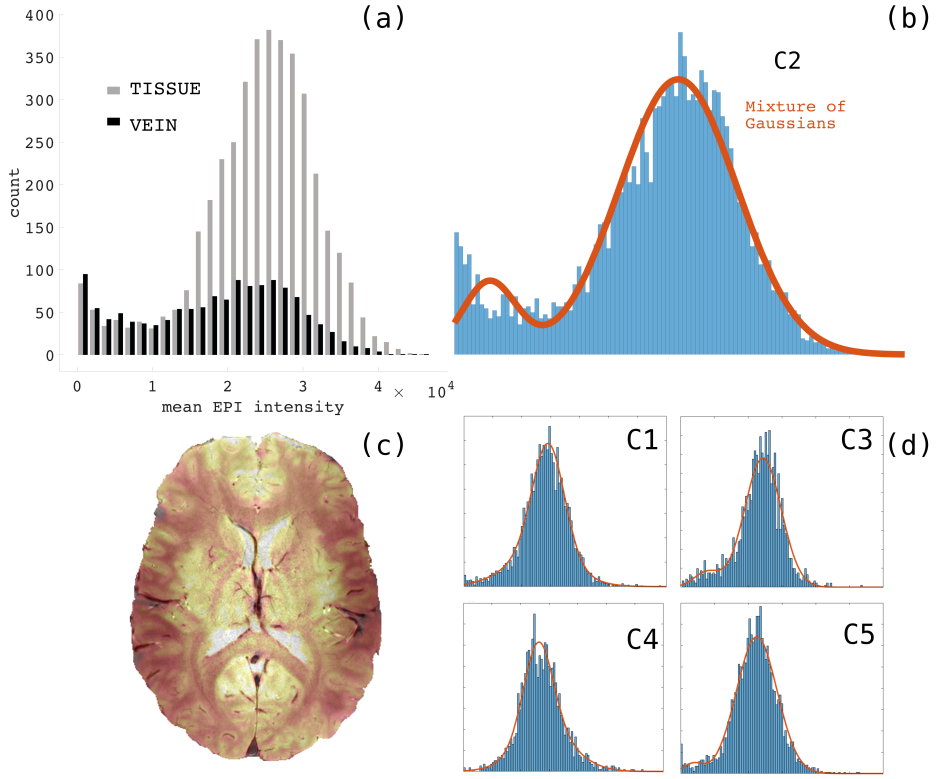


Figure 4.12: (a) Mean EPI intensity of a single HRF 5 s scan from one subject (dataset C2), derived from an ROI in visual cortex. Voxels are grouped based on which ROI (tissue/vein) they were defined to be attributed to as defined from the FLASH scan. Note that lower EPI signal intensity values correspond to veins. (b) The same histogram data overlaid with a Gaussian mixture model, which does not know the tissue/vein grouping from the ROIs, but merely assumes a cluster of 2. (c) An example mean EPI (hot colourmap) overlaid on a FLASH image (grey) for a subject. (d) As (b) for remaining subjects in datasets **C**.

For the latter ROIs, the index values from the previously performed k-means clustering (which is blind to tissue or vein ROIs) were used to see how much of each cluster belongs to either a venous or tissue voxel, as described in

section 4.6.1.

4.6.5 *k*-means clustering

k-means clustering is a technique that assigns a set of data points (n) into a set of clusters (k), by assigning each data point into the closest cluster, based on its mean. This can be described as unsupervised classification of patterns into groups. A commonly used algorithm is *Lloyd's* (Lloyd, 1982) which partitions the data by iterative refinement. The algorithm proceeds along two steps: an assignment step and an update step.

The assignment works as follows: first, each data point is assigned to the nearest of k initial centres, whose mean has the shortest squared Euclidean distance. For two points, q and p, in n dimensions, the Euclidean distance between them is given by the Pythagorean formula:

$$d(q,p) = \sqrt{(q_1 - p_1)^2 + (q_2 - p_2)^2 + ... + (q_n - p_n)^2} \tag{4.2}$$

$$= \sqrt{\sum_{i=1}^{n} (q_i - p_i)^2} \tag{4.3}$$

In the second step, the cluster centres are computed as the centre of mass of all the points assigned to it, the *centroid*. Each cluster centre is then moved to this new centroid - this is the new mean. These two steps are repeated until the assignment stabilizes: each iteration involves finding the centroid of each cluster, then re-assigning the data points based on how close they are to the new cluster centroids. *Lloyd's algorithm* is similar to the construction of a "Voronoi diagram": for each site p_k, the corresponding Voronoi cell R_k is every point in a Euclidean plane whose distance to p_k is shorter or equal

to the distance from itself to another site.

k-means clustering was performed on the parameters from the fitting of the double-gamma function (output from *lsqcurvefit*, MATLAB). An important question is how spatially variable the measured HRF is in terms of the 8 descriptive parameters across visual cortex, which can be evaluated using these spatial maps.

This analysis route is visualized by pathway **(i)** in Figure 4.6.

4.7 Results: HRF fitting and separation

4.7.1 Vein-masking

The acquisition of a high-resolution ($(0.5\text{ mm})^3$ isotropic) T_2^*-weighted scan allowed veins to be identified in regions of interest in the visual cortex. Figure 4.13 shows vein masks overlaid on each subject's FLASH scan from protocol datasets **C**.

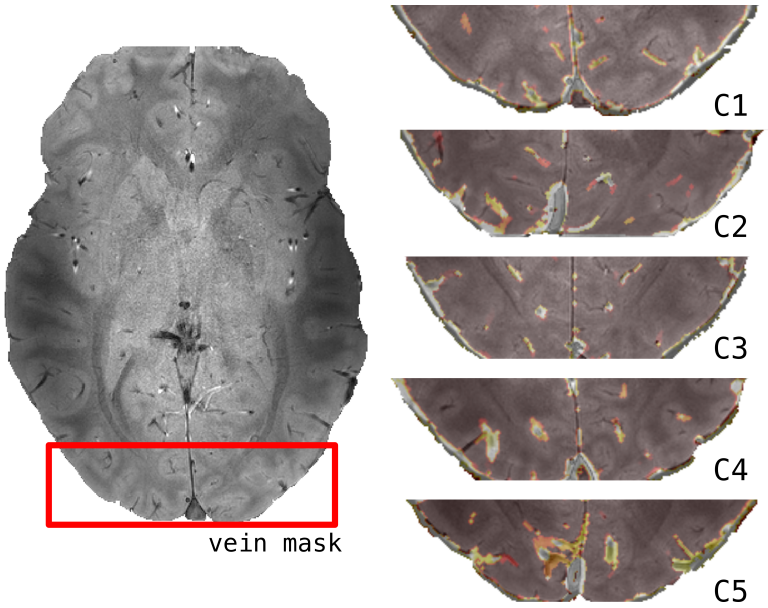


Figure 4.13: Vein masks overlaid on high-resolution FLASH scans for every subject in datasets **C**. A good correspondence between vein and tissue can be seen.

Three methods were used to define tissue and vein ROIs: 1) ROIs based on thresholding the FLASH scan; 2) applying a threshold to the mean intensity EPI image to identify veins using a Gaussian mixed model distribution on the EPI data alone; 3) A common mask formed by the intersection of 1) and 2). A representative image of these masks is shown in Figure 4.14. The vein mask from the FLASH scan denotes a larger extent of voxels as venous,

whereas the mean EPI intensity ROIs are more stringent.



Figure 4.14: Tissue and vein masks derived from the high-resolution FLASH scan (left), the mean intensity ROIs using a Gaussian mixture model find the vein/tissue boundary threshold (middle) and the intersection of the FLASH and mean intensity masks (right). Black = vein, white = tissue. The vein masking was performed across the entire cortical depth.

Grouping the voxel timeseries' according to a vein ROI or tissue ROI, the HRF parameters can be plot as a function of tissue or vein (Figure 4.15). For the 5 s HRF scan, it can be seen that there are very few differences between tissue/vein ROIs, according to the vein mask, in terms of HRF parameters. Generally, those voxels corresponding to a venous ROI have slightly higher amplitudes, which is expected since veins tend to have a larger BOLD response. It must be noted that there are fewer venous voxels than tissue voxels (see Table 5) - this was confirmed from both the vein mask derived from the FLASH scan ROIs and the mean EPI intensity ROIs.

4.7.2 *k*-means clustering

The use of 2 clusters provided the best qualitative separation within the 8-dimensional HRF parameter data (amp, ttp, fwhm, prom, uamp, uttp, ufwhm, uprom - see section 4.6.1), however, the only parameters of interest that separated well were TTU and the undershoot FWHM. This is difficult to visualise as there are far fewer veins than tissue, which is evident in

Percentage of veins vs. tissue	
Dataset	% veins
C1	8.41
C2	7.83
C3	5.44
C4	6.34
C5	2.78

Table 5: The percentage of veins compared to tissue from a retinotopy-thresholded ROI visual cortex, across all subjects in datasets **C**. It is evident that are very few venous voxels identified by the intersection of the FLASH vein mask and the EPI intensity threshold.

Figures 4.16 and 4.17. By finding the corresponding HRFs (per voxel) that belonged to either cluster 1 or 2, it was possible to derive cluster-specific HRFs. Projecting this back onto a flattened brain in the form of an overlay, there isn't any clear pattern visible (see Figure 4.18). Additionally, when plotting the HRFs according to which cluster they belong to there are no striking differences. Using k-means clustering with 3 clusters or more models the lower amplitude signals in the data.

Finally, while the spatial map of vein clustering provides a good perspective to identify any striking spatial patterns, a more quantitative descriptive analysis was performed. Following the k-means clustering, which provides an index value indicating which voxel belongs to which cluster, e.g. 1 or 2, it was assessed as to whether there was any consistency between clustering index and which ROI (tissue or vein, taken from the vein mask scan, described previously in section 4.7.1) the voxel belonged to. One hypothesis would be that voxels near to veins correspond to one cluster moreso than the other, and the same for tissues. By plotting this in Figure 4.19, it can be seen that there is no correspondence between clustering and vein-masking visible, across all subjects in datasets **C**.

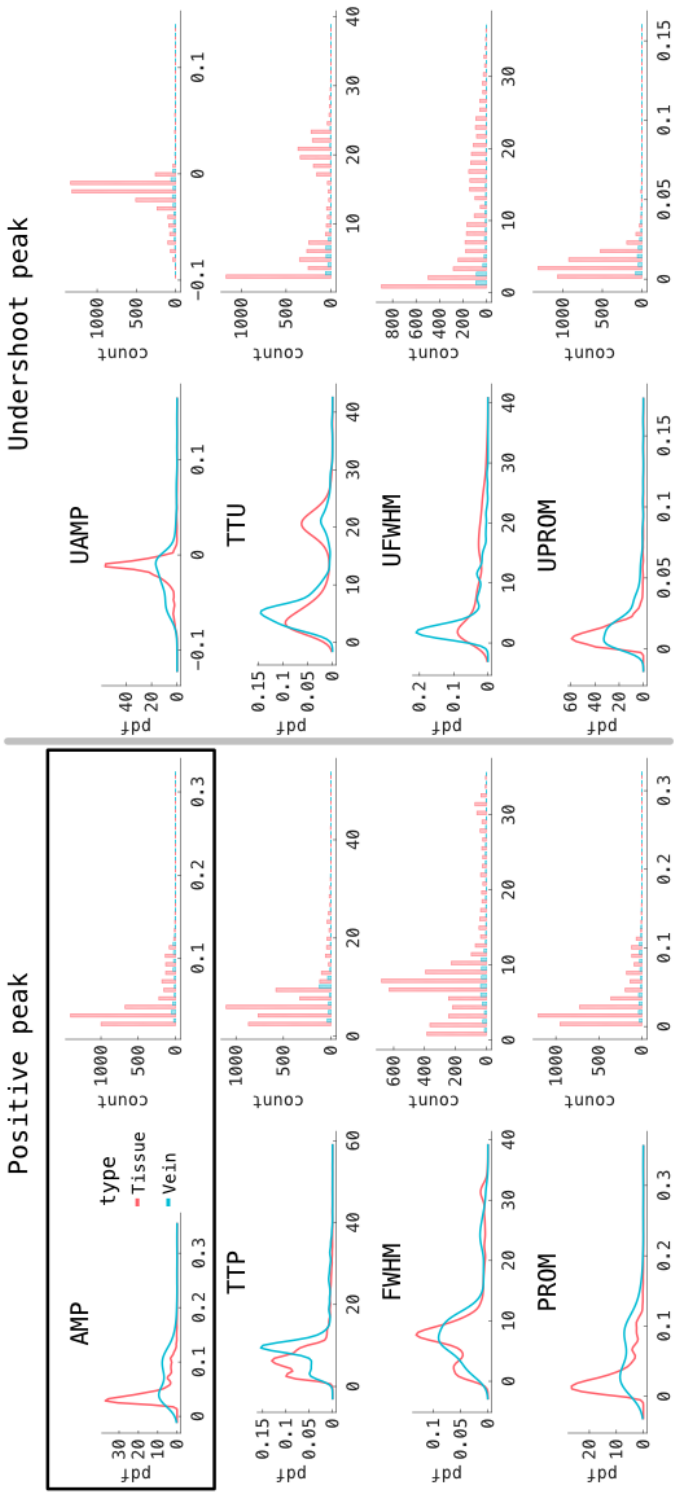


Figure 4.15: Intersecting tissue and vein ROIs were created from the high-resolution FLASH scan ROIs and the Gaussian mixed model ROIs. For each of the 8 HRF descriptive parameters (see section 4.6.1), voxels were binned and grouped according to whether it belonged to a vein (blue) or tissue (red) ROI. A probability density function of the same bins was plot, which allows any differences between groups to be clearer. Data are shown from dataset B2 5 s HRF scan. PDF=probability density function.

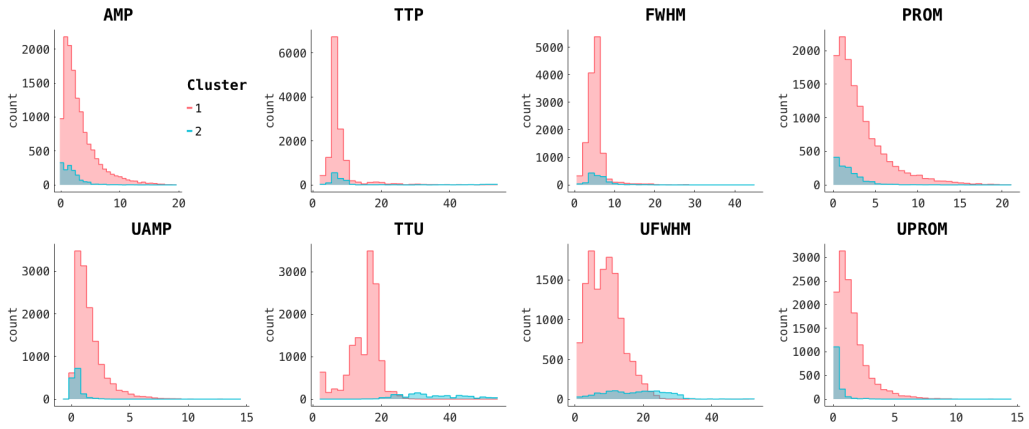


Figure 4.16: The voxel counts belonging to one of two clusters based on running k-means on 8-dimensional HRF parameter data. The parameters that seem to cluster independently and possibly drive separation, are TTU and UFWHM. Data are shown from all subjects in dataset **C**.

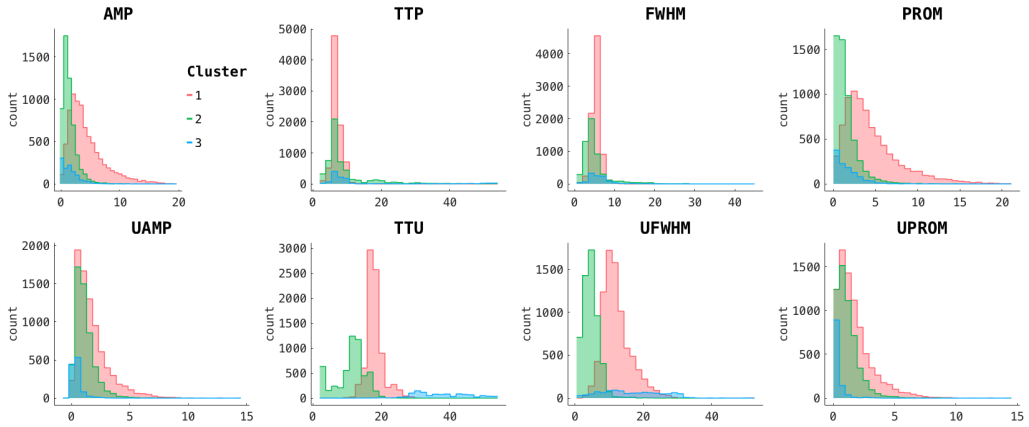


Figure 4.17: The voxel counts belonging to one of three clusters based on running k-means. It can be seen that the main cluster from Figure 4.16 has been split into two. Data are shown from all subjects in dataset **C**.

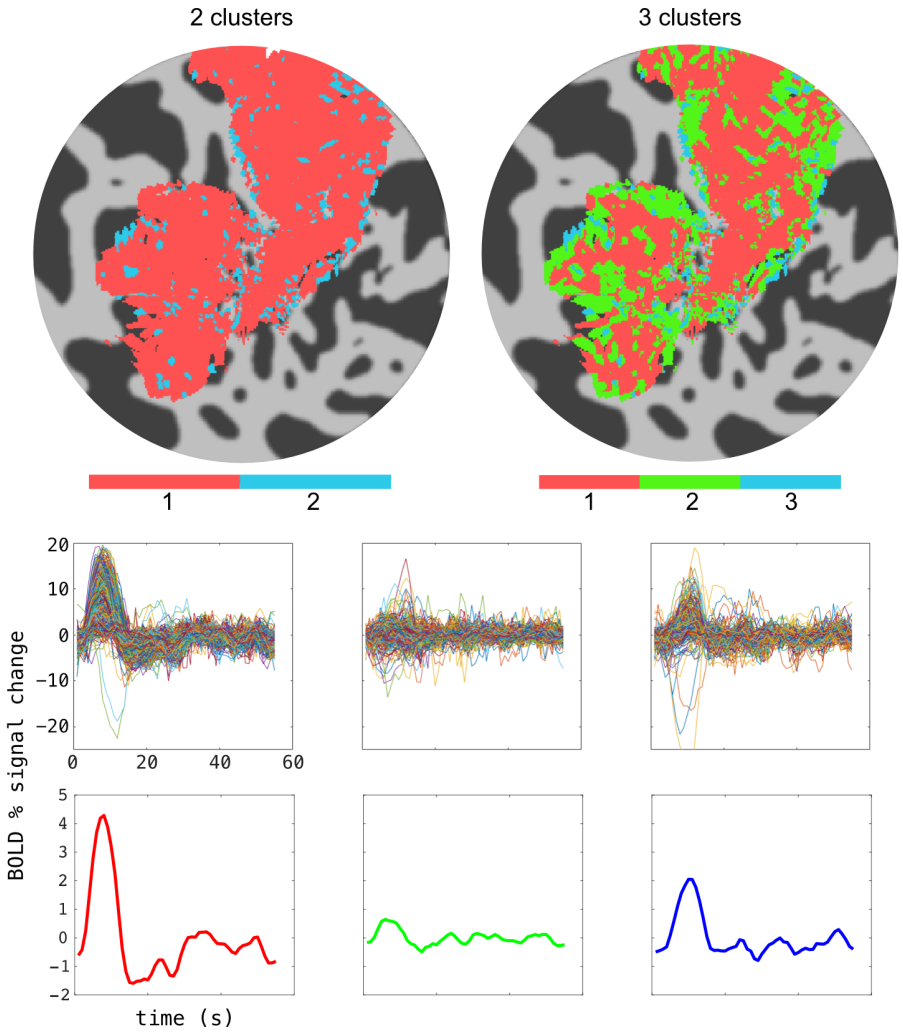


Figure 4.18: The k-means analysis projected onto the subject-specific flattened patch of visual cortex. Top) There is no clear pattern visible in the spatial locations, regardless of whether 2 or 3 clusters are used. Bottom) The HRFs plotted according to whether they belonged in cluster 1, 2 or 3; there is little difference in terms of HRF shape between 2 clusters, with a third cluster modelling the residual in the data. Top plots are all voxel HRFs in that cluster, bottom plots are mean HRFs in that cluster. Data are from dataset C2.

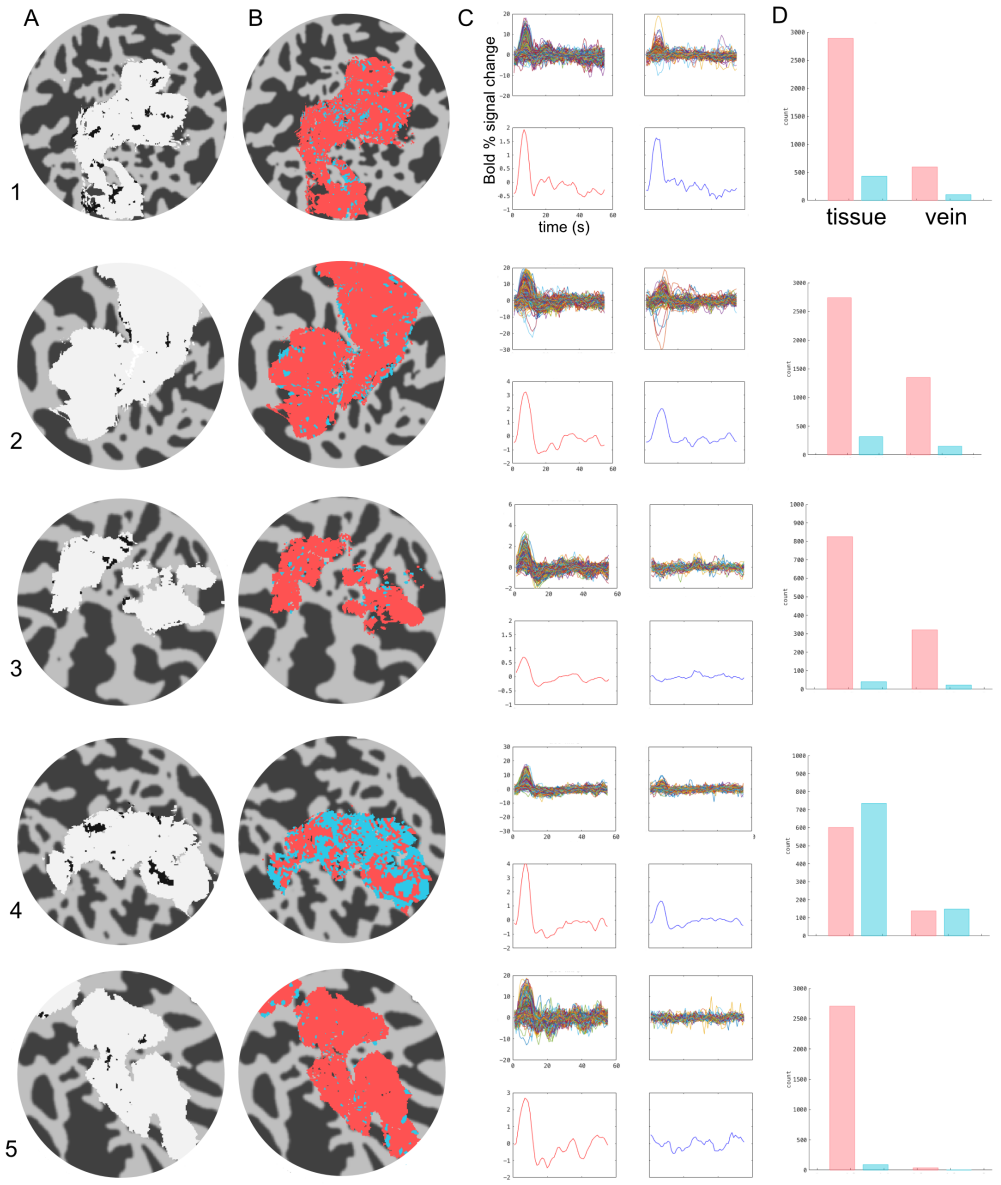


Figure 4.19: A) Vein masks, B) k-means clustering, C) cluster-specific HRFs and D) tissue/vein HRF to cluster relationship, across 5 subjects from datasets **C**. The voxels corresponding to either a vein ROI or a tissue ROI (from the acquired vein mask) were compared with their cluster index (from k-means clustering. There are naturally more voxels belonging to tissue than the venous ROI, although there does not seem to be any clear correspondence between vein mask ROI and cluster index.

4.8 Methods: pRF mapping

4.8.1 pRF tests: pathway (ii)

For the pRF experiments in protocol **B** (see Table 3), retinotopy and pRF modelling were performed. The retinotopic output from the wedge scans was used to define the ROI upon which pRF analysis was performed. To assess the similarity between the retinotopy and pRF analyses, the retinotopy phase and the pRF polar angle were compared. This was performed by computing the circular correlation between retinotopy and pRF angles (Berens, 2009).

Following the standard pRF analysis, the measured HRFs were used in the model using a novel "informed" pRF method, which bypassed the pRF's own HRF fitting algorithm. It was hypothesized that the pRF HRF modelling can lead to extreme values that are not representative of actual HRFs.

4.8.2 Retinotopic mapping

The retinotopy data in this chapter were first analysed using traditional methods (Engel et al., 1994): Fourier analysis was performed, extracting the component at the fundamental frequency of the stimulus sequence. The best fitting sinusoid at the stimulus frequency gives the coherence. The phase of the response at the same frequency measures the time delay between the fMRI signal and onset of a stimulus cycle, and therefore where in the visual field that stimulus was presented. Spatial maps of coherence show the areas of strongest modulation; the phase maps can be used to define the different cortical areas, e.g. V1/V2.

4.8.3 pRF mapping

For the pRF analysis, a 2D-Gaussian (3 parameters: x, y, standard deviation σ) model was used with 7 HRF parameters (timelag, full-width-at-half-maximum (FWHM), undershoot amplitude, undershoot FWHM, undershoot timelag, and two HRF offset parameters) (Dumoulin and Wandell, 2008). These parameters are fitted non-linearly, together with the Gaussian fit, hence resulting in a 10-parameter model.

The acquisition of a 1 s and a 5 s HRF scan allowed HRF-informed mapping. While a 1 s ON period provides a better estimate of a neural response (an instantaneous spike lasting 1 second with no rise/fall time back to baseline), the BOLD SNR of the timeseries will be lower, and may be noise-limited, even in the visual cortex, thus this was compared with a 5 s ON period.

The time-averaged HRF was extracted per voxel, from both the 1 s and 5 s fMRI scans separately. For a single pRF fitting procedure, the per voxel HRFs (e.g. the 1 s HRFs) were entered into the pRF model, bypassing the HRF parameters, i.e. the pRF model now only fit for 3 parameters.

Specifically, for each voxel, during the pRF non-linear fitting procedure, the model response estimated from the x, y and σ was convolved with a measured HRF, taken from the HRF scan. These voxels were in the same space, so there were no registration/mislocalization errors. In the standard pRF model fitting, the HRF parameters are changed on each iteration of the non-linear least squares fit, however, here instead the measured HRF was kept fixed, allowing only x, y and σ to vary. Statistically, this reduces the degrees of freedom of the pRF model, alleviating the chances of artificial r^2 inflation by overfitting.

Four pRF fits were assessed: 1) The regular pRF (10 parameter 2D-Gaussian model), which included the pRF's own HRF fitting procedure; and user-

input HRFs; 2) The pRF with a 1s HRF; 3) The pRF with a 5 s HRF; and 4) The pRF with a 5 s Wiener-deconvolved HRF.

For the latter, a deconvolution analysis was performed to extract the HRF to 1 s of neural activity with the added benefit of possessing a higher SNR than the "true" measured 1 s HRF. It is known that deconvolution is highly susceptible to noise. By providing an estimate of the noise in a non-activating cortical region, an improved deconvolved HRF is resolved (Wiener deconvolution) (Glover, 1999; Papoulis, 1977).

An additional analysis compared the retinotopy phase and pRF polar angles from 4 different pRF analyses: the regular pRF, the pRF using the Levenberg-Marquardt algorithm (LMA), the HRF-informed pRF (see Section 4.11.1), and the HRF-informed pRF using the LMA.

This pipeline can be followed via pathway **(ii)** in Figure 4.6.

4.9 Results: pRF mapping

Figure 4.20 shows retinotopy and pRF parameter maps from a representative subject. The retinotopy maps depict very high coherence values, indicating strong modulation of the BOLD response at the stimulus frequency. For the pRF analysis there were high values of r^2 across much of visual cortex. The two analyses produced comparable maps of visual field angle, as evidenced by the phase map (retinotopy) and polar angle map (pRF). To allow a direct comparison of the maps from retinotopy and pRF analyses, pRF visual field angles were mapped into the domain $[0\ 2\pi]$.

Figure 4.21 shows an example of a strongly modulated voxel from the pRF analysis (r^2=0.95). Table 6 shows the maximum r^2 and the number of voxels fitting above 0.5, across subjects. These data are from the final protocol (**C**) as detailed in Table 4.

pRF r^2 comparison (B)				
Dataset	pRF type	Max r^2	Voxels % $r^2 > 0.5$	Hemi-sphere
C1	B (fwd)	0.84	4.35	L
	B (rev)	0.78	13.09	L
	B (fwd) + 1s	0.65	2.26	L
	B (fwd) + 5s	0.663	1.70	L
	B (fwd) + W	0.66	2.20	L
C2	B (fwd)	0.90	45.22	R
	B (rev)	0.89	40.56	R
	B (fwd) + 1s	0.64	0.60	R
	B (fwd) + 5s	0.83	22.64	R
	B (fwd) + W	0.70	3.84	R
C3	B (fwd)	0.71	8.94	R
	B (rev)	0.72	6.71	R
	W (fwd)	0.77	9.50	R
	W (rev)	0.94	39.06	R
	W (rev) + 1s	0.79	9.04	R
	W (rev) + 5s	0.89	19.42	R
	W (rev) + W	0.89	21.02	R
C4	B (fwd)	0.85	25.17	R
	B (rev)	0.80	15.90	R
	W (fwd)	0.91	26.85	R
	W (rev)	0.92	27.08	R
	W (rev) + 1s	0.78	13.82	R
	W (rev) + 5s	0.84	16.25	R
	W (rev) + W	0.80	16.76	R
C5	B (fwd)	0.87	19.97	R
	B (rev)	0.86	20.78	R
	W (fwd)	0.94	49.08	R

W (rev)	0.93	51.20	R
W (rev) + 1s	0.92	29.04	R
W (rev) + 5s	0.87	25.48	R
W (rev) + W	0.90	24.93	R

Table 6: Maximum pRF r^2 values shown for every scan analysed, from a large visual ROI, for each paradigm (W = Wedges, B = Bars). The percentage of voxels fitting above 0.5 are also indicated - the number of voxels analysed for each pRF scan is of the order of 1000. The high values of r^2 and large number of good fitting voxels is apparent, however, this is variable between subjects. For the best fitting pRF scan, e.g. the reverse wedges, the HRF-informed pRF was run, using either 1 s, 5 s or Wiener (W) deconvolved HRFs; it is apparent that the fits are lower.

To compare pRF fitting algorithm, pRF polar angles were subtracted from the retinotopy phase values and the circular variance was computed for these differences. Figure 4.22 shows that while the maps are comparable, there is no clear trend in which algorithm to use. Circular variance of the difference plots per subject is shown in Figure 4.24. The variance is generally quite small and varies across subjects; the polar angle plots for a single subject are shown in Figure 4.23.

Figure 4.20: Left) Retinotopy parameter maps showing the coherence (co) and phase (ph) for the left hemisphere (lh) and right hemisphere (rh). Spatial parameter maps of coherence and phase are consistent with previous retinotopy literature with smooth transitions in polar angle across the visual cortex. Right) Population Receptive Field (pRF) parameter maps for the right hemisphere from the 2D Gaussian + HRF (10 parameter) model, shown for a single scan (forward drifting bars), on the right hemisphere, from dataset B2. The pRF parameter maps show A) a r^2 map, a measure of the model fit to the data; B) polar angle; C) Eccentricity; and D) pRF size, measured as the standard deviation of the 2D Gaussian.

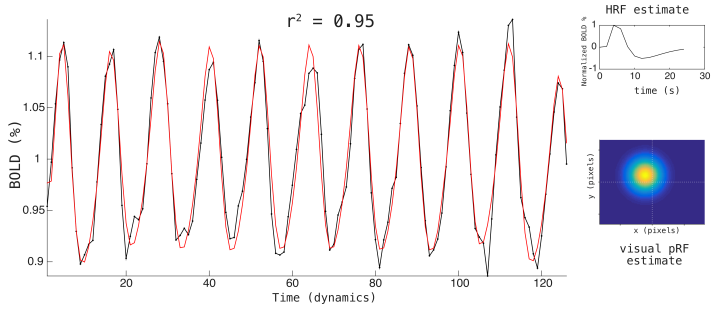


Figure 4.21: Population Receptive Field (pRF) fit to the data, for a single voxel, to the reverse wedges scan. Black line = data; Red line = pRF fit. A depiction of the pRF for this voxel is seen on the bottom right. The pRF's version of the HRF is shown in the top right

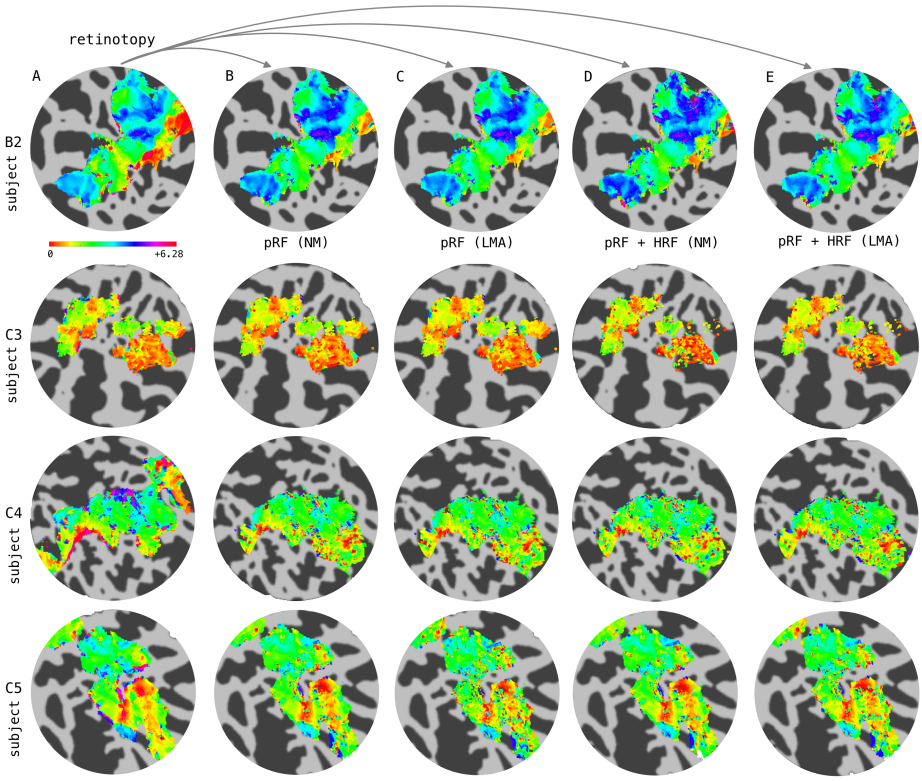


Figure 4.22: Comparing phase from retinotopy and polar angle from pRF mapping. A) Retinotopy phase, B) pRF polar angle, C) pRF using Levenberg-Marquardt (LMA), D) HRF-informed pRF polar angle, E) HRF-informed polar angle using LMA.

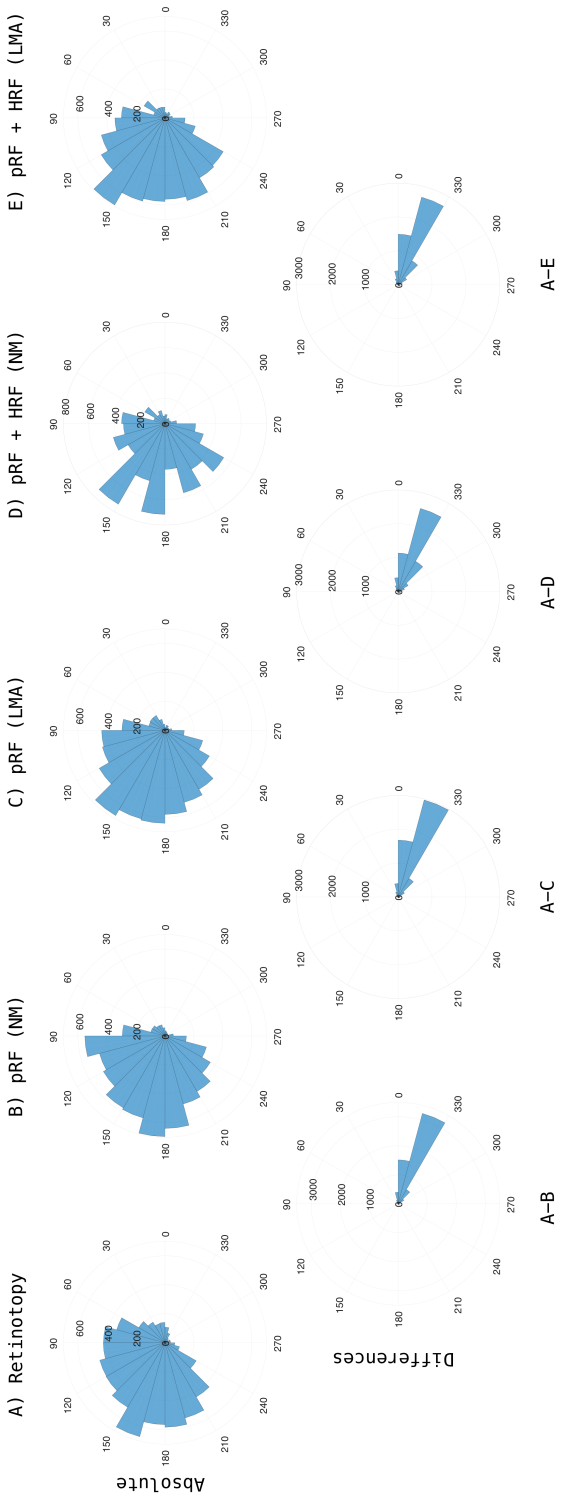


Figure 4.23: Polar angle histograms are shown for subject **B2**. The columns correspond to the columns in Figure 4.22. A) Retinotopy phase, B) pRF polar angle, C) pRF using the LMA polar angle, D) HRF-informed pRF, E) HRF-informed pRF using the LMA. F,G,H and I are difference plots of phase. F) A-B, G) A-C, H) A-D, I) A-E. A large spread indicates a larger variance.

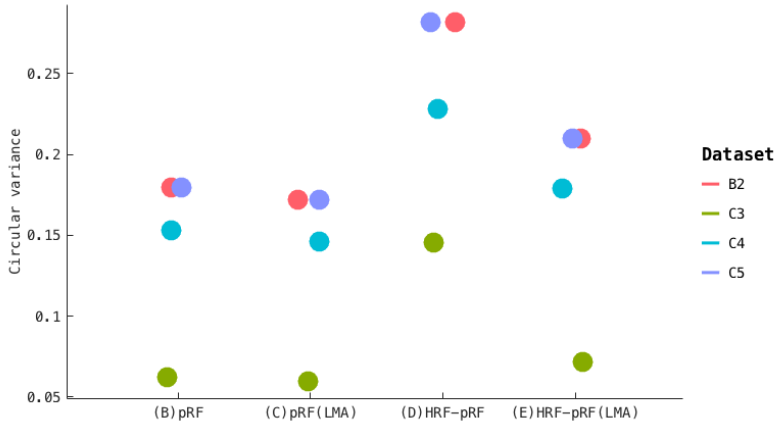


Figure 4.24: The circular variance for each polar angle difference plot (between retinotopy phase and pRF polar angle) is computed across subjects. Circular variance is bounded in the interval [0 1]. A large spread of values is indicated by a large variance and is close to 1. Columns are consistent with Figure 4.22

4.10 Methods: Comparing the pRF's and measured HRFs

4.10.1 Final protocol (C)

The final analysis pipeline was validated on 5 datasets using the scans listed in Table 4. For all 5 datasets, both pathways **(i)** and **(ii)** were followed from Figure 4.6. HRF fitting was performed for both 1 s and 5 s acquired HRF scans, producing spatial parameter maps. k-means clustering and vein masking using the high-resolution FLASH scan were performed on the 5 s scan for each subject. Retinotopy and standard pRF analyses (2D-Gaussian) were performed and the 1 s, 5 s and the 5 s Wiener-deconvolved HRF were input into the pRF model as described in Section 4.8.3.

4.10.2 Comparison of the pRF derived HRF with the measured HRFs

An important question is how well the pRF models the HRF from the data, or does the fit produce a high r^2 at the expense of an unrealistic HRF fit. This question can be probed by comparing the pRF's fitted HRFs to the measured HRFs in the same session from the same subject to provide a quantitative comparison.

Here, the measured HRFs are fit using the pRF's HRF fitting algorithm to generate 7 HRF parameters and a confidence interval for every subject. This is compared to a "real" or "true" HRF. By inspecting the pRF's HRF estimates and separating these according to r^2, one can determine whether the pRF is adopting a "physiologically true" HRF shape for strong fits, or is just minimizing residuals.

4.11 Results: Comparing the pRF's and measured HRFs

4.11.1 HRF informed pRF fits

The mean of the 1 s, 5 s HRF and the 5 s Wiener-deconvolved HRFs are shown in Figure 4.25. The HRF-informed pRF analysis using these fits are shown in Figure 4.26. For all subjects in dataset **C** it can be seen that the pRF's version of HRF provides the best fit to the data. Notably, since the pRF fitting will tune the HRF parameters without any physiologically-relevant boundaries to optimize r^2. While the fits to the data may be good, the curves may be unrealistic HRFs. Here, the *adjusted* r^2 was calculated, which penalizes extra parameters added to the model. It is shown that the 5 s HRF-informed maps look more similar to the pRF than the 1s HRF (due to noise) and Wiener-deconvolved, and are in fact more physiologically true than the regular pRF.

Figure 4.27 shows the number of voxels fitting above $r^2 > 0.5$, across all subjects in dataset **C**. For the HRF informed pRF, the percentage of voxels fitting above 0.5 varies widely, likely depending on the regular pRF fit. The percentile differences across subjects is also shown. In all cases, the regular pRF performs better than the HRF-informed fit.

4.11.2 Comparing pRF HRFs to measured HRFs

Comparing the pRF's fitted HRF to a measured HRF is key to validating the physiological accuracy of the pRF model. The pRF's estimate of the HRF faceted by r^2 percentile is shown in Figure 4.28. With increasing r^2, few of the pRF HRF shapes look like typical haemodynamic response shapes.

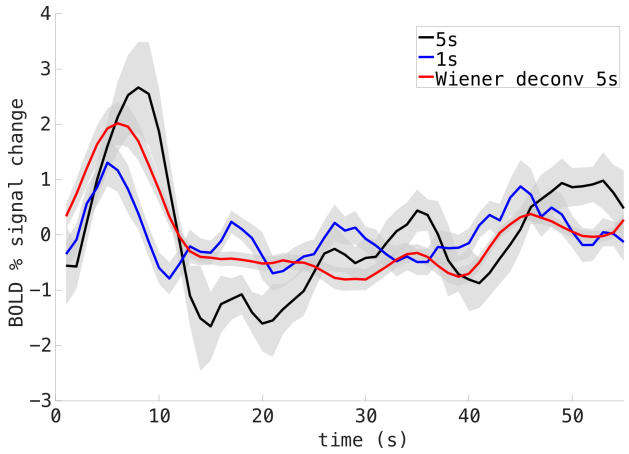


Figure 4.25: The mean (across voxels in a visual ROI) of 1 s, 5 s, and Wiener deconvolved HRFs, for a single subject, on a single hemisphere. It can be seen that, as expected, the HRF in response to a 1 second stimulus is much shorter than the 5 s stimulus, and has a lower peak amplitude. The Wiener-deconvolved mean HRF has a greater peak than the 1 s HRF, but has a similiar rise time.

This indicates that during the pRF fitting the model serves to minimize the residuals of the non-linear least squares problem, but does this at the expense of this not being within physiologically-relevant constraints.

Figure 4.29 shows that the pRF's HRFs have similar TTPs and FWHMs, however, they have much lower amplitudes.

One can also refit the measured HRFs using the pRF's HRF fitting equation, to provide parameter values that are directly comparable to the pRF's HRFs. Since it is known that this set of parameter values represents a "good" HRF, one could constrain the pRF's HRF fitting using these values. Figure 4.30 shows a histogram of the pRF's HRF parameters from one subject (**C2**). Figure 4.31 shows the lower and upper bounds of the confidence intervals for each parameter, across all 5 subjects in dataset **C**, as well as the means. These confidence intervals are found from fitting a normal distribution to each parameter separately. Table 7 details the means and standard deviations of each of the pRF's HRF parameters, averaged across

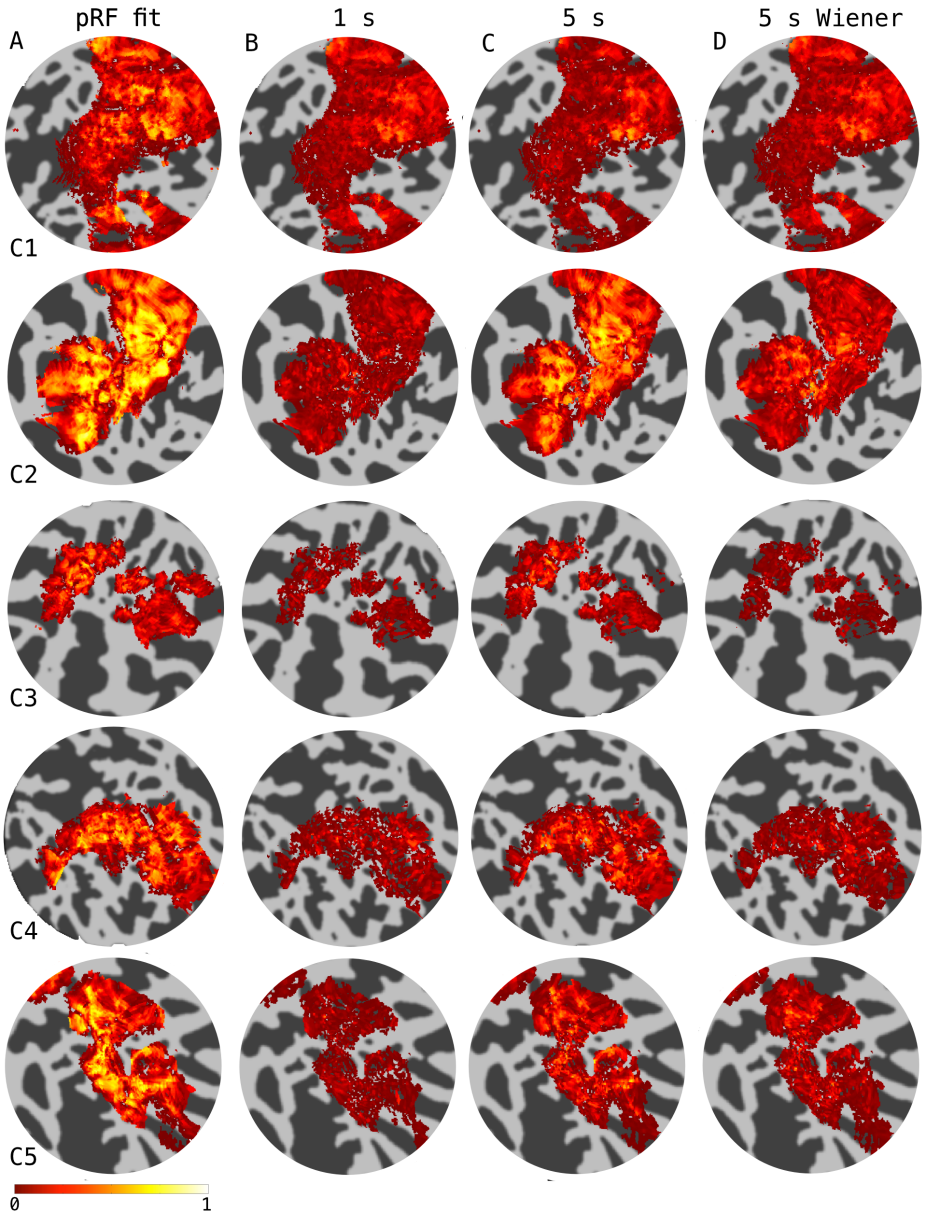


Figure 4.26: Adjusted r^2 maps from the pRF. The adjusted r^2 penalizes the statistic as extra variables or parameters are included in the model. A) pRF with 10 fitted parameters from the concatenated scan; B) pRF inputting the 5 s "measured" HRFs; C) pRF inputting 1 s HRFs; D) pRF inputting Wiener deconvolved 5 s HRFs.

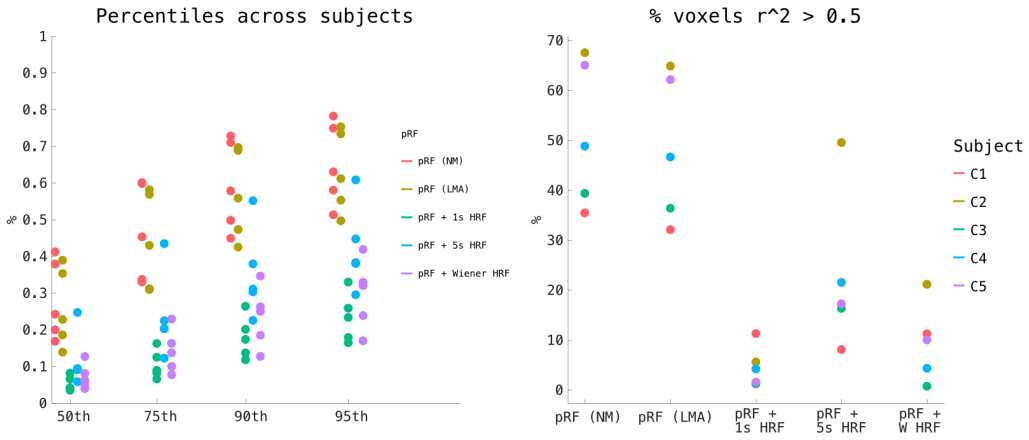


Figure 4.27: Left) r^2 thresholds corresponding to percentiles from the pRF across 5 subjects (datasets **C**). The regular pRF model fits are generally higher than the HRF-informed models. Note also that the HRF-informed models are similar in the percentile cut-offs. Right) The percentage of voxels that have $r^2 > 0.5$, from the pRF.

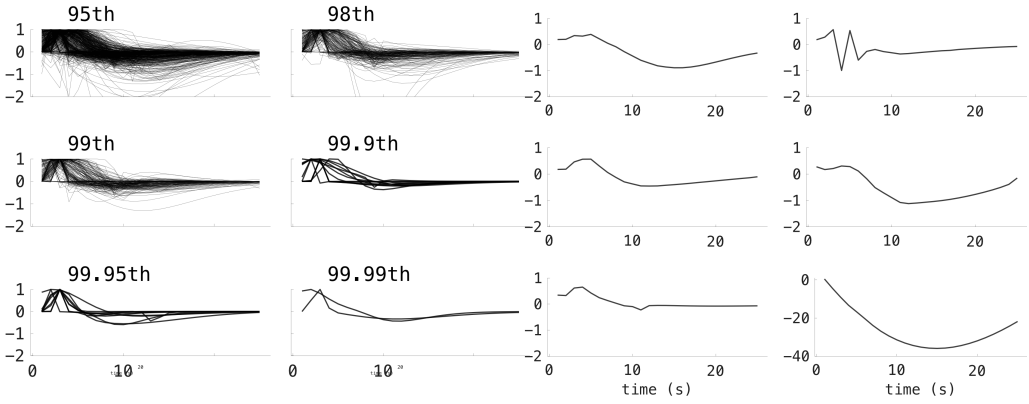


Figure 4.28: A) pRF's estimate of the HRF divided by r^2 percentile, for all subjects in dataset **C**. B) The mean of each plot in A is shown alongside.

5 subjects in dataset **C**.

An additional analysis was performed to compare optimization algorithms in the pRF fitting procedure. The pRF data presented in this chapter uses the

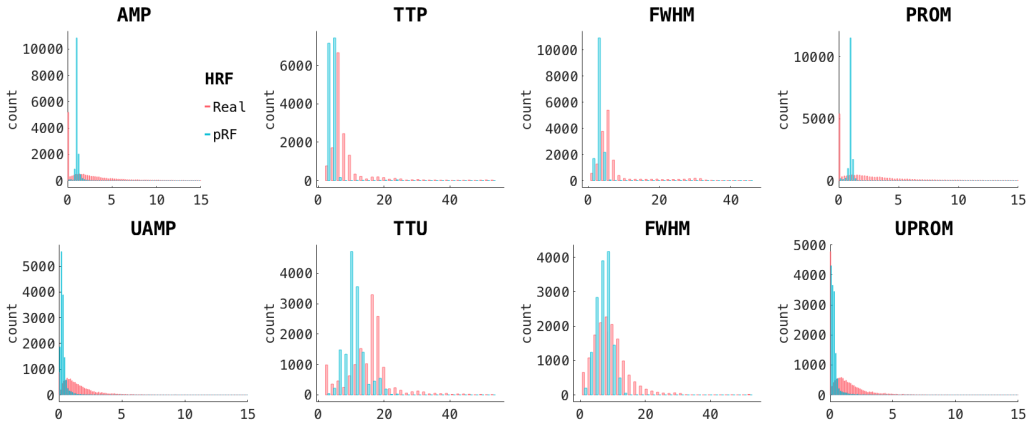


Figure 4.29: Comparison of the pRF generated HRF estimate to a measured HRF, across all subjects in dataset **C**. Red bars = measured HRFs. Blue bars = pRF's HRF estimate. The AMP and PROM x-axes are in arbitrary amplitude units. The TTP and FWHM are in units of time (s).

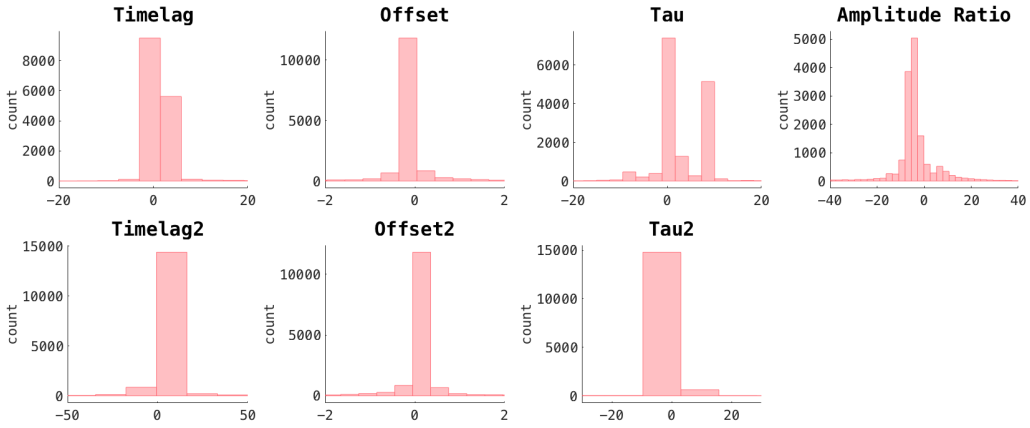


Figure 4.30: Parameters that are output from the pRF's HRF fit. The range of values displayed here are based on all subjects' (dataset **C**) measured HRF that was refit using the pRF's HRF equation. The histogram is calculated by taking into account all voxels within a visual ROI.

Nelder-Mead algorithm (see Appendix 8), which is an unconstrained search, thus avoiding any local minima. A constrained non-linear optimization algorithm, such as the Levenberg-Marquardt (LMA) (Marquardt, 1963) was

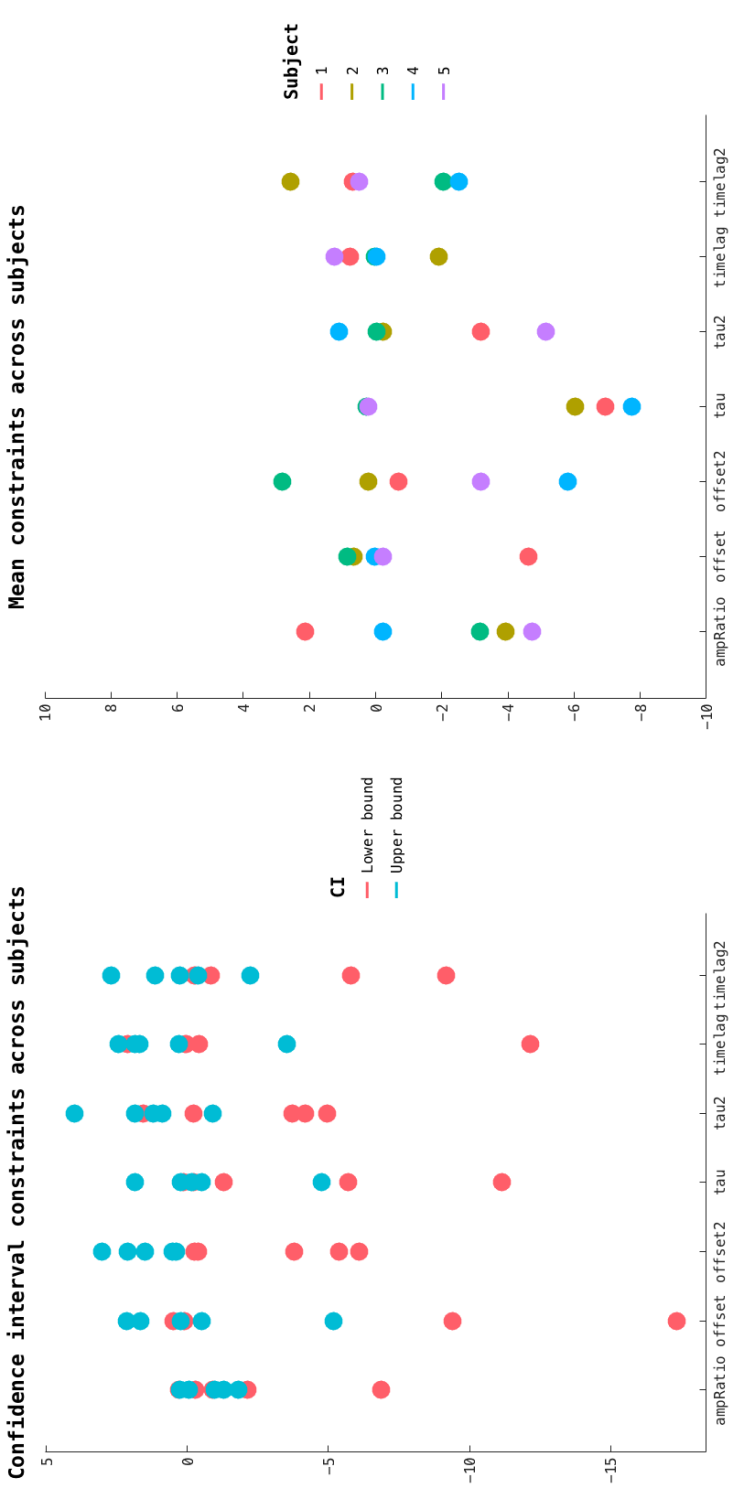


Figure 4.31: The 5 s HRF for 5 subjects (datasets **C**) was refitted using the pRF's HRF fit equation. For each parameter, a probability distribution was fit to the voxel histogram (see Figure 4.30), and the mean and standard deviation was found. The lower and upper bounds for the confidence intervals about the mean are plotted here, i.e. the 95 % limits, which thus defines a range within which a measured HRF can be described by the pRF's HRF fit.

pRF constraints in Dataset C		
pRF parameter	Mean	Standard deviation
Timelag	0.40	30.65
Offset	-0.13	4.82
Tau	1.98	22.60
Amplitude ratio	-3.90	34.46
Timelag2	-3.33	120.24
Offset2	0.13	4.81
Tau2	-4.78	88.74

Table 7: Means and standard deviations averaged across 5 subjects in dataset **C**. Care should be taken when interpreting these numbers as evidenced by the large standard deviations. For each parameter, a normal distribution is fitted and the mean, standard deviation and confidence intervals were calculated. This was done for each subject, using all the measured HRFs.

performed on a single pRF scan from each subject in dataset *C*, to compare the pRF's HRF shapes. Figure 4.32 shows that the pRF's estimate of the HRF using the LM algorithm is more akin to a realistic HRF, although, still not ideal.

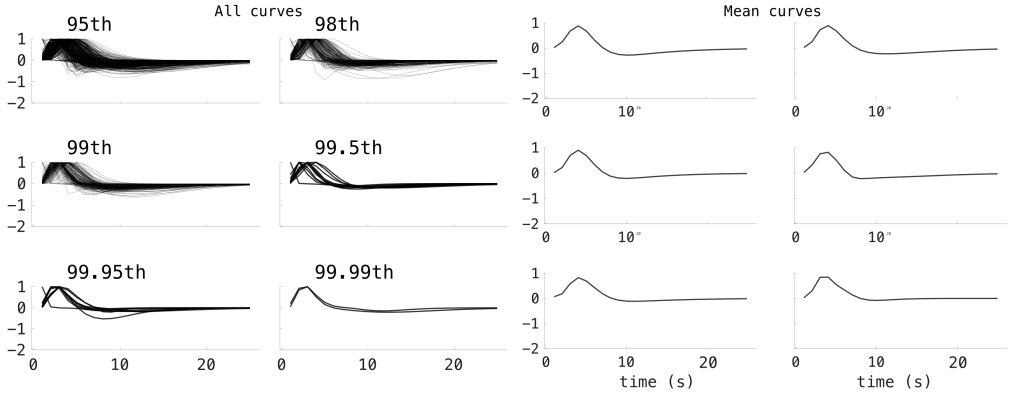


Figure 4.32: A) pRF's estimate of the HRF divided by r^2 percentile, for all subjects in dataset **C** using the Levenberg-Marquardt optimization algorithm. B) The mean of each plot in A is shown alongside.

4.12 Discussion

This Chapter sought to perform pRF modelling in the visual cortex and integrate measures of HRF in these pRF models. accurately measure HRFs in visual cortex and integrate these with pRF modelling. The datasets here provide some baseline HRF measurements at 7 T using a multiband factor to provide a short TR while maintaining coverage of the entire visual cortex (see Chapter 6).

4.12.0.1 pRF mapping and HRF

Here, population receptive field (pRF) mapping has been implemented in visual cortex, producing similar results to the literature using the simple 2-dimensional Gaussian pRF model (Dumoulin and Wandell, 2008). Maps of r^2 show good model fits. Polar angle and eccentricity maps also indicate good correspondence with the stimuli shown. Patterns of receptive field size can also be discerned. Comparisons between pRF polar angle and retinotopy phase produced similar circular variance. HRFs to visual stimuli were successfully measured with high temporal resolution (TR 1 s) in the visual cortex at 7 T and produced parameter maps that have been used here to inform modelling.

Here, it is attempted to extend the pRF model by informing this with HRF parameters; values collected in an additional measurement of the HRF, with both the use of a 1 s or 5 s visual stimulus assessed. It was shown that while the pRF model fits are weaker, they eliminate a source of artificial enhancement by reducing the degrees of freedom in the model fit. This is justified by comparing the pRF's estimate of the HRF to a measured HRF from the same voxel, acquired in the same scanning session.

Qualitatively and quantitatively, the pRF's estimate of the HRF proved to

be an inaccurate depiction of a "true", measured HRF, and instead the pRF model serves to minimize r^2 without any physiological boundaries. A set of constraints can be defined from the measured HRFs by fitting them to the HRF algorithm used in the pRF model - this could potentially be used as limits in the regular pRF fitting, thus improving the validity of the pRF model. The means and confidence intervals for a set of constraints have been derived from 5 subjects (Figure 4.31 and Table 7). It is shown that the use of a constrained optimization method such as the Levenberg-Marquardt algorithm may be better suited to pRF fitting, ensuring the HRF parameters are more realistic.

We predicted that the 1 s HRF would be ideal, however in reality, due to CNR limits, it may have provided a worse fit than the 5 s HRF. It is shown here that a 5 s HRF provides better r^2 maps than the 1 s due to lower CNR in true data. While there are large differences in r^2 between different HRF-informed maps, the derived outputs, specifically polar angle maps look very similar between different HRFs. Thus, while the r^2 is lower, the stimulus relevant maps look similar to the regular pRF and thus a 5 s ON period is recommended for a HRF-informed model.

4.12.0.2 HRF fitting and vein masking

Through the acquisition of high resolution FLASH structural scans, and the EPI data, it was possible to identify voxels with a large venous contribution. It should be noted, however, that the continuous visual stimulus during pRF and TW mapping reduces transients in draining veins, i.e. there is a wave of stimulation such that blood flow and oxygenation in large vessels are relatively constant during the experiment (Heeger and Ress, 2002).

Voxelwise spatial maps of HRF parameters were derived from fitting a double gamma function curve to the data. The parameters of interest were time-

to-peak, full-width-at-half-maximum and peak amplitude (the same set of parameters were found for the undershoot part of the HRF as well). Voxels that belonged to either a vein or tissue ROI were identified but no striking differences in HRF parameters were observed, implying a lack of spatial separation over the large visual ROI.

To address the question of vein separation using an independent method, k-means clustering was performed (Arthur and Vassilvitskii, 2007) of the fitted parameters, in 8-dimensional space, to identify any physiologically relevant clustering. We have shown that voxels in a large visual ROI belonging to different clusters do not coincide discretely with the spatial locations of veins or non-veins, rather much of early visual cortex is defined by strong, positive HRF shapes. Increasing the clusters to 3 did not provide any additional information regarding HRF shape, and the addition of any more clusters served to only segregate different noise signals.

The outcome of this is that only a small percentage of voxels provide a venous contribution, and that veins don't have very different shapes, justifying the use of a HRF-informed pRF model.

To translate the above methodology into the somatosensory domain, there should be little difference between the HRF-informed pRF results in terms of goodness of fit. This would validate the use of a longer (5 s) stimulus period in somatosensory cortex, where a short (1 s) stimulus period would not be feasible due to the SNR limitation. However, it can be seen that pRF model fits for the HRF-informed models (1 s and Wiener-deconvolved) are dissimilar to the 5 s HRF. This may be due to the intrinsic noise introduced during deconvolution (Glover, 1999) and the SNR limitation of a very short stimulus (1 s). It is suggested that the use of a 5 s stimulus in somatosensory cortex will provide equivalent fits to a modelled impulse response.

4.13 Conclusion of Chapter

In this Chapter, high-resolution 1.5 mm isotropic fMRI data in visual cortex have been acquired and retinotopy and pRF parameter maps produced, robustly across participants. To cover the whole of early visual cortex with a TR of 1 s for high temporal estimation of the visual HRF, multiband 3 was implemented. HRF fMRI scans were collected, eliciting a strong haemodynamic response in visual cortex, in response to 1 s and 5 s stimulation, separately.

The 2D-Gaussian, pRF model for the visual cortex was altered to accommodate convolution of "measured HRFs"; taken from the 1 s or 5 s HRF scans, with Wiener deconvolution also performed on the 5 s HRFs, to mimic the pRF's impulse response function while also keeping high SNR. It is shown that while the "HRF-informed" pRF model provides poorer fits to data, the efficacy of the method reduces artificial enhancement of r^2 due to the pRF tuning its own fitted HRFs to non-physiologically informed values. Additionally, the measured HRFs provide a proposed set of constraints for 7 T HRFs that could be used to restrict the pRF's estimate of the HRF. It is recommended to use at least a 5 s HRF for the HRF-informed model, albeit pRF outputs (polar angle) look similar between HRF models (1s, 5s or Wiener-deconvolved).

From the 1 s and 5 s HRF scans, a double gamma function was fitted to each voxel to derive a set of 8 parameters that describe the HRF shape, such as time-to-peak, etc. The acquisition of a high resolution T_2^* structural scan allowed veins to be identified in visual cortex. When identifying voxel contributions to the fitted HRF parameters, according to whether it lied near a vein or in tissue, we saw little to no separation of HRFs from the vein-mask. To confirm this finding, we used k-means clustering to see whether indexed values of voxels across visual cortex informed us about the shapes of the HRFs, i.e. would we see venous shapes and tissue HRF shapes?

Consistent with the vein mask analyses, we saw no clear segregation within clusters, with the HRFs according to each cluster looking very similar. This was compared quantitatively using a contingency histogram, which found no correspondence between a voxel's index (cluster) value from k-means clustering, and whether it belonged to the vein or tissue ROI.

This Chapter provides a unique perspective into pRF mapping in visual cortex, showing that real HRFs can be input in the pRF, and it can be argued that these r^2 outputs, while lower, are more accurate. A HRF scan that has a 5 s ON period can be used successfully in the pRF following deconvolution, implying that in noisier cortices, such as somatosensory cortex, this "HRF-informed pRF" may provide more truthful estimates of pRF r^2 values. Indirectly, one can also used the measured HRFs to constrain the pRF's HRF estimates, thus improving the validity of the pRF. Finally, we have shown that there is no discernible pattern of HRF shape differences across early visual cortex, at 7 T - the majority of HRFs tend to be strong and positive.

CHAPTER 5

5 Population Receptive Field Mapping in Somatosensory Cortex

5.1 Overview of chapter

In this Chapter, the development of population receptive field mapping (pRF) in somatosensory cortex in healthy volunteers is described. This procedure was validated by comparison with complementary travelling wave (TW) analyses performed on the same fMRI scans. pRF modelling provides more information than the TW - this has been a successful topic of research in visual cortex. It is unknown whether the pRF method can be adapted to primary somatosensory cortex (S1) in response to somatosensory stimulation. S1 yields an intrinsically lower BOLD response, and hence the pRF mapping may suffer from this. A key parameter that is estimated using pRF mapping is the receptive field size; a measure of which would provide neural population size non-invasively in S1.

Limitations of the current model are discussed as are possible optimization strategies. The development of this work builds on pRF mapping performed in the visual cortex (Chapter 4) and has been used to inform somatotopic mapping paradigms in patient populations (Chapter 6).

This work was presented as an oral "power pitch" presentation and electronic poster at ISMRM 2017, Hawaii, entitled: *Population Receptive Field Mapping of Human Somatosensory Cortex at 7 T*. Abstract #251.

5.2 Introduction

The primary focus of this experimental chapter is the development of methods of somatosensory mapping, including "travelling wave" (TW) and "population receptive field" (pRF) analyses. This is applied to data acquired in healthy volunteers at 7 T and initial patient data in Focal Hand Dystonia (FHD).

The pRF method provides more information than TW analysis, for example, an estimate of pRF size can be found ((Dumoulin et al., 2017; Fracasso et al., 2016; Schellekens et al., 2017). It is predicted that receptive field size is not consistent across the digits or palm, for example, electrophysiology has shown that RF size decreases in the proximal to distal direction (i.e. smaller RFs in the digit tips), although they are more densely packed, more distally (Iwamura, 1998; Johansson and Vallbo, 1979; Mountcastle, 2011). Therefore, one hypothesis is a steady increase in variance along the cortical representation of the digits in the distal to proximal direction.

Section 5.4 describes the methods of data acquisition at 7 T, using a 32-channel Nova head coil (Study **A**) to collect pilot pRF datasets. Here, we describe the development of the somatosensory pRF, as well as the complexities of model selection (Gaussian vs. Multi-parameter) and optimization algorithms. Challenges in displaying the fitted model weights on a 2D image led to novel ways of parameterising the model outputs.

Section 5.6 describes measures of TW robustness (Study **B**) and Section 5.8 investigates whether traditional TW data could be analysed using the pRF method (Study **C**). Additionally, the TW was correlated with the results of pRF analysis for confidence in our method.

Section 5.10 describes the comparisons made between the Nova head coil and MR Coils surface coils, using temporal signal-to-noise (tSNR) to assess

whether gains could be achieved using the surface coils (Study **D**). Following this insight, pilot pRF datasets were collected on the MR Coils surface coils.

The development of somatosensory pRF modelling is exemplified by Figure 5.16. It is shown that the Nova coil outperformed the MR Coils surface coils in terms of practicality, SNR and coverage. The TW somatotopic maps correlated well with the pRF, although a limitation of the current somatosensory pRF model is that it only fits for a small proportion of voxels measured (albeit fitting well); this hampers any interpretation of pRF "size" - the area in sensory space that a stimulus will elicit firing of a particular population of neurons - from derived overlays, which require that most voxels fit well over a somatosensory region of interest. It is suggested that this is attributed to the lower SNR in the somatosensory cortex as compared to the visual cortex. Finally, we show that there is little difference between somatosensory pRF optimization algorithm choice (Nelder-Mead or Levenberg-Marquardt) in terms of r^2.

5.3 Background

5.3.1 The Somatosensory Cortex

The skin contains many different types of sensory receptors that respond to a multitude of sensations such as touch, temperature and proprioception; each with individual receptive fields, that are spatially preserved from receptor to cortex. Primary afferent fibres of mechanoreception for example, include the Merkel cell (pressure/texture), Meissner corpuscle (motion), Ruffini corpuscle (stretching), and the Pacinian corpuscle (vibration); each with differing stimulus adapting characteristics (Abraira and Ginty, 2013) (see Figure 5.1). With regards to mapping cortical representations of touch, it has been shown that receptor density declines inversely with receptive

field size, e.g. on the hand.

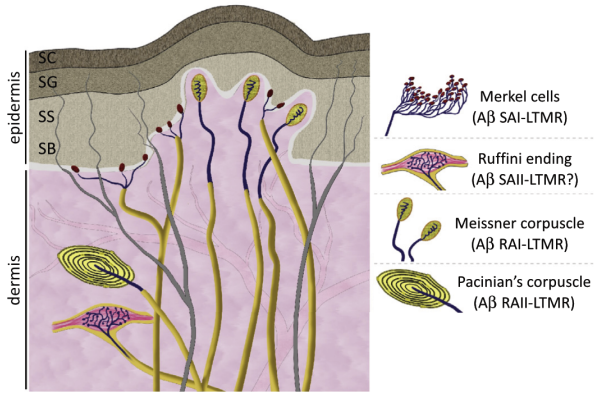


Figure 5.1: Glabrous skin contains four different types of mechanoreceptors used to mediate touch. LTMR: low threshold mechanoreceptors (respond to mechanical stimulation). SA/RA: Slow/Fast adapting firing patterns to sustained mechanical stimulation. Aβ: sensory neuron classification based on size, myelination and conduction velocity.

The somatosensory cortex is located posterior to the central sulcus in the parietal lobe and comprises Brodmann areas 1, 2, 3a, and 3b (see Figure 5.2).

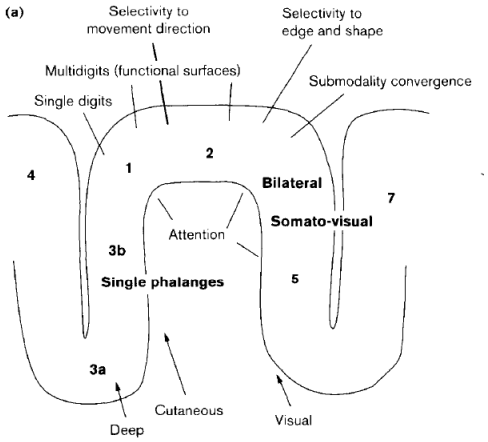


Figure 5.2: The organization of somatosensory Brodmann areas in the human brain. Adapted from (Iwamura, 1998).

Neighbouring relationships between receptors and neurons in somatosensory cortex are topographically constant, and thus can be mapped, i.e. the somatosensory system is 'somatotopic' (Penfield and Rasmussen, 1950). In 1937, Penfield performed osteoplastic craniotomy on conscious patients to stimulate the cortex via electrodes, and measure the motor and sensory representations in the brain (Penfield and Boldrey, 1937). He mapped the somatosensory region by selective stimulation and patient response, thus a pioneering investigation into the somatosensory homunculus began. In the same year, Woolsey measured cortical potentials in the anesthetized monkey, during tactile stimulation, and successfully mapped somatosensory cortex, paralleling Penfield's work (Marshall et al., 1937)

Investigations into somatosensory cortex have identified further subdivisions into areas 3a and 3b, identifying functional hand/digit separations in monkeys (Iwamura et al., 1983); hierarchical processing, i.e. increasing in RF complexity (unique neurons responding selectively to specific stimulus features/separate and variable representations of the digits) as one moves in a rostro-caudal direction (Iwamura, 1998); and multiple representations of the body (Kaas et al., 1979). Other work utilised *von Frey* hairs (tungsten needle electrodes): single unit recordings of the median nerve classified individual mechanoreceptive units, e.g. rapidly adapting versus slow adapting units (Johansson et al., 1980), and their respective receptive fields. They confirmed overall RF density increases in the proximo-distal direction of the hand, as well as differing cell types being present in different quantities across the glabrous region (Johansson and Vallbo, 1979).

Since somatosensory cortex is thought to be highly plastic, several invasive experiments in primates have provided interesting results. Map structure is altered following nerve transection, digital amputations or cortical lesions (Merzenich et al., 1983, 1987). Following deafferentiation, cortical reorganization involved the expansion of adjacent digit areas into the area represented by the amputated area, which maintained topography, i.e. a limited

topographic expansion, as well as the creation of isolated islands where neurons were not driven by tactile stimulation, dubbed 'silent zones' (Merzenich et al., 1984). The same group has also shown receptive field size is proportional to inverse cortical magnification (the area of cortical representation divided by sensory area), and are smallest at the digit tips (RF size), and increase towards the digit base (Sur et al., 1980). We relate this finding to how measures of pRF size can be found from fMRI in the visual cortex - the variability in RF size in somatosensory cortex would imply that it would be a viable region to investigate this parameter.

The somatosensory cortex is divided into primary (S1) and secondary (S2) cortices. Many studies have concentrated on functional parcellation of S1, where individual body parts can be delineated (Ann Stringer et al., 2014; Blankenburg et al., 2003, 2006; Gelnar et al., 1998; Kuehn et al., 2014; Mancini et al., 2012; Nelson et al., 2009; Overduin and Servos, 2004; Rocchi et al., 2016; Schweisfurth et al., 2014; Schweizer et al., 2008; Stavrinou et al., 2007; Stringer et al., 2011), whereas S2 has proved to be more difficult to map with fMRI. Invasive and more recent fMRI studies have suggested that S2 is located along the upper bank of the lateral sulcus. It has also been shown that S2 similarly contains a somatotopic organization of the body, though digits may be to a less fine-scale (Sanchez Panchuelo et al., 2018).

5.3.2 Mapping Somatosensory Cortex

The first reports of somatosensory mapping obtained with fMRI began using a 'sliding window' technique on the skin surface, e.g. Servos et al. (Servos et al., 1998) delivered a series of moving air puffs along the arm, in a proximal-distal (and vice versa) direction, during fMRI collected using a surface coil. They identified multiple regions (areas 3b and 1) in the cortex representing the arm, and also assessed phase reversals, which provided a distance map along the arm, i.e. more distal arm regions are more inferior in

somatosensory cortex, since the phase-delay is shortest in the distal-proximal condition. The air puff technique has also been applied to investigating digit somatotopy, by applying the stimulus along single digits, successfully producing digit maps at 4 T (Overduin and Servos, 2004).

There has been a wealth of studies using naturalistic and non-naturalistic stimuli, to measure digit somatotopy during fMRI in the past two decades; they typically resolve the individual digits in S1 (Kurth et al., 1998), using pneumatically activated vibratory stimulators (Gelnar et al., 1998), piezoelectric stimulators (Maldjian et al., 1999; Nelson and Chen, 2008; Schweizer et al., 2008), innocuous electrical current (Blankenburg et al., 2003), manual brushing (van Westen et al., 2004), or even natural stroking (Martuzzi et al., 2014).

At higher field strengths (7 T), a travelling wave (TW) protocol has been established which successfully maps somatotopic representations, with high fidelity (see Figure 5.3). Piezoelectric stimulators are activated in sequence, such that a wave of activity is generated starting from D1 (thumb) to D5 (little finger) in one functional scan; the order is then reversed in a second scan. A key study identified D1 and D2 represented laterally and inferiorly, whilst D3, D4 and D5 represented medially and superiorly, corresponding to area 3b (Sanchez-Panchuelo et al., 2012a, 2010).

Within-digit parcellation has also been demonstrated in a variation of this same paradigm (Sanchez-Panchuelo et al., 2014). Our group in Nottingham also compared the TW paradigm to an event-related one (ER), i.e. where locations are stimulated in random sequence, with jittered gaps (Besle et al., 2013). Those studies showed that both designs provided similar somatotopic maps of the 5 digits, however, the ER design allowed measurement of overlapping representations. The TW was found to be more efficient, requiring only 6 min at 7 T to map S1, compared to 24 min for the ER design. Subsequent work utilizing the ER design measured digit overlap in detail, using

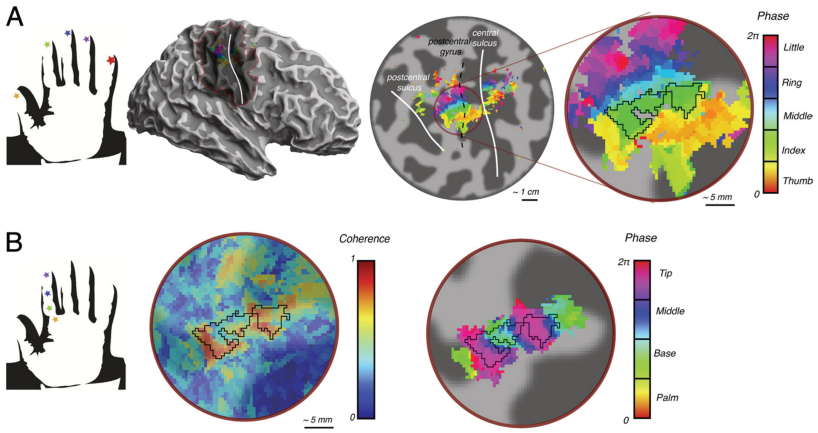


Figure 5.3: Maps of digit phase correspondence are shown for between and within digit paradigms. Adapted from (Sanchez-Panchuelo et al., 2012a).

1.5 mm isotropic voxels: they observed that more posterior regions of S1 exhibited greater digit overlap, whereas voxels in anterior regions respond preferentially to single fingertip stimulation (Besle et al., 2014).

The travelling wave is analysed as follows: Fourier analysis decomposes the voxel timeseries into phase, amplitude and coherence values. Coherence quantifies the correlation of the voxel timeseries with the best fitting sinusoid at the stimulus frequency; this outputs a contrast-noise-ratio, where a value close to 1 implies the signal modulation at the stimulus frequency is large relative to noise. The phase of the response (at the same frequency) measures the time delay between the fMRI signal and onset of a stimulus cycle, and is related to the spatial location of digits. If the TW paradigm is performed with periodic stimulation of the 5 digit tips (D1-D5), then a smooth transition should be visible in the phase map as the phase transitions from short (early) phase delays to later delays, mapping sequentially to each digit stimulated in turn. An example of TW analysis following 5 digit stimulation is shown in Figure 5.4.

fMRI is based on measuring the BOLD effect; this 'haemodynamic response' is not instantanaeous, but instead incorporates a delay of 5 - 6 s before reach-

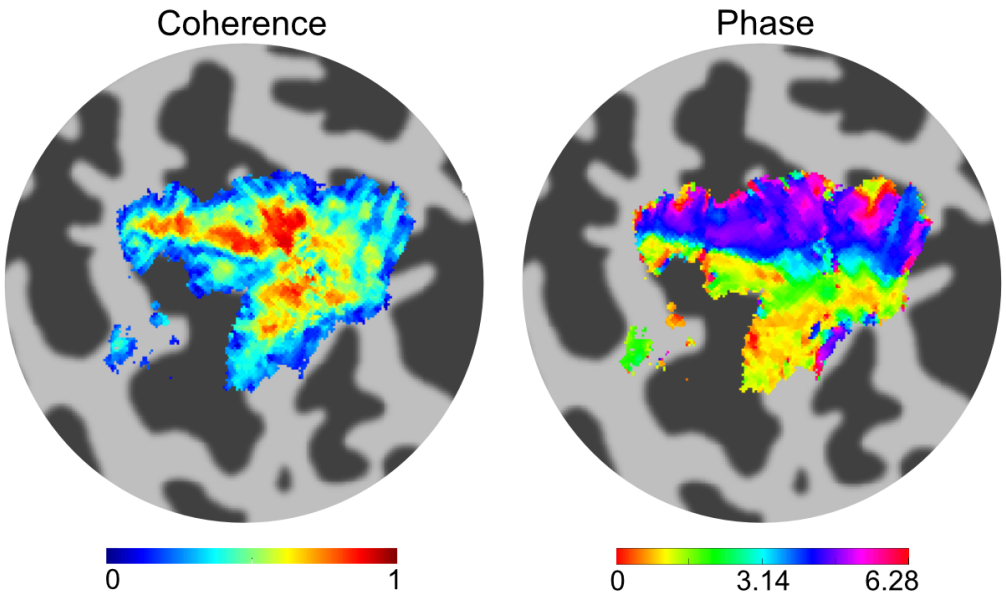


Figure 5.4: Coherence and phase maps following a travelling wave (TW) experiment, in somatosensory cortex. The stimulus comprised 12 cycles of 24 s per digit, using a piezo-electric vibratory device. The Fourier-decomposed maps are shown on a flattened cortical patch. 5 phase boundaries (digit transitions) can be seen; each bin is of length $2\pi/5$.

ing its peak response. This delay is a challenge to efficient experimental design, as one wants to maximise the fMRI signal modulation to a stimulus, without worrying about phase onsets. The residual haemodynamic delay can be cancelled out (in this particular experimental setup) by the following process: forward-shifting the forward and backward TW scans by a certain number of TRs, time reversing the backward scans, then averaging the forward scan and the transformed backward scan. This non-trivial process is performed to extract the phase value corresponding to a single digit; ensuring the digit phase falls into the middle of a phase bin, e.g. for 5 digits, the index finger would have a value of $\frac{3\pi}{10}$, the middle of the $[\frac{\pi}{5}\,\frac{2\pi}{5}]$ phase bin.

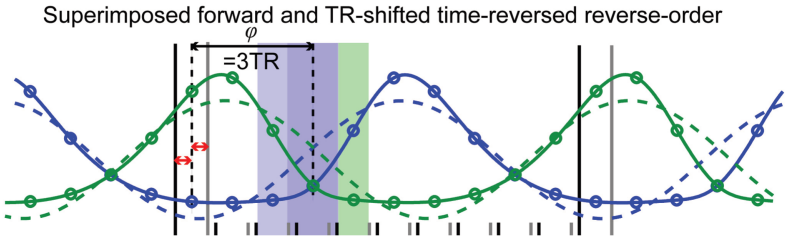


Figure 5.5: Localization of digit-phase correspondence, from TW paradigm.
Blue) A simulated timeseries corresponding to D2, during 5 digit stimulation, from D1-D5, TR = 2 s. Open circles indicate datapoints sampled at unknown acquisition time. The overall stimulation period lasts for 10 TRs, with a duty cycle of 20 %. The dashed blue line is the best fitting cosine wave (to calculate coherence).
Green) The time-reversed, reverse stimulation timeseries for D2 is overlaid on the forward timeseries. Phase is computed relative to acquisition samples, such that the symmetry point between forwards and reverse timeseries (the digit-phase value) is independent of acquisition time and the haemodynamic delay.
The reverse timeseries is shifted by an additional TR, so that the point of symmetry moves by half a TR. This makes interpretation of the phase bins simpler. During the analysis, TR shifts of -3 to 0 are tested, to find the best coherence for each volunteer, since the degree of shifting depends on volunteer-specific haemodynamics.
Figure caption and Figure reproduced from (Besle et al., 2013)

5.4 Methods A: Data Acquisition and Paradigm Optimisation

5.4.0.1 Study A: Travelling wave (TW) and population receptive field (pRF) data

Seven fMRI 32-ch Nova head-coil population receptive field (pRF) datasets (**A**) were acquired for analysis. The paradigms tested were based on a travelling wave (TW) protocol (sequential piezo-stimulation of the 5 fingertips of one hand); within-digit (proximal to distal) stimulation of phalanges along the digits; between digit stimulation; and diagonal stimulation across the

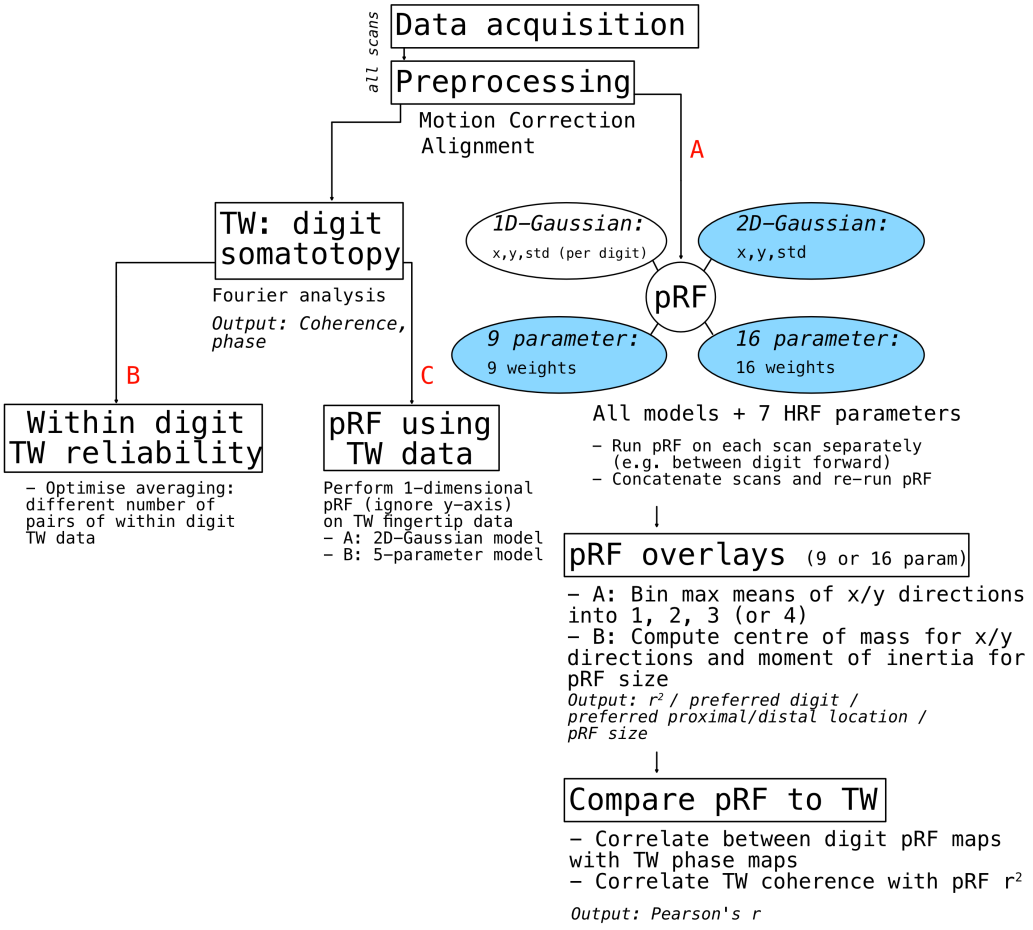


Figure 5.6: The analysis pipeline is shown for this Chapter. A, B and C refer to the pathways used for Nova coil data.

hand (see Table 8 and Figure 5.7).

Subjects were scanned on a 7 T Philips Achieva scanner to obtain functional MRI data (GE-EPI BOLD, TE 25 ms, TR 2000 ms, SENSE 2.5, and high resolution structural MRI data (T_1-weighted, Phase Sensitive Inversion Recovery (PSIR) images, $0.3 \times 0.3 \times 1$ mm^3 resolution). Functional data were analysed using a Fourier based method (see Appendix 8) and somatotopic phase maps were visualized on a cortical flat map, using previously acquired

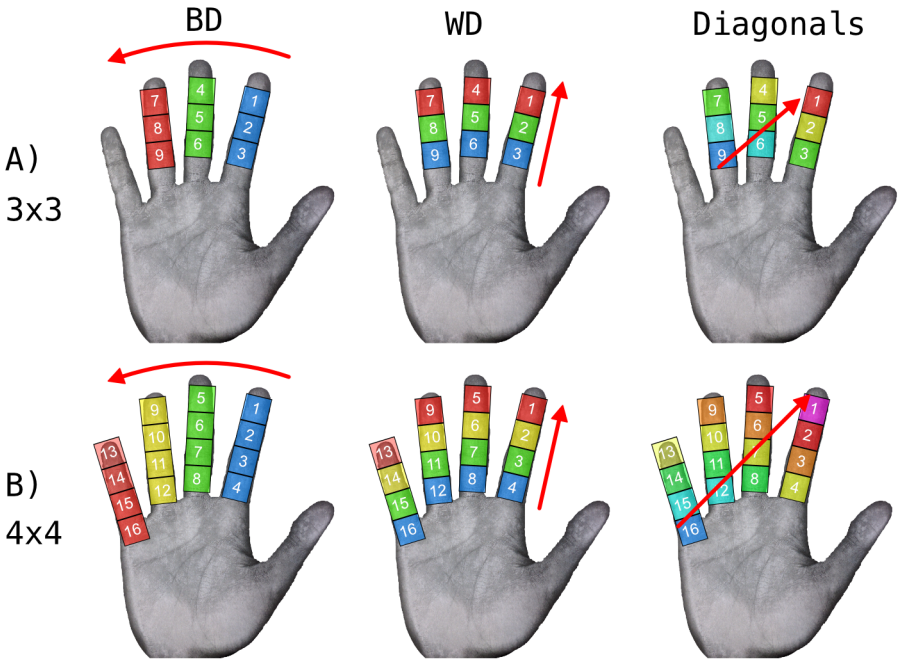


Figure 5.7: Sequence for between digit (BD), within digit (WD) and diagonal stimulation shown on a hand. Note, arrows depict the forward direction only, whereas, in all cases, the paradigm was collected in a reverse order as well. A) Paradigm across 9 stimulators, i.e. a 3×3 grid. B) Paradigm across 16 stimulators, i.e. a 4×4 grid. The sites are colour coordinated according to which sites were simultanaeously stimulated.

high-resolution PSIR images. Data were analysed in mrTools (Gardner lab, Stanford): Motion correction was performed and the data were aligned to a high-resolution T_2^* scan acquired during the same scan session.

The somatosensory stimulation for all paradigms was performed using vibrotactile piezo-electric (non-magnetic) stimulators. These were loosely attached via velcro to a poly(methyl methacrylate) sheet (Figure 5.8). The data acquired utilized 9 or 16 separate stimulators (Figure 5.7), and the stimulators were setup specific to each subject. For the TW procedure, only the finger tips were stimulated; this was performed by placing the stimulators in a rigid plexiglass hand (see Chapter 6 for this setup). Each stimulator is independently controlled via an Arduino board (Arduino, 2016) and amplifier

A: Nova Coil pRF data				
Dataset	Resolution (mm^3)	MB factor	pRF model	Hand
A1	1.50	2	3x3	Right
A2	1.50	2	3x3	Right
A3	1.25	1	3x3	Right
A4	1.25	1	3x3	Right
A5	1.25	2	4x4	Right
A6	1.25	2	4x4	Right
A7	1.25	2	4x4	Left

Table 8: Nova coil pRF data are shown for seven subjects at different spatial resolution, multiband factor, pRF models. MB = Multiband.

box.

For datasets A1-A4, the paradigms used the setup shown schematically in Figure 5.7 A with 9 independently controlled stimulators: 3 stimulators on each of digit 2 (D2), digit 3 (D3) and digit 4 (D4). For datasets A5-A7, 16 stimulators were utilized in an 'extended' pRF paradigm: 4 stimulators on each of D2, D3, D4 and D5, as shown schematically in Figure 5.7 B. The 4×4 stimulator setup is shown in Figure 5.8.

Traditionally, TW analysis is performed on the digit tips, but if multiple stimulator sites are simultaneously "ON" on the same digit (travelling across digits) one can still resolve digit maps (Sanchez-Panchuelo et al., 2014). Thus, our pRF datasets, which incorporated between and within digit stimulation could also be used for TW analysis; this proved to be a good test of pRF validity.

Quality assurance (QA) of the fMRI data was assessed by calculating the temporal signal-to-noise ratio (tSNR) and visual confirmation. Temporal SNR is the voxelwise mean functional signal over time divided by the standard deviation of the signal. A pre-processing pipeline for QA was simplified in collaboration with Dr. Kevin Aquino, available on Github:

https://github.com/nottingham-neuroimaging/qa.

5.4.0.2 Travelling Wave (TW) paradigm

The TW paradigm involves forward and reverse stimulation of the fingertips of one hand with timings of 4 s ON stimulation, thus one cycle takes 20 s. This is modified slightly from (Sanchez-Panchuelo et al., 2010). This cycle is usually repeated a number of times. Here, this paradigm was tested with 8 and 10 cycles, producing robust modulation in each case.

Forward and reverse scans were averaged and the coherence, phase and amplitude were calculated using the method described previously in (Besle et al., 2013) (see also Appendix 8).

5.4.0.3 Population Receptive Field (pRF) paradigm

Within each scan session, three pRF experiments were performed. These comprised 'between-digit' (BD), 'within-digit' (WD), and 'diagonal' stimulation (Figure 5.7).

Using 9 stimulators, both BD and WD stimulation involved the stimulation of each line on a 3×3 grid. For example, combined stimulation of sites [1, 2, 3; 4, 5, 6; 7, 8, 9] for BD and [1, 4, 7; 2, 5, 8; 3, 6, 9] for WD were performed with an ON period of 6 s, thus one cycle lasted 18 s. For the diagonal stimulation, there were 5 stimulation 'lines' (for example, [7; 4, 8; 1, 5, 9; 2, 6; 3]), with a 6s ON period per line and 5 lines leading to a 30 s cycle.

The BD and WD paradigms were also acquired in a reverse order, i.e. BD forward: [1, 2, 3; 4, 5, 6; 7, 8, 9], and BD reverse: [7, 8, 9; 4, 5, 6; 1, 2, 3]. Both BD and WD stimulation can only have two directions for a 'wave' of

stimulation to travel. For the diagonal stimulation, there are 4 directions across the 5 stimulation lines, and these were pseudo-randomised for the scanning session. Typically, 12 cycles were performed for each BD and WD stimulation, and 8 cycles for each diagonal stimulation.

The BD, WD and diagonal paradigms were also performed using 16 stimulators on a 4×4 grid (see Figure 5.7). The stimulation timings were slightly altered to a 4 s ON period, with a single cycle lasting 16 s (for both the BD and WD conditions). In this case, the diagonal stimulation spanned 7 lines, and thus each cycle lasted 28 s. To compensate, 7 cycles of the diagonal paradigm were collected (instead of 8) for the 4×4 pRF, thus maintaining consistent timings overall.

For study **A**, two sets of BD scans (forward and reverse), four sets of WD scans (2 pairs of forward and reverse), and two sets of Diagonal scans (forward and reverse for each diagonal), were acquired, in this order. For the 3×3 paradigm, each BD and WD scan lasted 216 s (108 dynamics), and the diagonal scan lasted 240 s (120 dynamics). For the 4×4 paradigm, each BD and WD scan lasted 192 s (96 dynamics), and the diagonal scan lasted 196 s (98 dynamics). TW analysis was used to confirm D2-D5 somatotopy.

First, within scan reliability was assessed by running the pRF analysis individually on two separate scans which were acquired with the same paradigm (e.g. within digit forward) in a single session. To assess the pRF method across paradigms, the fMRI scans were split up according to the paradigm run, e.g. between digit or within digit. The pRF was run on these "grouped" scans, and any changes in goodness of fit were investigated. Finally, individual pRF scans were concatenated into one large timecourse, upon which the method was run. Note that special care is taken to account for the discontinuities in time when concatenating multiple fMRI timeseries' together. The pRF model is not run over the entire concatenated timecourse, rather, on each individual timecourse, e.g. the between digit scan.

For visualization, all overlays are displayed on flattened individual cortices, extracted from Freesurfer (Fischl et al., 1999).

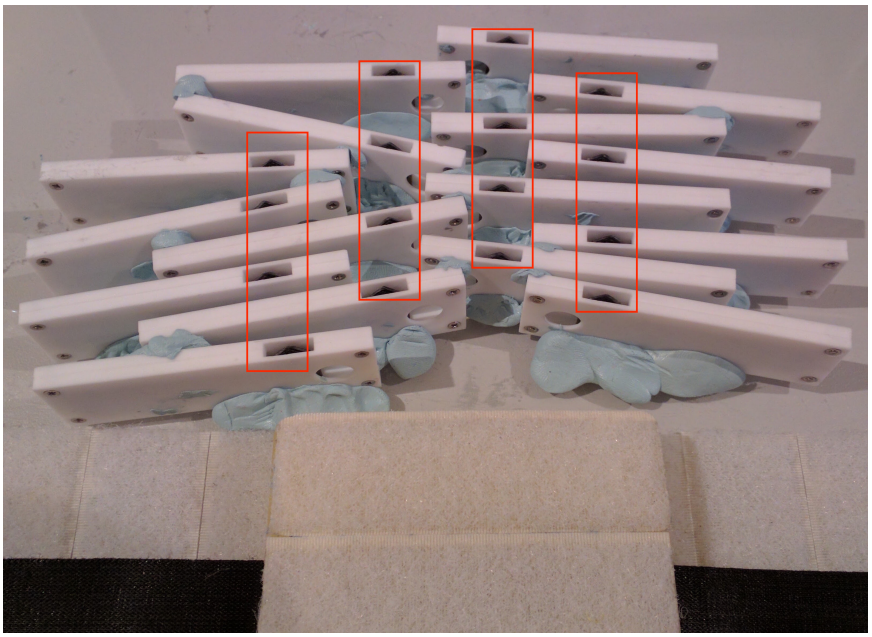


Figure 5.8: Prototype stimulator setup for a single participant's right hand for a 4×4. 16 stimulators are pictured, which are independently run. Red boxes indicate approximate position of where digits 2-5 lie. Wiring not shown.

5.4.1 Development of pRF Models for somatosensory domain

The pRF methodology was adapted from visual neuroscience, specifically from (Dumoulin and Wandell, 2008), and applied to the somatosensory domain (Figure 5.9). The original code (Gardner Lab, Stanford) runs in the MATLAB environment and uses part of a custom suit of tools (mrTools).

Initially a two-dimensional Gaussian function was used as a pRF model (Dumoulin and Wandell, 2008), however. this model proved a poor fit to somatosensory data. This can be explained since there are discontinuities in

the sensory space of the hand and thus a smooth, continuous function such as a Gaussian will logically not perform well in a somatosensory model as it does in the visual domain. To address this, initially, a one-dimensional (1D) Gaussian function was assessed (in the direction of the digits being stimulated): this takes account of sensory discontinuities, and ensures the model is only concerned with activity constrained to the digits. Results showed little difference to the 2D Gaussian model, and any further analyses using the 1D model was halted.

A '9-parameter' model was then developed. This model assigned a weight to each point of stimulation on the digits (9 locations for a 3×3 grid), which had no limits. Therefore, for each voxel timecourse, 9 such 'weights' were output following the non-linear fitting algorithm; these weights describe how much the response coincident with each stimulator affected the voxel's sensory location, i.e. the model seeks to find the best combination of 9 weights that models the response of the best fitting voxel. Knowledge of these weights allowed overlays to be calculated which describe the voxel's corresponding sensory location, e.g. which digit is preferred.

A 3×3 grid (see Figure 5.10) was chosen to represent somatosensory digit space depicting D2, D3, and D4 with each digit divided into three phalanges. In comparison to the visual pRF model, where the model space is typically a grid of 1024×768 pixels, the somatosensory pRF model is restricted with only 9 pixels. This is a coarse interpretation of the neuronal populations along each digit: the phalanges are not standard measures of distance along a digit, nor do they reliably contain discrete neuronal receptive fields, i.e. they have been shown to overlap (Besle et al., 2014). Ultimately, the coarseness is determined by the number and size of stimulators, which itself is hardware limited.

Overall, the pRF model fits were found to be better for the 9 parameter model (see Results 5.5), and upon extension to 16 stimulators, a '16-

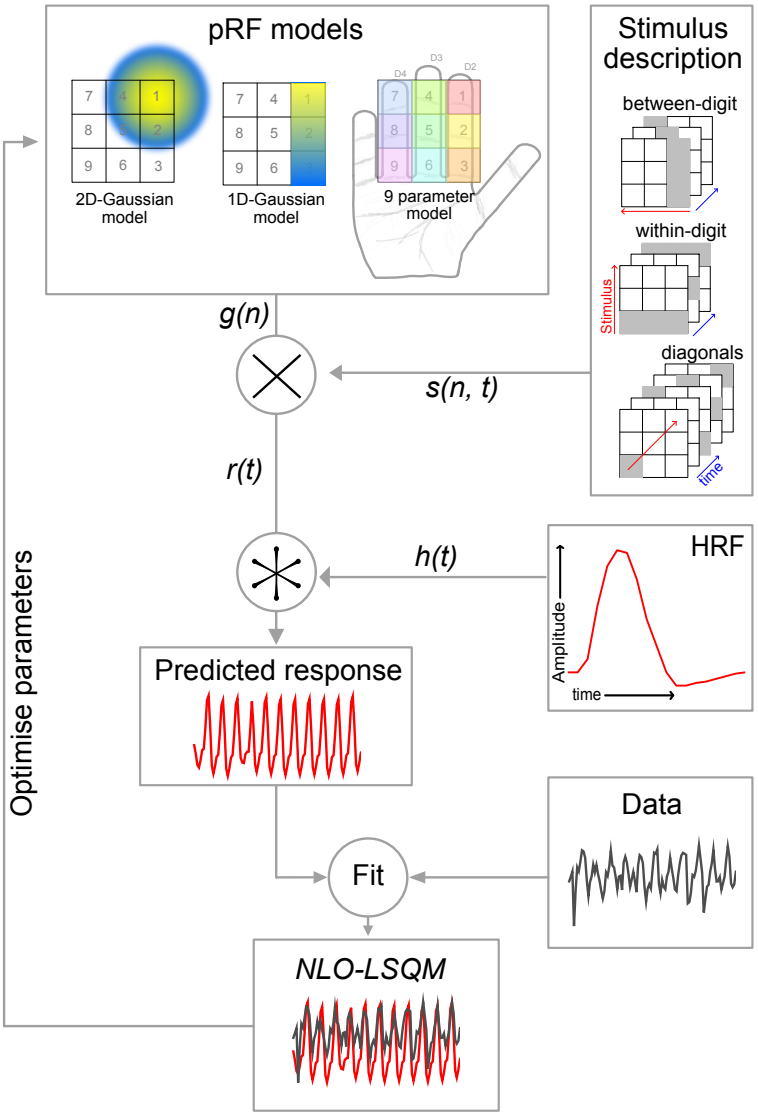


Figure 5.9: The somatosensory 3x3 pRF model. The pRF model $g(n)$ type is overlapped with the stimulus description $s(n,t)$, producing the overlap $r(t)$. This is convolved with a HRF $h(t)$ to produce the predicted response or timeseries, which is then fit to the data using a non-linear optimization algorithm (least squares). By optimising the model type, one can improve the fit. The best fitting model is determined by calculated the coefficient of determination (r^2) for each voxel output.

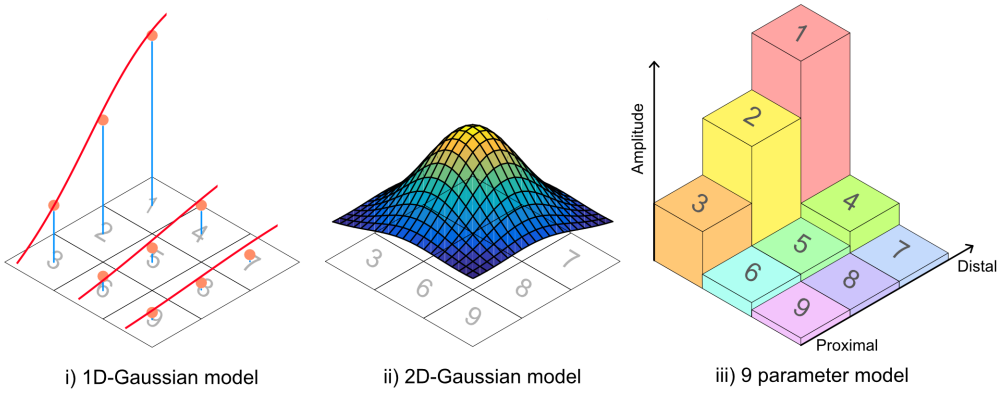


Figure 5.10: An isometric artistic visualization of the three pRF models developed for somatosensory cortex. All models are superimposed over a 3×3 grid, which depicts the 9 phalanges of D2, D3, and D3 of the right hand. The amplitude is in arbitrary units.

parameter' model was developed, whereby for each voxel, 16 weights defined the pRF shape or model best predicting its response to a known pattern of stimulation (see Figure 5.11).

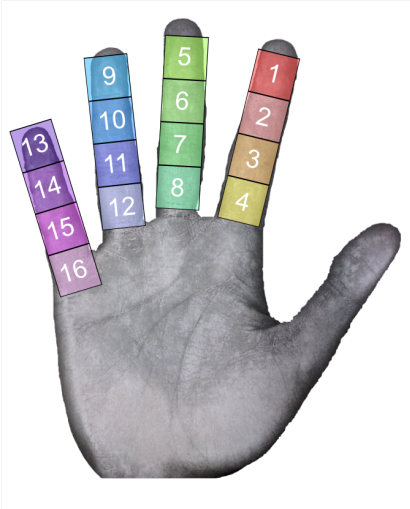


Figure 5.11: Participant hand showing 16 weights output from model. Each number refers to the position of a stimulator.

5.4.2 HRF parameters

The pRF predicted timeseries (found from the overlap of the stimulus description and model shape) must be convolved with a HRF to account for the sluggish fMRI signal. The pRF fitting procedure allows a canonical or 'fitted' HRF to be used, i.e. one where the parameters are estimated by non-linear least squares. A 'fitted' HRF will be unique to each voxel, however, this accuracy comes at a statistical cost, since the degrees of freedom (DOF) are increased by adding extra parameters to the model fit. For example, in addition to the 16 weights for the '16 parameter' model, an extra 7 parameters are added to define the HRF comprising: the time before the rise of the HRF (*time lag*), the width at full half maximum of the HRF (*tau*), the time lag before the rise of a second gamma function, the amplitude of this second gamma function, as well as its tau (2 extra parameters defined the peak and undershoot offsets). Hence, it may be closer to the truth to call the '16 parameter' model a '23 parameter' model. See Chapter 4 for more detail regarding the pRF's HRF parameters.

5.4.3 pRF Model outputs

The pRF fitting procedure outputs the following parameters: the r^2 between the model prediction and the data, a 3×3 colour grid depicting the model response (for the 3×3 model), and an interactive stimulus description (where one can highlight what stimulation paradigm happened when). Colour-map outputs included a preference of each voxel for proximal or distal locations on the grid ('prefPD'), a preference for which digit ('prefDigit'), and receptive field size ('rfHalfWidth').

The receptive field (RF) size overlay was calculated from the 9 (or 16) parameter model by calculating the variance of the model weights, and plotting this single number for each voxel.

For each voxel, the weights were used to indicate the sensory spatial sensitivity of its location, i.e. where on the digit was represented the most. In the simplest case, the maximum value of the means (of the weights) in the y direction (indicating whether a voxel preferred more proximal or distal stimulation), and in the orthogonal x direction (indicating which digit the voxel preferred). A limitation of this method is the 'harshness' of this binning, i.e. the values of prefDig and prefPD can only take values of 1, 2, 3 (or 4 in the 16 parameter case), with nothing in between, hence, the relative amplitudes of the weights are ignored and this can mask the underlying trend. One can argue that in the x direction, the discontinuities between the digits validates this 'winner-takes-all' approach, but this negates the smooth transitions along a digit that occur in the y direction. The resultant 'winner-take-all' maps were displayed using a non-interpolating 3 (or 4) colour map.

5.4.3.1 Centre of mass overlays

A second overlay method was developed to more accurately summarise the model weights without binning data, thus providing a smoother or more continuous overlay whereby voxels could take non-integer values. In this method the centre of mass of the model weights was calculated for each voxel fitted. The center of mass is the mean position of all parts of a system: in our case, the weights are given by each of the 9 (or 16) numbers, and the distances are equidistant values on a 3×3 or 4×4 grid. This results in a decimal number, which can be represented on a colour map using a continuous colour scale. For each voxel, the centre of mass is a coordinate pair (x,y), indicating the prefDig and prefPD location, respectively.

$$COM_x = \frac{m_1. * x_1 + m_2. * x_2 + ...}{m_1 + m_2 + ...} \tag{5.1}$$

where COMx is the centre of mass in the x-direction (the above is repeated for the y-direction, thus giving an x,y coordinate for each voxel), m represents the weight corresponding to each x position.

Alternatively, the pRF size can be calculated by finding the moment of inertia (or rotational inertia) of the weights. This scalar value describes how difficult it is to change the rotational velocity of an object around a given rotational axis. In this case, the axis was chosen to be the centre of mass (unique to each voxel), and it was hypothesized that as one moves further from the axis, the moment of inertia will increase; a larger pRF size will be indicated by a larger moment of inertia.

$$\begin{aligned} I &= m_1 . * r_1^2 + m_2 . * r_2^2 + ... \\ &= \Sigma m_i r_i^2 \end{aligned} \tag{5.2}$$

where I is the moment of inertia, calculated about the rotational axis (centre of mass) indicated by r, the distance to the axis. m represents the weight, per voxel.

5.4.4 Correlating pRF mapping results with TW results within subjects

To determine the validity of the pRF method, the Pearson's r was calculated between the TW between digit phase and the pRF between digit maps, within subjects. The between digit TW was chosen rather than the within-digit TW maps, since the phase transitions (corresponding to different digits) are better delineated in individual between-digit maps compared to within-digit maps.

Correlations were performed of: r^2 (pRF) with coherence (TW); prefDig (pRF) with phase (TW); and coherence (TW) with phase (TW).

The pRF overlays used for the above comparisons were the 'winner-take-all' maps. The 'centre of mass' overlays were also assessed, correlating phase (TW) with prefDig (pRF COM). Additionally, the prefDig overlay in the 'winner-take-all' approach was compared to the 'centre of mass' approach. PRF size (in both pRF overlay types) was correlated with the prefDig and prefPD, to identify any trends hidden by the overlay maps.

5.4.5 Non-linear least squares algorithm choice

Following insights from Chapter 4, a constrained non-linear optimization algorithm, the Levenberg-Marquardt (LM), was compared to the unconstrained, Nelder-Mead (NM) algorithm. For all 9 datasets (7 Nova and 2 Surface coil datasets), somatosensory pRF mapping was performed in 4 ways: 1) Gaussian Nelder-Mead, 2) 9 (or 16) parameter Nelder-Mead, 3) Gaussian LMA, 4) 9 (or 16) parameter LMA. An example of all the parameter maps this generates is shown for a single subject in Figure 5.30. These are all based on the winner-take-all method of displaying parameter values (see Section 5.4.3).

5.5 Results A: Data Acquisition and Paradigm Optimisation

5.5.0.1 Study A: TW and pRF data

This section provides pRF results on the Nova coil. A single participant's data are taken as an exemplar for visualization; this subject performed both

a 3×3 and a 4×4 stimulator pRF scan. Table 9 shows the model fits across subjects, with the maximum r^2 ranging from $r^2 = 0.36$ to 0.79.

A: pRF fits			
Dataset	max r^2 (single voxel)	no. voxels fitted	pRF model parameters
A1	0.43	3141	9
A2	0.62	1655	9
A3	0.43	1669	9
A4	0.64	1941	9
A5	0.36	974	16
A6	0.79	2401	16
A7	0.38	856	16

Table 9: pRF fits, see Table 8 for details on datasets acquired. For each dataset, 8 pRF runs were concatenated, and the model fit was performed on this timecourse, per voxel (two sets of between digit, 2 sets of diagonals, 4 sets of within digit. The maximum r^2 is shown for a single voxel. The number of voxels upon which the fit was performed was determined by thresholding the TW coherence maps. Note that the pRF fitting algorithm is an intensive computational procedure that is very sensitive to length of timecourse, number of voxels, model type, etc.

Figures 5.12 and 5.13 display the model fits of the 9 and 16 parameter models, respectively for a concatenated time course (multiple paradigm runs, e.g. Between digit forward, Within digit forward, etc.). In both cases, the model fit is good (r^2 of 0.62 and 0.79). However the predicted response fits much better than for the concatenated scan (Table 10). For example, Figure 5.14 shows the between digit scans only, with Table 10 showing the higher r^2's.

Figures 5.15 and 5.16 display the overlays output from both TW and pRF analyses. Phase maps from the TW analysis indicate good digit separation (3 digits for Figure 5.15 and 4 digits for Figure 5.16. Separation for the pRF outputs are much "patchier", with large skews in preferred digit, i.e. many voxels seem to prefer the same digit. Note that some of the sparseness of the map is due to thresholding to remove the lowest (90^{th} percentile).

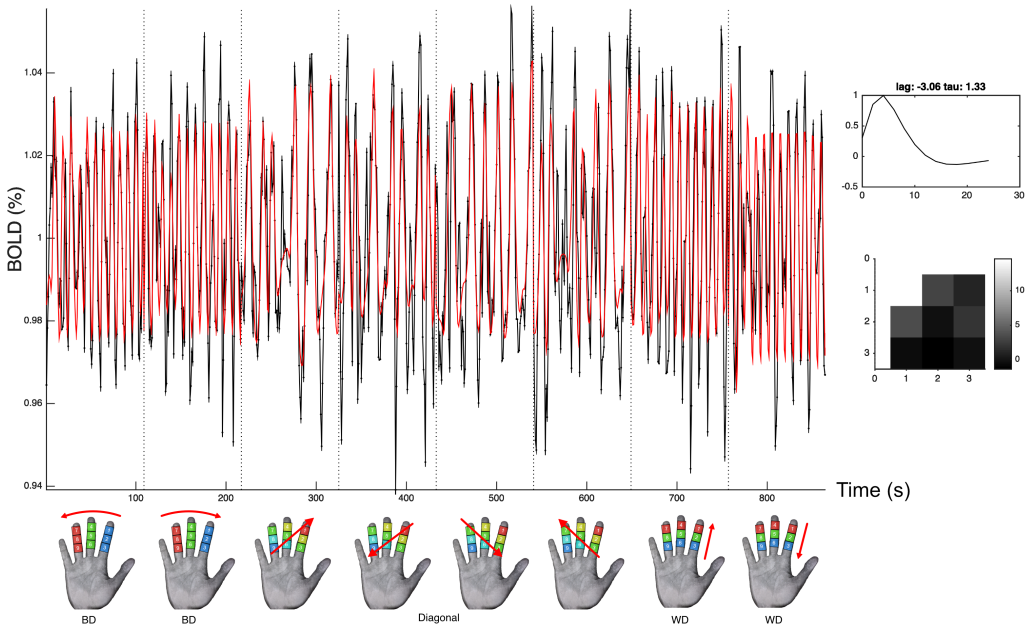


Figure 5.12: pRF model fit for a single subject, on a 3×3 grid (9 parameters). The black timecourse is data from a single voxel, whilst the red is the fitted pRF timeseries. $r^2 = 0.62$. The scan has been concatenated from 8 pRF paradigm runs in a single scan session; the paradigm for each scan is shown on a hand below the timeseries. The top right of the image indicates the fitted HRF, and below this is the model pRF model response (or model weights).

A6: pRF fits		
pRF paradigm	no. runs	max r^2
Between	2	0.83
Within	4	0.77
Diagonal	2	0.83

Table 10: pRF fits for a single participant (Dataset A6). The concatenated timecourse was split based on stimulation paradigm. This resulted in 3 shortened timecourses, of between, within, and diagonal stimulation. Overall, the fits are higher than for the concatenated timeseries (Table 9). This may be due to fewer "bad" timepoints aggravating the fit and/or less noise.

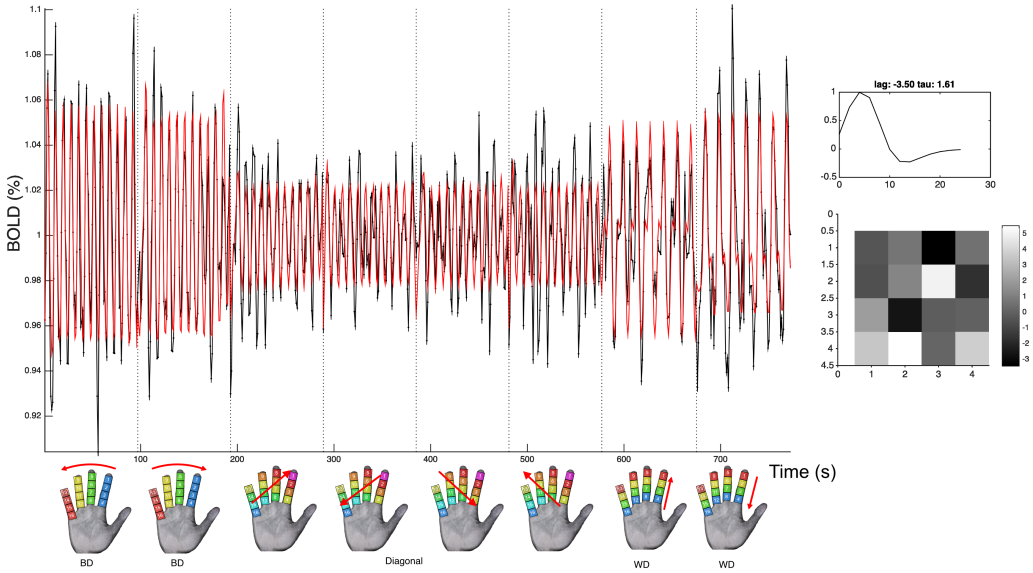


Figure 5.13: pRF model fit for a single subject, on a 4×4 grid (16 parameters). Here, the fit had an $r^2 = 0.72$.

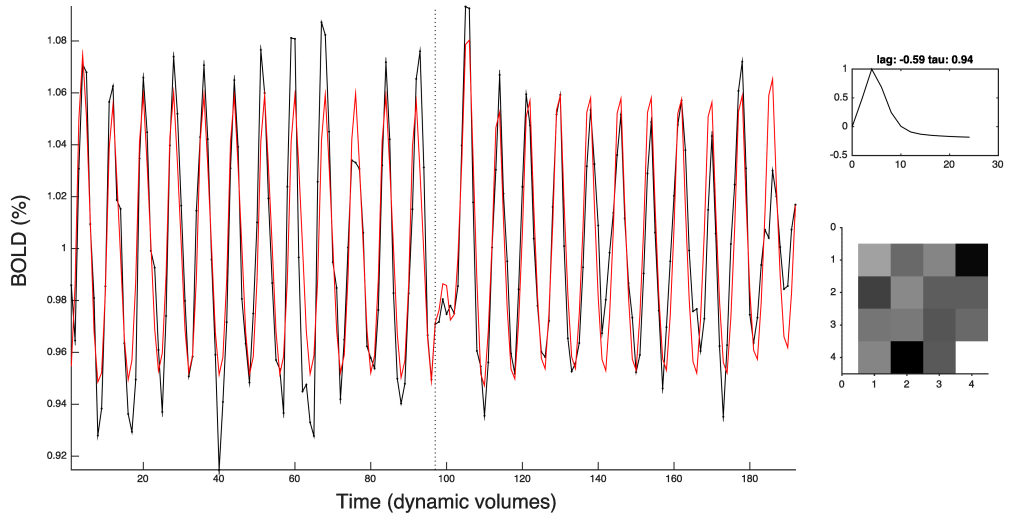


Figure 5.14: pRF model fit for a single subject, on a 4×4 grid (16 parameters) across 2 runs of the between digit scans only. Note that $r^2 = 0.83$ is higher than the entire concatenated timeseries (see Table 9, Dataset A6).

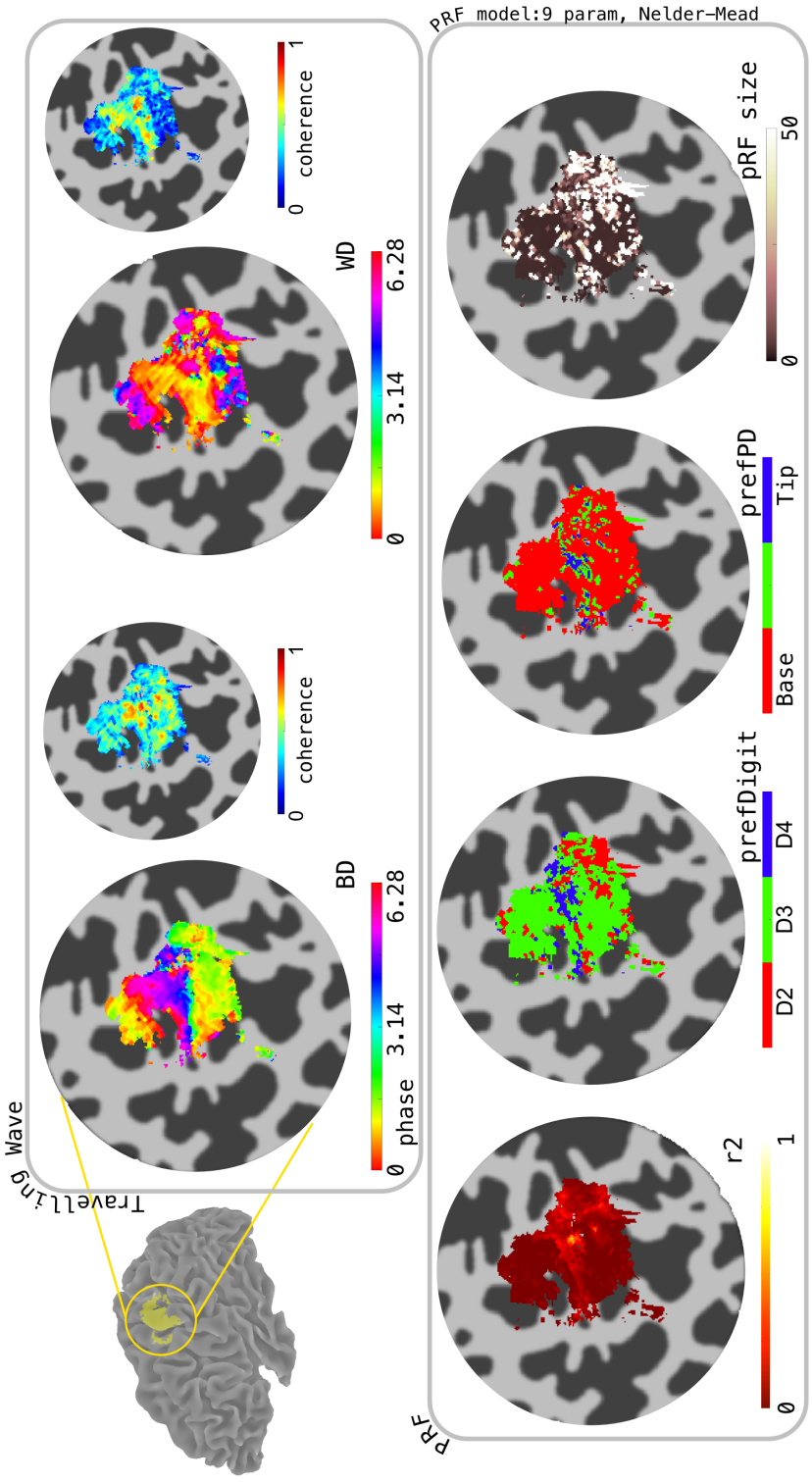


Figure 5.15: TW and pRF overlays displayed on a flattened cortex, for a single participant (Table 8, dataset A2). Top: Between digit and Within digit coherence and phase maps, Bottom: pRF overlays showing r^2, prefDig, prefPD ('winner-take-all') and pRF size overlays.

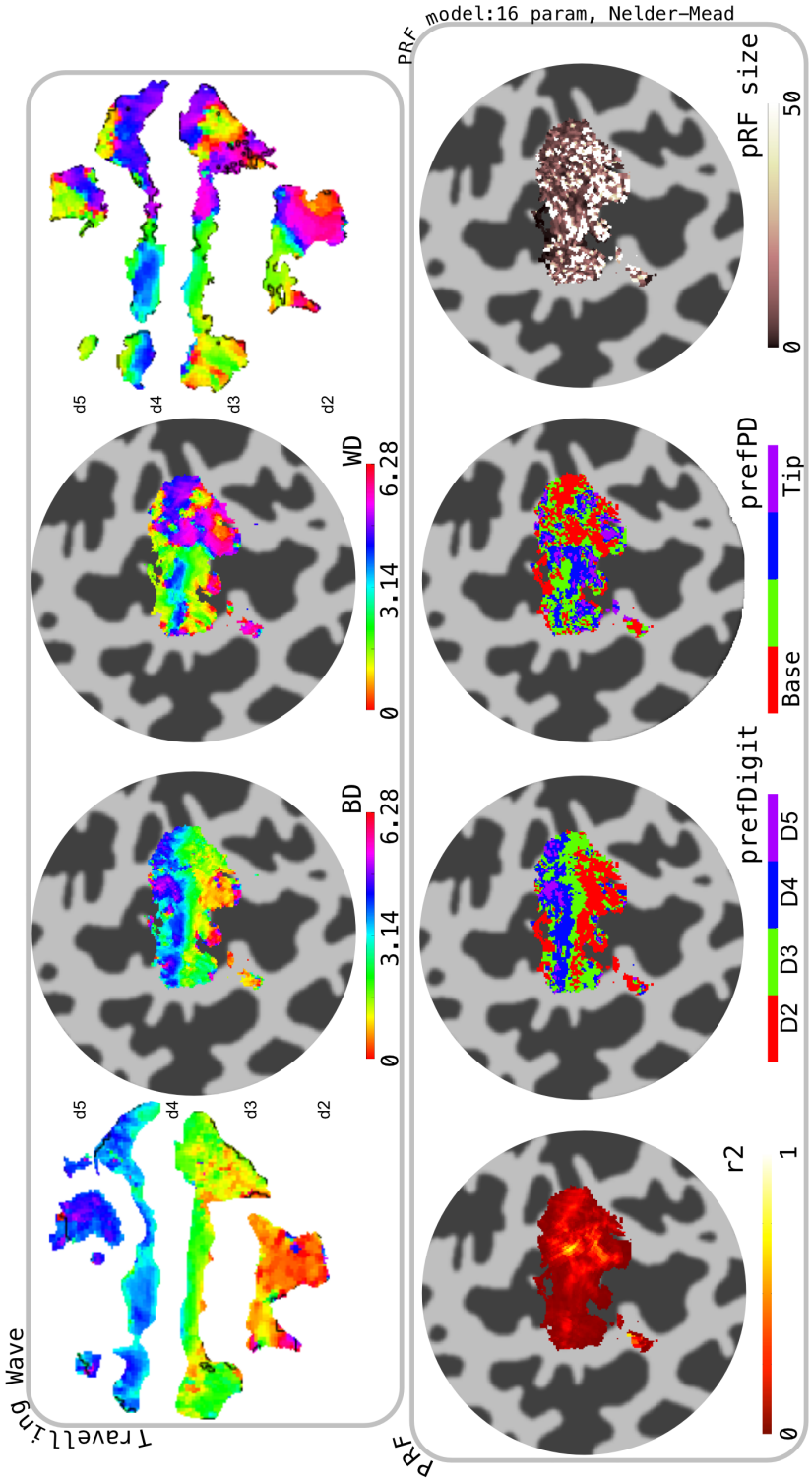


Figure 5.16: TW and pRF overlays displayed on a flattened cortex, for a single participant (Table 8, dataset A6). Top: Between digit and Within digit phase maps, with exploded digits for easier visualization of phase transitions. Here, 4 phases should be identiable (in the BD), since 4 digits were stimulated. Bottom: pRF overlays showing r^2, prefDig, prefPD ('winner-take-all') and pRF size overlays.

5.6 Methods B: Optimising within-digit maps

5.6.0.1 Study B: Using the Nova coil to assess TW within-digit robustness

To determine the optimum fMRI paradigm for acquiring pRF data, two datasets (**B**) were acquired to determine the optimal number of repeated scans and the achievable temporal SNR. Since it is known that the between digit scans (of the 3×3 and 4×4 grid) are generally quite robust ((Sanchez-Panchuelo et al., 2012a, 2014)), data were only acquired to assess the within digit paradigm. Two datasets were acquired using a 32-ch Nova coil on two different subjects, with 3 or 4 pairs of within-digit forward and reverse scans (6 or 8 scans overall), see table 11).

B: Within-digit TW data				
Dataset	Resolution (mm^3)	Runs	Stim setup	MB factor
B1	1.25	8	4x4	2
B2	1.25	6	4x4	2

Table 11: Within digit datasets. Two participants were scanned using a 32-ch Nova coil. This data were not used for pRF modelling, rather, for determination of the optimum number of within digit runs. Optimum is defined as yielding a coherence map close to 1. MB = Multiband

For each dataset, the forward and reverse pairs were averaged into 1 pair (2 scans), 2 pairs (4 scans), 3 pairs (6 scans) and 4 pairs (8 scans). The scans chosen in each pair were randomized such that every possible combination from the 8 scans was identified. pRF analysis was not run on these data, only TW analysis was performed and robustness was identified by comparing coherence overlays (a measure of how well the sinusoid fits to the activated brain region, at the stimulus frequency), and phase overlays.

5.7 Results B: Optimising within-digit maps

5.7.0.1 Study B: TW within-digit robustness

To assess within digit robustness, the following data were taken from a single participant during one scan session, during which 8 runs of the within digit stimulation with a 4×4 grid were performed.

Figure 5.17 shows TW coherence and phase maps averaged across 2, 4, 6 or 8 runs of within-digit stimulation. It can be seen that there is a steady increase in coherence, CNR and amplitude of activation as one increases the number of within-digit pairs (Figure 5.19. Visually, there is an improvement in coherence from 2 to 4 runs, and then only small, incremental increases from 4 to 8 runs. The phase maps are robust (and consistent) for only 2 within digit runs.

Figure 5.18 shows coherence and phase values correlated for 1 versus 4 pairs, 2 versus 4 pairs, and 3 versus 4 pairs. There is a moderate improvement in coherence from 1 to 2 pairs, and little improvement from 2 to 3 pairs. Thus, it was concluded that 4 within digit scans are sufficient (2 pairs of forward and reverse) for the TW and for the pRF.

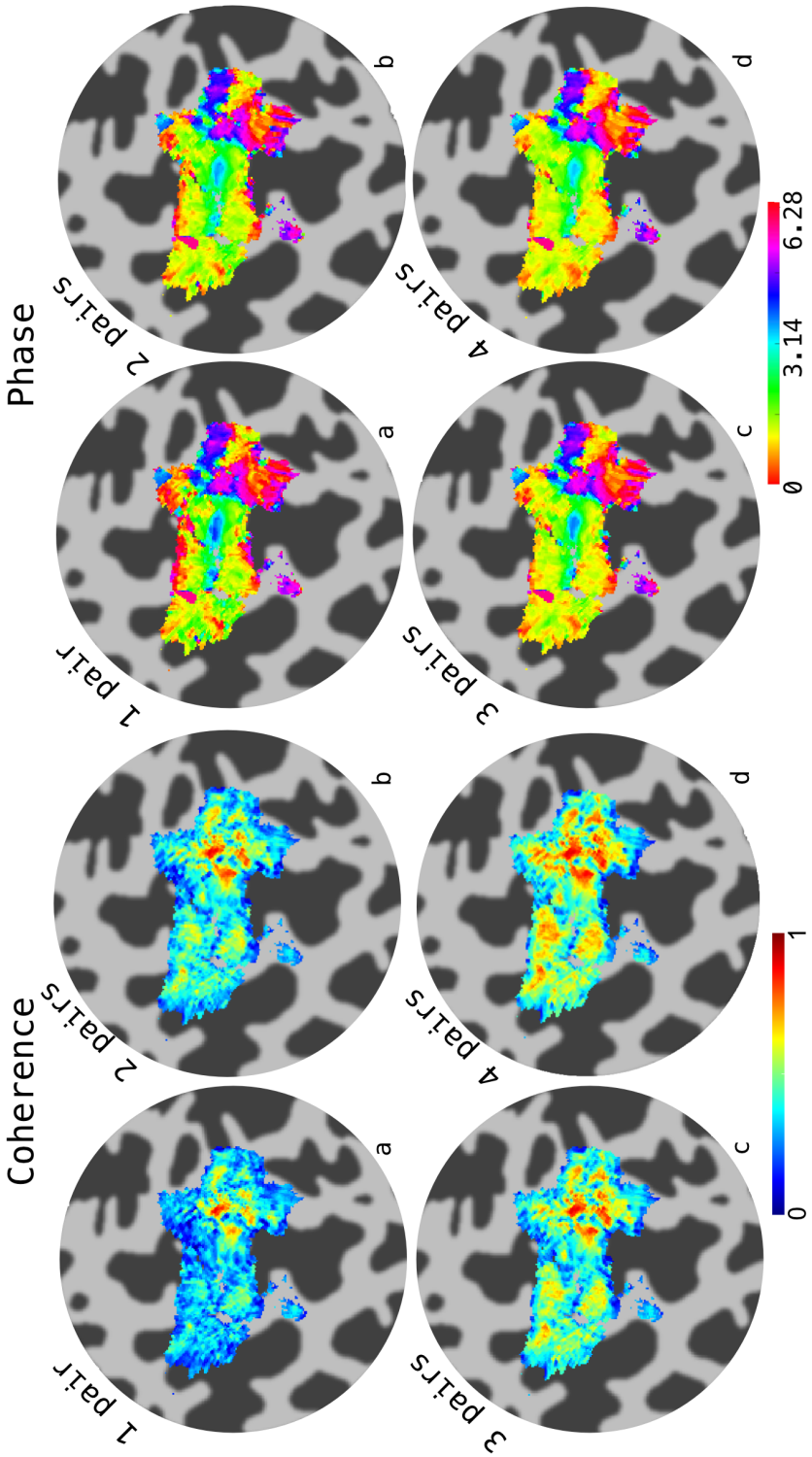


Figure 5.17: TW within digits coherence and phase maps for a single participant are shown, averaged across (a) 1 pair, (b) 2 pairs, (c) 3 pairs and (d) 4 pairs of runs, acquired in a single scan session. Each pair constitutes a forward scan and reverse scan, which are averaged together, and TR shifted to account for the haemodynamic lag (for phase map correction). Coherence is found by fitting a sinusoid at the stimulus frequency. Coherence values increase as the number of averages increases. Phase values do not visibly change as the number of averages increase.

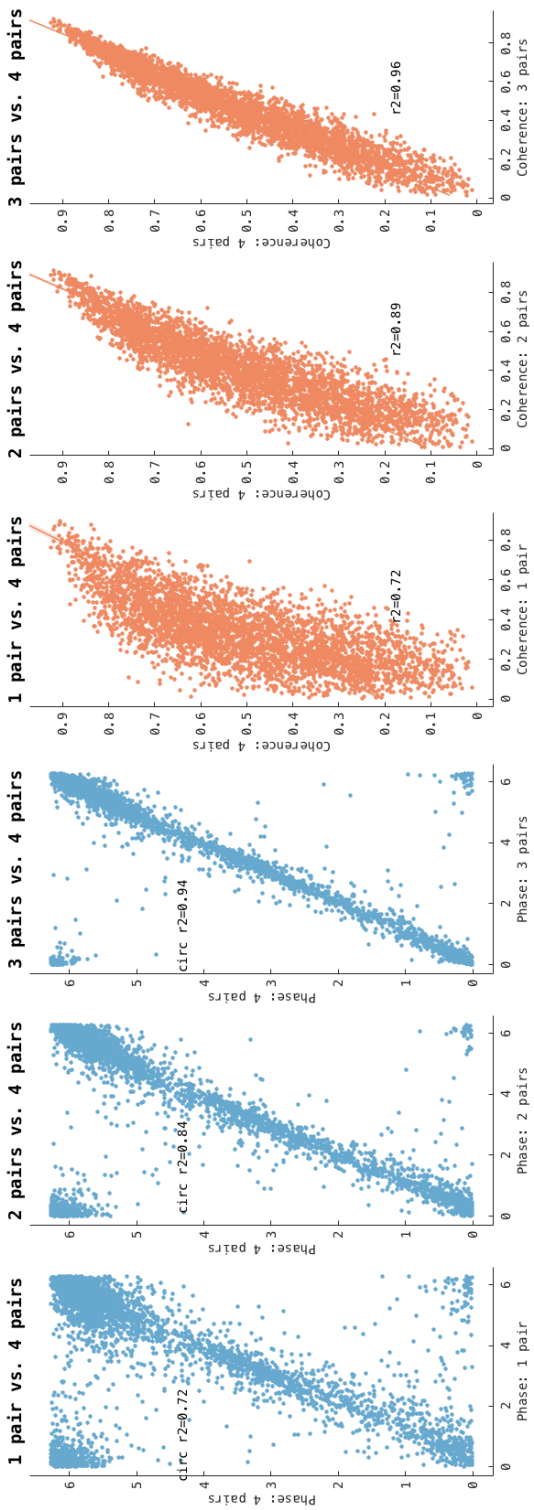


Figure 5.18: Left) Coherence from 1 pair / 2 pairs / 3 pairs correlated with coherence from 4 pairs of within-digit runs. Values indicate correlation coefficient (Pearson's r). Right) Phase from 1 pair / 2 pairs / 3 pairs correlated with phase from 4 pairs of within-digit runs. Circular correlation coefficient is indicated on the graphs (`circ_corrcc` in MATLAB).

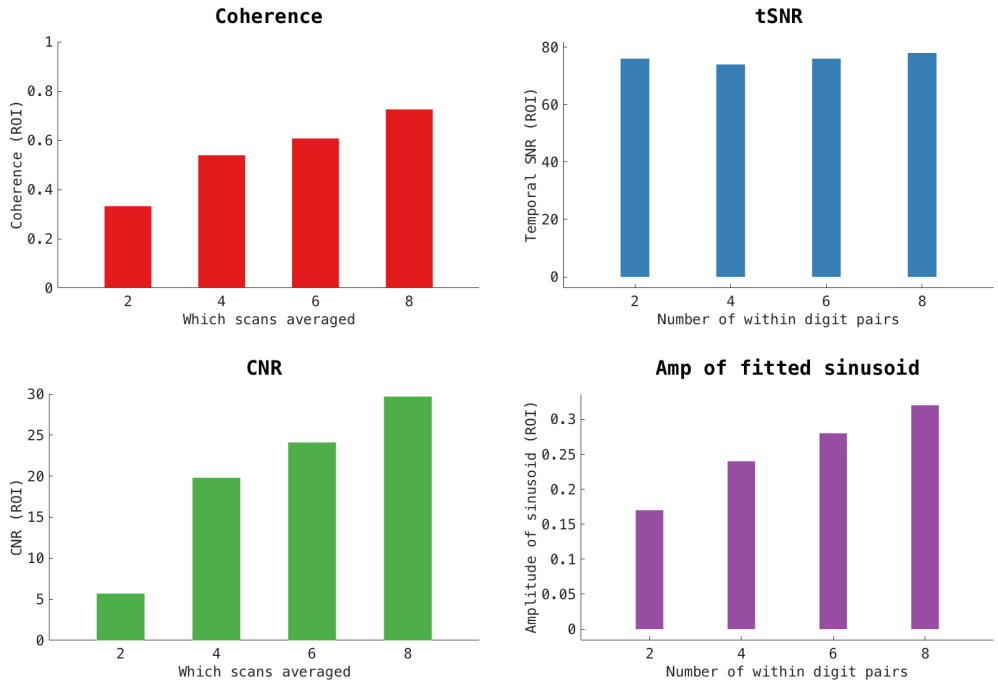


Figure 5.19: A comparison of summary values taken from multiple repeats of within digit scans. From top left to bottom right: the coherence in the region of interest pictured in Figure 5.17, is compared with the number of within digit pair scans; the temporal SNR is compared across pairs; the contrast noise ratio is compared across pairs; the amplitude of the fitted sinusoid (the degree of fitting is given by the coherence), compared across pairs. In all cases, the more pairs of within digit runs, the parameter of interest increases. The largest jump (for coherence, CNR and amplitude) is from 2 scans to 4 scans (1 pair to 2 pairs).

5.8 Methods C: Comparing TW and pRF analysis

5.8.0.1 Study C: pRF analysis using TW data

A further analysis involved performing a modified pRF analysis on the TW data. The stimulus image used in this case was a 1-dimensional '1-by-5' sequence, where the y-parameter was fixed to be 1 and x was allowed to vary across the fingertips. Two models were compared: a 2D-Gaussian model (including HRF parameters), and a "Five-parameter" model, where each parameter was linked to a digit tip (see Section 5.4.1). These data were acquired on a 32-channel Nova coil, with the same paradigm and scan parameters as a TW scan (see Section 5.4.0.2). This analysis allowed assessment of whether the pRF could be used on a TW design.

Six fMRI runs of the TW paradigm were performed in a single subject (3 forward and 3 reverse). Scan parameters were: TR 2 s, Multiband factor 2, 40 slices, 120 dynamics per scan.

The TW data pairs were split up to assess differences caused by attention, motion or temporal SNR. 7 different averages were performed: 1+2, 3+4, 5+6, 1+2+3+4, 1+2+5+6, 3+4+5+6 and 1+2+3+4+5+6. In each case, a coherence and phase map was calculated.

In each of the 7 averages, a pRF analysis was performed producing r^2 maps, preferred digit, (preferred proximal-distal was ignored since it should always be 1) and receptive field size. Here, r^2 spatial maps were compared to coherence spatial maps, however, simulations show that the relationship between both parameters is not linear, thus, any direct comparison must consider this. For visualization purposes, one set of r^2 maps was square-rooted.

5.9 Results C: Comparing TW and pRF analysis

5.9.0.1 Study C: pRF analysis

Here, the pRF analysis was performed on TW data. The TW for all 3 pairs of scans produced good coherence (Figures 5.20 and 5.21) in somatosensory cortex and moderate to high tSNR. Only 6 averages are shown here: 1+2, 3+4, 5+6, 1+2+3+4, 1+2+5+6 and 1+2+3+4+5+6. By inspection, the 1+2 average provided the best TW coherence and phase maps; note that the scan number indicates the temporal order, with scan 1 acquired first and scan 6 last.

The coherence and phase values from each average were extracted and pairs were correlated, i.e. 1 pair versus 3 pairs and 2 pairs versus 3 pairs. In each case, there was a strong correlation in the coherence and phase values, with the expected stronger correlation for the 2 pairs vs. 3 pairs than the 1 pair vs. 3 pairs (see Figure 5.22).

A 2-dimensional Gaussian model (where the y-parameter would be expected to stay fixed, but was not restricted to do so) and also a five-parameter model (Five-hdr, hereafter) were used. Both models included 7 additional HRF parameters (see Section 5.4.2). Both the Gaussian-hdr and Five-hdr provided similar pRF fits, with similar maximum per voxel r^2's (e.g. 0.77 for both models, on the 1+2 scan), and similar percentage of voxels fitting above $r^2 = 0.25$ (7% and 7.5%, respectively). However, due to the winner-take-all approach of the Five-hdr, which emulates the same protocol as the previously discussed 9-parameter and 16-parameter models, the harsh binning leads to an unconstrained map that in some cases may be meaningless, regardless of the large r^2 (see Figure 5.23).

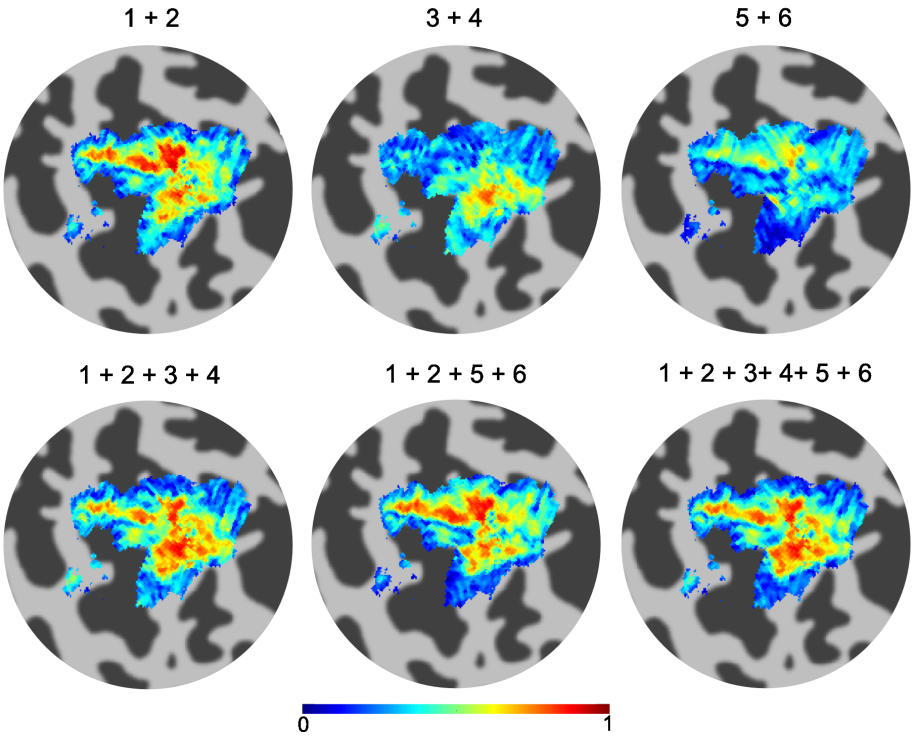


Figure 5.20: 6 differently averaged TW maps. Scans 1, 3 and 5 are forward scans, while scans 2, 4 and 6 are reverse scans. It can be seen that the 1+2 average provides the strongest coherence, and as one moves to increasing pairs (2 pairs > 3 pairs), the overall coherence and coverage improves.

To identify the relationship between coherence (TW) and r^2 (pRF) in real data, values from from a single average (1+2) were plot against each other along with plots of r against coherence, which provided a linear fit (see Figure 5.24). As expected, the r maps better correlated with the coherence maps, with only a slight drop in parameter power (see Figure 5.25).

5.9.0.2 Correlating TW and pRF data

The data in Figures 5.26 - 5.29 show the between digit TW coherence and phase values, and the pRF r^2 and preferred digit overlays. Consistently, there is a strong correlation between the pRF and TW methods: Figure

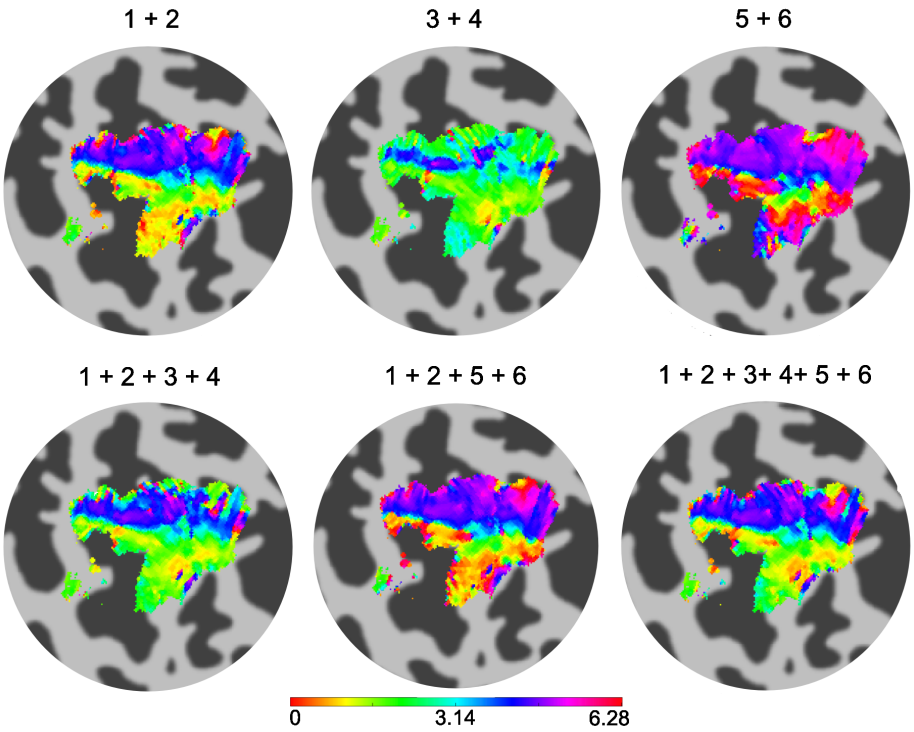


Figure 5.21: 6 differently averaged TW phase maps. As in Figure 5.21, 1+2 has the most logical phase progression map, with 3+4 providing the worse - this is seen when averaging more pairs with the 3+4 average; the phase map looks worse.

5.26 shows that the pRF r^2 and TW coherence correlate linearly across digits; Figure 5.27 shows that the voxel distribution is separated according to TW phase values, however, it is strongly skewed to D2, D3 and D4 (more voxels in the pRF code for these digits), and this is also seen in Figure 5.28. The 'centre of mass' overlay, which shows a smooth transition across phase, indicates changes in digit correspondence and is consistent with the 'winner-takes-all' method, Figure 5.29.

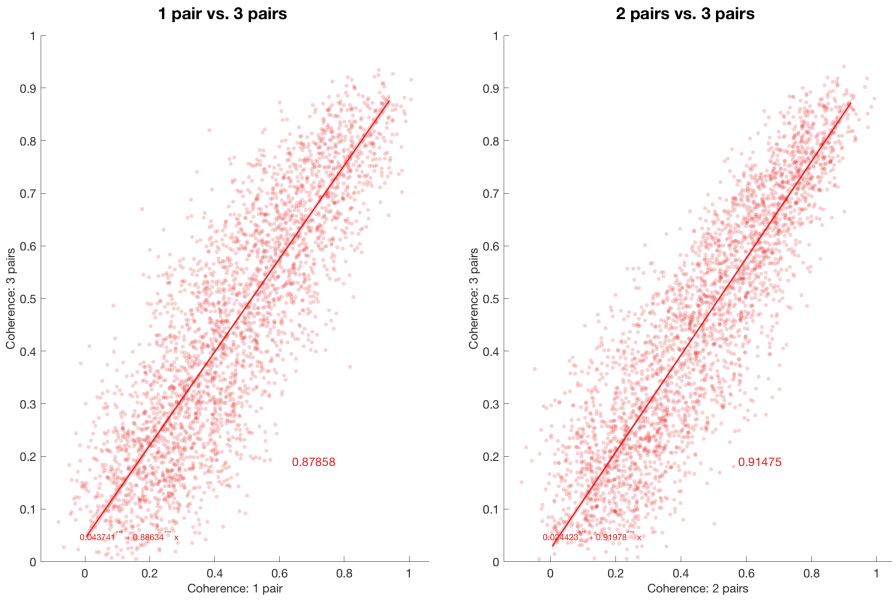


Figure 5.22: Correlating coherence values from a single pair (1+2) and 2 pairs (1+2+3+4) to the 3 pair average (1+2+3+4+5+6).

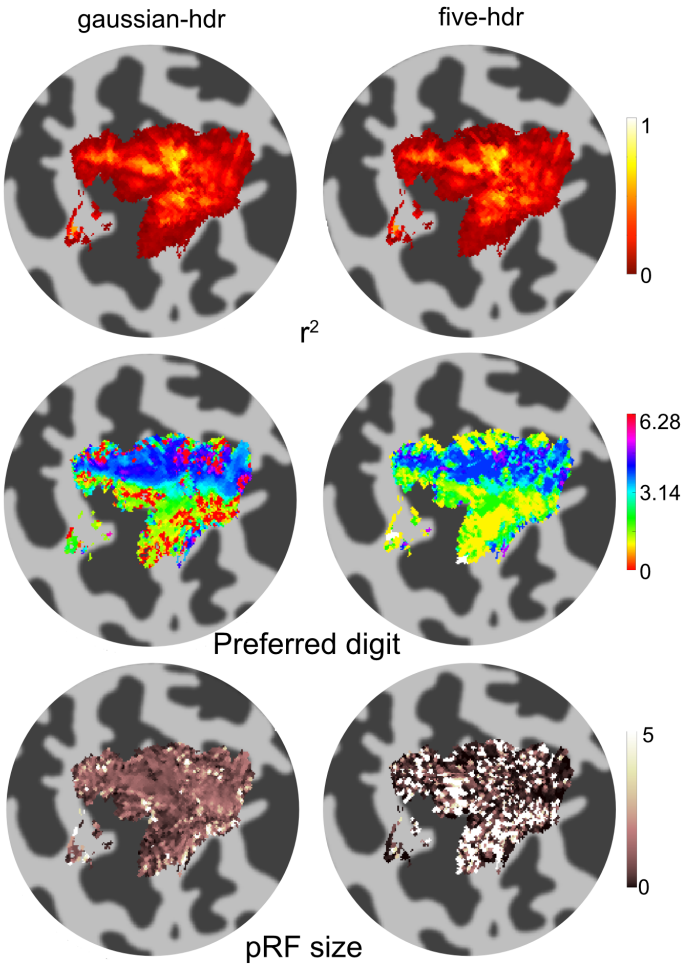


Figure 5.23: The Gaussian-hdr and Five-hdr models spatial parameter maps based on the same '1 by 5' stimulus sequence. Note that the Gaussian model has smooth transitions in phase, whereas the Five-hdr model is binning each digit, leading to 5 block colours in the phase map. While the r^2 maps look similar, the receptive field size maps are vastly different, with many voxels exhibiting extreme values in the Five-hdr map.

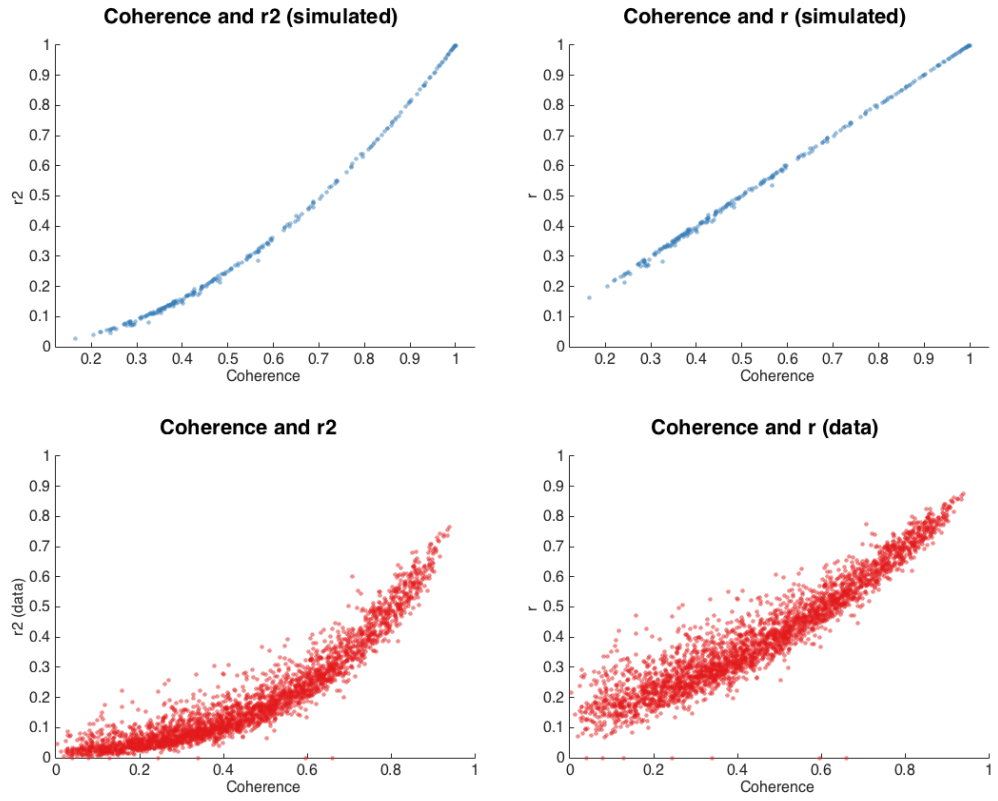


Figure 5.24: The relationship between coherence and r and r^2. Top row) Simulated data shows a non linear relationship between r^2 and coherence, but a linear dependency with r. Bottom) Real data provides a similar trend (data taken from the 1+2 average).

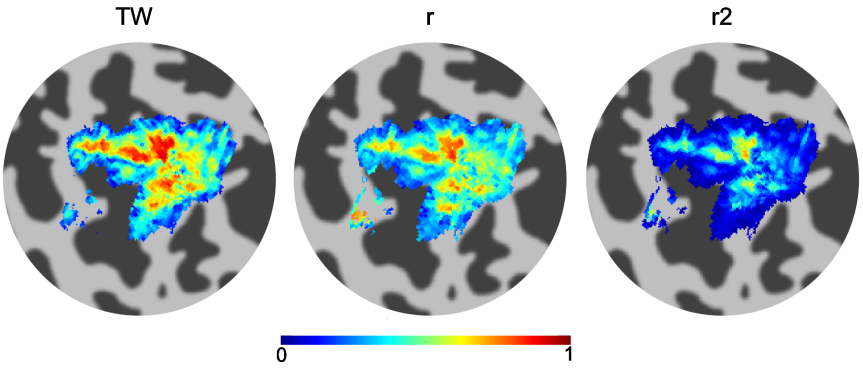


Figure 5.25: Spatial maps of coherence, r and r^2. The r^2 (pRF) and coherence (TW) maps look dissimilar, with only a small pattern of similarity. Note that due to the non-linear relationship between r^2 and coherence, an r map is more appropriate (middle).

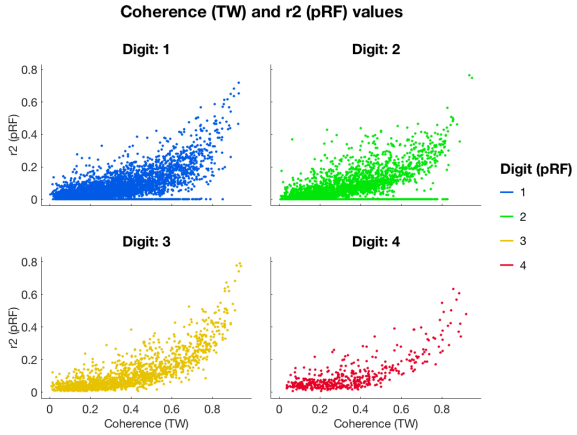


Figure 5.26: r^2 (pRF) correlated with coherence (TW), and split by prefDig (pRF). If the coherence correlated strongly with r^2, one would expect a linear relationship across all 4 digits. This is evident here, however, whilst significant, the distribution is quite noisy. This may be due to lack of thresholding based on the r^2 fit. Data are from all subjects in dataset **A**.

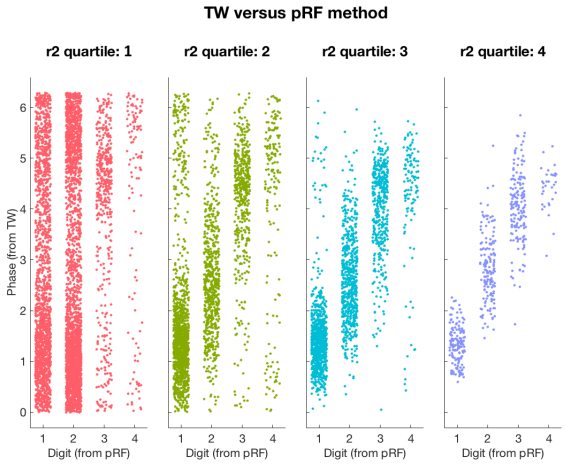


Figure 5.27: Voxel distribution across the phase (TW), and colour coded by digit (prefDig), is shown. The data are further split into quartiles based on r^2, such that, each column displays a stratified 25 %, and hence the 4^{th} quartile represents the top 25 % of voxel fits. Ideally, 4 separate groupings should be identifiable, corresponding to clear separations in the phase maps. This does occur, however, one can see that most voxels seem to have a preference for the index and middle fingers (D2, D3). Data are from all subjects in dataset **A**.

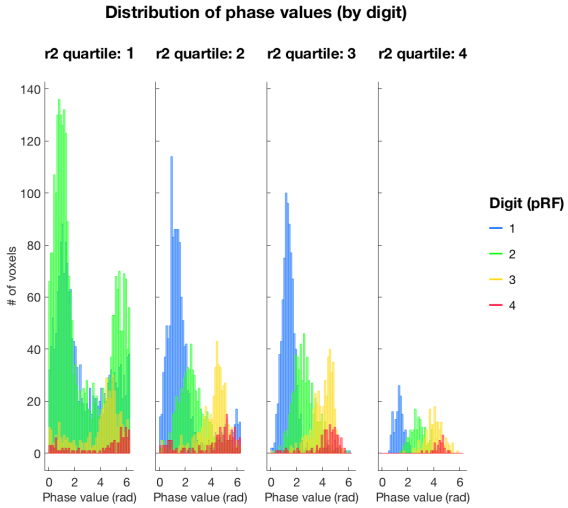


Figure 5.28: Phase distribution across digits (an alternative view to Figure 5.27. In this view, it is clear that there are 4 separate phase representations in the TW overlay, split up by prefDig (pRF). The overlay is based on the 'winner-takes-all' binning of digits in the pRF fitting. Again, the columns stratify the data into quartiles, based on r^2 fits. Data are from all subjects in dataset **A**.

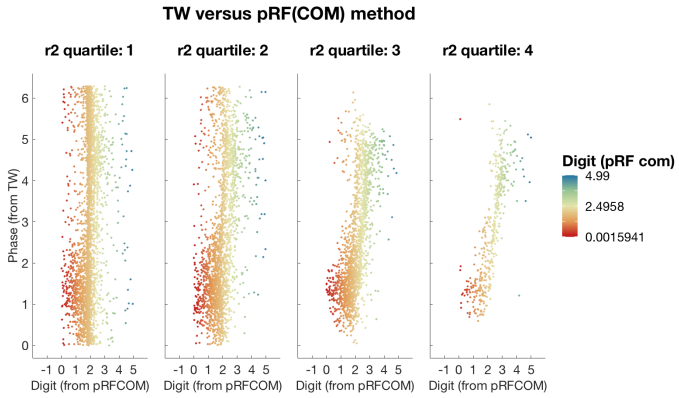


Figure 5.29: The phase distribution across digits, using the 'centre of mass' overlay from the pRF fit. Similarly to Figure 5.28,4 separate phase transitions are visible, even across a continuous color range. Data are from all subjects in dataset **A**.

5.9.0.3 pRF algorithms: Nelder-Mead (NM) vs. Levenberg Marquardt (LM)

Figure 5.31 compares the r^2 maps across all subjects between the NM or LM algorithms. There is little difference between methods, although the plots (right columns) indicate a slight preference of higher r^2 for the NM algorithm.

Quantitatively, to compare the NM and LM algorithms the circular variance of the difference between phase values from the between-digit travelling wave and pRF preferred digit parameter map was plot, as performed in Chapter 4. A large circular variance indicates low consistency between phase angle and preferred digit map, with phase values spread out in a polar histogram. These plots and difference plots are shown for a single subject in Figure 5.32. For all subjects (Dataset **A**), the circular variance is plotted against algorithm (Figure 5.33) and subject (Figure 5.34). Similar to r^2, the circular variance is similar within subjects, regardless of algorithm used.

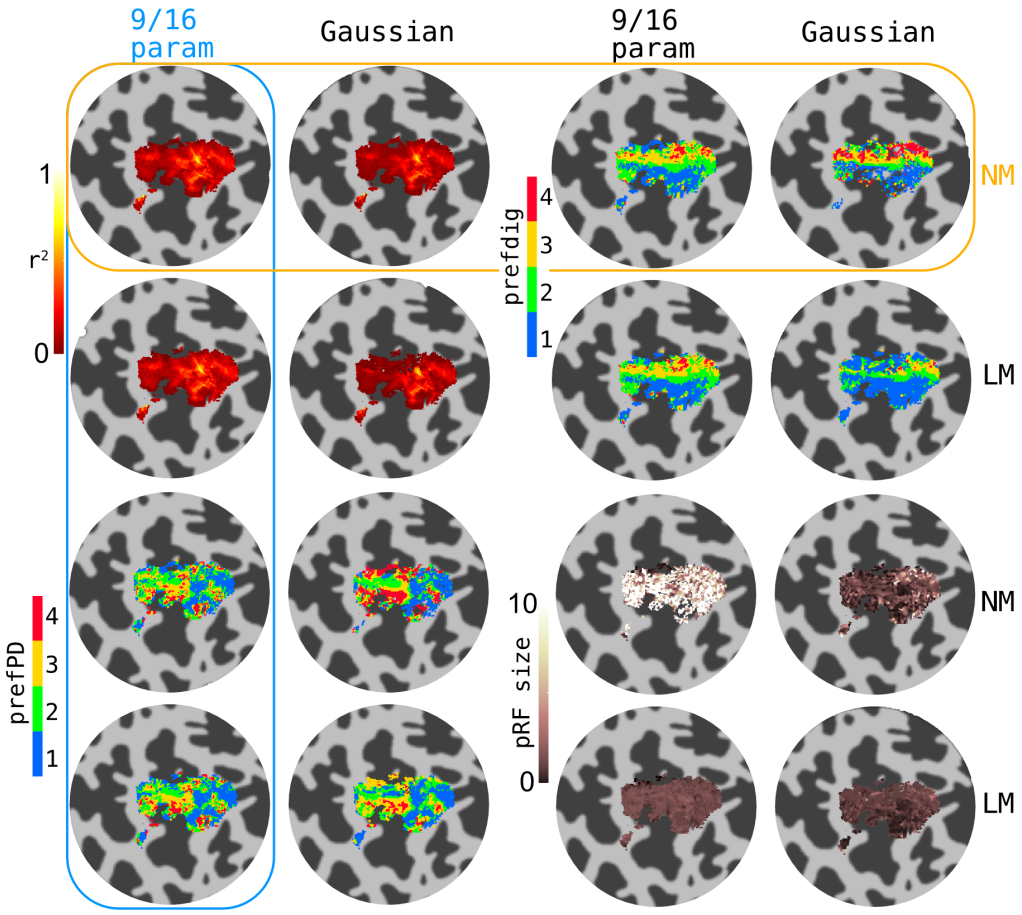


Figure 5.30: pRF mapping performed 4 different ways (2 algorithms, 2 models) shown here on a single subject (Dataset **A6**), however, this was performed in all subjects (n=9), leading to 36 separate pRF analyses and 144 parameter maps. In all cases, HRF parameters were fit using the pRF. Here, since a 4×4 stimulation grid was used, there are four possible delineations in the between digit (prefdig) and within digit (prefPD) conditions. NM = Nelder-Mead. LM = Levenberg-Marquardt. Each row corresponds to one algorithm, and each column corresponds to one pRF model. In this subject, the 16 parameter model has better r^2 fits, however, improvements in parameter maps are less clear.

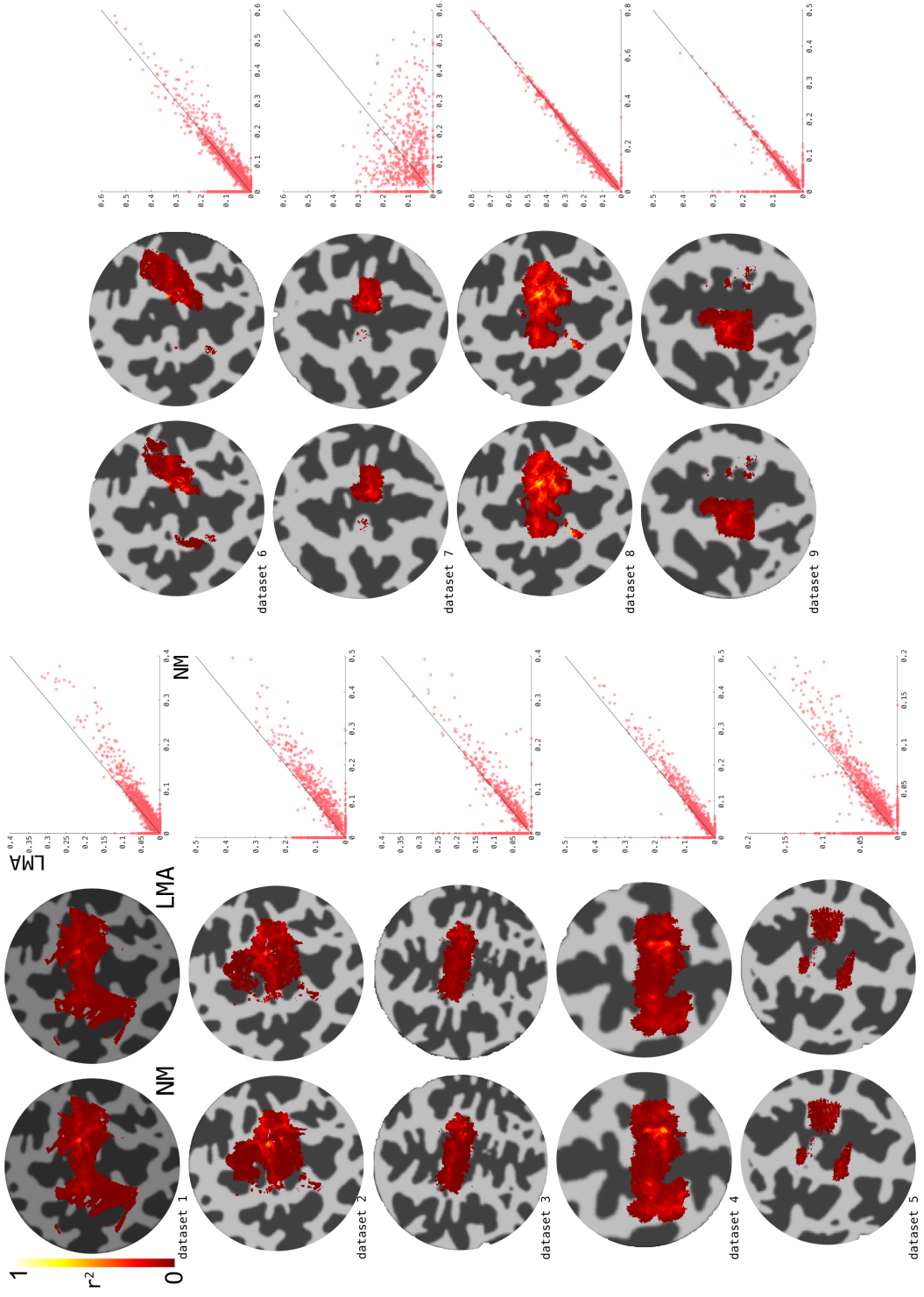


Figure 5.31: pRF r^2 across all subjects, comparing Nelder-Mead (NM) and Levenberg-Marquardt (LM) algorithms. There is little qualitative difference in r^2 between algorithms.

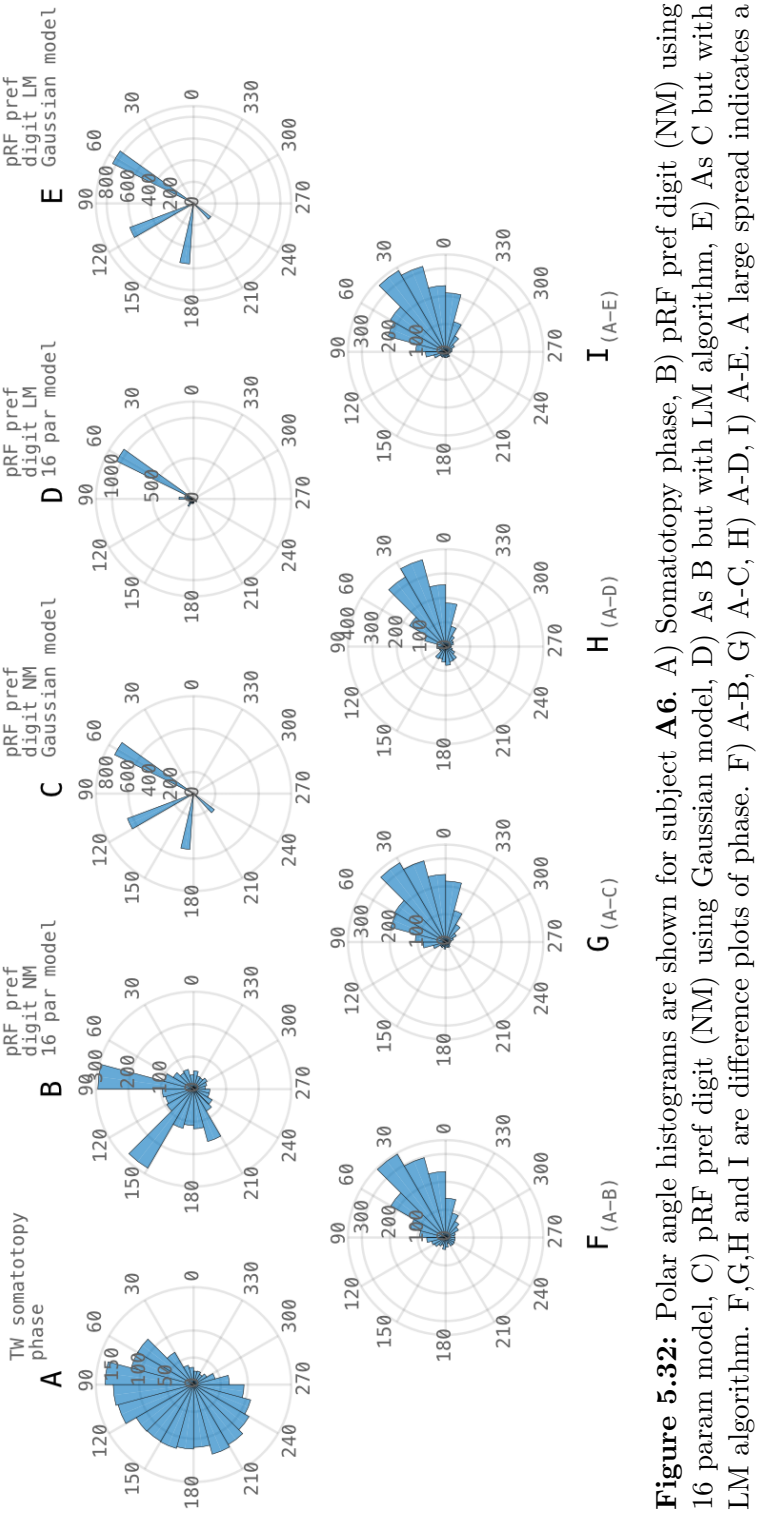


Figure 5.32: Polar angle histograms are shown for subject **A6**. A) Somatotopy phase, B) pRF pref digit (NM) using 16 param model, C) pRF pref digit (NM) using Gaussian model, D) As B but with LM algorithm, E) As C but with LM algorithm. F,G,H and I are difference plots of phase. F) A-B, G) A-C, H) A-D, I) A-E. A large spread indicates a larger circular variance.

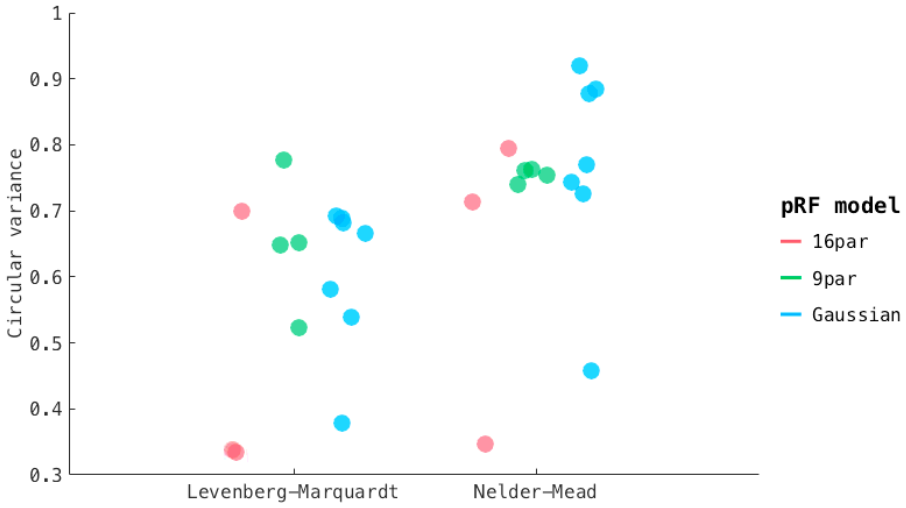


Figure 5.33: Circular variance of the difference phase plots for all subjects (Nova coil **A**) split across algorithm. Similar to r^2, there is little difference between algorithm, however, the Nelder-Mead seems to have a higher circular variance overall.

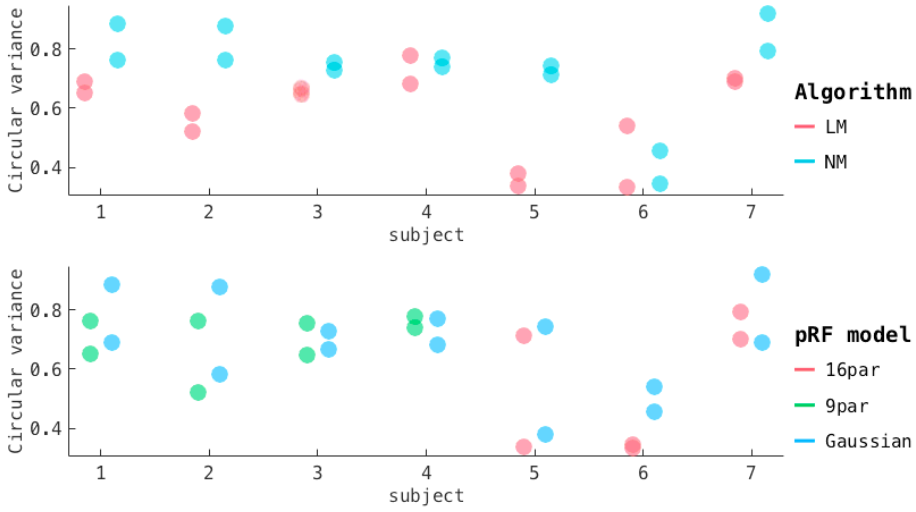


Figure 5.34: Circular variance of the difference phase plots for all subjects (Nova coil **A**) split across subject. There is a slight trend for the Nelder-Mead algorithm to have higher circular variance than the LM algorithm, but this is not consistent across subjects.

5.10 Methods D: Data acquisition and Surface coil paradigm optimisation

5.10.0.1 Assessing image and temporal SNR to potentially improve pRF mapping

This section explores the use of surface coils (Figure 5.35). For pRF mapping a smaller voxel size may allow a more homogeneous neural population to be measured, and hence the more valid is the assumption that the entire neural population within that voxel is driving the response, i.e. has similar tunings. Therefore, if increased spatial resolution is provided by the surface coil (across a smaller region), e.g. 1 mm^3, then this may provide more reliable estimates for the pRF outputs. The issues of using a surface coil are the extra practicalities, e.g. how to position the coils in a robust and reliable fashion, which can negate the ability to perform such a scan in patient populations. Furthermore, since the surface coil only receives signals focally over the region it is placed, data coverage can be an issue, i.e. failing to acquire data in all of somatosensory cortex.

To assess the potential gains of using a surface coil placed over the somatosensory cortex, compared to the Nova coil, task-free data were acquired from 5 scan sessions (Study **D**) with different protocols (see Table 12) to determine the achievable tSNR. Assessments were made of temporal SNR (tSNR) calculation and visual inspection of image quality. All tSNR measurements were taken across 20 dynamics.

5.10.0.2 Acquisition of TW and pRF data

Two 7 T fMRI pRF datasets using the 32-channel MR Coils surface coils (2 separate 16-channel coils) were collected. Temporal SNR values were

Nova and surface coil data (D)					
Dataset	Coil	Resolution (mm^3)	MB factor	SENSE	TR (s)
D1	Nova/Surface	1.5	1/2	2.5	2/3.5
D2	Surface	1.5	2	2.5	2
D3	Surface	0.8x0.8x1	1	2.5	2
D4	Surface	0.8x0.8x1	1/2/3	2/2.5/3/4	2
D5	Surface	0.8x0.8x1/2/1.5	1/2/3	2.5	.75/1/2

Table 12: Details of five datasets acquired to assess tSNR using the surface coils. D1 provided a reference for Nova coil and was swapped for the surface coil in the same session. Surface coil data (D2-D5) were then exclusively collected on a number of subjects to assess quality and placement of the coil. Data were acquired across spatial resolutions, multiband (MB), SENSE factors and TRs.

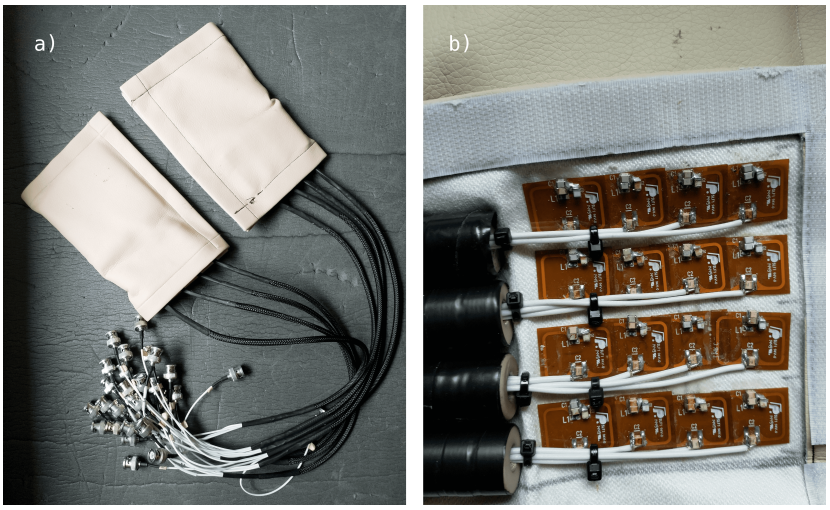


Figure 5.35: a) A pair of MR Coils surface coils used in combination (16 channels separate, 32 channels together). b) 16 channels shown from one coil.

calculated for these datasets for comparison with the 32-ch Nova-coil data, see Section 5.10.0.1.

The data were collected using the 3×3 grid using an identical paradigm as described in Section 5.4.0.1. Data were pre-processed in the same manner as for the Nova coil data (Section 5.4.0.2).

D: Surface Coil pRF data				
Dataset	Resolution (isotropic mm^3)	MB factor	pRF model	Hand
D6	1.00	1	3x3	Right
D7	1.00	1	3x3	Right

Table 13: Data collected on two subjects using the two 16-channel surface coils. MB = Multiband factor.

5.11 Results D: Data acquisition and Surface coil paradigm optimisation

5.11.0.1 Temporal SNR

The tSNR of the surface coils is high at the surface of the brain and drops off with increasing distance from the coil centre. This provides a strong, focal area of high tSNR. For imaging a specific area, e.g. somatosensory cortex, a smaller FOV may be preferred. It is hypothesized that the greater tSNR can be traded off for higher spatial resolution (smaller voxel sizes).

Here, an approximate 2 x drop in tSNR from the Nova to the surface coils was seen, however, this was expected given the reduction in volume of 3.375 times (moving from 1.5 mm isotropic (Nova) to 1x1x1 mm (surface). Although it seems that the Nova coil has higher tSNR at the same voxel resolution as the surface coil, the tSNR for the surface coil at a higher resolution is consistent, see Figure 5.36.

For axial acquisition, it is evident that the surface coil, placed over the left hemisphere, has only a very focal receive FOV, Figure 5.37.

Assessing the surface coil alone, with a tilted sagittal acquisition, one can see that as one increases MB factor, the tSNR worsens (Figure 5.38). One

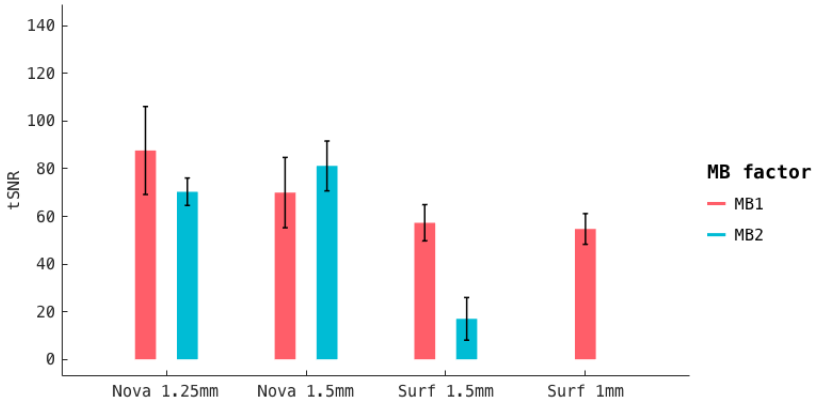


Figure 5.36: tSNR values were taken from datasets **C** and **D**. The mean tSNR was calculated within a scan session, across a somatosensory ROI (see Figure 5.37). The data are compared across coils, as well as across multiband factors (1 or 2) and voxel resolutions. All tSNR values are only calculated on the first 20 dynamics of each scan.

can also alter the resolution, stratifying sagitally acquired surface coil scans across multiband factor. It is evident, again, that the tSNR and image quality suffers at a higher multiband factor on the surface coil, in this orientation (Figure 5.39). Acquiring data at 1 mm isotropic resolution (Figure 5.40) on the surface coil results in higher tSNR, comparable (if not better) to the same data acquired at 1.5 mm isotropic on the surface coil, indicating that one can safely increase the resolution, without a large drop in tSNR (in a small FOV).

5.11.0.2 TW and pRF data

The pRF model outputs for the pilot two surface coil datasets are shown in Figure 5.41. This shows a moderate fit for concatenated scans, consistent with the Nova coil pRF data. The model outputs in Figure 5.43 show a similar trend to the Nova coil data, i.e. clear digit delineation (in this case, 3 digits) but a sparse pRF coverage. Note also that this particular dataset

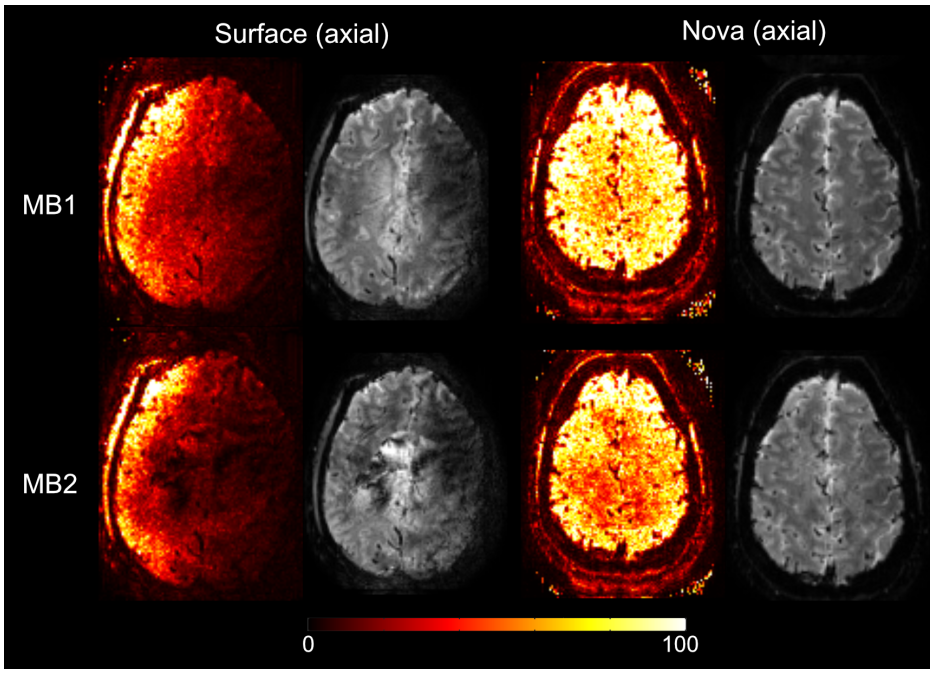


Figure 5.37: tSNR and mean images. Left) Images acquired using a surface coil placed on left hemisphere. 1.5 mm isotropic voxel size. Data are shown across multiband factors 1 (no multiband) and 2. Right) For the same voxel size, Nova coil data are shown. tSNR values are substantially higher for Nova coil data. There are also clear artifacts/distortion occurring outside the surface coil's field of view.

suffers in its activation maps, due to poor coverage, exemplifying the issue of non-robust placement of the surface coil on the subject's head.

Figure 5.42 displays the fit percentiles and number of voxels fitting above r^2 across both Nova coil (**A**) and Surface coil (**D**) pRF datasets. Compared to pRF fitting in visual cortex (see Chapter 4), the number of voxels with a high r^2 is much lower.

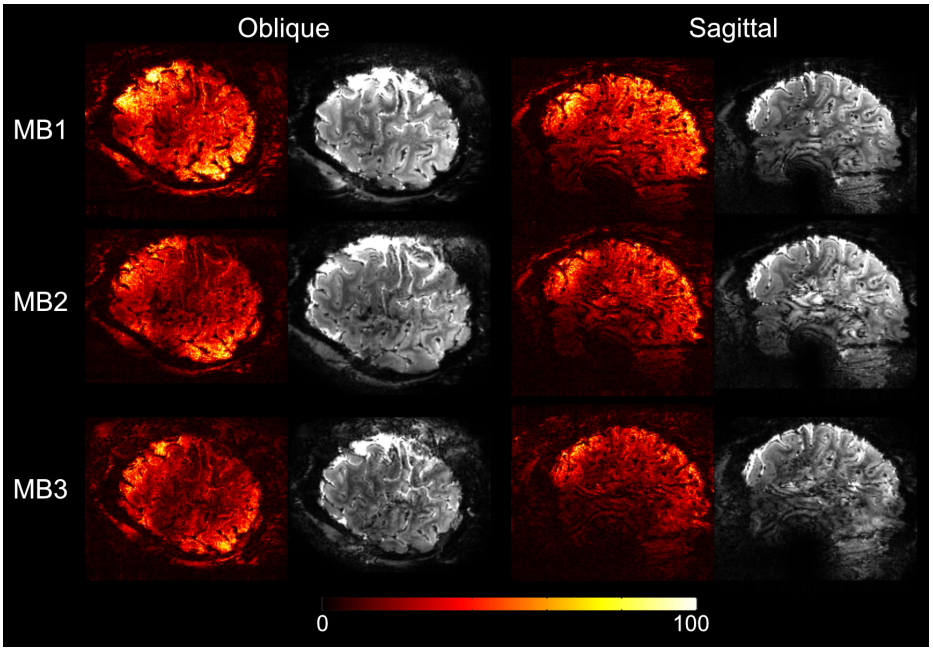


Figure 5.38: tSNR and mean images acquired on a surface coil. Left) The coil was placed at an oblique angle on the left hemisphere. Right) Here, sagittal images were acquired by moving the surface coil lower. Images are shown across multiband factors (1, 2 and 3). Data acquired at 0.8x0.8x1 mm. Significant distortions occur as the multiband factor is raised.

D: Surface Coil pRF fits			
Dataset	max r^2	no. voxels fitted	pRF model parameters
D6	0.23	2783	9
D7	0.58	1750	9

Table 14: pRF fits are shown for subjects D6 and D7. See table 13 for reference. For each dataset, 8 pRF runs were concatenated, and the model fitting was performed on this timecourse, per voxel (two sets of between digit, 2 sets of diagonals, 4 sets of within digit. The maximum r^2 is for a single voxel. The number of voxels fitted over was determined by thresholding the TW coherence maps, as well as unique subject anatomy. Note that the pRF fitting algorithm is an intensive computational procedure that is very sensitive to length of timecourse, number of voxels, model type, etc.

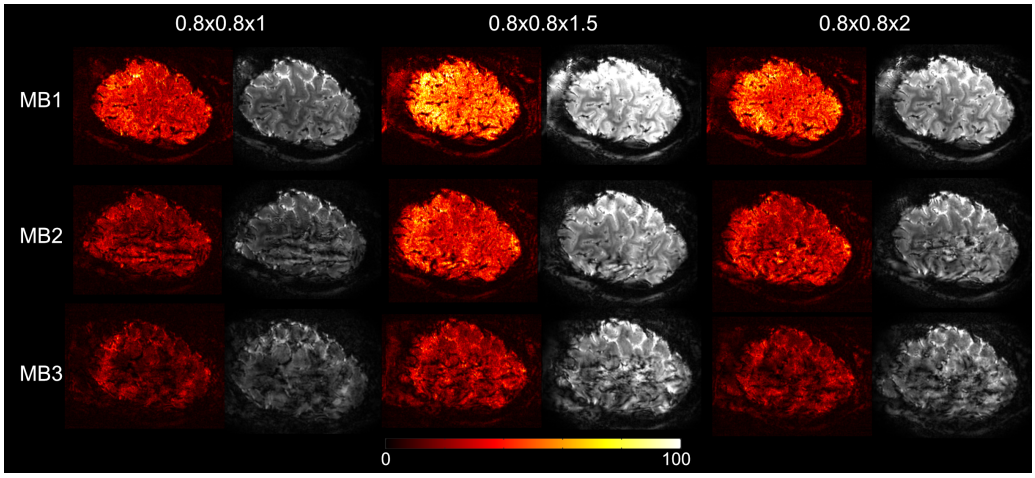


Figure 5.39: tSNR and mean images acquired on a surface coil, at different voxel resolutions. The three columns indicate three different resolutions (0.8x0.8x1, 0.8x0.8x1.5, 0.8x0.8x2 mm). Data are shown across multiband factors (1, 2 and 3). Similarly to Figure 5.38, distortions are apparent at higher multiband factors. Additionally, tSNR is lower at smaller voxel sizes.

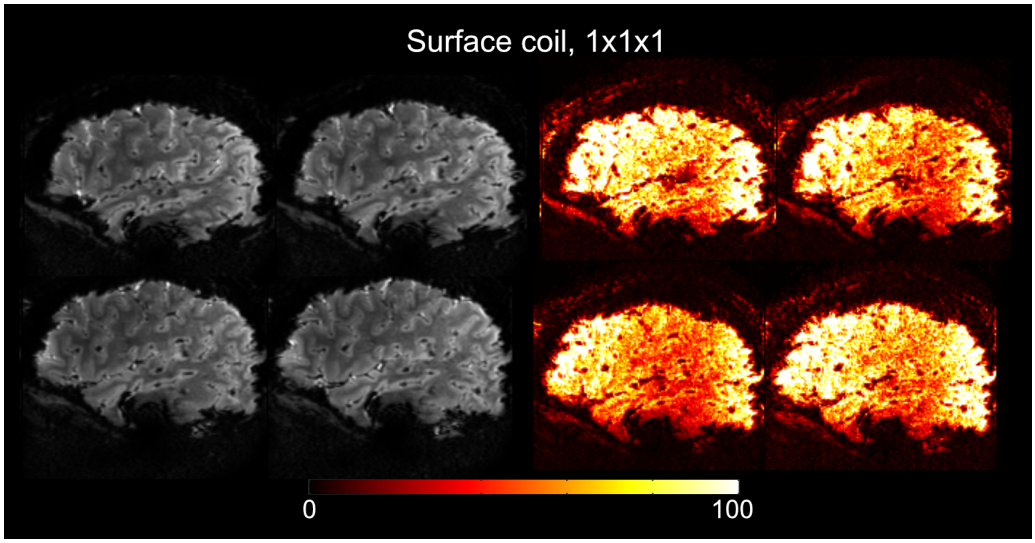


Figure 5.40: tSNR and mean images acquired on a surface coil, at 1x1x1 mm voxel resolution.

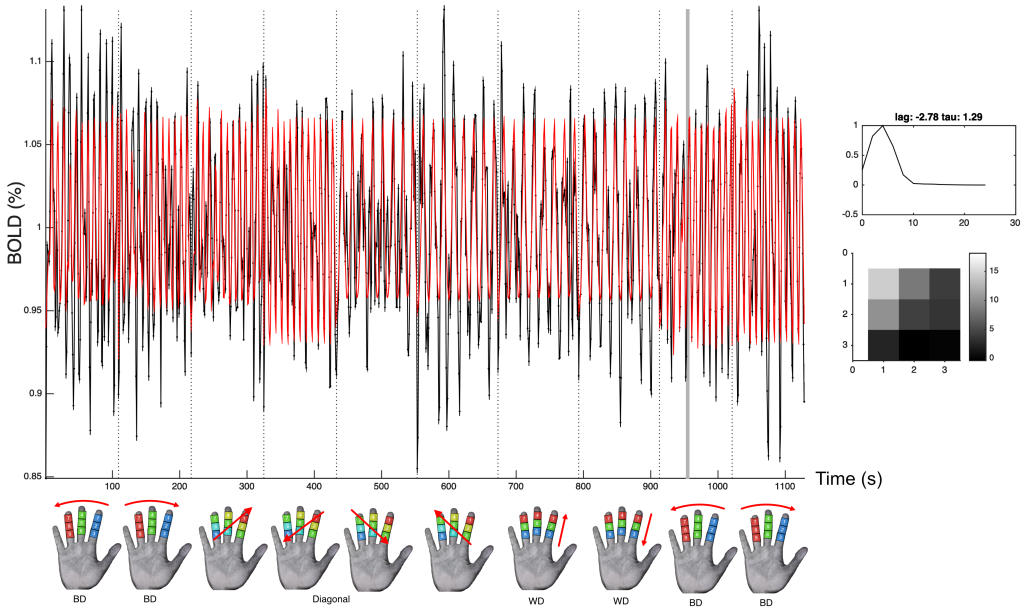


Figure 5.41: pRF model fit for a single subject, on a 3×3 grid (9 parameters), using a surface coil. The black timecourse is data from a single voxel, whilst the red is the fitted pRF timeseries. $r^2 = 0.58$. The scan has been concatenated from 10 pRF paradigm runs in a single scan session. The top right of the image indicates the fitted HRF, and below this is the model pRF model response (or model weights).

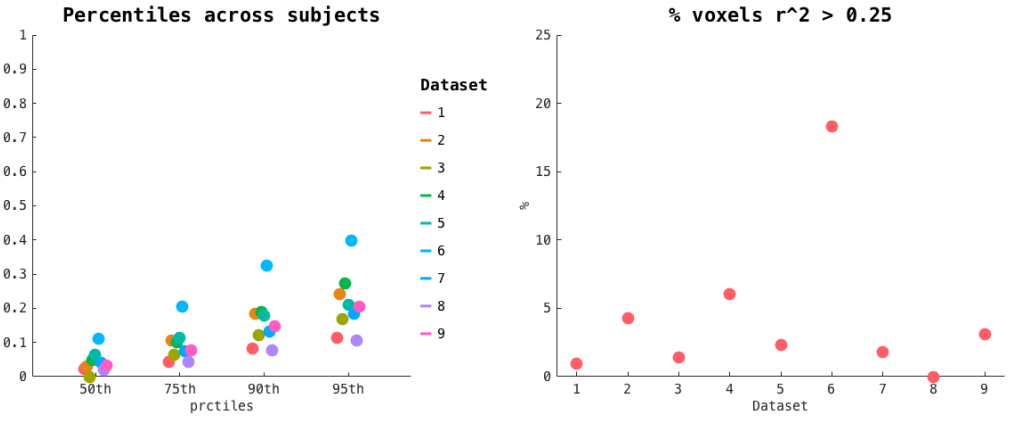


Figure 5.42: Left) pRF percentiles across datasets **A** and **D** pRF are shown. Right) The number of voxels fitting above $r^2 > 0.25$ is displayed.

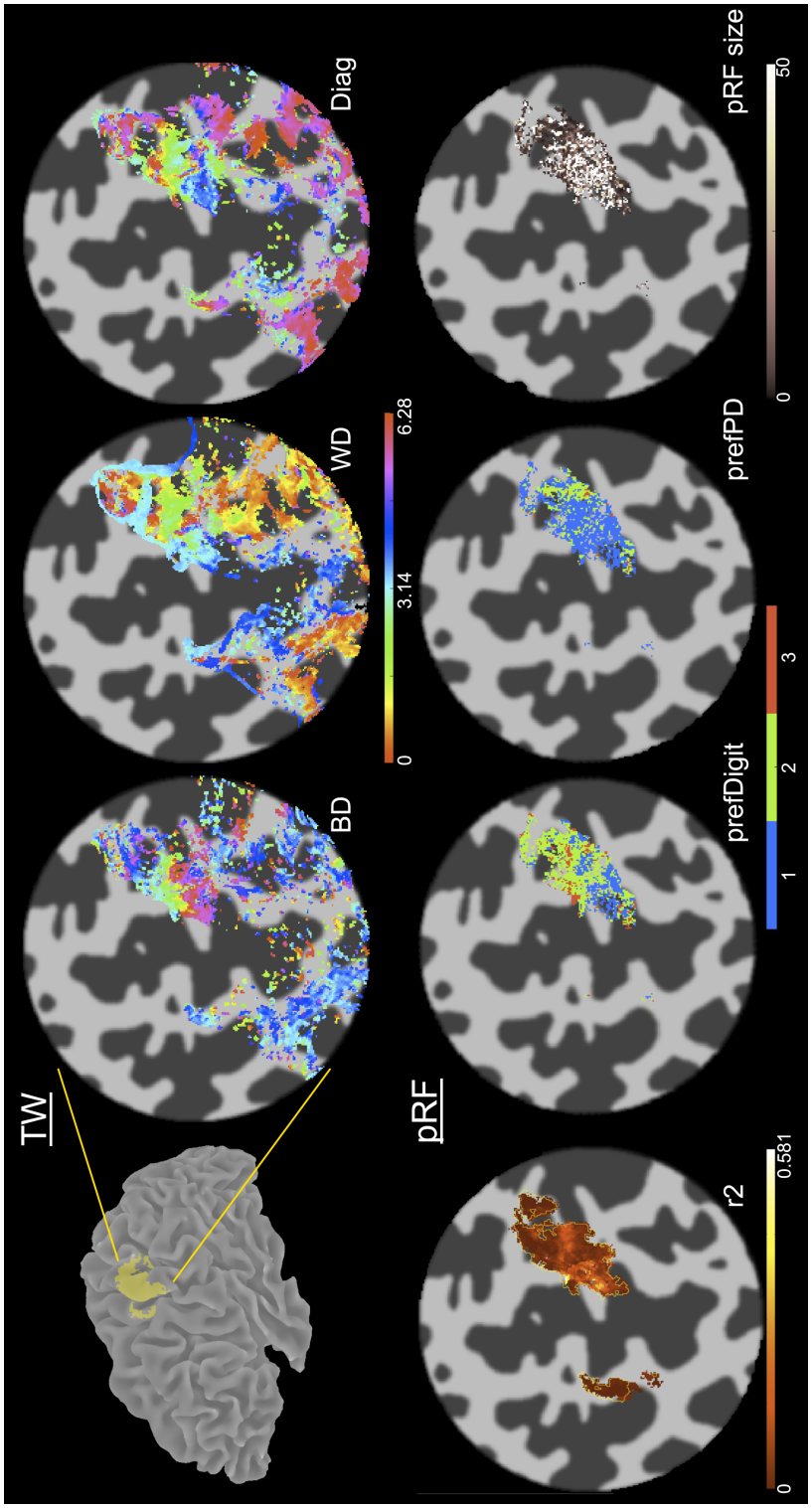


Figure 5.43: TW and pRF overlays displayed on a flattened cortex, for a single participant (table 13, dataset 2). Top: Between digit and Within digit phase maps. Bottom: pRF overlays showing r^2, prefDig, prefPD ('winner-takes-all') and pRF size overlays.

5.12 Discussion

This Chapter studies pRF mapping in somatosensory cortex using piezoelectric stimulators delivering stimulation to digit sites, producing within digit and between digit stimulation patterns.

5.12.0.1 Somatosensory TW and pRF

The between digit TW stimulation is known to be robust. Results show that using the minimum of four within digit scans (2 pairs of forward and reverse scans) provides sufficient coherence across a region of interest. The correlation of the pRF mapping digit overlays to TW digit overlays was significant for between and within digits. Separate digit transitions have been identified in two methods of pRF overlays: 'winner-takes-all' and 'centre of mass'. With the move to more stimulators and more complex models, visualization of overlays on a flattened cortex may prove to be difficult to interpret, and hence graphical summaries may be more suitable.

The pRF can be used on TW data, which only utilizes a single dimension in y (since we are only stimulating the fingertips), unlike previously described somatosensory pRF models, e.g. 9-parameter. The maps of r are comparable to TW coherence spatial maps. The preferred digit map also parallels the TW phase map, albeit slightly noisier. While the work here is pure somatosensory stimulation, recently, pRF mapping of the sensorimotor cortex during a flexion / extension task has been successfully performed, along with estimates of pRF size (Schellekens et al., 2017). This work found the largest pRF sizes in primary motor cortex (M1), and that the little finger (D5) produced the largest pRF sizes as compared with the other digits. However, generally, there is no clear trend across the digits (in postcentral gyrus) in pRF size.

Generally, it was found that only a small proportion of voxels fit the pRF model "well" ($r^2 > 0.5$). This small proportion of good fits is consistent across all datasets (Figure 5.42).

One can split the concatenated functional scan into paradigm specific scans and run the pRF individually. This produces better fits, which is to be expected since there is less noise and fewer anomalous timepoints that aggravate the fit. Additionally, one can also split up the data into functional scans, and run the pRF individually on each scan, to measure paradigm consistency: there is little to no difference in the pRF fitting.

The ultimate question framed by the use of the pRF is whether one can elucidate pRF size. Unfortunately, due to the poor fitting across a large area, any patterns of pRF size are limited.

Even though the data fits well for a small number of voxels, it may be that our model is not complex enough to capture the tunings of the remaining voxels. Currently, a linear model is assumed that consists of 16 weights (+ HRF parameters), corresponding to the number of stimulators on the hand. Constrained models such as a 2D gaussian shape have produced poorer fits, and have since been discarded. One proposed idea is to model non-linearities in the data, e.g. adding a static non-linearity into the model. This has been shown to improve pRF model fits in visual cortex (Kay et al., 2013a). More complex models such as those using a variance-like non-linearity, which was dubbed a 'second order contrast' model (Kay et al., 2013b), are aims in somatosensory cortex to which future work should investigate.

Additionally, it may be that altering or even simplifying the current experimental paradigm will provide more robust pRF maps, e.g. stimulation with many stimulators along a single digit. One possible explanation is that the stimulator perceptual intensity is higher for the index finger (D2), and lower for digits that fit poorly. One way to test whether this mechanism is at work is to measure the psychophysical thresholds of participants prior to a scan,

and possibly to alter the stimulus paradigm in light of the outcome.

The work performed in Chapter 4 could be used to inform the somatosensory pRF model. In the simplest case, one could acquire strongly elicited HRF data from somatosensory cortex within the same session as pRF data are collected. These would improve the statistical validity of the model. There are good model fits for the pRF performed on the TW data, and therefore within this paradigm is where this question should be addressed.

The ultimate goal is to standardize a paradigm and a model that successfully allows pRF size in somatosensory cortex to be mapped using high spatial resolution fMRI in individual participants.

The pRF method was performed using the multi-parameter (9 or 16 parameter depending on stimulator setup) and the 2D-Gaussian models. Each model used either the Nelder-Mead (unconstrained) or Levenberg-Marquardt (constrained) non-linear least squares optimization algorithm, to determine the fit parameters for the pRF method. It was found that regardless of Nova or surface coil, there was little difference between mean r^2 of algorithms or models. Circular variance between TW phase and pRF preferred digit was higher (and thus a worse comparison) for the Nelder-Mead algorithm, however, this difference was only slight and may be affected by overall data quality (and hence subject differences). Visually however, the multi-parameter models produce better-looking pRF overlays compared to the 2D-Gaussian models. It is suggested that for the somatosensory pRF models, an independent, weighted parametric model (e.g. 9 or 16 parameter model) using either optimization algorithm is acceptable.

5.12.0.2 Surface coil TW and pRF

In an attempt to increase robustness a surface coil was employed. Temporal SNR (tSNR) comparisons of Nova and surface coils (see Section 5.11.0.1),

revealed a drop in tSNR from Nova to surface, of approximately 2 times, at the same resolution (1.5 mm isotropic) over a somatosensory ROI.

The use of a surface coil potentially provides an increased SNR in a smaller field of view, and since the coil is placed very close to the region of interest, a high coil sensitivity can be achieved. In this work, functional data acquired from 2 16-channel surface coils, at 1 mm isotropic resolution has been assessed.

Measuring the computational properties of neurons using fMRI is dependent on the voxel size (the spatial resolution of the scanner), and the experimental paradigm chosen to elucidate neural activation. Population receptive field (pRF) mapping becomes more valid the more homogenous the neural population is in a voxel (Wandell et al., 2015). The gains in functional SNR can be traded for higher spatial resolution at high field strengths, and using a 32-channel head Nova coil, pRF data has been acquired here at 1.5 and 1.25 isotropic mm.

Coverage can be an issue, which is highly dependent on coil placement: currently, an EEG cap is used for reference and medical tape (Micropore surgical tape) for securing the coil to the head. In dataset D7 (table 13), coverage issue were noted, which detrimentally affected analysis since there were no data in regions of interest. For these reasons, any patient studies would likely not be performed using the surface coil (see Chapter 6 for the paradigms developed in patient populations).

Practically, it is suggested that the Nova coil is sufficient for pRF mapping using current coarse models, however, as more complex models and stimuli are developed, the spatial resolution afforded by the surface coil may benefit the method more.

5.13 Conclusion of Chapter

This work has described the development of a 9 and 16 stimulator setup for pRF mapping of the somatosensory cortex. Additionally, the pRF method was applied to a travelling wave (TW) paradigm, with comparable results. A key finding is that for some voxels, the current somatosensory pRF model fits very well, however, many voxels fit poorly; this can be seen most clearly when compared to the TW coherence maps.

Correlating the TW to the pRF overlays, there is good agreement (as measured by Pearson's R correlation) between the two techniques. A novel set of overlays have been developed (centre of mass/moment of inertia) for measuring different aspects of neural tunings in voxels that prefer certain spatial locations, as well as overlays for measuring pRF size.

Finally, the choice of optimization algorithm does not seem to have a large effect on pRF overlays, however, visually, the choice of a multi-parameter pRF model (such as the 9 or 16 parameter models used in this Chapter) is better than a Gaussian model. Further research into the haemodynamic responses of the pRF fit and pRF overlay generation, and hence using a more complex model, will provide greater insight into the best somatosensory pRF method.

CHAPTER 6

6 Behavioural and Clinical Studies

6.1 Overview of chapter

In this Section, background and motivations for measuring somatosensory maps in a Focal Hand Dystonia (FHD) patient population are detailed.

The development of quantitative sensory testing (QST) is described. This robust battery was set-up prior to implementation on patients and provides important complementary data to the fMRI measurements. Amplitude thresholding and temporal discrimination are performed using a 2-alternative forced choice paradigm. Additionally, a grating orientation task (GOT) was used to measure spatial discrimination; this was hypothesized to be altered in FHD patients.

Subjects then underwent fMRI, including a somatosensory travelling wave (TW) paradigm. In this chapter, a standardized battery of fMRI paradigms was set-up to measure different functional properties of somatosensory cortex in patients.

The underlying hypothesis of these experiments is that the somatosensory maps in patients will be different from those in healthy controls. In particular, previous fMRI literature has found reduced inter-digit distances, overlapping activity, and changes in BOLD activity compared to control subjects in FHD patients.

Five FHD patients were scanned with the fMRI battery, ≈4 weeks after a Botulinum-Toxin (Botox or BoNT) injection, along with 3 age and sex

matched healthy controls. The data presented in this chapter form the first subjects recruited as part of a larger dataset. Data collection of this is ongoing, with patients returning 3 months after Botox injection to undergo both fMRI and a parallel Magnetoencephalography (MEG) study.

Here, a standardized behavioural and fMRI battery was developed and initial data collected in controls and FHD patients. Approximately 4 weeks following a Botox injection there is a qualitative difference in behavioural measures between controls, but no striking differences between patients and controls' fMRI data. Digit cortical distance and digit overlap also showed little to no differences between groups.

This work was submitted as an abstract to ISMRM 2019, Montreal, entitled: *Assessing somatotopic and mototopic organization in Focal Hand Dystonia using high-resolution 7T fMRI.*

6.2 Background and Motivations

Focal Hand Dystonia is a sensorimotor disorder which manifests as involuntary movements, tremors and general weakness in the affected hand (The Dystonia Society, 2014). It has been shown that FHD patients exhibit abnormal somatosensory digit representations, including reduced interdigit distance, which has been characterized as a "blurred" somatotopic arrangement (Butterworth et al., 2003; Nelson et al., 2009).

Here, quantitative sensory testing (QST) will be performed in all patients scanned, as well as in healthy controls. These behavioural measures will be used to quantify the psychophysics of normal versus patient populations. The battery includes temporal discrimination, amplitude thresholding and spatial acuity.

In previous studies (see Section 5.3.2 in Appendix 8), functional MRI data acquired from healthy controls have been used to develop robust and reliable cortical mapping procedures. Here, these methods will be used to determine whether FHD patients display a departure from "normal" cortical hand maps. The travelling wave (TW) procedure is extremely robust, with correlation analysis producing excellent phase maps when fMRI responses are relatively weak in amplitude (Sanchez-Panchuelo et al., 2012a). For a detailed description of the methodology, see Appendix 8 and Chapter 5.

In addition to the TW digit maps, during this thesis I have also developed population receptive field mapping (pRF) in somatosensory cortex (see Chapter 5): a model-based method which allows flexible stimulation type to output parameter maps, such as preferred digit location and pRF size. Since the TW data are collected using a phase-encoding design, pRF mapping can also be performed on these data.

The aim of these tests was to develop a paradigm to ultimately assess whether differences exist between healthy controls and FHD patients and whether treatment affects the cortical representation of the digits, i.e. treatment with Botox injection for FHD patients (Cohen et al., 1989; Jankovic et al., 1990).

6.3 Focal Hand Dystonia

The cause of Focal Hand Dystonia (FHD) is clinically undetermined, however, risk factors include repetitive movements, such as those performed by writers and musicians. Generally, FHD is task-specific, i.e. it manifests during certain activities only.

The epidemiology of FHD is difficult to determine due to differences in

methodology: patient admissions are low since it is a non-fatal disease and only a portion of those living with the disease are treated (and hence recorded); additionally, diagnosis uncertainty is common and may lead to an underestimation of dystonia in the populace. A meta-analysis of 15 studies found an overall prevalence of primary dystonia of around 16 per 100,000 (Steeves et al., 2012) - FHD was included though this subgroup was not separated from other dystonias. Another meta-study assessed 20 studies that separated groups based on early or late-onset of the disease and found values ranging from 3-50 per million (early-onset) and 30-7320 per million (late-onset) of primary dystonia (Defazio, 2010). One study suggests that hand dystonia can be as high as 1 in 2500 (Torres-Russotto and Perlmutter, 2008).

Dystonia can be hereditary. A mutation in the DYT1 gene causes the production of a defective protein, *Torsin A*, which is related to the control of muscle movement and control, however, the penetrance of this mutation is low ($\approx$ 30-40%) (Fiorio et al., 2007). It is suggested in the literature that behavioural abnormalities can be considered an endophenotype, i.e. a biomarker of FHD. Generally, somatosensory temporal discrimination thresholds (TDT) are raised in both affected and unaffected hands, correlate with disease severity, as well raised spatial discrimination thresholds being raised (Defazio et al., 2007). Interestingly, abnormal TDTs were found in carriers of a dystonia gene without clinical manifestation, as compared to non-carrier relative and healthy controls (Bradley et al., 2009; Fiorio et al., 2007).

To treat FHD, Botulinum Toxin A (Botox, BoNT-A) is commonly used. Botox has a paralysing effect in humans; binding to pre-synaptic neurons and altering calcium ion influx, which in turn affects the release of acetylcholine into the synapse leading to a feeling of weakness. In dystonia, an injection of Botox induces relief of involuntary spasms (Cohen et al., 1989). In one study of the treatment's efficacy in FHD, average maximum improvement

lasted 7 weeks, with 77 % of 22 patients with FHD reporting a "definite improvement" (Jankovic et al., 1990). Another study followed up 20 FHD patients who received Botox treatment over the course of 10 years (Lungu et al., 2011): they found that musicians were more likely to wait longer between injection intervals, that women experienced a larger benefit, and that the dose increased over time. They concluded that the treatment is safe and at least mildly effective. In a meta-study looking at the long-term efficacy of Botox, it was reported that 50 % of FHD patients report mild benefit compared to 80 % for cervical and 90 % for blepharospasm, indicating a lower response rate in hand dystonia (Ramirez-Castaneda and Jankovic, 2013).

More recently, fMRI has been used to investigate the cortical dynamics of dystonia, specifically FHD. Although the disease manifests physiologically as a motor disorder, there are significant differences and alterations which occur in the somatosensory cortex. Patients with focal hand dystonia were scanned using fMRI at 3 T, during vibrotactile stimulation of the digits. Results showed a reduced inter-digit distance, reversal of the ordering of D2 and D5, and under-activation in secondary somatosensory cortex (Butterworth et al., 2003).

Other studies have confirmed such changes in somatosensory cortex in subjects with writer's cramp, who additionally exhibited overlapping activity (Nelson et al., 2009). These authors also found specific compression effects, with D1 (thumb) shifting into the space normally occupied by D2, and D4/5 were also shifted towards D1. More recently, impairments in functional connectivity (FC) between sensorimotor cortices, that correlated with disease severity, measured using resting-state fMRI, were found in subjects with writer's cramp. The authors suggested a pathogenetic role of the cerebellum (Dresel et al., 2014).

Taken together, this suggests the hypothesis that there are neuro-plastic

changes that can be measured in the pre- and post-treatment phases of FHD with fMRI.

6.4 Behavioural measures

6.4.1 Literature review

In FHD, many studies have investigated changes in temporal discrimination and spatial acuity and these are summarised below.

Somatosensory temporal discrimination (TDT) involves presenting very short stimuli to digit 2 (D2) and then digit 3(D3) (or vice versa) consecutively and requires the subject to identify on which digit they feel the stimuli first. Literature values indicate that the TDT is elevated in FHD, suggesting an enlargement in receptive field size and/or possibly overlap.

The grating orientation task (GOT) is used to measure spatial acuity, by presenting horizontal or vertical square-wave gratings cut into plastic domes on the digits (see Section 6.4.2 and Figure 6.3). For the GOT, thresholds for healthy controls tend to lie in the range 0.96 - 1.25 mm for D2 (Craig and Lyle, 2001; Grant et al., 2006; Sathian and Zangaladze, 1996). It can be shown from Table 15 that GOT thresholds for patients can be 1 mm (or more) larger than for controls, depending on the study.

There is some literature identifying improvements in FHD patients following physiotherapy, e.g. hand exercises or writing tasks (Bleton, 2010). Additionally, another study found an improvement (based on a neurological dystonia severity scale - Fahn scale) in the GOT following a braille training task undergone for 8 weeks (Zeuner et al., 2002).

Of interest to this study, is whether or not there are changes associated with

FHD behavioural measures			
Task	Patients (SD)	Controls (SD)	n (patients/ controls)
GOT (Zeuner et al., 2002)	2.38 mm (+/- 1.09)	1.95 (+/- 1.01)	10/10
GOT (Molloy et al., 2003)	2.61 mm (0.38)	1.46 (0.40)	15/11
GOT (Sanger et al., 2001)	2.48 mm (0.72)	1.49 (0.61)	9/10
TDT (Bara-Jimenez, 2000)	96.7 ms (43.6)	64.4 (15.5)	14/13
TDT (Sanger et al., 2001)	107 ms (41)	46 (49)	9/10

Table 15: Data are pooled from multiple papers (cited within), indicating the values for controls and patients performing a grating orientation task (GOT), using the standard set of 8 domes on the index finger; and for the TDT task. In all cases, patients were not given Botox treatment for at least 3 months prior.

behavioural measures following treatment of Botox injections for FHD, in addition to neural changes measured by fMRI or MEG as detailed in Section 6.2.

6.4.2 Methods: Optimising behavioural measures

Before performing patient studies, it was important to first set up a robust battery of measurements in healthy subjects. This was chosen to be performed on the digits to assess i) *amplitude threshold*, ii) *temporal discrimination threshold* and iii) *spatial acuity*. The psychophysics theory behind these measures is explained in more detail in the Appendix. Additionally, a handedness questionnaire was collected on patients and healthy controls (details in Appendix 8).

i) For the *amplitude threshold task*, custom-built piezo-electric (plectrum) stimulators placed in a plexiglass "hand-holder" were used. These are very adaptable and keep the stimulators in a position such that the fingertip of each digit can comfortably lie on the tip of the plectrum (Figure 6.1).

A 1up-2down forced-choice staircase paradigm was performed. For every 1

incorrect response, the amplitude was increased by 3 units (the stepsize), and for every 2 correct responses, the amplitude was dropped by 3 units. The Levitt rule was applied (Levitt, 1970), in which the stepsize is halved after the 1st, 3rd, 7th and 15th reversal (the experiment stopped after 8 reversals). On each trial, 2 stimuli were presented separated by a fixed temporal gap, with one having a larger amplitude than the other - this was altered on the staircase to identify the amplitude threshold at 75% accuracy. For the controls and patients, amplitude thresholding was performed in D2 at 31 and 200 Hz, in both hands.

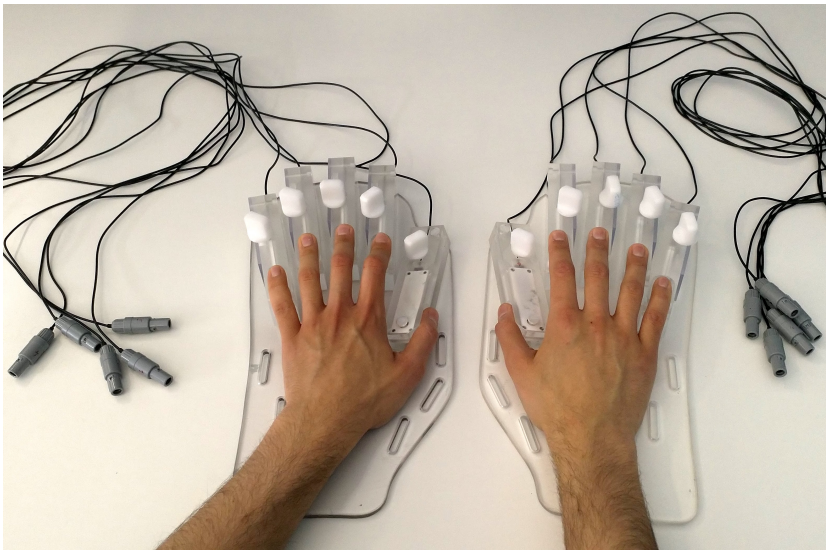


Figure 6.1: MR-compatible plexiglass "hands" used for behavioural testing and the travelling wave fMRI paradigm. Each of the 10 holders, upon which the author's digits are placed, contains an independently controlled piezo-electric stimulator (see Chapter 5 for a closer look). Each piezo-electric holder can be adjusted to accommodate the majority of hand sizes and shapes. The non-restrictive design allows for fast set-up and tear-down, easing volunteer and patient burden.

ii) The *temporal discrimination threshold (TDT) task* was measured using a 2up-1down forced choice staircase (Levitt rule). Since the TDT takes longer, requiring only a single correct response to drop the temporal gap was found to be the optimum way of carrying out the experiment. In each trial, 2 stimuli were presented to D2 and D3 of the dominant hand (affected

hand in patients), separated temporally by a gap - this was altered on the staircase to identify the threshold where the observer could distinguish two stimuli 75% of the time.

In addition to using the piezo-electric stimulators, a Brain Gauge was used (Tommerdahl, 2017). This is a pneumatic mouse-like device which can be used to deliver a battery of psychometric tests (Figure 6.2). For our purposes, only the TDT option was used (known as "temporal order judgement (TOJ)" in the cortical metrics app). Both piezo-electric and Brain Gauge TDT tasks were performed in both hands.



Figure 6.2: The Brain Gauge. This is a device used to perform a variety of behavioural tests such as reaction time, temporal discrimination, etc. (Tommerdahl, 2017). Here, we used the temporal discrimination program as a comparison for the TDT performed with the piezo stimulators. Note that this device, unlike the piezos, is not MR-compatible. This device has only 2 pneumatic actuators (small black dots), used exclusively for D2 and D3.

iii) The *grating orientation task (GOT)* used for assessment of spatial acuity was adopted from the large literature in this area (Craig, 1999; Craig and Lyle, 2001; Grant et al., 2006; Johnson and Phillips, 1981; Sathian and Zangaladze, 1996). This experiment comprises presenting square-wave gratings

in either a proximal or lateral orientation. In a 2-alternative forced-choice (2AFC) paradigm, the observer must state which orientation they feel. Here, we used a method of constant stimuli (MOCS) procedure to determine the spatial acuity threshold. For a set of 8 gap widths (mm), 20 trials were performed on each width, counterbalancing the presentation order, and having a 50:50 proportion of both orientations per width. Due to time constraints, only the spatial acuity of the index finger (D2) in the dominant (Healthy Controls, HC), or affected hand (Patients, PA) was measured. The threshold was determined by fitting a psychometric curve to the data, and finding the width at 75% correct responses.



Figure 6.3: Spatial Domes for Grating Orientation Task (GOT). These are the custom-milled set of 13 domes, ranging from 0.35 mm (second from the bottom left) to 6 mm (top right), which were used in healthy controls and patients.

The GOT is preferred to alternative procedures, such as the two-point discrimination (2PD) wheel. There is controversy in the literature suggesting that the 2PD task is susceptible to severe biases, e.g. intensity cues may

cause one point to always be discriminated from two points, due to it feeling "sharper" (Craig and Johnson, 2000).

Following pilot studies (Section 6.4.3) in healthy controls, it was found that the standard set of 8 dome widths was unsatisfactory to accurately measure the spatial acuity threshold. This was based on participant feedback - there were too many gap widths that were too small, so subjects were responding at chance levels for many of the domes. Thus the two smallest widths were removed (0.35 and 0.5 mm) and two wider widths inserted (1.75 and 2.5 mm) to provide more data points in the region of the ogive curve where subjects are responding above chance and thus provide more accurate thresholds.

Additionally, it was hypothesized that in patients, the spatial thresholds would be higher than in healthy controls, and hence larger widths were included (4, 5 and 6 mm). In a set of pilot experiments in patients an optimum set of 8 widths were found.

A standard operating procedure (SOP) for the complete behavioural paradigm was created and this can be found in the Appendix 8.6.0.1.

6.4.3 Results: Optimising behavioural measures

Here, the pilot behavioural data and fMRI data (A) collected prior to running the standardized battery in patients (PA) and healthy controls (HC) is outlined.

6.4.3.1 QST: Amplitude and TDT thresholds

Nine control subjects underwent the amplitude threshold task and temporal discrimination threshold (TDT) task. Amplitude thresholds are shown at 31 Hz and 200 Hz in Figure 6.4 for the piezo-electric stimulator. Figure

6.5 shows the comparison between for the TDT task for piezo-electric and Brain Gauge stimulators, while Figure 6.6 shows the associated correlation. Means and standard deviations are shown in Table 16. Significance tests for hand dominance, as well as stimulator difference, showed no effect of hand for the TDT. For the amplitude thresholds, there was no significant effect of hand dominance, or frequency dominance (Table 17).

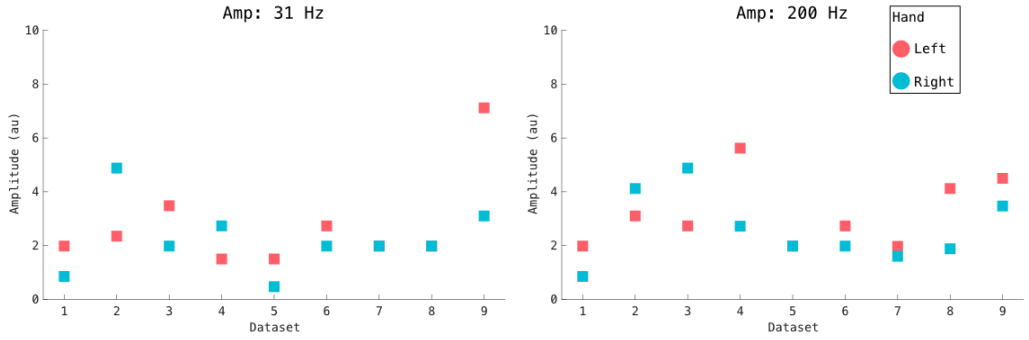


Figure 6.4: Amplitude (AMP) measurements using the piezo-electric stimulators, across 9 healthy controls.

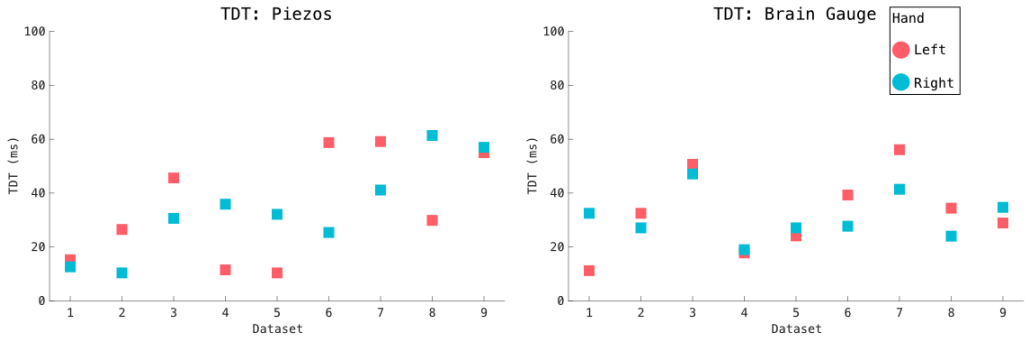


Figure 6.5: TDT measurements using the piezo-electric stimulators and Brain Gauge, across 9 healthy controls.

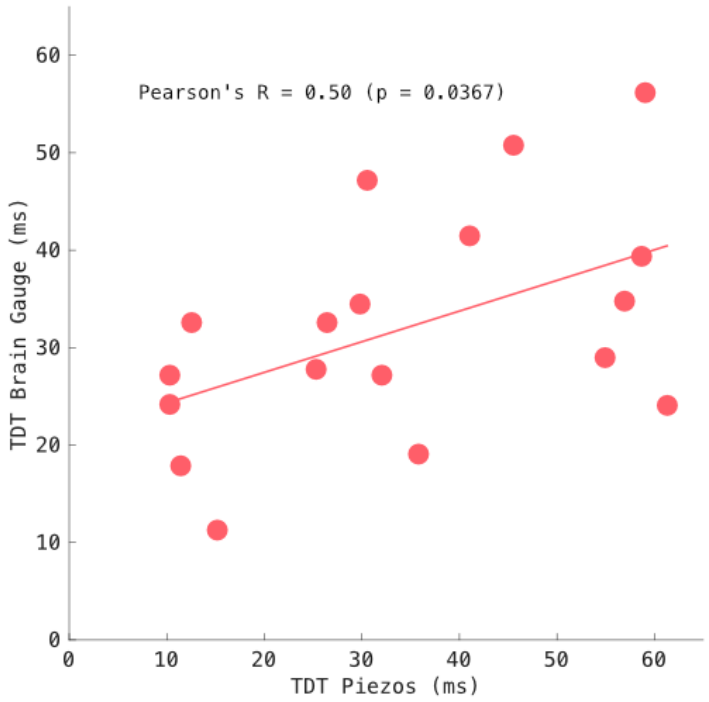


Figure 6.6: TDT was correlated between the piezo-electric stimulators and the Brain Gauge, for the 9 subjects shown in Figure 6.5 and combined data from both hands. Despite a qualitative difference in stimulus, there was still a significant correlation between TDT.

Task	Mean (SD)
Amp 31 Hz (au)	2.48 (1.52)
Amp 200 Hz (au)	2.90 (1.29)
TDT Brain Gauge (ms)	31.98 (11.68)
TDT piezos (ms)	34.36 (18.38)

Table 16: Mean and standard deviation for the amplitude threshold task and TDT task in pilot healthy controls (n = 9).

6.4.3.2 QST: Grating Orientation Task (GOT)

To determine the optimum set of gap widths for the GOT, two paradigms were tested in eight healthy control subjects. The literature standard set of

8 widths (Craig, 1999) were used [0.35 0.5 0.75 1 1.2 1.5 2 3], and then an altered set of 8 widths were used [0.75 1 1.2 1.5 1.75 2 2.5 3]; the latter of which removed the two smallest gap widths and added more intermediary widths based on subject feedback.

Figure 6.7 shows the spatial acuity measured in the dominant hands from using the altered set of 8 widths across a pilot set of 8 subjects, with a mean (SD) spatial acuity of 1.51 mm (0.31). This was in agreement with literature (Table 15).

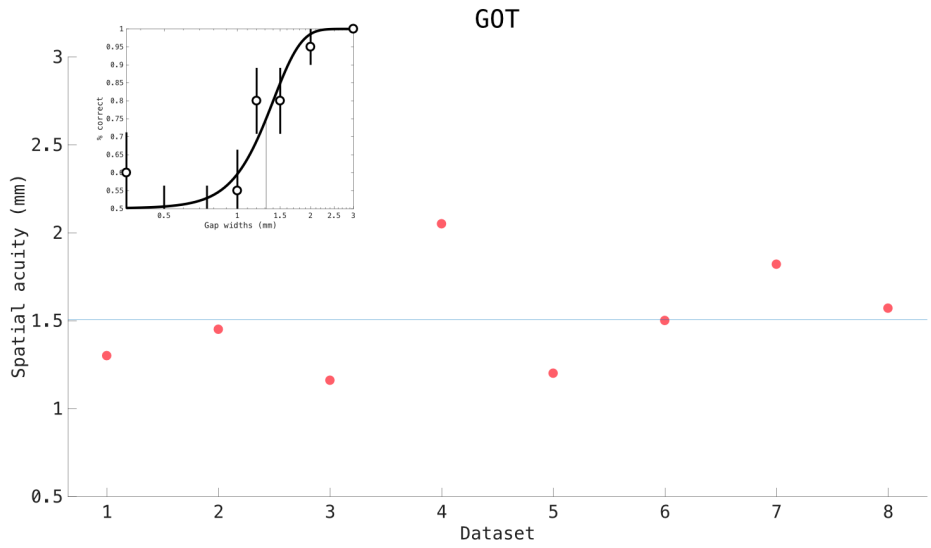


Figure 6.7: Results of the GOT performed in 8 healthy controls, on D2 of the dominant hand, using the altered set of widths. An example GOT plot is shown. Blue line indicates mean spatial acuity of 1.5 mm (0.3 SD).

6.4.3.3 QST: Significance testing

In healthy controls, t-tests were performed on the amplitude, TDT and the GOT data to determine whether there were any effects of hand dominance, modality effects and frequency dominance. In all cases, there was no significant ($p < 0.05$) effect - contrasts are summarised in Table 17. Since the

GOT is only performed in the dominant or affected hand in the main study due to time constraints, it was important to determine that there was little difference between GOT performance between hands in the healthy control subjects.

Significance testing		
Paradigm	Contrast	p-value
TDT (piezos)	Hand dominance	0.519
TDT (brain gauge)	Hand dominance	0.766
TDT	Piezos vs. brain gauge	0.382
Amplitude disc.	D2 31 Hz hand dominance	0.873
Amplitude disc.	D5 31 Hz hand dominance	0.078
Amplitude disc.	D2 200 Hz hand dominance	0.658
Amplitude disc.	D5 200 Hz hand dominance	0.052
Amplitude disc.	D2 (rh) freq dominance	0.375
Amplitude disc.	D5 (rh) freq dominance	0.627
Amplitude disc.	D2 (lh) freq dominance	0.320
Amplitude disc.	D5 (lh) freq dominance	0.451
Spatial acuity	Hand dominance	0.409

Table 17: T-tests performed across participants, testing for hand dominance, frequency dominance or modality dominance. In each case, there was no significant ($p < 0.05$) difference between conditions.

6.4.3.4 QST: Pilot patient GOT

In pilot patient studies (n=3), it was found that 4, 5, and 6 mm were correctly discriminated in the GOT 100 % of the time. In these patients, a longer GOT was performed that involved using all 11 domes available to determine patient response to each width uniquely (see Figure 6.8). The final set of widths to use for the healthy controls and patients are shown in Table 18.

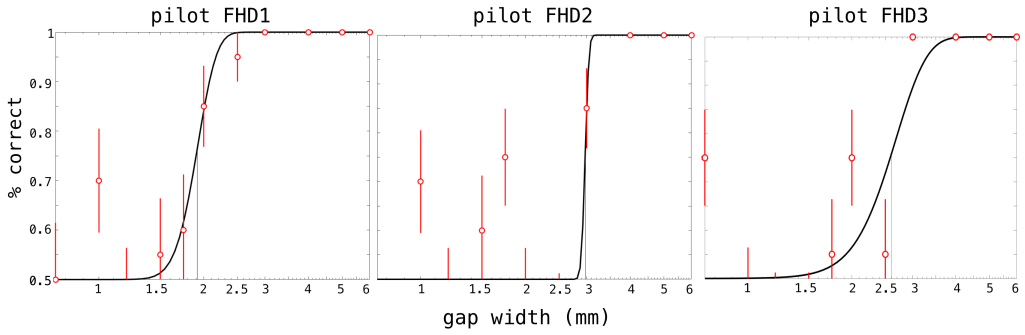


Figure 6.8: All 11 available dome widths were used in a single GOT session on pilot patients (n=3) to determine the ideal set of 8 widths for use in patients. It was hypothesized that larger widths would be necessary in patients compared to healthy controls to reliably ascertain patient spatial acuity. From left to right, thresholds are indicated by the vertical dashed line: 1.92, 2.97, 2.6 mm for these FHD patients. These are all larger than any healthy control in Figure 6.7, and in line with literature Table 15.

GOT width sets	
Group	Widths
HC	[0.75 1.0 1.2 1.5 1.75 2.0 2.5 3.0]
PA	[0.75 1.0 1.5 1.75 2.0 2.5 3.0 4.0]

Table 18: Following pilot studies in HC (n=8) and PA (n=3), two different gap width sets were chosen to be used in the GOT. The PA task substitutes the 1.2 mm width for the 4 mm width, since it was more likely for patients to achieve 100 % correct at 4 mm.

6.4.4 Results: Behavioural measures in patients

In this Section, results are presented of the behavioural and fMRI data collected from 5 post-Botox patients and 12 healthy controls (9 from the pilot behavioural section described above + 3 healthy controls pooled together), using the same hardware and experimental set-up as described in Section 6.5. Post-Botox is defined as 4 weeks following injection.

Figures 6.9, 6.10 and 6.11 show the behavioural results of the amplitude thresholds, TDT and spatial acuity respectively, for the patient group (n = 5). It can be seen that the patient data has a larger group mean and standard deviation than for healthy controls (Table 19) and that the TDT in the patient group is much larger for the piezos than the Brain Gauge.

Patient QST		
Task	Group	Mean (SD)
Amp 31 Hz (au)	HC	2.79 (1.89)
	PA	3.96 (2.44)
Amp 200 Hz (au)	HC	3.06 (1.62)
	PA	4.33 (2.88)
TDT piezos (ms)	HC	37.18 (22.04)
	PA	87.91 (45.59)
TDT Brain Gauge (ms)	HC	31.36 (13.18)
	PA	46 (26.62)
GOT (mm)	HC	1.55 (0.34)
	PA	2.8 (1.37)

Table 19: Mean and standard deviation for the amplitude threshold, TDT task and GOT, in healthy controls (n = 12) and FHD patients (n = 5). One additional patient was included for the GOT (n = 6), however this patient's fMRI data were unuseable due to excessive head motion.

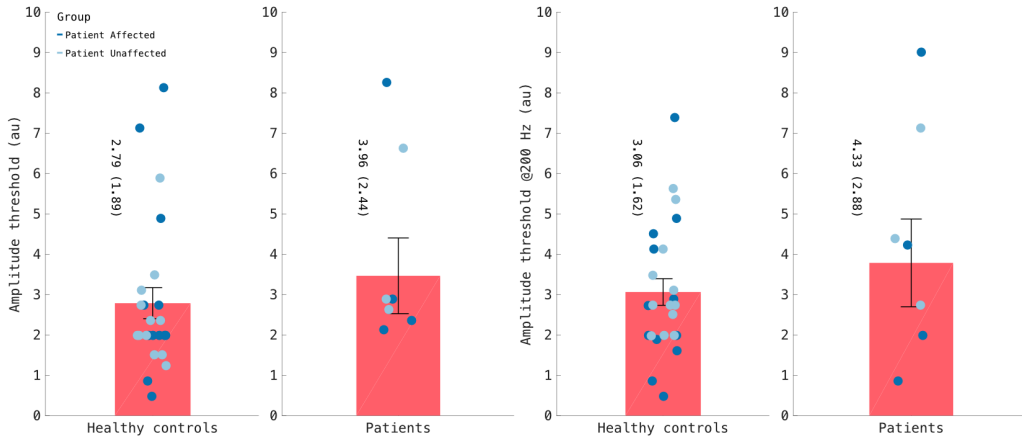


Figure 6.9: Patient amplitude threshold data (blue dots) compared to all healthy controls (including pilot data) with mean (SD) shown.

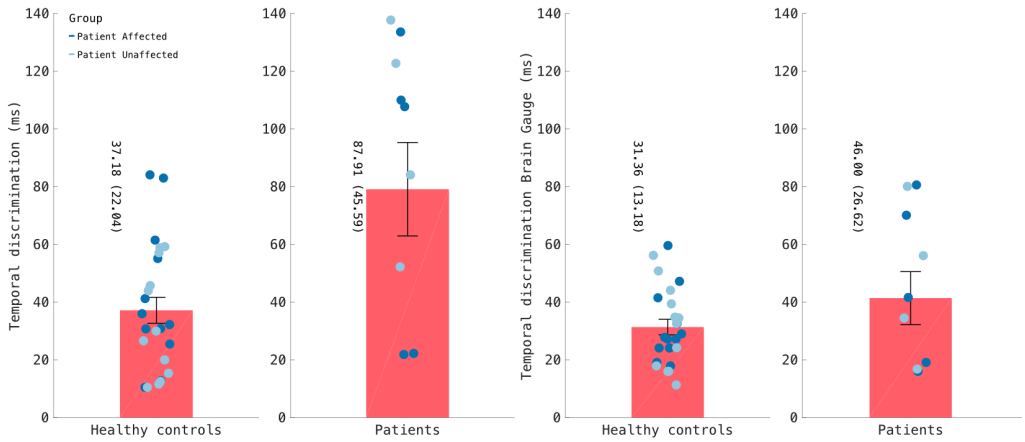


Figure 6.10: Patient temporal discrimination data (blue dots) compared to all healthy controls (including pilot data) with mean (SD) shown. Note the larger TDT recorded using the piezos than for the Brain Gauge.

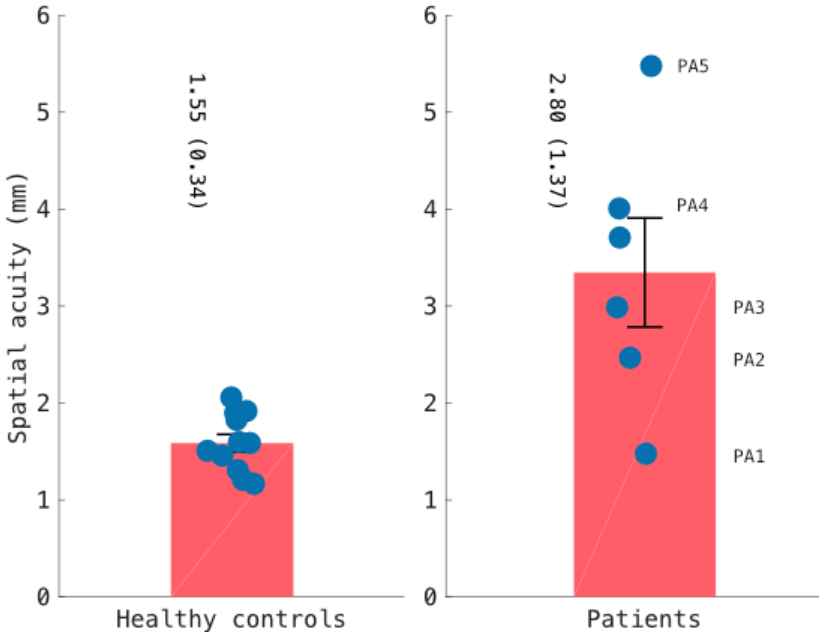


Figure 6.11: Patient spatial acuity data compared to all healthy controls (including pilot data), with mean (SD) shown. One additional patient was included for the GOT (n = 6), however this patient's fMRI data were unusable due to excessive head motion.

6.5 Methods: Optimising fMRI data acquisition and paradigms

All data were acquired on a 7 T Philips Achieva scanner, using a 32-channel Nova head coil (Nova Medical). The protocol is described in Table 20. Prior to collecting data in healthy controls and FHD patients, the development of a standardized fMRI protocol was necessary. Seven datasets (Table 21) were acquired during the development of the fMRI battery (datasets A). Four of these datasets included the finalised procedure and are denoted as the "dry run" datasets. RETROICOR (details in Section 6.5.1.1) was performed on all the data, correcting for respiratory and cardiac physiological noise, followed by motion compensation.

fMRI battery		
Order	Scan	Repeats
(i)	Resting state	1
(ii)	Travelling wave	4
(iii)	ON-OFF	2
(iv)	High-resolution T_2^*	1
(v)	MPRAGE	1
	* *Volunteer comes out* *	
(vi)	Motortopy	2

Table 20: Following a (i) resting state scan, (ii) forward and reverse TW scans were performed on both hands. An (iii) event-related ON-OFF scan was then performed on the dominant (control) or affected (patient). (iv, v) Structural scans were performed for anatomical registering and Freesurfer segmentations. Finally, the volunteer came out of the scanner to attach an accelerometer glove and a (vi) motortopy scan was performed on the dominant (control) or affected (patient) hand.

The fMRI and behavioural battery was subsequently performed on 5 FHD patients (PA), 4 weeks post-Botox and 3 healthy controls (HC) (datasets B).

Pilot fMRI datasets: A	
Dataset	Paradigm
A1	Multiband testing
A2	ON-OFF testing
A3	Motor / accelerometer testing
A4	Dry run 1
A5	Dry run 2
A6	Healthy control 1
A7	Healthy control 1 repeat

Table 21: Datasets acquired for pilot testing in healthy controls prior to patient studies.

(i) Resting state data

First, a resting-state fMRI scan (rs-fMRI) was performed. Rs-fMRI provides a measure of functional connectivity in somatosensory regions. Analysis of the resting state data is beyond the scope of this thesis but were collected for the larger project.

rs-fMRI parameters: MB4, TR 1500 ms, TE 25 ms, Matrix size: 128x128x72 slices (18 * 4), 200 dynamics, $(1.5\ \text{mm})^3$ isotropic voxels.

(ii) Travelling Wave

Digit somatotopy was performed on the traveling wave (TW) data. This is a robust method, eliciting digit maps with good reliability. This is a key measure, whereby we hypothesize to find distorted or shifted phase maps in FHD patients. The TW was performed on all digits on both hands, for both forwards and reverse directions (four scans overall). TW forward and reverse data were averaged, and the coherence, phase and amplitude were calculated using Fourier analysis, as described previously (Besle et al., 2013) and outlined in Appendix 8.

TW and motor fMRI scan parameters: MB3, TR 2000 ms, TE 25 ms, Matrix size: 128x128x48 slices (16 * 3), 80 dynamics, $(1.5\ \text{mm})^3$ isotropic voxels, SENSE 1.5, Halfscan 0.7, Flip angle 80 °.

(iii) ON-OFF

The final fMRI paradigm was an event-related "ON-OFF" paradigm. This was devised to measure digit overlap across digits D2, D3 and D4. Additionally, this paradigm could be used to derive HRFs for use in a somatosensory HRF-informed pRF model (see Chapter 4 for more detailed reasoning behind this). Several pilot studies were performed (data not shown) to determine the ideal combination of stimulus repeats, length of stimulus on-times and fMRI acquisition parameters. This was performed in the dominant or affected hand only. Two scans were acquired using different (randomised) stimulus sequences.

ON-OFF fMRI scan parameters: MB3, TR 1000 ms, TE 25 ms, Matrix size: 128x128x36 slices (12 * 3), 285 dynamics, $(1.5\ \text{mm})^3$ isotropic voxels, SENSE 1.5, Halfscan 0.7, Flip angle 57 °.

(iv and v) Structurals

High resolution T1-weighted structural scans were acquired using a Magnetization Prepared Rapid Gradient-Echo (MPRAGE). Functional data were aligned to a high-resolution T_2^* scan acquired during the same session. Freesurfer was run on every subject's MPRAGE structural image, providing surfaces and flat maps for further analysis.

MPRAGE scan parameters: 1 mm isotropic, TR 7.3 ms, TE 3.4 ms, Matrix size: 256x256x180.

(vi) Motortopy

A motor-version of the somatosensory TW was designed to elicit responses in the motor cortex. During piloting, two versions of the motor paradigm were assessed: a) a visually-cued, slow flexion/extension of the digits in sequence, and b) a cued fast tapping paradigm (both in the air). The visual cue comprised a set of 5 white disks blinking (1 per second, 4 repeats for each disk), for which the participant had to either tap in time to the blink, or perform a slow extension and flexion that followed a slower disk blink (2 seconds fade out, 2 seconds fade in, 1 repeat for each disk) (Figure 6.12).

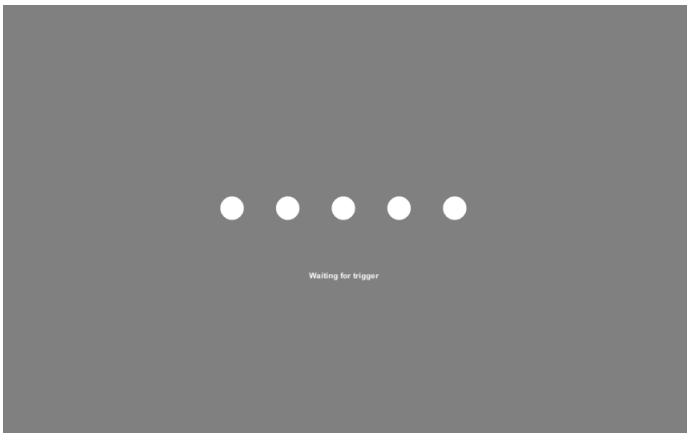


Figure 6.12: Each white disk blinks at 1 Hz for 4 s x 5 digits = 20s per cycle. The participant taps each digit in the air in time with the blinking.

Given that both paradigms were performed in both forwards and backward ordering, in an iterative sequence, i.e. D1, then D2 etc., the data could be analysed using Fourier analysis. It was decided that the faster tapping was easier to perform (reducing patient burden) and indeed provided stronger coherence maps following TW analysis. This was used in the study, with forward and reverse directions collected on the dominant (healthy controls) or affected hand (patients).

To enable assessment of the exact timing of movements for the motortopy experiment, a novel, custom-built accelerometer glove (Figure 6.13) was developed (Paul Glover). For a single hand (dominant or affected) an accelerometer was placed on each finger tip location of the glove using velcro.

These devices detect changes in acceleration in 3 axes allowing the tracking of digit movement during the motor tapping task. The accelerometer data were collected as a measure of quality control, to confirm that the participants were correctly performing the task inside the scanner. An example accelerometer trace is shown later in Figure 6.23.



Figure 6.13: Custom built, MR-compatible glove used to measure acceleration (and hence indirectly movement) of the digits during the motortopy fMRI experiment.

6.5.1 Pre-processing and Analysis

Physiological data (PPU and respiratory trace) were collected from every participant during the fMRI protocol. Associated physiological noise was removed from the data using RETROICOR (described below), the Travelling Wave and ON-OFF outputs analysed as described below. The aim was to produce a between-digit distance metric for the TW and a degree of digit overlap metric for the ON-OFF scans. The fMRI analysis pipeline is summarised in Figure 6.15.

6.5.1.1 Physiological noise correction

Data in previous chapters were acquired on a set of experienced MRI volunteers. In this section, external healthy controls and patients were recruited with little MRI experience, therefore, the probability of lower quality data due to motion, for example, increased. In addition to motion correction, physiological noise correction was performed to further improve SNR.

The BOLD signal, as measured by fMRI, can be modulated by physiological motion such as respiratory changes (breathing) and cardiac motion (blood flow). Both respiration and cardiac function can be measured using a pneumatic belt, and a peripheral pulse unit. These sources of noise can be considerable and hence degrade statistical significance. The spatial extent of physiological noise in the brain has been investigated, identifying global respiration effects (Noll and Schneider, 1994) and localised cardiac signal changes (near major blood vessels and CSF pools) (Dagli et al., 1999).

While noise in MRI is typically separated into random thermal noise σ_t and physiological noise σ_p, one can expand the physiological noise term further into 1) fluctuations in T_2^*, operating through the same mechanism as the BOLD signal (BOLD-like, σ_B), and 2) fluctuations due to cardiac and respiratory effects (non-BOLD-like, σ_{NB}): this implies that overall physiological noise is signal-dependent, and hence there exists a maximum SNR achievable, which also depends on field strength (Krüger and Glover, 2001).

$$\sigma = \sqrt{\sigma_t^2 + \sigma_p^2} \tag{6.1}$$

$$\sigma = \sqrt{\sigma_t^2 + \sigma_B^2 + \sigma_{NB}^2} \tag{6.2}$$

Figure 6.14 plots physiological noise and plot the ratio of physiological noise to thermal noise, versus voxel volume, at different values of B_0.

Physiological noise can be corrected by fitting a low-order Fourier to the data

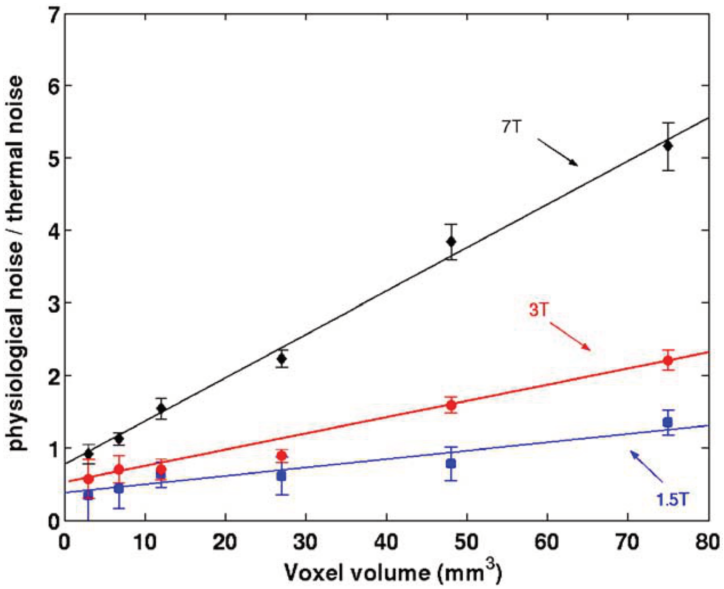


Figure 6.14: The ratio of physiological noise to thermal noise as a function of voxel volume. It can be seen that noise increases with field strength. Reproduced from Triantafyllou et al. (Triantafyllou et al., 2005).

based on the respiratory or cardiac phase from their respective cycles, during acquisition. An image-based method known as RETROICOR (Glover et al., 2000) was used in this work. The benefit of an image-based method compared to k-space method is that the spatial frequencies over which k-space method can operate is limited by SNR (the centre of k-space will have the highest SNR), whereas each pixel is treated differently in image-based methods, thus eliminating spatial frequency filtering and allowing local and global noise effects to be corrected for.

6.5.1.2 TW data analysis

For each digit, the phase map (between 0 and 2π) was divided into 5 equal bins, following thresholding at a coherence of 0.3. For the TW scans, there were 80 timepoints (dynamics) collected, and at a coherence of 0.3, this equates to a p-value of 0.0034 to generate a restricted ROI. The centre of

mass was calculated within this restricted digit ROI. This led to a set of 5 centre of masses on the phase map; upon which the point-to-point Dijkstra's and 3D Euclidean distances was measured. Therefore, from the TW phase maps, the total distance (D1 to D5) on the cortical surface between the centre of masses of each digit was measured. This was performed on data acquired from both hands. A description of Dijkstra's algorithm is described in the Appendix 8.3.

6.5.1.3 ON-OFF paradigm data analysis

Data acquired from the ON-OFF scans were first concatenated and then analysed in a General Linear Model framework: for every voxel, the fMRI timeseries were scaled and averaged to determine the voxel-wise HRF shape, given the event ON timings. This was fitted (non-linearly) using a double gamma function. Two sets of ROIs for D2, D3 and D4 were defined: 1) from the coherence maps, thresholded at 0.3, and 2) from the GLM, thresholded at a subject-specific Z-score. For all ROIs, the timeseries for every voxel in that ROI was extracted.

For the TW-defined ROIs, a HRF was calculated from this timeseries, e.g. the timeseries corresponding to a TW-defined D2, but overlayed on the GLM data. This is analogous to the method described in Chapter 4 that inputs measured HRFs into a pRF model.

6.6 Results: Optimising fMRI data acquisition and paradigms

Here, fMRI data acquired from pilot healthy controls are presented. The battery performed is analogous to that being performed in patient stud-

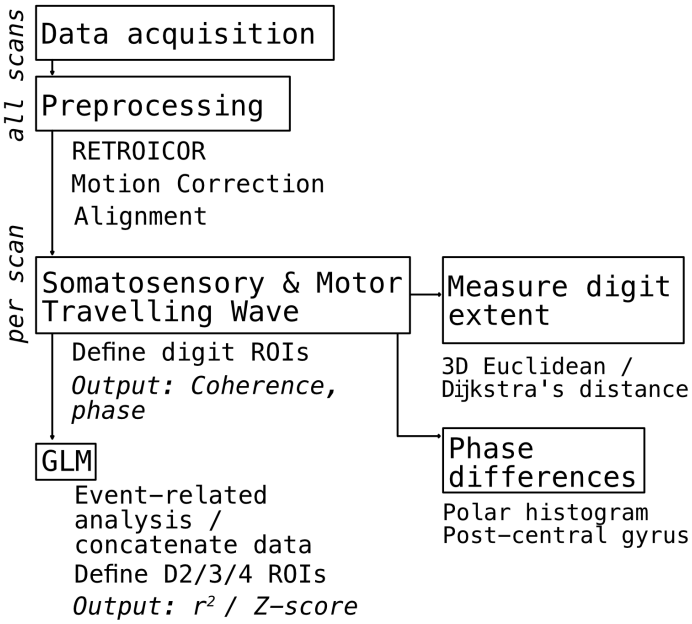


Figure 6.15: Processing pipeline of the travelling wave and GLM data. Following pre-processing, the ON-OFF fMRI scans were analysed in a GLM to derive specific regions of activitation corresponding to different digits. The TW data were analysed and these defined the digit ROIs, as well as provide maps of coherence and digit phase correspondence.

ies. During development, the multiband acquisition was first optimized for the differing scans, and the optimum ON-OFF time for the event-related paradigm was chosen.

6.6.0.1 fMRI: Multiband optimization

Prior to data collection it was necessary to optimise the through-plane and in-plane acceleration for fMRI parameters at 1.5 mm isotropic resolution. A multiband factor was assessed that provides a compromise between 1) maximum coverage over the sensorimotor cortex; 2) suitable TR to sample the HRF (for the ON-OFF scans) and 3) overall scan time for the subject.

Multiband images can suffer from signal leakage between slices and this is re-

duced by using a larger stack (Cauley et al., 2014) and thus band separation, and can be compromised when using SENSE acceleration both through-plane and in-plane (total acceleration factor = SENSE x MB). It was found that for a 48 slice stack, at TR 2 s, MB3 had less significant leakage than MB2, as is evident in Figures 6.16 and 6.17. For TR 1 s, 36 slices at MB3 proved to be a better compromise between coverage and acquisition speed than 24 slices at the same multiband factor.

6.6.0.2 fMRI: Somatosensory TW and ON-OFF piloting

Figure 6.18 shows travelling wave (TW) maps in both hemispheres in reponse to the somatosensory TW. The strong coherence values and well organized phase maps are evident of a robust paradigm.

Prior to the dry runs, a number of pilot scan sessions were run to determine the best timings and fMRI parameters for the ON-OFF paradigm. One can see strong BOLD activation in response to 5 s somatosensory stimulation, visible in the timecourses shown in Figure 6.19, with the mean HRF shown for each digit in Figure 6.20. This same scan was tested using 8 s of stimulation, using different multiband factors - the optimum length was chosen to be 5 s ON 24 s OFF. This was a trade-off between elucidating a strong HRF, overall scan time and optimal deconvolution for the pRF (see Chapter 4).

Figure 6.21 shows Z-score maps overlaid on a subject-specific flattened patch of cortex, following GLM analysis, which serves to derive beta weights for regressors of interest. It can be seen from the Z-score maps, as one proceeds from left to right, that the digit peak location moves in an inferior-superior direction, consistent with the representation of D2, D3 and D4 in somatosensory cortex.

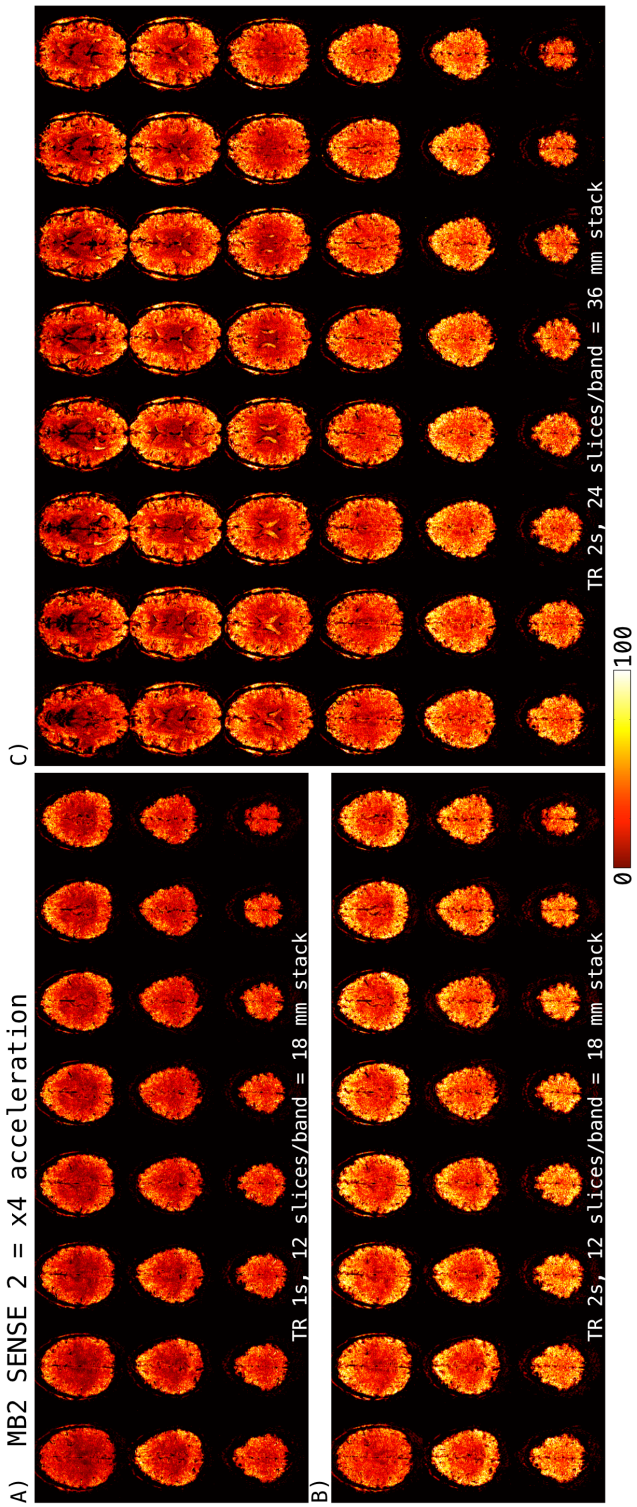


Figure 6.16: Multiband 2, SENSE 2 (x4 acceleration) tSNR images. A) Reducing to TR 1s (ON-OFF paradigm) limits the stack to 12 slices/band and results in significant leakage, which is apparent in B) TR 2s 12 slices/band. C) TR 2s data collected with 24 slices/band equivalent to a band separation of 36mm.

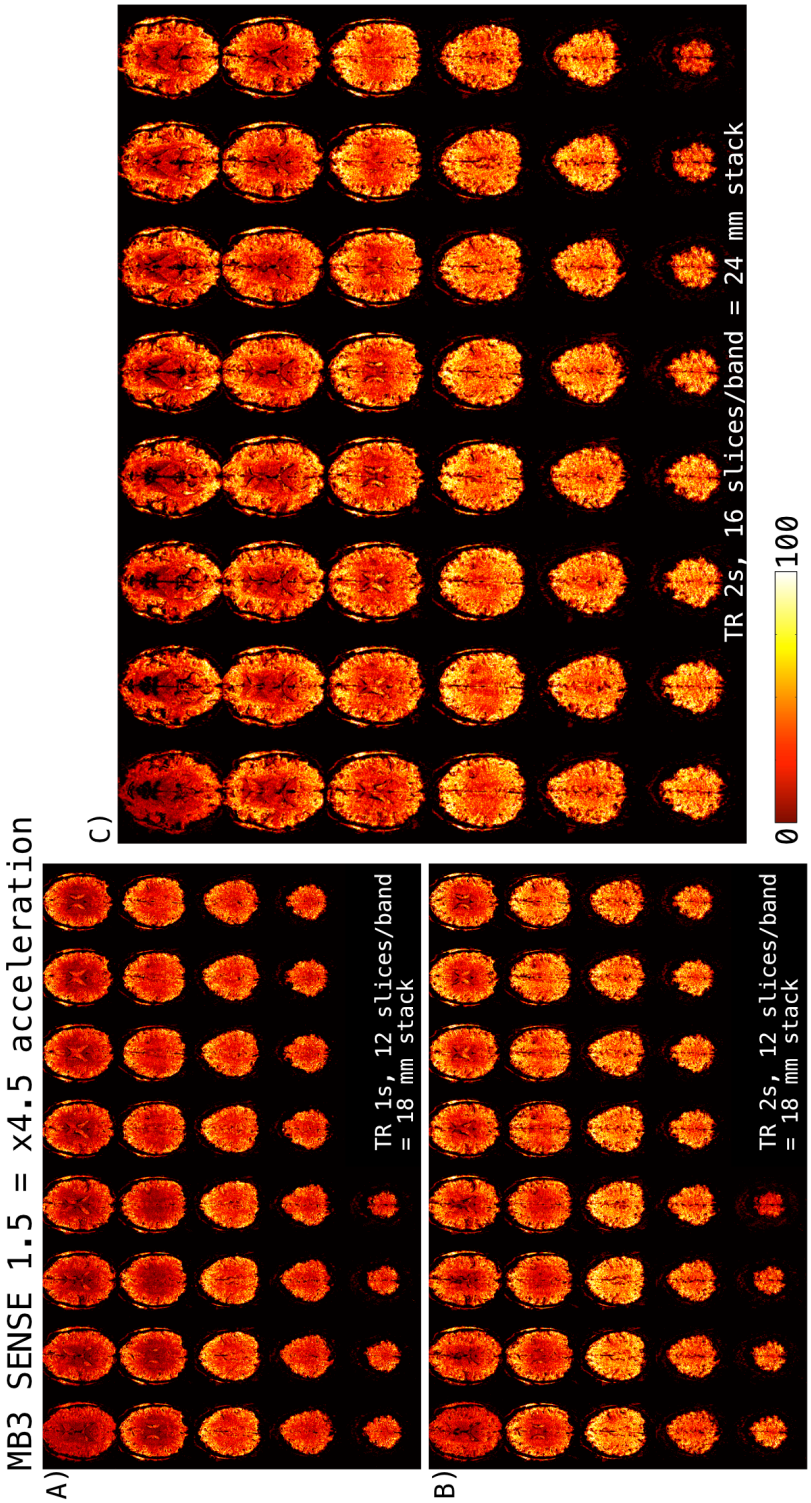


Figure 6.17: Multiband 3, SENSE 1.5 (x4.5 acceleration) tSNR images. A) Reducing to TR 1s limits stack to 12 slices/band, which is shown in B) 12 slices/band at TR 2s. Compared to Figure 6.16, MB3, SENSE 1.5 provides better tSNR homogeneity compared to MB2 SENSE 2. C) TR 2s data collected with 16 slices/band, equivalent to a band separation of 24mm.

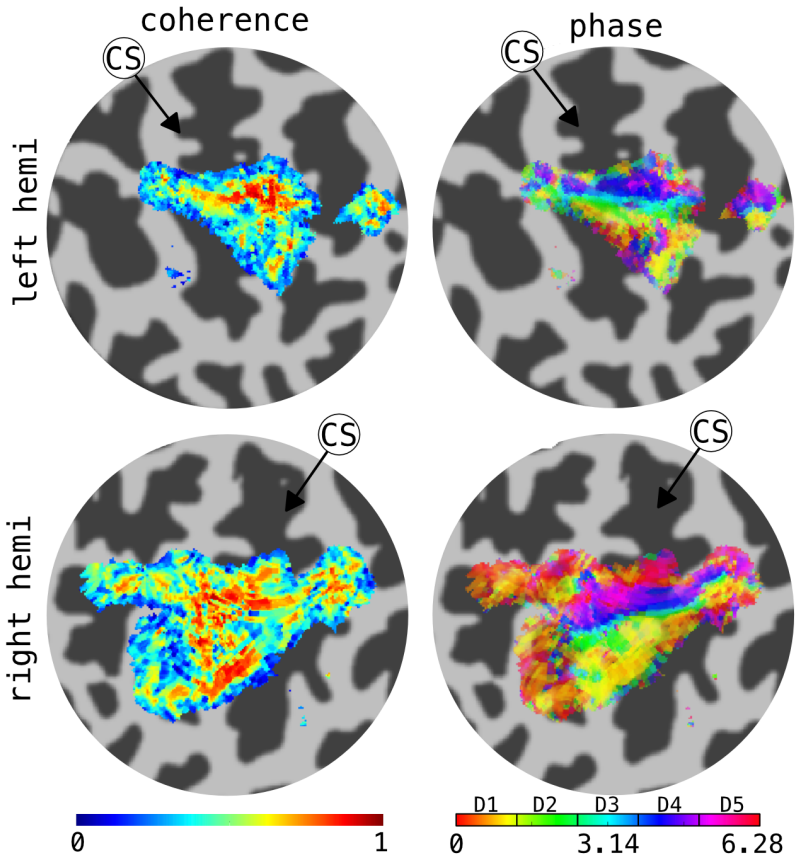


Figure 6.18: Travelling wave (TW) maps to right (dominant) and left hand stimulation for a single subject, on contralateral hemisphere. Data taken from dataset A5 (see Table 21).

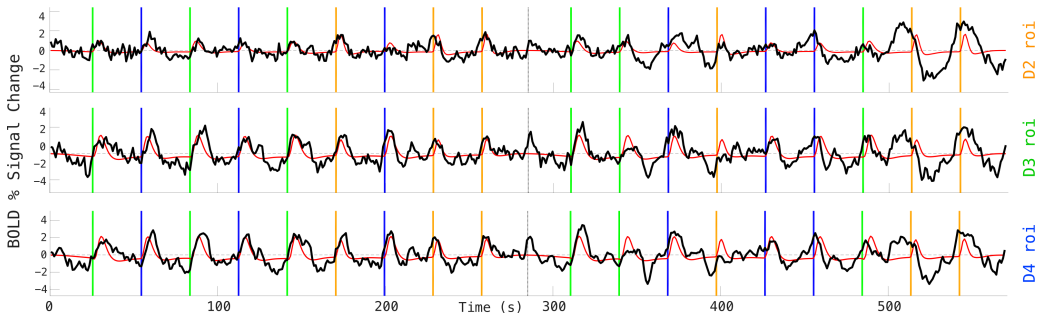


Figure 6.19: Timecourse across D2, D3 and D4 GLM-defined ROIs, concatenated from 2 ON-OFF scans in a single volunteer is shown. Strong activation can be seen at each ON-time. The coloured bars represent the ON time for D2 (orange), D3 (green), D4 (blue). The optimum ON-OFF time was chosen to be 5 s ON and 24 s OFF; this provided a reasonable scan length for the participant with enough time for 9 repeats (3 ON-OFFs per digits D2, D3 and D4). Data taken from dataset A2.

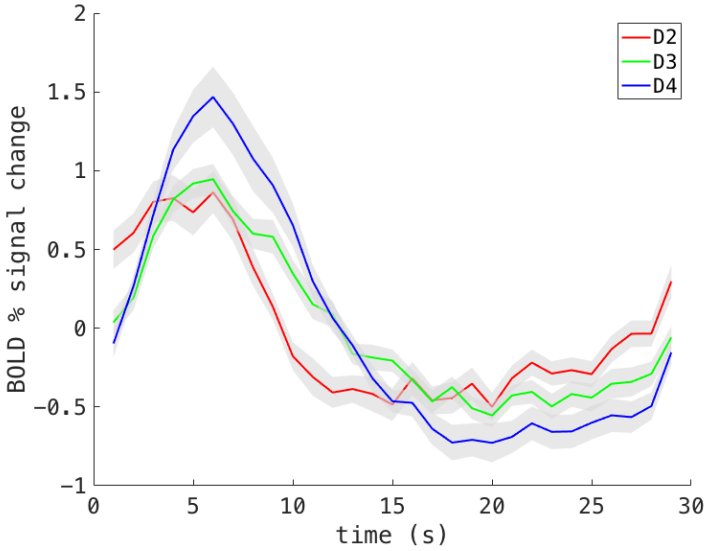


Figure 6.20: The mean HRF for each digit is shown from Figure 6.19

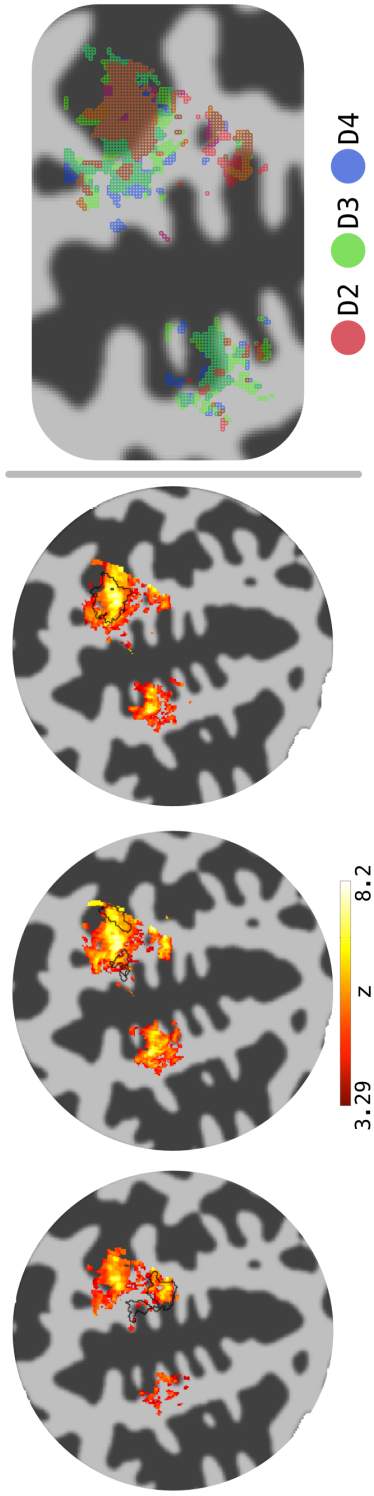


Figure 6.21: Z-score maps following the ON-OFF paradigm. The data from the two runs in the battery were concatenated. Digit ROIs (black lines) were imported from the TW analysis performed in the same scan session - it can be seen that the peaks for each digit lie within their respective TW ROI (left-right D2, D3, D4). Right) Overlap of digit activation.

6.6.0.3 fMRI: Motortopy and accelerometer piloting

Figure 6.22 shows the results of each of the two motortopy tasks which were piloted. While both the slow extension and fast tapping paradigms provided good quality data, the faster tap data had higher coherence and was also easier to perform. Associated accelerometer data are shown in Figure 6.23 and indicates good correspondence of finger movements to the paradigm timings, with a clear pattern of digit ordering.

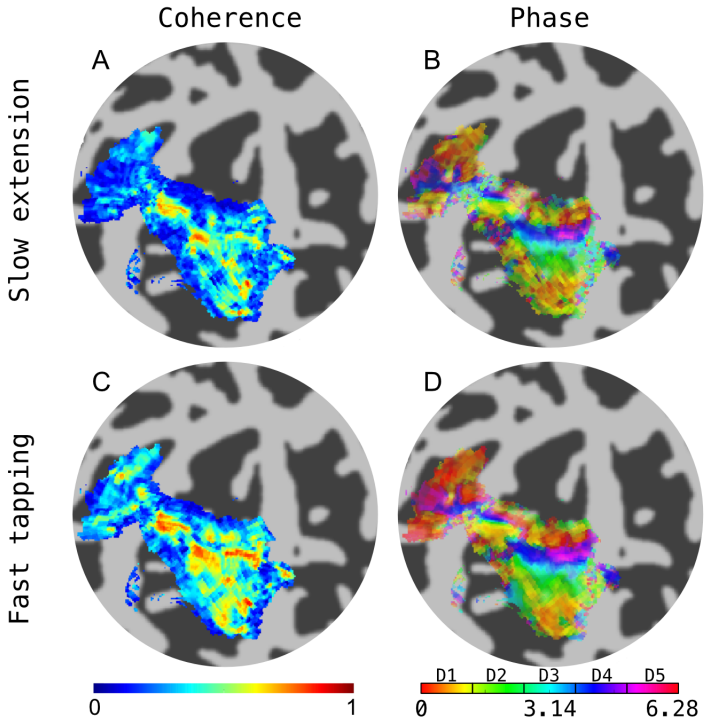


Figure 6.22: Motortopy Fourier analyses displayed on a flattened cortical surface, on the left hemisphere. Coherence maps indicate modulation at the stimulus frequency (A and C) and digit phase correspondence can be seen in the phase maps (B and D). Coherence and phase maps for the faster tap data (C and D) show better signal modulation and digit separation than the slower extension/flexion paradigm (A and B). Phase maps are weighted by coherence. Data are taken from dataset A1 (see Table 21).

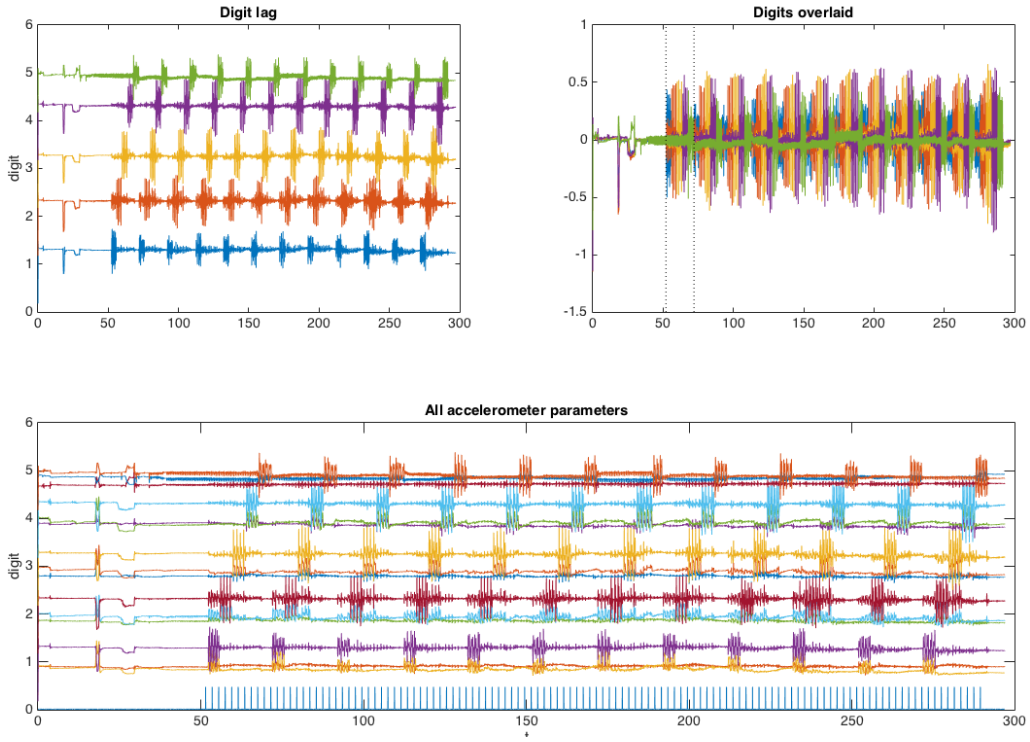


Figure 6.23: Accelerometer parameters from the fast tapping in air motor paradigm. Top left) A single axis of the accelerometer's acceleration is plotted for each digit across time. Top right) The graph from the left is collapsed across digits to confirm the continuous wave nature of the stimulus. Bottom) All 3 accelerometer axis parameters are shown, as well as the stimulus trigger from the scanner, which occurs on every dynamic (TR 2 s).

6.7 Results: Patient fMRI data

6.7.0.1 Patient and healthy control fMRI data

Functional MRI data were acquired from the same five post Botox patients on the same day as the behavioural testing. Data were also acquired from 3 (age-matched to patients) healthy controls. Figure 6.24 shows the healthy control data and Figure 6.25 shows the patient data. Mean tSNR values are shown below each pair of scans.

The Dijkstra's and 3D Euclidean distance between the centre of mass of each digit, per subject's TW data, across hands, is shown in Figure 6.26. While the 3D Euclidean distance shows little difference between groups (HC, n = 3, PA, n = 5), the patient Dijkstra's distance shows more separated values.

Additionally, tSNR maps were generated for each scan separately, across all dynamics and all slices, and provided in Appendix 8. The top 24 slices were selected for the mean tSNR value provided in the figures, as this is the region that analyses were performed in. Generally, tSNR is lower for the patient data compared with the healthy controls.

Figure 6.27 shows Z-score maps output from GLM analysis of the ON-OFF fMRI data. Some subjects have strong, separable activation to D2, D3 and D4 (HC2 and PA1), whereas others are sparse and noisy (PA2 and PA4). The HRFs corresponding to the TW-defined ROIs overlaid on the ON-OFF GLM data are also shown. These all show positive HRFs for each digit. HC1 had the presence of a large vein and so their ON-OFF data are not included here. PA3 and 5 had tSNR values < 30 and as such their ON-OFF data were not included in these results.

Figures 6.28 and 6.29 show motortopy data from HCs and PAs, respectively. These data all show strong modulation at the stimulus frequency and ordered

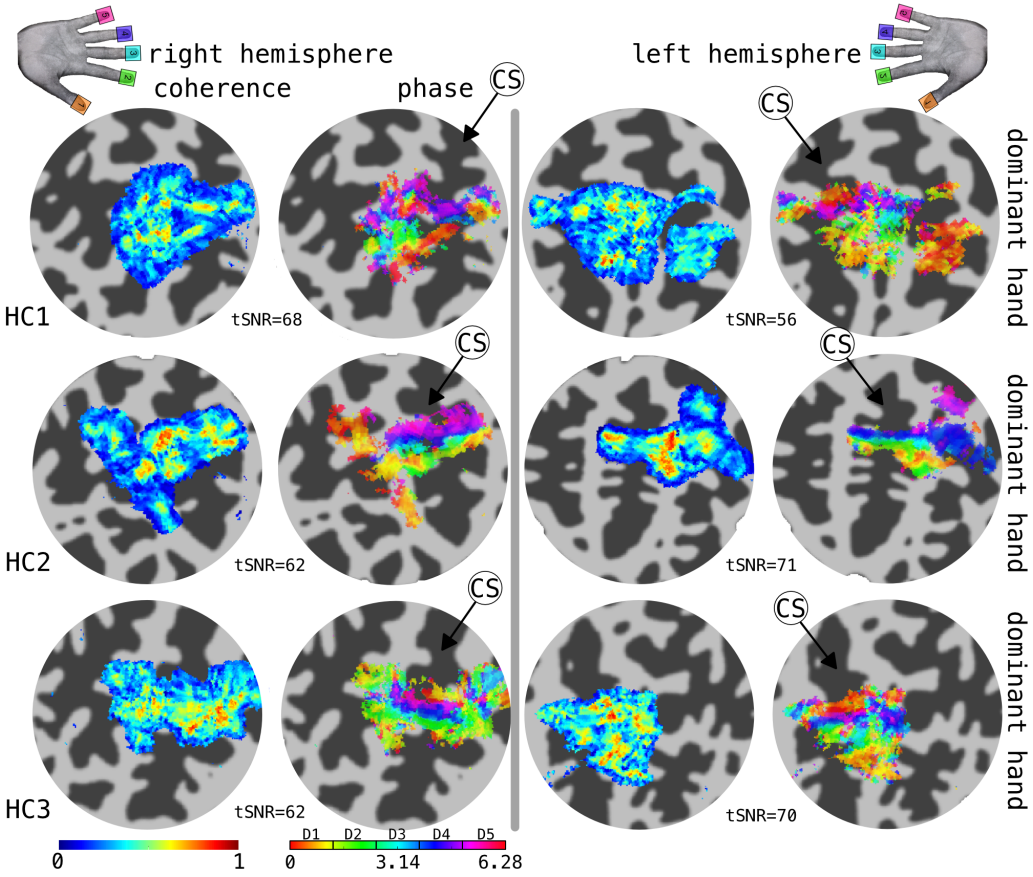


Figure 6.24: Healthy control coherence maps across both hemispheres (n = 3). CS=central sulcus. An ordered phase map can be seen in the postcentral gyrus.

phase maps, with predominant activity in the postcentral gyrus (compare to Figure 6.24 and 6.25 respectively), rather than precentral gyrus. Note that for some subjects, the accelerometer data are less clear, i.e. cycle-to-cycle amplitudes are lower and the accelerometer digit-specific timeseries' are generally noisier.

Figure 6.30 shows the Dijsktra's and 3D Euclidean distance performed on the motortopy TW data.

Since both the somatotopy and motortopy results elicit strong activation

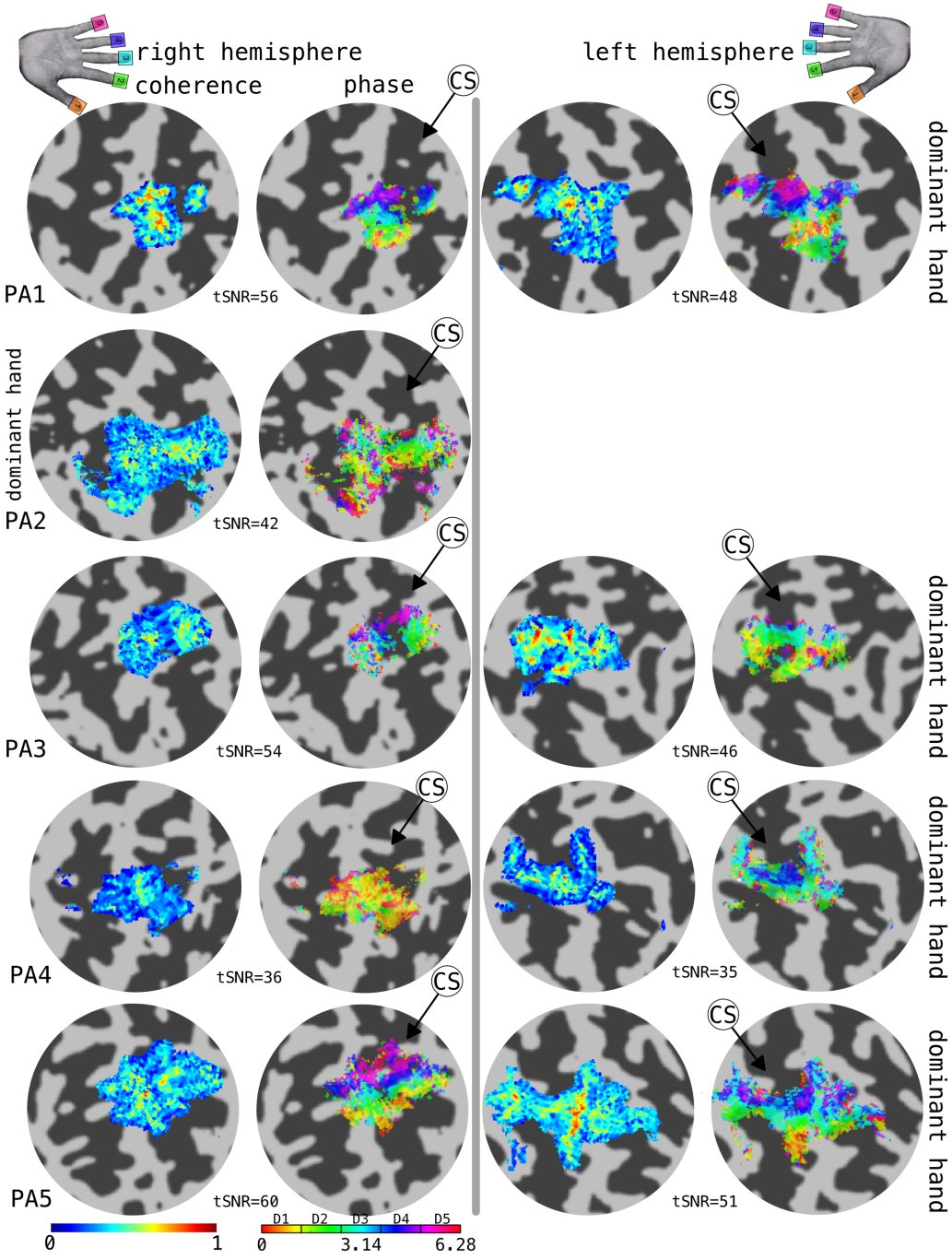


Figure 6.25: Patient coherence maps across both hemispheres (n = 5). Note that PA2 was a congenital amputee.

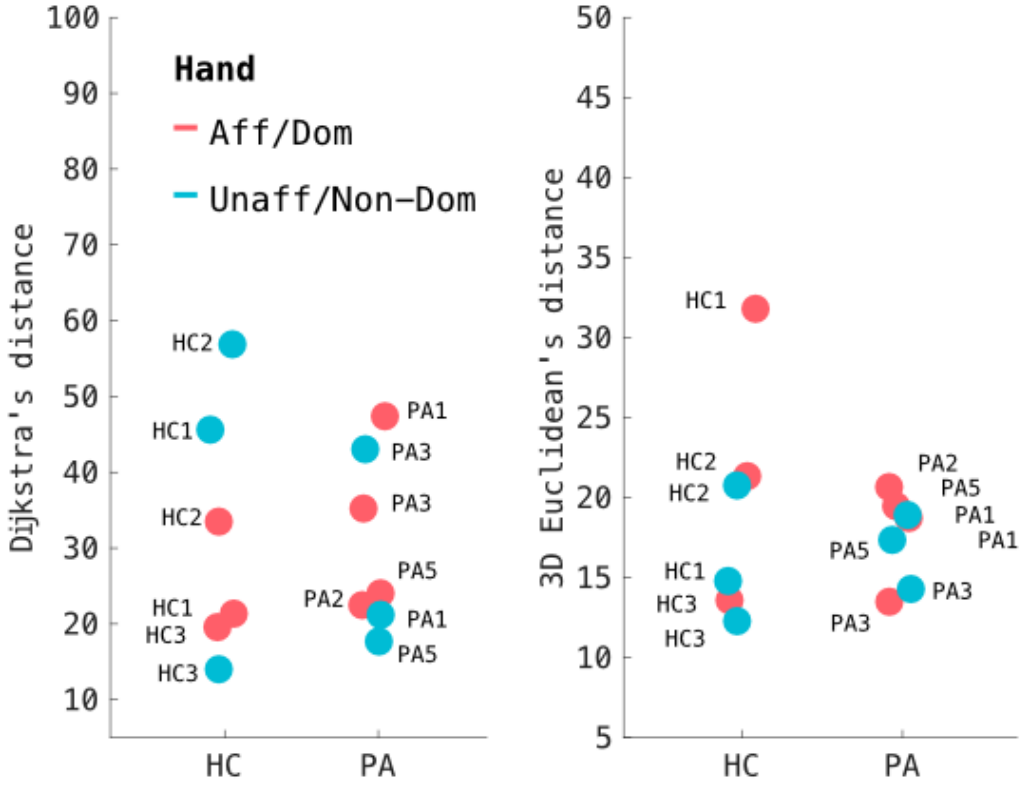


Figure 6.26: Comparison of the Dijkstra's and 3D Euclidean distances based on the centre of mass of digit specific coherence maps from the somatosensory travelling wave. PA4 was not included since there was no clear TW somatosensory pattern.

of the postcentral gyrus, a histogram of the phase difference between somatosensory and motortopy maps in the postcentral gyrus (using the somatosensory TW ROI) was generated. Figure 6.31 shows that there is good correspondence between maps, especially for HC3 and PA5.

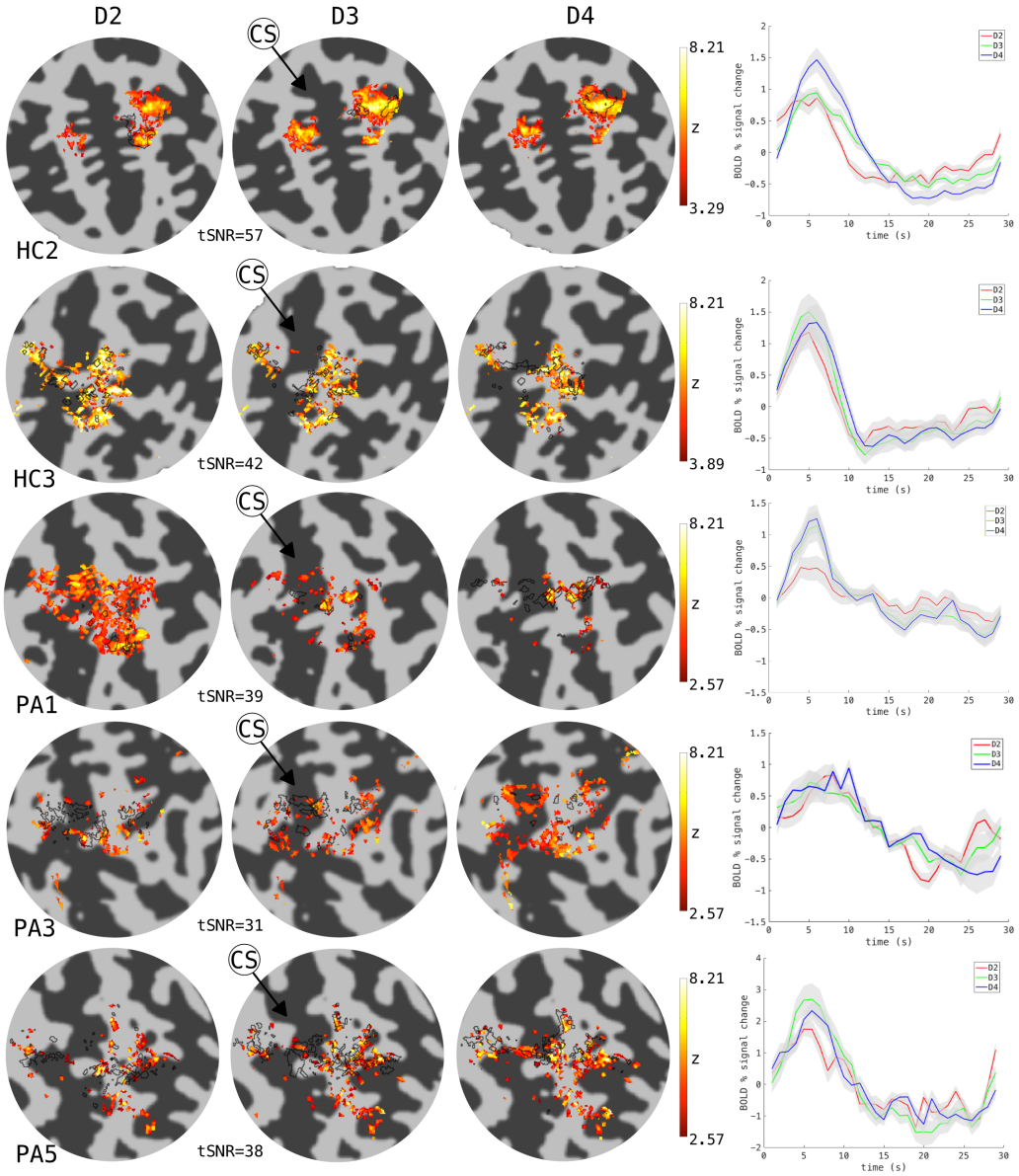


Figure 6.27: ON-OFF Z-score maps with TW ROIs overlaid for HC2, 3 and PA1, 3 and 5. The time-averaged HRF for each digit is shown.

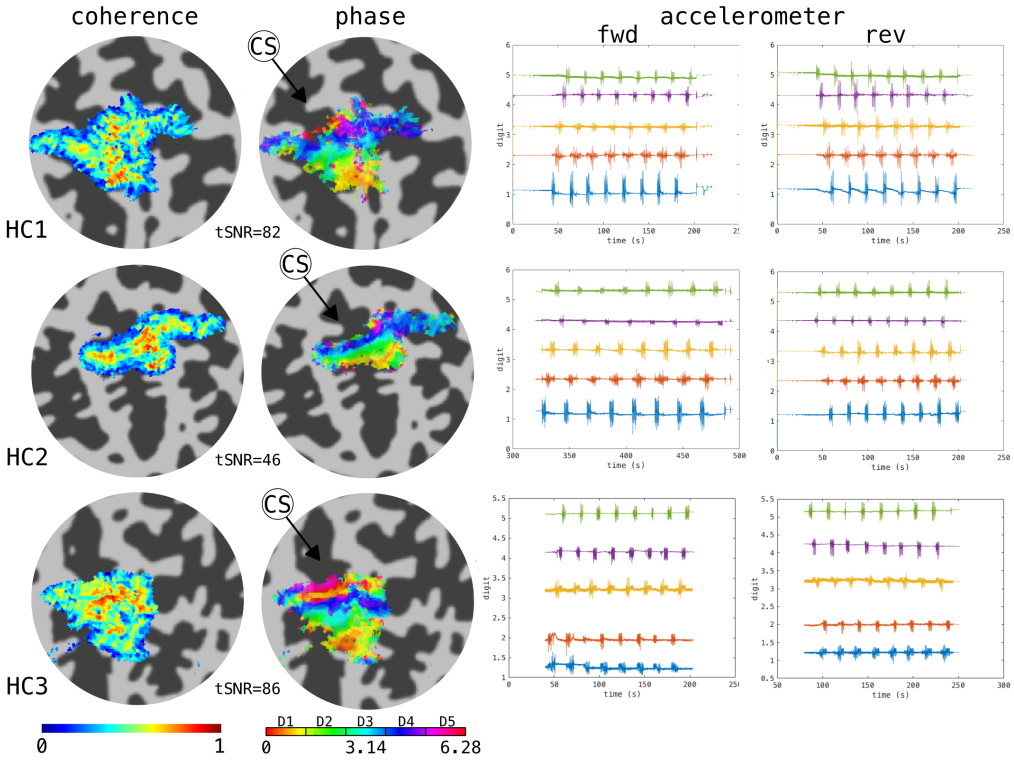


Figure 6.28: Healthy control motortopy maps, and the corresponding forwards and reverse accelerometer plots (right) for data collected on the dominant right hand (left hemisphere). Note an ordered pattern predominantly in the postcentral gyrus.

6.7.0.2 Correlating behavioural measures to fMRI data

In Sections 6.4.4 and 6.7 patient behavioural and fMRI data were discussed. It is acknowledged that there is insufficient data to compare the two. With the addition of more subjects, the behavioural data can be linked to the fMRI data and an example of such a comparison is shown in Figure 6.32. Here, the distances on the cortical surface based on the fMRI data were plotted against the temporal discrimination and spatial acuity data. One hypothesis is that a larger (worse) spatial acuity would correspond to a larger cortical digit distance, in FHD patients. For reference, the TDT data are

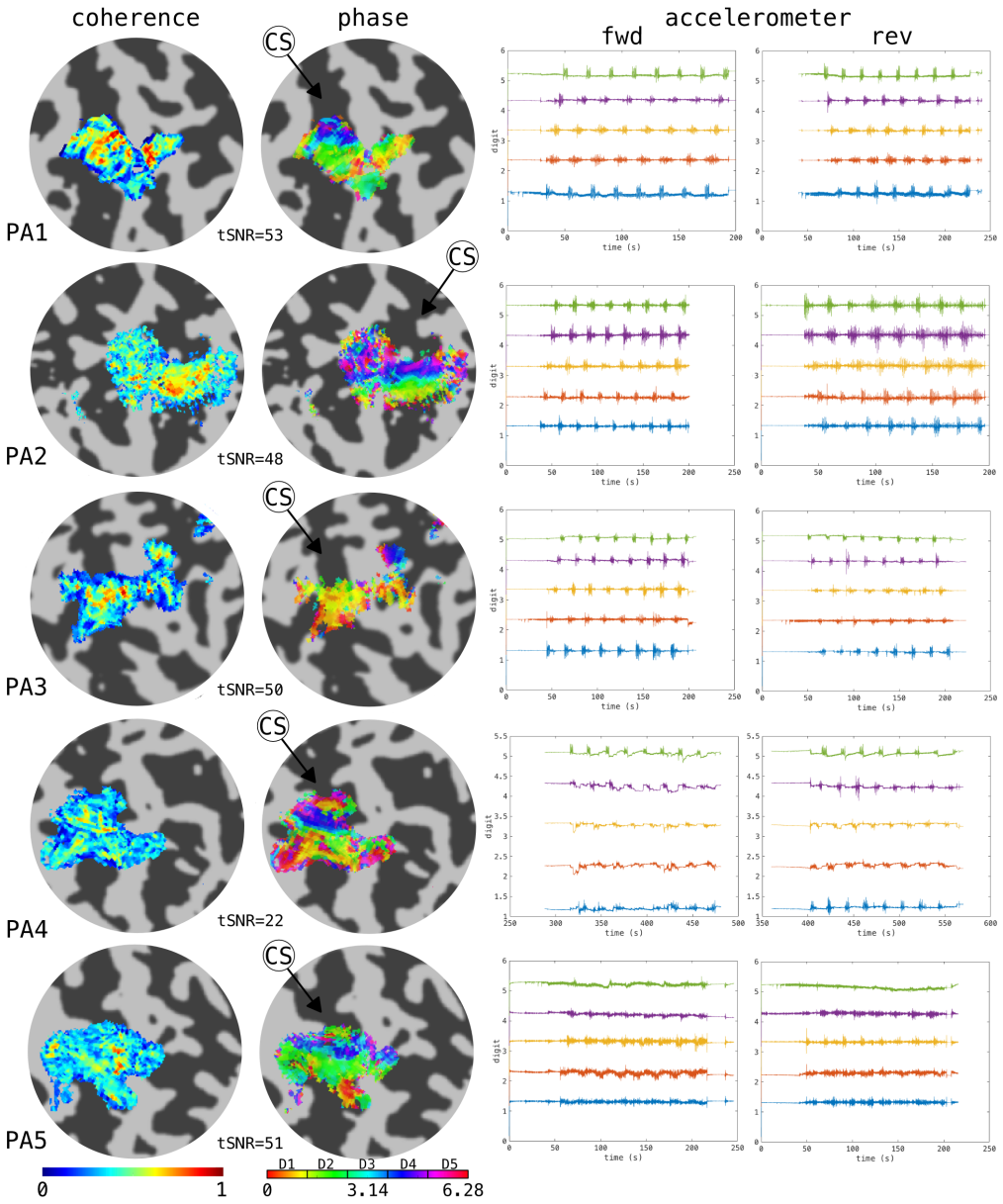


Figure 6.29: Patient motortopy maps and accelerometer plots for data collected on the dominant affected hand.

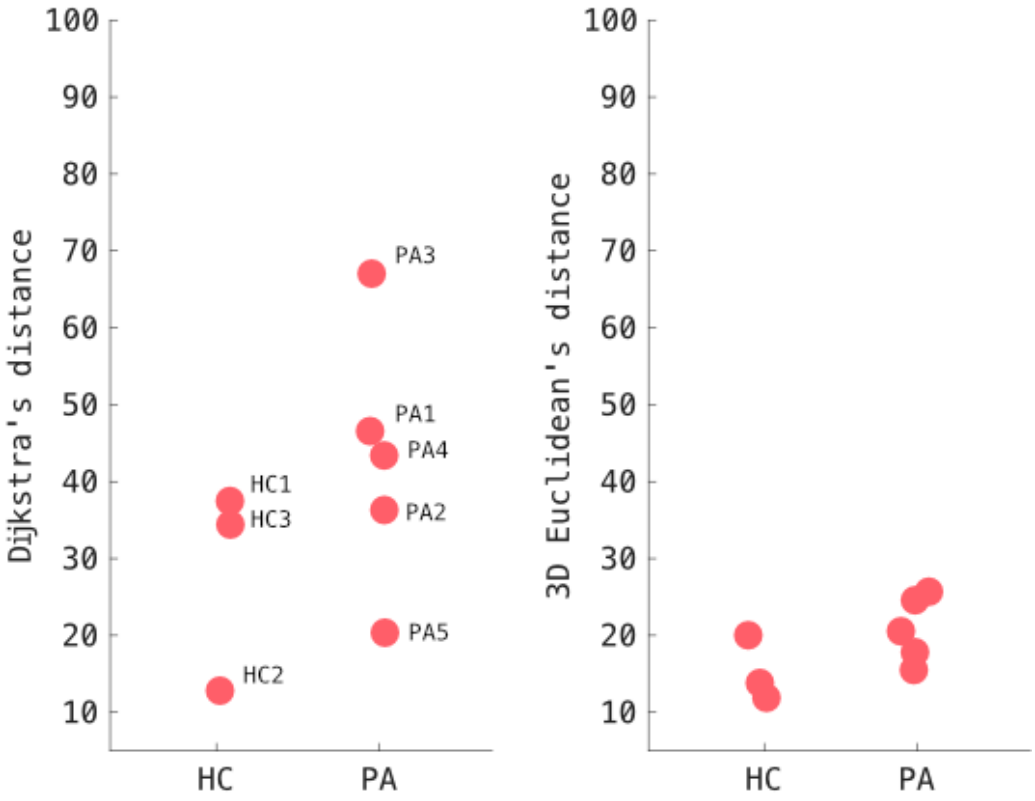


Figure 6.30: Comparison of the Dijkstra's and 3D Euclidean distances based on the centre of mass of digit specific coherence maps from the motortopy travelling wave.

also shown.

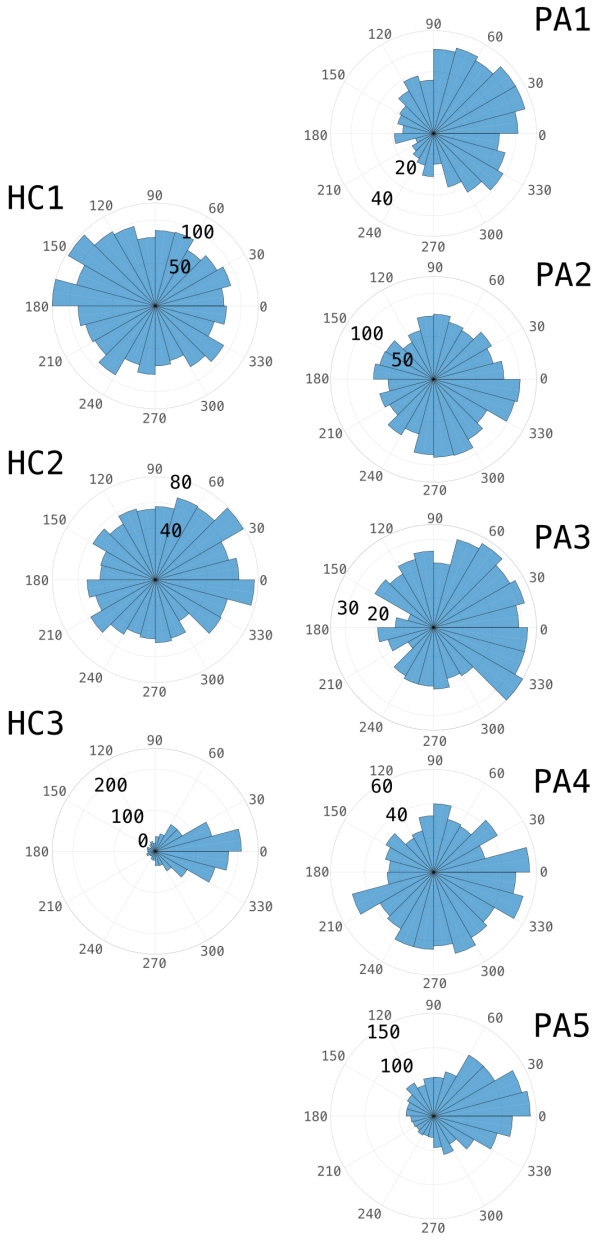


Figure 6.31: Phase difference plots between somatosensory TW and motortopy TW for each subject. Data shown for phase values within the somatosensory TW ROI.

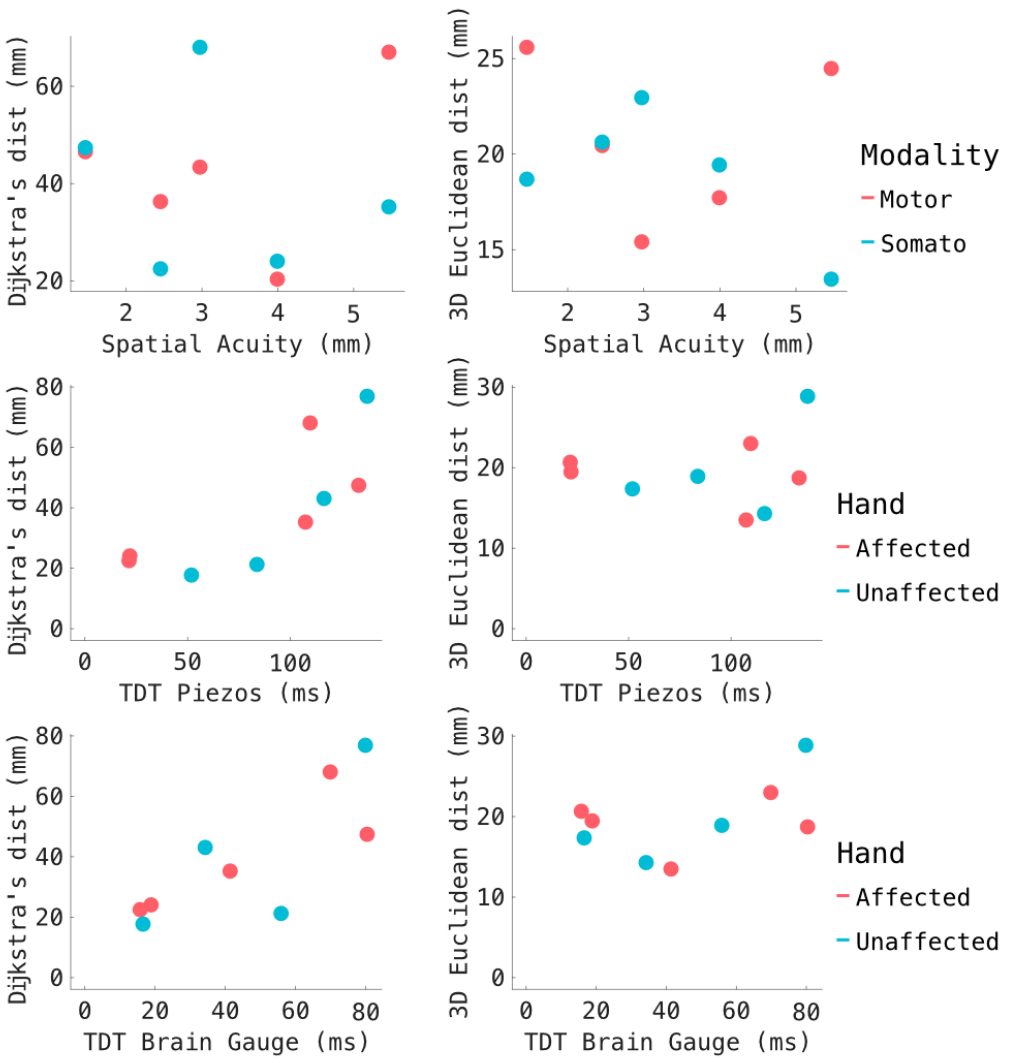


Figure 6.32: For patients, the Dijkstra's and 3D Euclidean distances calculated from the somatosensory and motortopy TW fMRI data are plotted against the temporal discrimination and spatial acuity (domes) data. This is an example of how one could link the behavioural measures to the fMRI data. The fMRI motortopy and somatosensory data for the affected hand only are compared with the domes, while both hands (but only somatosensory fMRI data) are compared for the TDT.

6.8 Discussion

In this Chapter, a behavioural and fMRI battery of experiments has been developed and performed on a cohort of healthy controls and patients with Focal Hand Dystonia. Development included a quantitative sensory testing (QST) battery to measure temporal discrimination (TDT), amplitude discrimination, and spatial acuity. The fMRI scan protocol included a somatotopy TW, event-related paradigm and motortopy TW, which are reported in this thesis Chapter, as well as resting state data and structural characterization for the larger study. Five FHD patients were scanned approximately 4 weeks after BoNT-A injection, the typical time for the Botox to have an effect in FHD. These data are therefore indicative of mapping post-treatment, but must be compared to a second dataset where the Botox has worn off (after 3 months) to identify the relative changes, if any, due to treatment. Because of the limits imposed by patient recruitment, a comparison of the QST and fMRI data at 3 months post-Botox is beyond the scope of this thesis, however, the results in this Chapter provide the necessary set-up.

Behavioural data showed a tendency in patients to have greater values of amplitude detection, temporal discrimination thresholds and spatial acuity. One hypothesis would be of significantly larger amplitudes and temporal discrimination thresholds as well as spatial acuity thresholds at 3 months post-Botox, compared to 4 weeks post-Botox.

Here, a somatosensory TW was used to deliver passive somatosensory stimulation which has been shown to provide a robust and reproducible method to assess functional organization in S1 (Sanchez-Panchuelo et al., 2014). Functional MRI data show that in both healthy controls (n = 3) and patients (n = 5), the somatosensory TW produces robust modulation at the stimulus frequency (from coherence maps) with visual characterization of digit phase in the postcentral gyrus. However, there is variability across individuals, with some patients exhibiting lower coherence values. The origin of

the lower tSNR values in patients was assessed to determine whether this was related to head motion, however, all subjects moved less than 1.5 mm (x,y,z) within a given scan. While the within scan motion was low, it must be recognised that for TW protocols, between scan motion can affect analyses since pairs of images are combined, e.g. forward and reverse TW scans. If there is movement between a forwards TW and a reverse TW, on the same hand, then this will be detrimental to any coherence and phase averaging performed.

A quantitative method to measure cortical digit distance was developed using both overall 3D Euclidean or Dijkstra's distance between the centre of mass of each phase bin. Qualitatively, there was little difference in digit distance with either measure, however, an effect may be present with larger group sizes, and such, tests of significance may be performed.

The lack of any difference between subjects' TW maps qualitatively and quantitatively is consistent with the efficacy of Botox treatment, i.e. one would not expect to see any difference if the Botox were affecting cortical digit representation. Large differences would indicate the Botox being purely a symptomatic treatment, these findings must be confirmed by comparison when the Botox is worn off. This can be performed by generating phase difference histograms between pre- and post-treatment.

The motor task TW data show stronger coherence values than for the somatosensory TW, with consistent patterns of digit representation in S1. Qualitatively, one can see that during low movement, the motortopy fMRI data are worse - this is evident from the accelerometer plots (e.g. PA 4 and 5). More quantitative analyses could be performed in the future using these accelerometer data to inform the modelling of the data. It is noted that patients with FHD may find it harder to perform the motor task with their affected hand, leading to smaller accelerations, and hence a lower CNR in coherence maps.

It has been shown previously that a motor task TW results in considerable activity in the postcentral gyrus, and this is also evident in the data presented in this chapter. Here, the phase maps generated from a passive somatosensory TW have been directly compared to the motor task, showing there is good correspondence of phase and thus digit mapping in the postcentral gyrus. It is hypothesized that there is strong interplay between S1 and M1, with S1 acting as a processing region for both sensory afferent inputs as well as a central node across the sensorimotor network. However, isolation of motor activity is difficult since the exact sources of these maps are unknown, e.g. they could be induced by stimulation of cutanaeous or subcutanaeous receptors or deeper proprioceptors (Kolasinski et al., 2016).

The ON-OFF paradigm showed that it was difficult to separate D2, 3 and 4 in subjects, with considerable overlap. Generally, overlap was quite high in healthy controls despite a vein mask being applied to remove draining veins common to all digits. In all cases, a digit-specific HRF could be extracted from the ON-OFF data, and hence this could be used to supplement future population receptive field (pRF) analyses, as described in Chapter 4. Once the somatosensory pRF has been optimized, differences in pRF overlays (such as pRF size) could be compared between patients and controls using the existing TW data.

6.9 Conclusion of Chapter

A standardized behavioural and fMRI battery has been developed and initial data collected in controls and FHD patients. This provides the foundation for continuing patient studies involving different FHD patients and other patient groups. The work performed in this Chapter will feed into the larger TOUCHMAP project that involves additional scanning in patients with Carpal Tunnel Syndrome, as well as Magnetoencephalography (MEG).

It has been shown that in Focal Hand Dystonia patients (n = 5), approximately 4 weeks following a Botox injection, there is some difference in behavioural measures between controls, but no striking differences between patients and controls' fMRI data. Digit cortical distance and digit overlap also showed little to no differences between groups. These findings suggest the efficacy of the Botox treatment, however, this can only be confirmed with a follow-up experimental session when the Botox has worn off after 3 months. Adding more patients and healthy controls to the groups is now required, and will allow comparisons between behavioural and fMRI data to be performed.

In the future, it will also be of interest to compare the patient data shown to that of healthy controls in an atlas space. For example, our group has generated a probabilistic atlas of digit mapping in healthy controls in fsaverage MNI305 space (Sengupta et al., 2018). From this map, the dice coefficient of each digit location in FHD patients could be assessed.

CHAPTER 7

7 Concluding Remarks

This thesis has focused on the development and application of methods for high resolution mapping of sensory cortices using functional magnetic resonance imaging (fMRI) at ultra-high field (7 T).

Specifically, Chapter 4 focused on population receptive field mapping in the visual cortex. The acquisition of a "HRF" scan allowed subject-specific HRFs to be introduced into the pRF model fitting procedure. Comparison with the pRF's unrealistic HRFs, when using an unconstrained model, showed that while the "HRF-informed" pRF provided weaker model fits the outputs were closer to the ground truth. The 5 s and Wiener-deconvolved HRFs provided similar r^2 maps to the pRF, but are a more physiologically true response. It was shown that the choice of fitting algorithm altered the pRF fit, with a constrained (Levenberg-Marquardt) providing a more realistic physiological fit. In future, pRF modelling could be improved by using a set of experimentally obtained HRF relevant constraints to additionally constrain the pRF model.

In Chapter 5, pRF modelling was developed for use in the somatosensory cortex, where responses are weaker and require the increased CNR available at 7 T. This was implemented using an array of bespoke piezo-electric stimulators. The choice of pRF model was assessed and shown to have a large impact in somatosensory cortex. The traditional 2D-Gaussian model was shown to underperform compared to multi-parameter models. Overall, the pRF method performed less well in somatosensory cortex than visual cortex. One likely reason is that this may be due to the lower functional SNR available, as well as the use of a simplified pRF model.

In Chapter 6, the setup and development of a standardized behavioural and fMRI battery for studying somatosensory function in focal hand dystonia (FHD) patients was described. This involved optimizing psychophysics procedures for temporal discrimination and spatial acuity; a travelling wave (TW) somatosensory paradigm together with the development of an event-related paradigm to measure HRFs in somatosensory cortex; the use of a bespoke accelerometer glove to track digit movements during a motortopy paradigm; and the optimization of fMRI parameters such as multiband factor and scan length for each of the protocols.

Behaviourally, amplitude thresholds, temporal discrimination thresholds and spatial acuity was raised in FHD patients. In FHD patients ($n = 5$) there was little qualitative and quantitative differences in TW somatotopic maps and digit overlap between healthy controls. Additionally, the motortopy TW data showed clear digit mapping in the postcentral gyrus for HCs, albeit with less apparent maps in FHD patients. This is consistent with patients receiving a Botox injection 4 weeks prior to the experimental session, indicative of treatment effectiveness. The same protocol will now be performed when the Botox has worn off after 3 months in the ongoing TOUCHMAP project.

In summary, the development of population receptive field (pRF) mapping has opened new avenues of questions to be addressed in model fitting and stimulus choice. Here, the pRF method has also been validated in visual cortex, a region possessing high functional SNR, providing a good proxy for prototyping extensions to the pRF. The haemodynamic response function (HRF) has been mapped spatially over visual cortex and has been used to ensure a more physiologically correct model. Finally, the cortical representation of the digits in patients with Focal Hand Dystonia has been measured using an optimized behavioural and fMRI battery, which required extensive protocol development.

7.1 Future Directions

The data collected on visual cortex has demonstrated the use of a HRF-informed pRF model. The acquisition of a single additional HRF scan was used to constrain the pRF, making its outputs closer to the ground truth, per subject. This addition could be used in more complex pRF models that have been developed and are liable to large degrees of freedom and overfitting. These measured HRF parameters can be used to constrain the pRF model, with suggested limits provided. In future studies, these methods could be applied to patients with visual deficits such as neurodegenerative effects of long-term visual cortex deafferentation.

In somatosensory cortex, only a few simple pRF models have been developed; these data are thus ripe for the extension to more complicated models. Exploring the relationship between the array of stimulators used on the digits and the chosen pRF model could help explain why the somatosensory pRF fits are much weaker than visual cortex. Insights from Chapter 4 imply that the use of subject-specific HRFs could be used to improve the somatosensory pRF model, at least statistically, and this will form future work.

Chapter 6 has demonstrated the feasibility of measuring somatosensory maps in focal hand dystonia patients, and it is important to collect additional data in this population using the protocol developed in Chapter 6. A comparison with a repeat visit at 3 months once the Botox has worn off will answer the question of whether treatment has affected the cortical representation of the digits. Insights from Chapter 4 and 5 could be used to perform an optimized pRF analysis on the existing TW data. Ultimately, one could perform pRF mapping in patient populations, using optimized, complex somatosensory pRF models, to identify differences in broad neural tunings, that correlate with disease. The work performed here is only the beginning of an exciting journey into sensory mapping.

8 Appendix

8.1 Deeper Insights into pRF Mapping

The phase from the TW that is calculated from a voxel's response relates to the mean receptive field centre within the voxel, whereas the population receptive field refers to a model that attempts to capture the entire voxel's response to a paradigm. A single voxel does not hold a single neuron, therefore there may be a variety of neurons with different firing sensitivities, tunings, preferences, etc. Relative to other imaging modalities, the volume of an imaged voxel (functional data) can range from a few mm^3, e.g. 1 mm^3 (1 mm isotropic) at 7 T to tens of mm^3, e.g. 48 mm^3 (4 mm isotropic) at 1.5 T, depending on the slice acquisition parameters and the magnetic field strength. An estimate of the amount of information inside a voxel thus heavily depends on the voxel size, i.e. a 55 mm^3 voxel contains 5.5×10^6 neurons, 2.2-5.5$\times10^{10}$ synapses, 22 km of dendrites and 220 km of axons (Logothetis, 2008). A 1 mm^3 voxel contains approximately 50000 neurons, of which only some will respond strongly to the experimental stimuli (Braitenberg and Schüz, 1998). These numbers serve to illustrate fMRI spatial specificity: only at the invasive electrophysiological level can we begin discussing what 'neuron x' cares about more than 'neuron y'. Even then, the receptive field measured by single-unit recordings (recording of a single neuron) is defined by its inputs from a larger network of neurons, of who's computations we know nothing of (Wandell and Winawer, 2015).

fMRI is limited to estimating what a 'population' of neurons cares more about than another population, rather than individual neurons, which can only be measured using invasive, electrophysiological methods; this naturally reduces the spatial resolution of RF estimates. Additionally, the BOLD response is an indirect measure of glucose metabolism that itself is an indirect

measure of neural activity (which is made up of excitatory and inhibitory processes, restoration of cell membrane potential, among others). The 'pRF' summarises the aggregate response of all the individual neuronal receptive fields in a voxel. On a side note, the contents of a fixed voxel volume may differ in different brain regions, e.g. between somatosensory cortex and visual cortex. It is known that the number of neurons under a mm^2 of cortical surface, and the density, is several times higher in the visual cortex, than anywhere elsewhere (Logothetis, 2008).

The steps for the pRF analysis are as follows: a model of the pRF is generated, e.g. this could be a 2D Gaussian with x and y defining the pRF centre, and a 'sigma' defining the spread - $g(x, y)$. Next, the stimulus $s(x, y)$ is described - this has been performed in MATLAB (Mathworks, 2014), via mrTools (Gardner, 2016). In the somatosensory domain, this is a set of matrices which tell the stimulators which phalanx to stimulate, in a user-defined sequence. The pRF model and the stimulus description are multiplied together to obtain the predicted pRF response, or the 'overlap' between the model and the stimulus description, denoted $r(t)$. This predicted pRF response is convolved with a haemodynamic response function (HRF), $h(t)$, giving the time series prediction, $p(t)$. This can be a canonical HRF, or one fitted to the data. Following convolution, the errors or 'residuals' are calculated between the predicted time series and the actual data. This is used to optimise the pRF parameters via a non-linear least squares minimization algorithm (see Section 8.1.4 for the specific algorithms used). The optimization of these receptive field parameters is taken as the best pRF for the measured voxel. Additionally, although we have used sinusoidally modulating stimuli here, the pRF can be calculated from any response modulating stimuli, e.g. drifting bars. This experimental flexibility is a key advantage of the pRF over the TW.

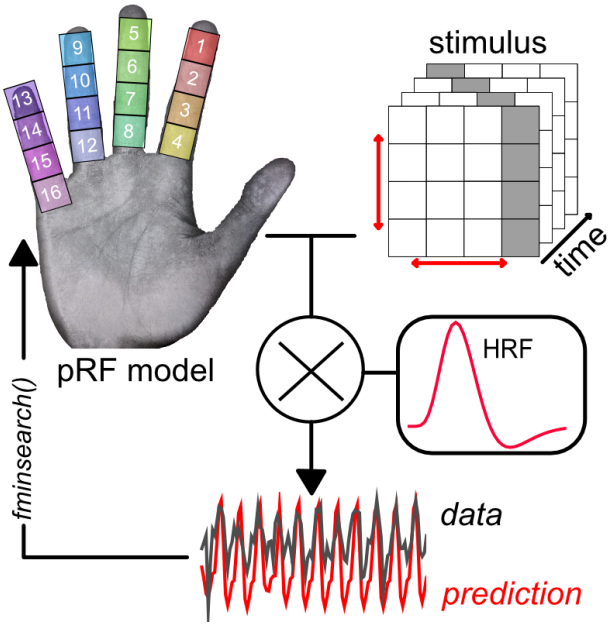


Figure 8.1: The somatosensory pRF model algorithm. In this example, there are 16 stimulators placed on the hand, with each parameter allowed to vary. This is overlapped with the stimulus description and convolved with an HRF. The residuals are minimised between the predicted response and the data using non-linear least squares. See Chapter 5 for an expanded figure.

8.1.0.1 Cortical unfolding

Following image acquisition, the intrinsic 2D topology is extracted from the segmented and subsequently 'unfolded' cortex, to simplify visualization of functional data. The nature of retinotopic and somatotopic data implies that distances and areas between cortical position of activity must be consistent when comparing the cortex as a 3D folded sheet, or as a 2D flatmap, since two points in the GM may be adjacent in 3D, but far apart in 2D (Warnking, 2002). Synonymously, the mapping between cortex and sensory space is 'homeomorphic' (preserves topography). Initially, geodesic (lines between two points on a sphere) distances are calculated on the region of interest via an algorithm (Dijkstra, 1959), followed by a projection of the cortical manifold onto the target surface (Fischl et al., 1999); this procedure

introduces fold-over and metric distortions. Following this 'unfolding', the flattening of the cortex requires further 'cuts' to display an entire hemisphere at once, by removing the curvature.

8.1.1 Extending the pRF model

In visual neuroscience, various pRF models have been prescribed to extend the model analysis to different stimuli, capitalising on the pRF method's stimuli independence, i.e. one simply has to translate physical stimuli into computer code which the model can interpret, be it visual or somatosensory stimuli. The original 2D Gaussian model in Dumoulin's paper has been extended to a difference of Gaussian (DoG) model, i.e. two Gaussians subtracted from one another, that has additional parameters - negative surround size and amplitude (Zuiderbaan et al., 2012). This extension allows modelling of below baseline fMRI signals and surround suppressive effects, and gave improved performance in predicting the actual fMRI timeseries in V1 (where the improvement in performance relative to the single Gaussian model was 14 %), V2, & V3. They confirmed the increase in pRF size with increasing eccentricity, found a similar increase in surround size and calculated a suppressive "index" (dividing the volumes of the two Gaussians), which decreased with eccentricity for V1 and V2, but increased for V3 - they suggest that suppression index becomes unstable as surround sizes increase relative to stimulus size. Furthermore, cross-validation of training and validation data subsets indicated that the additional variance explained by the DoG model was not simply due to an increase in the degrees of freedom, by adding additional parameters.

The key parameter of interest gained from the pRF over traditional retinotopy is pRF size, which is estimated from the standard deviation of the Gaussian model. One caveat in this estimation is that higher variance in neuronal positions (i.e. greater neural scatter) will increase the apparent

pRF size, without changing the actual pRF size(s). Simulations have shown that position scatter also affects the strength of the negative (surround) component of the pRF (Zuiderbaan et al., 2012). Thus, in areas of high position variance, estimates of pRF size will break down.

The pRF methods/models described so far assume linearity, i.e. responses to visual stimuli are linear summations of subsets of the whole stimulus. The addition of a compressive static non-linearity into the pRF model, following linear summation, increased the amount of variance explained (Kay et al., 2013a). By presenting partial contrast apertures and full apertures, one can see whether spatial summation is linear, i.e. the summed partial aperture responses should equal the response to the single full aperture: this was not the case. In visual field maps measured, the summation ratio was less than 1, indicating subadditive summation.

The compressive spatial summation (CSS) pRF model outperformed the linear (2D Gaussian) model across visual cortex, with a small improvement at V1, and increasing with eccentricity - this may be explained by the small pRF sizes in V1, such that, not many apertures cut through V1 pRF, for a given voxel. Thus, as pRF size increased, spatial compression did so correspondingly. The CSS pRF model converts the stimulus to a contrast image, is projected onto a 2D Gaussian, and multiplied by a static non-linearity. The authors suggest that the subadditive summation may be linked to BOLD-neural activity coupling. For example, this could be explained by diverse cell types, different types of neural activity, or neuronal position scatter.

Other studies have, by small changes to the 2D Gaussian model, extended the pRF method to allow processing of a large number of shapes, such as natural images via pictures or movies in decoding studies (Kay et al., 2008; Nishimoto et al., 2011), or even without specifying a specific pRF shape a priori and only constraining the search space by estimating a set of vector

weights by solving linear equations for a given voxel (Lee et al., 2013).

An upgrade to the CSS model involved adding a variance-like non-linearity, with eight free parameters in total; known as a second-order contrast (SOC) model (Kay et al., 2013b). The cascade model architecture incorporated two stages of linear and non-linear computations, and led to greater model accuracy in terms of r^2, outperforming all other previously tested models. The SOC model, with its substantially increased complexity can be extended further to account for different stimuli, and hence is a step towards more accurate models that encode neural activity.

An interesting extension of pRF mapping to another sensory domain involved measuring tonotopic maps and estimating bandwidth in auditory cortex (Thomas et al., 2015). Tonotopic maps were successfully reconstructed (in the presence of scanner acoustic noise), utilizing ascending and descending tone progressions, as well as random tone sequences. The pRF model used was a one-dimensional Gaussian, defined over log frequency, where the centre corresponded to the best frequency. The standard deviation was used as a measure of bandwidth. The method was compared to traditional phase-encoding methods (like the travelling wave), as well as using a difference of Gaussians. Results showed that tonotopic maps were similar between phase-encoding and pRF methods, however, the difference of Gaussian model did not provide additional accuracy. pRF mapping in auditory cortex eliminates the limitation of an orderly stimulus sequence, as required by phase-encoding methods. The authors suggest that the random tone sequences likely provide a more accurate method for measurement of fine-scale tonotopy. This work exemplified the successful adaptation of pRF mapping from visual to auditory cortex, providing the opportunity to develop non-traditional stimulus sequences, and identify auditory neural tunings.

8.1.2 Modelling the HRF

Having defined the model type and combined it with the stimulus description, the next step in building up the analysis / fitting procedure is to add an approximation of the HRF to realistically model the actual fMRI time-series. The fMRI response gives an indirect measure of neural activity via changes in cerebral blood flow, volume and oxygen consumption. The BOLD haemodynamic response varies depending on where in the brain it is elicited, and on stimulus type. However, the 'traditional' HRF shape can be said to include an initial dip (thought to result from immediate oxygen extraction), the rise to peak over a period of 5 s, and an undershoot (below baseline signal resulting from reduced blood flow and increased blood volume) (Huettel et al., 2004). The canonical form of the HRF can be parameterized ad hoc, but key measures of the curve are the amplitude, the time it takes from stimulus onset to full peak (latency of the response), and the width (often measured as the 'full-width-at-half-maximum' (FWHM)).

Mathematically, the BOLD contrast is modeled using a linear time invariant system (LTI). The BOLD signal $y(t)$ is a convolution (implying a linear system) of the stimulus description $s(t)$ and the haemodynamic response $h(t)$.

$$y(t) = (s * h)(t) \tag{8.1}$$

In fMRI analyses, one assumes that the HRF is convolved with the neural response; in the Fourier domain, this "smoothing" is simply a multiplication by a sliding window (point by point multiplication).

The HRF shape can be modelled using a difference (or double) gamma function. For the response function $h(t)$ over a series of timepoints t,

$$h(t) = \left(\frac{t}{d_1}\right)^{a_1} e^{-\left(\frac{t-d_1}{b_1}\right)} - c\left(\frac{t}{d_2}\right)^{a_2} e^{-\left(\frac{t-d_2}{a_2}\right)} \tag{8.2}$$

where $d_j = a_j * b_j$ and is the time to peak, and a set of default (canonical) parameters ((Glover, 1999)) are used as a starting point of $a_1 = 6$, $a_2 = 12$, $b_1 = b_2 = 0.9$ seconds, and $c = 0.35$.

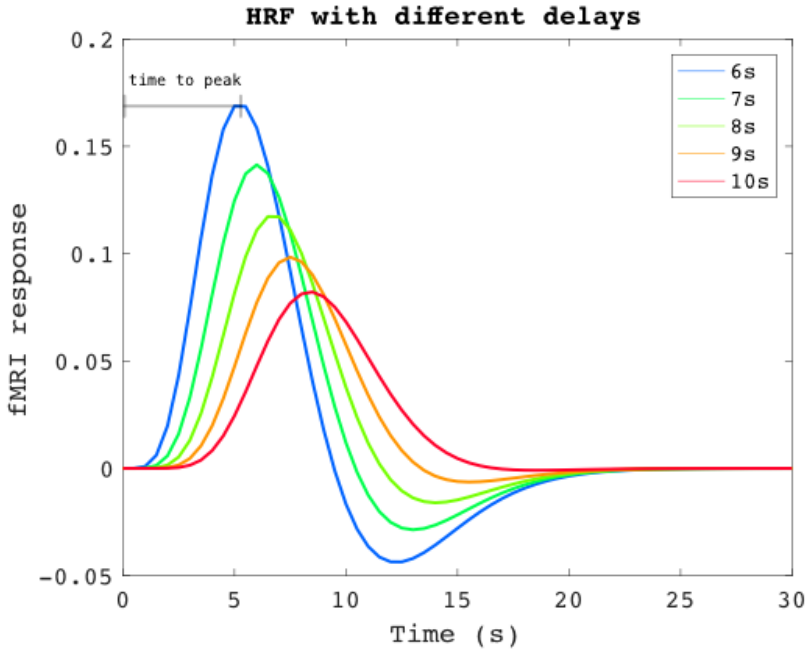


Figure 8.2: A set of estimated HRFs with different peak delays. The curves are modelled using a double gamma function (Worsley, 2001). Here, the delay is changed, however all other parameters are kept constant (Equation 8.2)

Despite the unclear relationships between neural activity (see Section 3.4), the haemodynamic response and the parameters we estimate, basic fMRI research has consistently demonstrated a link between task-related changes and measured BOLD signal; it has become common practice to assume that BOLD responses add linearly (Boynton et al., 1996), simplifying HRF modelling. The simplest linear transform model accounts for the HRF as

being a fixed 'canonical' shape, with only the height (amplitude) allowed to vary (Worsley and Friston, 1995).

To improve the estimates of the HRF, one can add derivatives with respect to time and duration making the analysis robust to small shifts in timings and durations, respectively (Henson et al., 2002); or one can use a finite impulse response basis set, in which the model estimates the HRF for every cognitive event, making no assumptions about the HRF shape - this is a very flexible method, however, the more basis functions (and hence the more complex the model), the more opportunities there are for errors when estimating the HRF (Lindquist et al., 2009). One may also use two gamma functions to model the HRF, i.e. one function to model the initial rise, another to model the post-stimulus undershoot. For instance, the models coded in the somatosensory pRF include a fixed HRF, a HRF fitted to the data, and a double gamma HRF as shown in Figure 8.2.

8.1.3 Least Squares Approximation

Optimizing the parameters of our predicted fMRI timeseries is achieved by fitting the predicted timeseries to the actual data. This is done by calculating the error between the two lines and minimizing it; otherwise known as least squares regression. Given n set of points on a graph, the error (for each point) is the squared distance from that point to a line passing through the cloud of points. This distance is known as the Euclidean distance or the *L2 norm* (see Chapter 4). Minimizing these values will provide the *best fitting* line in the least squares sense.

For problems in which the functions relating input and output are non-linear, linear regression cannot provide answers. Iterative methods (non-linear least squares) are thus required.

Following the least squares estimation, for example, optimizing the weights

of the RF model for a particular voxel, the coefficient of determination is calculated (R^2). R^2 indicates the proportion of variance in the data that is accounted for by the pRF model/predicted timeseries. Generally,

$$R^2 = 1 - \frac{SS_{residual}}{SS_{total}} \tag{8.3}$$

where $SS_{residual}$ is the sum of squared errors between the model and the data, and SS_{total} is the sum of squared errors between the data and the overall mean.

8.1.4 Non-Linear Optimization

A problem requiring non-linear optimization (NLO) will involve an objective function (the mathematical expression that has certain parameters which we are trying to minimise), general constraints and variable bounds on the parameter values. While real-life data are more likely to be non-linear than linear, non-linear models are much more difficult to optimize due to their intrinsic features. One particular problem of NLO is that it is hard to tell the difference between a local optimum from a global optimum, e.g. a curve may contain many troughs and peaks, any of which could trap the function into believing it had found a global minimum/maximum (Figure 8.3); there may be multiple feasible regions, which the minimizing function has no way of knowing about; and different initial parameters may produce different results, as well as different algorithms.

There are many different 'algorithms' that go beyond a least squares framework to provide search methods when dealing with very complex, multidimensional, constrained or unconstrained data sets, such as the Nelder-Mead algorithm (Nelder and Mead, 1965), and the Levenberg-Marquardt (Marquardt, 1963) - which are implemented in mrTools.

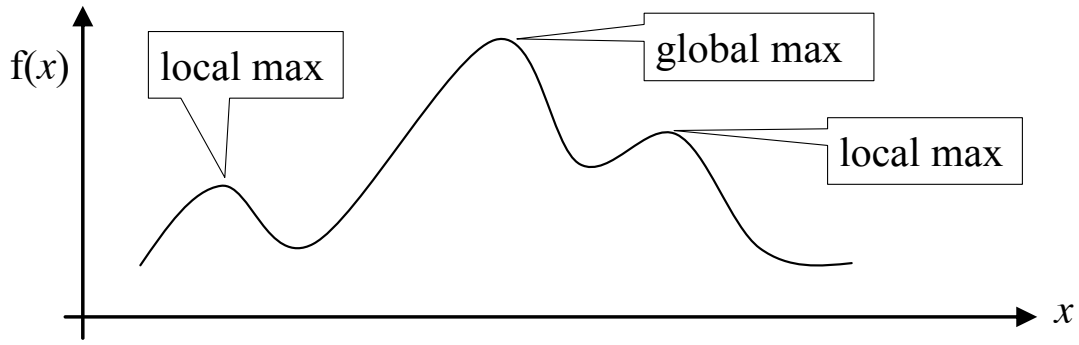


Figure 8.3: Example of an objective function. A comparison of local and global maxima.

There are numerous methods in NLO, such as bisection search, steepest descent, or pattern search algorithms. The first two methods require knowledge of first or second derivatives (to find gradients at a certain points), whereas pattern search (or 'direct search') methods are derivative-free. The term 'Pattern Search' was coined by Hooke and Jeeves in 1961 (Hooke and Jeeves, 1961), whom developed the derivative-free method utilizing a two-step procedure: an exploratory search (in which an improving direction of movement is found by perturbing variable in different directions and seeing if the value of the function improves or worsens), followed by a pattern move (the direction the function steps to), iterating the moves towards better and better values, and finishing with an exploratory search around the 'best' values before termination.

8.1.5 The Levenberg-Marquardt method

The Levenberg-Marquardt algorithm (LMA), also known as a 'damped' least squares method, combines a steepest descent algorithm (measuring the gradient at a given point, then taking a step in the negative direction until one

reaches a (local) minimum), with the Gauss-Newton algorithm (GNA). The GNA is based on Newton's method of optimization, which aims to find the roots of a double-differentiable function, but has the advantage of not requiring second derivatives. However, the GNA can only be used in minimizing sum of squares objective functions, which it assumes is quadratic.

All NLO algorithms are iterative: for a given parameter guess, the gradient is calculated, and a linear set of equations are set up to solve for the stepsize (or increment). Levenberg added a 'damping' parameter, λ which depending on its size at each iteration, allows the overall method to become more GNA-like (small values) or more steepest descent-like (large values). As we get closer to the minimum, λ becomes smaller and hence the LMA tends towards the GNA.

8.1.6 The Nelder-Mead method

The Nelder-Mead algorithm (NM) is another direct search method for multidimensional unconstrained minimization, using a 'simplex' (a geometric shape composed of $n + 1$ vertices in n-dimensions, e.g. 3 vertices in 2D). Each vertex of the triangle is evaluated and improving direction movements are made by transformations, such as reflecting away from the 'worst' point, expanding or contracting the triangle, and finally shrinking the triangle to the optimum (minimum). NM has become an extremely popular NLO algorithm, and is used very commonly in mathematical fields; the *fminsearch* algorithm in MATLAB for NLO uses NM.

A termination test follows each 'turn' of the NM cycle and will end the algorithm if the working simplex becomes small enough, or if the function values are close enough, or if the number of iterations breaches some upper limit. The subject of convergence is beyond the scope of this report, but suffice to say that very little is known regarding the convergence properties

of NM, though it has been proven to produce convergence results in 1D and 2D (Lagarias et al., 1998). The lack of a concrete convergence theory as well as NM's propensity to iterate over a vast number without substantial improvement in minimization are disadvantages to this method, however, its popularity does not stem from its solution accuracy, but rather its ability to quickly reduce function values to good estimates of the final solution.

8.2 Linear Least Squares

For n set of points on a graph, the error or the 'sum of the squared differences between the predicted and actual data' is defined as:

$$E = \sum_{i=1}^{n} (y_i - y_{LS}(x_i))^2 \tag{8.4}$$

where E is the error, $i = 1, 2..., n$ is the number of data points, y_{LS} is the predicted y at a point x_i.

If we assume that the line is linear, i.e. each successive increase from point to point along the line is constant, then we need to find the correct line equation, which will be of the form:

$$y = mx + c$$

where m = the gradient (slope) of the line, and c = the y-intercept. So Equation 8.4 becomes:

$$E = \sum_{i=1}^{n} (y_i - (mx_i + c))^2 \tag{8.5}$$

Thus, in order to find the overall error (all the individual errors summed), given certain x and y coordinates, we need to derive a form for m and c.

Briefly, the gradient is first solved via algebraic manipulation and setting the partial derivative with respect to m to 0, since a zero derivative indicates a zero slope, thus will be our 'minimum'. The final equations we get for m and c are:

$$m = \frac{\overline{xy} - \bar{x}\bar{y}}{\overline{x^2} - (\overline{x})^2} \tag{8.6}$$

and

$$c = \overline{y} - m\overline{x} \tag{8.7}$$

Note that bars above symbols indicate mean values.

Inserting n sets of x and y coordinates into Equations 8.6 and 8.7 will give us the best fitting line with the minimum squared error, for our linear least squares fitting problem. The non-linear least squares problem can be defined in terms of matrices (which is the form MATLAB prefers), and becomes more appropriate for the non-linear case, which we will define as a polynomial (for simplicity):

$$P_n(x) = m_0x^0 + m_1x^1 + m_2x^2 + ... + m_nx^2 \tag{8.8}$$

where P_n is a polynomial of order n, given x_i and y_i data points.

The error of a non-linear problem can then be solved similarly to the linear case (see Equation 8.5):

$$E = \sum_{i=1}^{n}(y_i - P(x_i))^2 \tag{8.9}$$

8.3 Dijkstra's distance

In Chapter 6, the distance covering the cortical area modulated by somatosensory stimulation was measured. Here, more detail is provided for the distance algorithm used.

Dijkstra's algorithm is used to find the shortest paths between nodes in a network or graph (Dijkstra, 1959). The algorithm operates by finding the finding the shortest path from the "source" node to all other nodes. This can also used to find the shortest distance between a source and destination, i.e. the algorithm will stop once the shortest path has been found (by finding all the paths to every node). In the general case, each node is assigned a temporary "cost" based on the paths used to get there, whereby each path or "edge" has a fixed cost.

To find the shortest distance between a source and destination node, Dijkstra's algorithm can be performed as follows:

1. Set the source node distance value as 0, and all other node values to ∞.
2. Find the node with the smallest distance value. If there are no unvisited nodes, or if the node value is ∞, then stop. This new node is the current node.
3. For all the nodes connected to the current node (neighbours), calculate their distance values by adding up the current node value + the travel cost. If the value calculated for a node is less than its value (if it has one), then make the lower value the new value. The current node is now considered "visited" and is not checked again.
4. Repeat steps 2-3.

The above algorithm will terminate once the destination node is reached after all nodes have been visited. This is because once the destination node

becomes the current node, and if there are no temporary nodes, then it means that we have reached our destination.

8.4 Psychophysics

Here, I describe the theory behind the behavioural tasks developed for the QST battery I used to determine whether differences exist between healthy controls and FHD patients.

Psychophysics is a branch of psychology that aims to investigate the relationship between sensations (ψ) and stimuli (ϕ). Early concepts of psychophysics involve the existence of a sensory "threshold", defined as the minimum amount of some stimulus required to evoke a sensation in the observer. This detection limit is known as the "absolute threshold" or RL (after the German *Reiz Limen*). Another concept is the "difference threshold" (DL after the German *Differenz Limen*), which is the change in stimulus required to evoke a noticeable difference, also known as a "Just Noticeable Difference" (JND).

All measures of threshold assessment (e.g. a stimulus that is perceivable in at least 50 % of trials) involve presenting the subject with a stimulus and asking if they perceive it or not. This may be in a simple *yes/no* structure, or something more complicated, such as a forced choice paradigm, which is explained below.

The Method of Constant Stimuli (MOCS) involves presenting a set of carefully chosen stimulus values that are *fixed*. For example, in a temporal difference measurement, the delay between stimulus 1 and 2 will be set to one of, say, nine pre-chosen values. The proportion of detections (e.g. *yes* responses) as a function of stimulus intensity can be plotted, which usually follows a psychometric curve shape called an "ogive", or s-shaped (see Fig-

ure 8.4). The stimulus intensity is plotted on the x-axis and the proportion of correct responses is plotted on the y-axis. A curve is fitted to the data points, and the proportion of correct trials corresponding to a percentage can be found along the curve, e.g. 0.75.

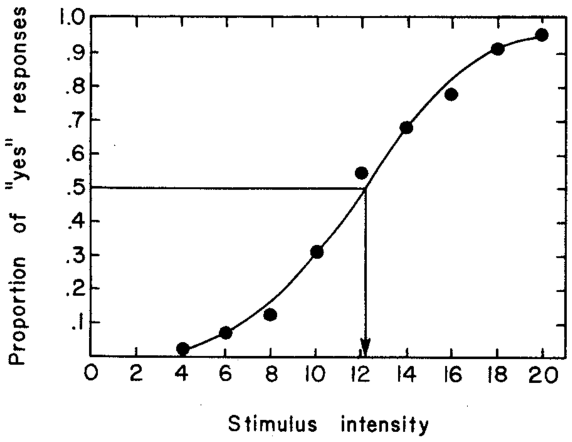


Figure 8.4: Psychometric curve (ogive) plotted following MOCS procedure. In this case, the threshold is defined as the stimulus intensity that can be detected 50 % of the time. Reproduced from Gescheider et al. 1985 (Gescheider, 1985)

To eliminate space and time-related biases, the pair of stimuli should be presented simultaneously in space and time, however, it would be practically impossible to discriminate stimuli. Thus, pairs of stimuli are presented consecutively on the same area (which can lead to a time error), or presented at the same time on different areas (which can lead to a space error). Space errors can be eliminated by presenting the comparison stimulus an equal number of times on both areas, e.g. on 50 % trials, the comparison is presented to the index finger, and to the middle finger for the remaining trials. Time errors manifest in the same way, e.g. there may be a preference to selecting the 2nd interval for magnitude determination. Again, this can be corrected by counterbalancing where the comparison trials fall (equally in either temporal interval). The assumption of counterbalancing is such that when all trials are combined, the time and space errors cancel out.

In MOCS, the number of stimulus values are fixed, and presented a fixed number of times, in contrast, the method of limits is more flexible. It is implemented as a staircase procedure that either decreases or increases the stimulus value, following a response. For example, a very strong stimulus is presented (well above threshold) and the subject will naturally respond correctly. The stimulus intensity is then reduced slightly, and the measurement repeated. The staircase is dropped down until the subject gives an incorrect response, at which point, the staircase reverses and the stimulus is increased until the stimulus can be perceived again, and so on. In this way, the absolute threshold can be found much more rapidly than with MOCS.

Errors of habituation (subject repeats the response after threshold has been reached) and errors of expectation (subject anticipates the stimulus at threshold and reports the change before it has actually occurred) can falsely decrease and increase thresholds, respectively (on descending trials). These are difficult to eliminate, but having a short trial series and alternating the starting point for the staircase mitigates the errors to some extent.

The method of limits can equally be used to find the difference threshold. For example, to determine the temporal discrimination, one would begin with a large temporal separation between two stimuli, then drop the separation until a transition point is reached (a reversal in subject's response), and then proceed as above.

The above is in fact a variant of the method of limits, which takes longer than the staircase-variant. This is because at each transition point, the staircase is reset, rather than simply reversed at that point. The staircase variation of the method of limits uses the average of a chosen number of reversals (e.g. after 8), to use as the threshold.

Another variation of the method of limits is the "forced choice" method, where instead of the subject deciding if a stimulus is present or not (*yes* or *no* responses), the subject is asked to state in which interval the stimulus

was presented (or in which location), e.g. 1 or 2 for first or second interval for a measure of stimulus magnitude presented continuously. Forced choice procedures eliminate biases towards selecting *yes* or *no* responses.

The method of adjustment is a highly interactive method that allows the subject to control the trial structure by increasing or decreasing stimulus intensity until it just detectable (in the case of measuring AL). For measuring DL, the subject is instructed to adjust the comparison stimulus so that it is as close as possible to the presented standard stimulus. This method of measuring DL is also known as the method of average error.

8.5 Temporal SNR images

Below are the temporal signal-to-noise ratio (tSNR) images displayed from Chapter 6. Temporal SNR is calculated voxelwise as the mean divided by the standard deviation, across all dynamics. All data is shown for the 4 somatotopy TW datasets, 2 motortopy TW datasets, and the 2 ON-OFF data sets. Note, the TW data is collected at a TR of 2s and the ON-OFF paradigm with a TR of 1s.

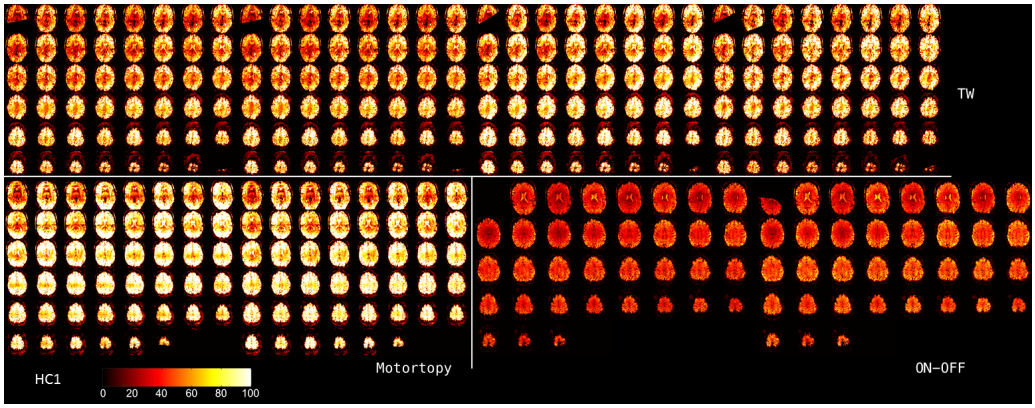


Figure 8.5: Healthy Control 1 (HC1)

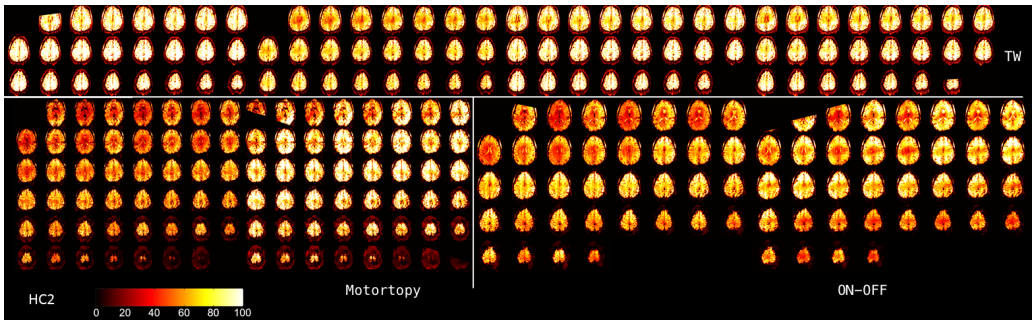


Figure 8.6: Healthy Control 2 (HC2)

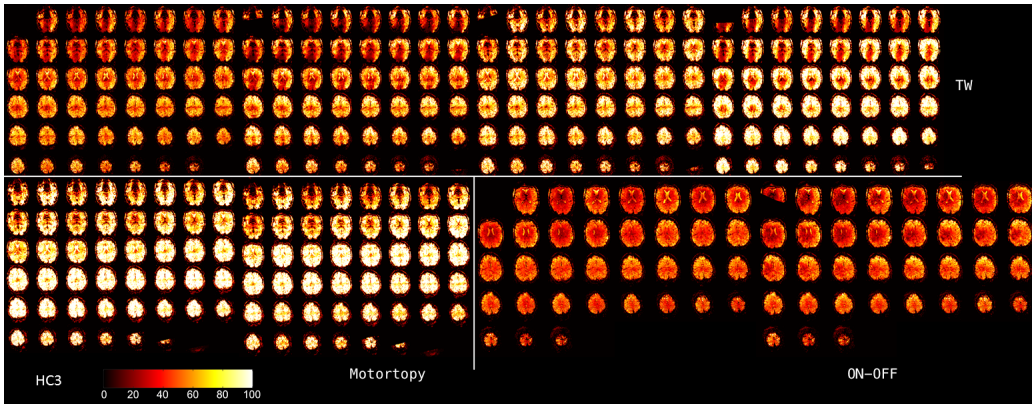


Figure 8.7: Healthy Control 3 (HC3)

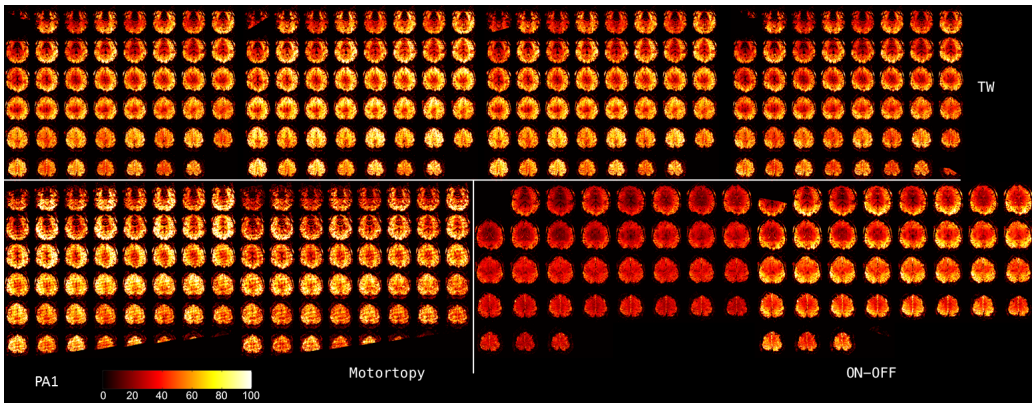


Figure 8.8: FHD Patient 1 (PA1)

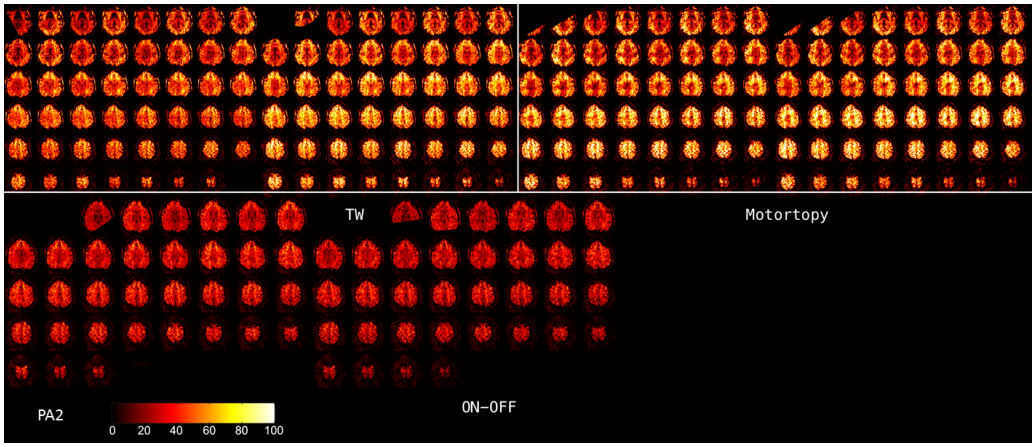


Figure 8.9: FHD Patient 2 (PA2) (amputee)

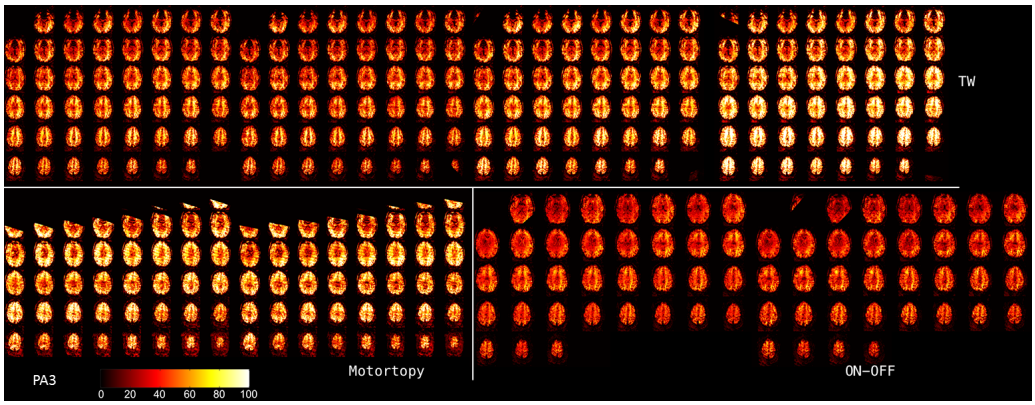


Figure 8.10: FHD Patient 3 (PA3)

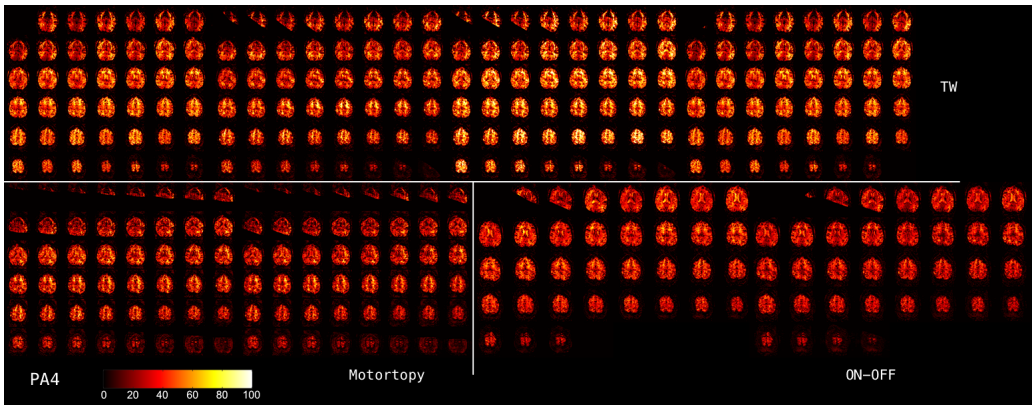


Figure 8.11: FHD Patient 4 (PA4)

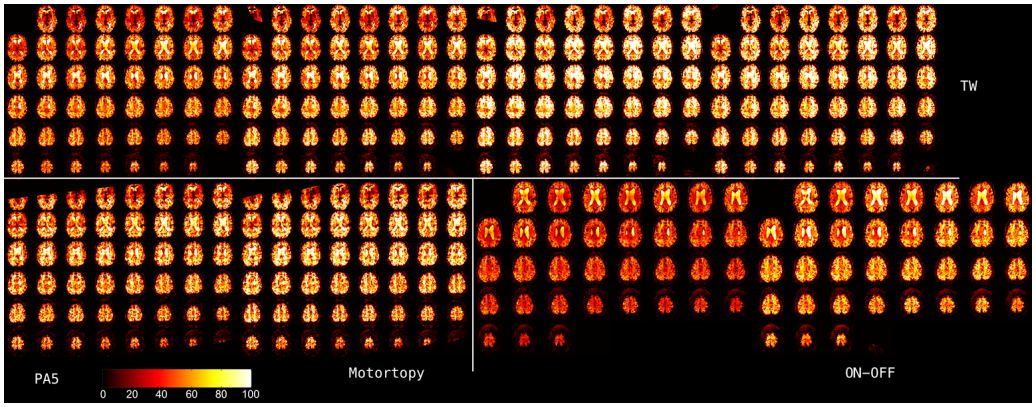


Figure 8.12: FHD Patient 5 (PA5)

8.6 QST

8.6.0.1 Questionnaires and Standard Operating Procedure

The following are the handedness questionnaire collected on patients and controls prior to any experiments, and the SOP used by the experimenter to perform QST, as detailed in Chapter 6.

HANDEDNESS QUESTIONNAIRE

NAME
AGE
SEX

Were you one of twins, triplets at birth or were you single born?.....
*Please indicate which hand you habitually use for each of the following activities by writing **R** (for right), **L** (for left), **E** (for either).
Which hand do you use:
1. To write a letter legibly? .....
2. To throw a ball to hit a target? .....
3. To hold a racket in tennis, squash or badminton? .....
4. To hold a match whilst striking it? .....
5. To cut with scissors? .....
6. To guide a thread through the eye of a needle (or guide needle on to thread)?
.....
7. At the top of a broom while sweeping? ……....
8. At the top of a shovel when moving sand? .....
9. To deal playing cards? .....
10. To hammer a nail into wood? .....
11. To hold a toothbrush while cleaning your teeth? .....
12. To unscrew the lid of a jar? .....

If you use the **RIGHT HAND FOR ALL OF THESE ACTIONS,** are there any one-handed actions for which you use the **LEFT HAND?** Please record them here: .....
.....
.....

If you use the **LEFT HAND FOR ALL OF THESE ACTIONS,** are there any one-handed actions for which you use the **RIGHT HAND?** Please record them here: .....
.....
.....

TOUCHMAP QST Battery

Document # **QST_1**	Title: **Quantitative Sensory Testing**	Print Date:
Revision # **1.1**	Prepared By: **Michael Asghar**	Date Prepared: 14/11/17
		Amendments: 10/08/18

Purpose: Provide procedure of quantitative sensory testing (QST) pre-fMRI or pre-MEG studies during patient/healthy volunteer scanning, for project TOUCHMAP.

Definitions: fMRI – functional magnetic resonance imaging; MEG – Magnetoencephalography; TDT – temporal discrimination threshold; GOT – grating orientation task; FHD – focal hand dystonia; CTS – carpal tunnel syndrome; QST – quantitative sensory testing; PA – patient; HC – healthy control; PZ – piezo-electric "plectrum" stimulators.

Codes:

Codes for running the battery are available from Github.

1. TDT (PZ) – *tempDiscmgl* (nottingham/somatoStimulation)
2. TDT (Brain gauge) - https://www.corticalmetrics.com/braingauge
3. Amplitude thresholding – *pRF_staircase* (somato-pRF/helper_functions)
4. GOT – *go_mocs* (nottingham/somatoStimulation)

Equipment and words of advice:

- 1x Macbook
- 2x Arduinos: Small (TDT) and Large: In between testing, they must be switched over, which is simply performed by switching off the amplifier box, changing the BNC cables over, and restarting the amplifier.
- 1x amplifier box
- 1x USB-to-arduino cable
- 1x power lead for amplifier box
- Set of GOT domes – red box
- Piezos (in plexiglass hand)
- Brain Gauge "mouse"
- 1x control box for PZ

In each case, make sure that the relevant MATLAB code is communicating with the correct port. On a mac, open a terminal and type ls /dev/tty*

Ideally, one should perform all the tests in one hand, and then proceed to other hand. The brain gauge is easiest to explain, and that can be performed without much operator instruction, giving you time to set up the PZs.

The GOT is the most operator-intensive session, since you must be ready to input the user's answer into the MATLAB prompt. Due to the nature of the task, adding a catch loop would slow down the process considerable, thus pay maximum attention to what you are pressing. The easiest is to ask the PA/HC to say "1" for vertical/proximal and "2" for horizontal/lateral.

For the TDT and amp discrimination, I have found it easiest to just use one plexiglass hand, making sure to inform the PA/HC that inputs "1" and "2" are flipped for the other hand.

July2018 – I have now implemented a subject-friendly input method. The subject can now input either the "upArrow" key or the "downArrow" key to indicate forwards and sideways, respectively.

After every procedure, make sure to type *delete(instrfindall)* or type *ccp* which is a script that does the same thing.

After every procedure, please make a note of the stimfile saved in touchmap/data. Additionally, make a note of which hand you did first for the Brain Gauge TOJ.

Procedures

1. Pre-setup
    a. Connect the amplifier box to a power supply. Don't switch on yet. Make sure all amplifier dials are set to "5".
    b. Connect all 10 "A" (or B) BNC connectors to the amplifier box, from the Large Arduino.
    c. Connect the Large Arduino to the laptop, via USB.
    d. Connect the PZs to the control box in the correct order (labelled).
    e. (For the TDT PZ) Unplug BNC connectors 2 and 3, and insert the two connectors for the Small Arduino. For the left hand, Small Arduino cable 1 should go to 8 on the amplifier, and cable 2 to 7. For the right hand, 1 should go to 3, and 2 should go to 2. Disconnect the Large Arduino and connect the Small Arduino via USB to the laptop. You can check if the inputs are flipped since when running *tempDiscmgl*, it will tell you if correct or not.
    f. Switch on the amplifier.

2. TDT (PZ)

    a. Make sure the Small Arduino is connected.

    b. Type *tempDiscmgl* into the MATLAB command window. Assuming all paths are set, this should run correctly. Make sure the Arduino port code is correct in *initialize_serial_port*, and also make sure you are using the path *Nottingham/somato_stimulation* and not the repository *Somato_Stimulation*.

    c. Once triggered (press “5”), the code will present two short buzzes, one to each of digit 2 and 3, and the code will then wait for the subject to press either a “1” or a “2”, depending on which buzz came first. “1” is for index, “2” is for middle – these can be switched around easily for subject comfort.

    d. The code should end after the threshold is found (8 reversals). To prematurely stop, press “Esc”.

    e. Make sure to *delete(instrfindall)* or *ccp* each time you re-run a code, otherwise, there will be port issues.

    f. (Note) You can type *tempDiscmgl(1)* to suppress info (for patients).

3. TDT (Brain Gauge)

    a. Connect the Brain Gauge device to the laptop.

    b. Open Google Chrome and select the Brain Gauge app (Apps, then the Brain Gauge icon). Make sure you have it downloaded: https://www.corticalmetrics.com/braingaugeapp

    c. Setup a new participant, following the on-screen instructions. When you start the battery, pause it by clicking on the back arrow and start the “TOJ Simple” procedure. Results are accessed by logging into the Brain Gauge app as Susan Francis.

    d. Quit the app by pressing CMD+Q on the mac.

4. Amplitude Thresholding

    a. (If connected as TDT PZ) Reconnect BNC connectors 2 and 3 (or 7 and 8 for the left hand) from the Large Arduino to the amplifier box. Connect the Large Arduino via USB to the laptop.

    b. Type *pRF_staircase(2)* into the MATLAB command window to run the code for D2. Type any number from 1-5 depending on which digit you want to test. (or 6-10 if using the left plexiglass hand).

c. Upon triggering with a “5”, the code will send a buzz to each digit with a temporal gap. The subject’s job is to determine which buzz was stronger, in which interval (“1” or “2”). In order to determine which interval happened when, the subject is presented with a text display on each interval, as well as a simultaneous “PING!” noise (headphone recommended).

d. The code should finish itself, else press “Esc” to prematurely stop. Then, *delete(instrfindall).*

e. This task must be done at 2 different frequencies. To change the frequency after a task, go to *ardtest.m* and scroll down until you see *freq = ‘031’;* Change this to 200 or 031 as suitable.

f. (Note) Type *pRF_staircase(2,1)* to initiate a verbose, debugging version.

5. Grating Orientation Task

a. Other than the laptop (and the domes), there is no need for any other hardware.

b. Type *go_mocs* into the MATLAB command window. On each trial, the code will present instructions to the experimenter, i.e. whether the dome should be placed horizontally or vertically on the index digit of the subject. Upon verbal response, the experimenter should enter either a “1” (0 degrees/proximal) or a “2” (90 degrees/lateral). This is quite cognitively taxing, since the experimenter has to process 3 things at once: hearing the subject’s response, entering the response correctly, and placing the dome with the instructed orientation on the digit. Make sure you enter the response correctly, as for speed purposes (it is a slow experiment), there is no way to stop the code/undo other than restarting the code.

c. There is now a subject-friendly version that allows them to input the response themselves using the arrow keys (see above), making this easier for the experimenter (ignore b).

d. For each new dome width, it is recommended to depress the dome on the subject’s index finger prior to starting the trial so that they can distinguish the difference between “forwards/proximal” and “sideways/lateral”.

e. It is important to try to apply the same amount of force each time, and at the same position on the index finger. Do not roll the dome along the oriented direction, as this will bias the results.

f. The dome width sizes are written faintly on the reverse of the dome.

Battery:

TOUCHMAP QST Battery

1.0 GOT: PRE-CHECK

1.1 Operator should decide on which set of 8 spatial domes to use on the patient. This is best decided by trial/error of testing a few domes widths on the PA's index finger (affected hand) or HC (dominant hand).

1.2 Width sizes available (mm): 0.35 0.5 0.75 1.0 1.2 1.5 1.75 2.0 2.5 3.0 4.0 5.0 6.0.

1.3 Based on pilot data taken in a subset of patients, we decided on a healthy battery and patient battery: [0.75 1 1.5 1.75 2 2.5 3 4] for PAs and [0.75 1 1.2 1.5 1.75 2 2.5 3] for HCs.

2.0 MEG BEHAVIOURAL ORDER - FHD

2.1 Handedness Q/A

2.2 TDT (Brain Gauge) – bilateral

2.3 TDT (PZ) – bilateral

2.4 Amplitude thresholding (PZ): D2 30/200 Hz – bilateral

2.5 GOT – index (affected/dominant hand)

- Time – 50 mins

3.0 MEG BEHAVIOURAL ORDER - CTS

3.1 Handedness Q/A + Boston CTS

3.2 TDT (Brain Gauge) – bilateral

3.3 TDT (PZ) – bilateral

3.4 Amp thresholding (PZ): D2/D5, 30/200 Hz – bilateral

3.5 GOT

- Time – 60 mins

4.0 FMRI BEHAVIOURAL ORDER - FHD

4.1 Handedness Q/A

4.2 GOT

4.3 TDT (Brain Gauge) – bilateral

4.4 TDT (PZ) – bilateral

4.5 Amp thresholding (PZ): D2 30/200 Hz – bilateral

5.0 FMRI BEHAVIOURAL ORDER - CTS

5.1 Handedness Q/A + Boston CTS

5.2 GOT

5.3 TDT (Brain Gauge) – bilateral

5.4 TDT (PZ) – bilateral

5.5 Amp thresholding (PZ): D2/D5, 30/200 Hz – bilateral

References:

Contact details:

- Technical issues: Michael Asghar ppxma7@nottingham.ac.uk
- General: Susan Francis susan.francis@nottingham.ac.uk

References

Abraira, V. and Ginty, D. (2013). The sensory neurons of touch. *Neuron*, 79(4):618–639.

Aguirre, G., Zarahn, E., and D'Esposito, M. (1998). The Variability of Human, BOLD Hemodynamic Responses. *Neuroimage*, 8(4):360–369.

Ann Stringer, E., Qiao, P. G., Friedman, R. M., Holroyd, L., Newton, A. T., Gore, J. C., and Chen, L. M. (2014). Distinct fine-scale fMRI activation patterns of contra- and ipsilateral somatosensory areas 3b and 1 in humans. *Hum. Brain Mapp.*, 35(9):4841–4857.

Arduino (2016). Arduino.

Arthur, D. and Vassilvitskii, S. (2007). K-Means++: the Advantages of Careful Seeding. *Proc. eighteenth Annu. ACM-SIAM Symp. Discret. algorithms*, 8:1027–1025.

Bandettini, P. A., Wong, E. C., Hinks, R. S., Tikofsky, R. S., and Hyde, J. S. (1992). Time course EPI of human brain function during task activation. *Magn. Reson. Med.*, 25:390–397.

Bara-Jimenez, W. (2000). Sensory Discrimination Capabilities in Patients with Focal Hand Dystonia. *Ann. Neurol.*, pages 361–407.

Benjamini, Y. and Hochberg, Y. (1995). Controlling the False Discovery Rate : A Practical and Powerful Approach to Multiple Testing. *J. R. Stat. Soc. Ser. B*, 57(1):289–300.

Benson, N., Jamison, K. W., Arcaro, M. J., Vu, A., Glasser, M., Coalson, T., Van Essen, D., Yacoub, E., Ugurbil, K., Winawer, J., and Kay, K. (2018). The HCP 7T Retinotopy Dataset. *bioRxiv*, pages 1–36.

Berens, P. (2009). CircStat : A MATLAB Toolbox for Circular Statistics. *J. Stat. Softw.*, 31(10).

Besle, J., Sanchez-Panchuelo, R.-M., Bowtell, R., Francis, S., and Schluppeck, D. (2013). Single-subject fMRI mapping at 7 T of the representation of fingertips in S1: a comparison of event-related and phase-encoding designs. *J. Neurophysiol.*, 109(9):2293–2305.

Besle, J., Sanchez-Panchuelo, R. M., Bowtell, R., Francis, S., and Schluppeck, D. (2014). Event-related fMRI at 7T reveals overlapping cortical representations for adjacent fingertips in S1 of individual subjects. *Hum. Brain Mapp.*, 35(5):2027–2043.

Blaimer, M., Breuer, F., Mueller, M., Heidemann, R. M., Griswold, M. A., and Jakob, P. M. (2004). Smash, Sense, Pils, Grappa. *Top. Magn. Reson. Imaging*, 15(4):223–236.

Blamire, A., Ogawa, S., and Ugurbil, K. (1992). Dynamic mapping of the human visual cortex by high-speed magnetic resonance imaging. *PNAS*, 89:11069–11073.

Blankenburg, F., Ruben, J., Meyer, R., Schwiemann, J., and Villringer, A. (2003). Evidence for a rostral-to-caudal somatotopic organization in human primary somatosensory cortex with mirror-reversal in areas 3b and 1. *Cereb. Cortex*, 13(9):987–993.

Blankenburg, F., Ruff, C. C., Deichmann, R., Rees, G., and Driver, J. (2006). The cutaneous rabbit illusion affects human primary sensory cortex somatotopically. *PLoS Biol.*, 4(3):0459–0466.

Bleton, J. P. (2010). Physiotherapy of focal dystonia: A physiotherapist's personal experience. *Eur. J. Neurol.*, 17(SUPPL. 1):107–112.

Bloch, F. (1946). Nuclear induction.

Boynton, G., Engel, S., Glover, G., and Heeger, D. (1996). Linear systems analysis of functional magnetic resonance imaging in human V1. *J. Neurosci.*, 16 (13):4207–4221.

Bradley, D., Whelan, R., Walsh, R., Reilly, R. B., Hutchinson, S., Molloy, F., and Hutchinson, M. (2009). Temporal Discrimination Threshold: VBM evidence for an endophenotype in adult onset primary torsion dystonia. *Brain*, 132(9):2327–2335.

Braitenberg, V. and Schüz, A. (1998). *Cortex: Statistics and Geometry of Neuronal Connectivity*. Springer-Verlag, Heidelberg, 2nd edition.

Breuer, F. A., Blaimer, M., Heidemann, R. M., Mueller, M. F., Griswold, M. A., and Jakob, P. M. (2005). Controlled aliasing in parallel imaging results in higher acceleration (CAIPIRINHA) for multi-slice imaging. *Magn. Reson. Med.*, 53(3):684–691.

Buckner, R. L. (1998). Event-related fMRI and the hemodynamic response. *Hum. Brain Mapp.*, 6(5-6):373–377.

Butterworth, S., Francis, S., Kelly, E., McGlone, F., Bowtell, R., and Sawle, G. V. (2003). Abnormal cortical sensory activation in dystonia: An fMRI study. *Mov. Disord.*, 18(6):673–682.

Cauley, S. F., Polimeni, J. R., Bhat, H., Wald, L. L., and Setsompop, K. (2014). Interslice leakage artifact reduction technique for simultaneous multislice acquisitions. *Magn. Reson. Med.*, 72(1):93–102.

Cohen, L. G., Hallett, M., Geller, B. D., and Hochberg, F. (1989). Treatment of focal dystonias of the hand with botulinum toxin injections. *J. Neurol. Neurosurg. Psychiatry*, 52(3):355–63.

Craig, J. C. (1999). Grating orientation as a measure of tactile spatial acuity. *Somatosens. Mot. Res.*, 16(3):197–206.

Craig, J. C. and Johnson, K. O. (2000). The Two-Point Threshold: Not a Measure of Tactile Spatial Resolution. *Curr. Dir. Psychol. Sci.*, 9(1):29–32.

Craig, J. C. and Lyle, K. B. (2001). A comparison of tactile spatial sensitivity on the palm and fingerpad. *Percept. Psychophys.*, 63(2):337–347.

Dagli, M., Ingeholm, J., and Haxby, J. (1999). Localization of cardiac-induced signal change in fMRI. *Neuroimage*, 9:407–415.

Dale, A. M. and Buckner, R. L. (1997). Selective averaging of rapidly presented individual trials using fMRI. *Hum. Brain Mapp.*, 5(5):329–340.

de Graaf, R. a., Brown, P. B., McIntyre, S., Nixon, T. W., Behar, K. L., and Rothman, D. L. (2006). High magnetic field water and metabolite proton T1 and T2 relaxation in rat brain in vivo. *Magn. Reson. Med.*, 56(2):386–394.

De Martino, F., Yacoub, E., Kemper, V., Moerel, M., Uludag, K., De Weerd, P., Ugurbil, K., Goebel, R., and Formisano, E. (2016). The impact of ultra-high field MRI on cognitive and computational neuroimaging. *Neuroimage*.

Defazio, G. (2010). The epidemiology of primary dystonia: Current evidence and perspectives. *Eur. J. Neurol.*, 17(SUPPL. 1):9–14.

Defazio, G., Berardelli, A., and Hallett, M. (2007). Do primary adult-onset focal dystonias share aetiological factors? *Brain*, 130(5):1183–1193.

Deshmane, A., Gulani, V., Griswold, M. A., and Seiberlich, N. (2012). Parallel MR imaging. *J. Magn. Reson. Imaging*, 36(1):55–72.

Dhond, R. P., Ruzich, E., Witzel, T., Maeda, Y., Malatesta, C., Morse, L. R., Audette, J., Hämäläinen, M., Kettner, N., and Napadow, V. (2012). Spatio-temporal mapping cortical neuroplasticity in carpal tunnel syndrome. *Brain*, 135(10):3062–3073.

Dietrich, O., Reiser, M. F., and Schoenberg, S. O. (2008). Artifacts in 3-T MRI: Physical background and reduction strategies. *Eur. J. Radiol.*, 65(1):29–35.

Dijkstra, E. W. (1959). A note on two problems in connexion with graphs. *Numer. Math.*, 1(1):269–271.

Dresel, C., Li, Y., Wilzeck, V., Castrop, F., Zimmer, C., and Haslinger, B. (2014). Multiple changes of functional connectivity between sensorimotor areas in focal hand dystonia. *J. Neurol. Neurosurg. Psychiatry*, 85(11):1245–1252.

Dumoulin, S. and Harvey, B. (2012). Reconstructing human population receptive field properties. *J. Vis.*, 23(1):41–45.

Dumoulin, S. O., Fracasso, A., van der Zwaag, W., Siero, J. C., and Petridou, N. (2017). Ultra-high field MRI: Advancing systems neuroscience towards mesoscopic human brain function. *Neuroimage*, 1(September 2016):0–1.

Dumoulin, S. O. and Wandell, B. A. (2008). Population receptive field estimates in human visual cortex. *Neuroimage*, 39(2):647–660.

Duong, T. Q., Yacoub, E., Adriany, G., Hu, X., Uurbil, K., and Kim, S. G. (2003). Microvascular BOLD contribution at 4 and 7 T in the human brain: Gradient-echo and spin-echo fMRI with suppression of blood effects. *Magn. Reson. Med.*, 49(6):1019–1027.

Duvernoy, H. M., Delon, S., and Vannson, J. L. (1981). Cortical blood vessels of the human brain. *Brain Res. Bull.*, 7(5):519–579.

Elbert, T., Pantev, C., Wienbruch, C., Rockstroh, B., and Taub, E. (1995). Increased Cortical Representation of the Fingers of the Left Hand in String Players. *Science (80-.).*, 270(5234):305–307.

Engel, S., Rumelhart, D., Lee, A., Glover, G., Chichilnisky, E., and Shadlen, M. N. (1994). fMRI of Human Visual Cortex. *Nature*, 369.

Engel, S. A. (2012). The development and use of phase-encoded functional MRI designs. *Neuroimage*, 62(2):1195–1200.

Engel, S. A., Glover, G. H., and Wandell, B. A. (1997). Retinotopic organization in human visual cortex and the spatial precision of functional MRI. *Cereb. Cortex*, 7(2):181–192.

Fiorio, M., Gambarin, M., Valente, E. M., Liberini, P., Loi, M., Cossu, G., Moretto, G., Bhatia, K. P., Defazio, G., Aglioti, S. M., Fiaschi, A., and Tinazzi, M. (2007). Defective temporal processing of sensory stimuli in DYT1 mutation carriers: A new endophenotype of dystonia? *Brain*, 130(1):134–142.

Fischl, B., Sereno, M. I., and Dale, A. M. (1999). Cortical Surface-Based Analysis. *Neuroimage*, 9(2):195–207.

Fox, P. T., Raichle, M. E., Mintun, M. A., and Dence, C. (1988). Nonoxidative glucose consumption during focal physiologic neural activity. *Science*, 241(4864):462–464.

Fracasso, A., Petridou, N., and Dumoulin, S. O. (2016). Systematic variation of population receptive field properties across cortical depth in human visual cortex. *Neuroimage*, 139:427–438.

Frahm, J., Bruhn, H., Merboldt, K. D., and Hänicke, W. (1992). Dynamic MR imaging of human brain oxygenation during rest and photic stimulation. *J. Magn. Reson. Imaging*, 2(5):501–505.

Gardner, J. (2016). *mrTools*. The Gardner Lab, Stanford, California.

Gelnar, P. A., Krauss, B. R., Szeverenyi, N. M., and Apkarian, A. (1998). Fingertip Representation in the Human Somatosensory Cortex: An fMRI Study. *Neuroimage*, 7(4):261–283.

Gescheider, G. (1985). PSYCHOPHYSICS Method, Theory and Application.

Glockner, J. F., Hu, H. H., Stanley, D. W., Angelos, L., and King, K. (2005). Parallel MR Imaging : A User's Guide. *RadioGraphics*, 55905:1279–1297.

Glover, G. H. (1999). Deconvolution of Impulse Response in Event-Related BOLD fMRI1. *Neuroimage*, 9(4):416–429.

Glover, G. H., Li, T.-Q., and Ress, D. (2000). Image-Based Method for Retrospective Correction of Physiological Motion Effects in fMRI: RETROICOR. *Magn. Reson. Med.*, 167(December 1999):162–167.

Grant, A. C., Fernandez, R., Shilian, P., Yanni, E., and Hill, M. A. (2006). Tactile spatial acuity differs between fingers: a study comparing two testing paradigms. *Percept. Psychophys.*, 68(8):1359–1362.

Griswold, M. A., Jakob, P. M., Heidemann, R. M., Nittka, M., Jellus, V., Wang, J., Kiefer, B., and Haase, A. (2002). Generalized Autocalibrating Partially Parallel Acquisitions (GRAPPA). *Magn. Reson. Med.*, 47(6):1202–1210.

Haase, A., Frahm, J., Matthaei, D., Hanicke, W., and Merboldt, K. D. (1986). FLASH imaging. Rapid NMR imaging using low flip-angle pulses. *J. Magn. Reson.*, 67(2):258–266.

Hahn, E. L. (1950). Spin echoes. *Phys. Rev.*, 80:580–594.

Handwerker, D. A., Ollinger, J. M., and D'Esposito, M. (2004). Variation of BOLD hemodynamic responses across subjects and brain regions and their effects on statistical analyses. *Neuroimage*, 21(4):1639–1651.

Heeger, D. J. and Ress, D. (2002). What does fMRI tell us about neuronal activity. *Nat. Rev. Neurosci.*, 3(2):142–151.

Henson, R., Price, C., Rugg, M., Turner, R., and Friston, K. (2002). Detecting Latency Differences in Event-Related BOLD Responses: Application to Words versus Nonwords and Initial versus Repeated Face Presentations. *Neuroimage*, 15(1):83–97.

Hooke, R. and Jeeves, T. A. (1961). " Direct Search" Solution of Numerical and Statistical Problems. *J. ACM*, 8(2):212–229.

Hubel, D. H. (1959). Single unit activity in striate cortex of unrestrained cats. *J. Physiol.*, 147(2):226–238.2.

Hubel, D. H. and Wiesel, T. N. (1977). Ferrier Lecture: Functional Architecture of Macaque Monkey Visual Cortex. *Proc. R. Soc. B Biol. Sci.*, 198(1130):1–59.

Huettel, S. A. A., Song, W., and McCarthy, G. (2004). *Functional Magnetic Resonance Imaging*. Sinauer Associates, Inc., Sunderland, Massachusetts, 3rd edition.

Ibrahim, T. S., Lee, R., Baertlein, B. A., Abduljalil, A. M., Zhu, H., and Robitaille, P. M. L. (2001). Effect of RF coil excitation on field inhomogeneity at ultra high fields: A field optimized TEM resonatior. *Magn. Reson. Imaging*, 19(10):1339–1347.

Iwamura, Y. (1998). Hierarchical somatosensory processing. *Curr. Opin. Neurobiol.*, 8(4):522–528.

Iwamura, Y., Tanaka, M., Sakamoto, M., and Hikosaka, O. (1983). Functional subdivisions representing different finger regions in area 3 of the first somatosensory cortex of the conscious monkey.

Jankovic, J., Schwartz, K., and Donovan, D. T. (1990). Botulinum toxin treatment of cranial-cervical dystonia, spasmodic dysphonia, other focal dystonias and hemifacial spasm. *J. Neurol. Neurosurg. Psychiatry*, 53(8):633–9.

Johansson, R. S. and Vallbo, A. B. (1979). Tactile sensibility in the human hand: relative and absolute densities of four types of mechanoreceptive units in glabrous skin. *J. Physiol.*, 286:283–300.

Johansson, R. S., Vallbo, Å. B., and Westling, G. (1980). Thresholds of mechanosensitive afferents in the human hand as measured with von Frey hairs. *Brain Res.*, 184(2):343–351.

Johnson, K. O. and Phillips, J. R. (1981). Tactile spatial resolution. I. two-point discrimination, gap detection, grating resolution, and letter recognition. *J. Neurophysiol.*, 46(6):1177–1192.

Kaas, J. (1991). Plasticity Of Sensory And Motor Maps In Adult Mammals. *Annu. Rev. Neurosci.*, 14(1):137–167.

Kaas, J., Nelson, R., Sur, M., Lin, C., and Merzenich, M. (1979). Multiple representations of the body within the primary somatosensory cortex of primates. *Science (80-.).*, 204(4392):521–523.

Kay, K., Naselaris, T., Prenger, R., and Gallant, J. (2008). Identifying natural images from human brain activity. *Nature*, 452(7185):352–355.

Kay, K. N., Winawer, J., Mezer, A., and Wandell, B. A. (2013a). Compressive spatial summation in human visual cortex. *J. Neurophysiol.*, 110(2):481–494.

Kay, K. N., Winawer, J., Rokem, A., Mezer, A., and Wandell, B. A. (2013b). A Two-Stage Cascade Model of BOLD Responses in Human Visual Cortex. *PLoS Comput. Biol.*, 9(5).

Keltner, J. R., Carlson, J. W., Roos, M. S., Wong, S. T., Wong, T. L., and Budinger, T. F. (1991). Electromagnetic fields of surface coil in vivo NMR at high frequencies. *Magn. Reson. Med.*, 22(2):467–480.

Kolasinski, J., Makin, T. R., Jbabdi, S., Clare, S., Stagg, C. J., and Johansen-Berg, H. (2016). Investigating the Stability of Fine-Grain Digit Somatotopy in Individual Human Participants. *J. Neurosci.*, 36(4):1113–1127.

Krüger, G. and Glover, G. (2001). Physiological noise in oxygenation-sensitive magnetic resonance imaging. *Magn Reson Med*, 46(4):631–637.

Kuehn, E., Mueller, K., Turner, R., and Schütz-Bosbach, S. (2014). The functional architecture of S1 during touch observation described with 7 T fMRI. *Brain Struct. Funct.*, 219(1):119–140.

Kurth, R., Villringer, K., Mackert, B. M., Schwiemann, J., Braun, J., Curio, G., Villringer, a., and Wolf, K. J. (1998). fMRI assessment of somatotopy in human Brodmann area 3b by electrical finger stimulation. *Neuroreport*, 9(2):207–12.

Kwong, K. K., Belliveau, J. W., Chesler, D. A., Goldberg, I. E., Weisskoff, R. M., Poncelet, B. P., Kennedy, D. N., Hoppel, B. E., Cohen, M. S., and Turner, R. (1992). Dynamic magnetic resonance imaging of human brain activity during primary sensory stimulation. *Proc. Natl. Acad. Sci.*, 89(12):5675–5679.

Lagarias, J. C., Reeds, J. A., Wright, M. H., and Wright, P. E. (1998). Convergence Properties of the Nelder–Mead Simplex Method in Low Dimensions. *SIAM J. Optim.*, 9(1):112–147.

Larkman, D. J., Hajnal, J. V., Herlihy, A. H., Coutts, G. A., Young, I. R., and Ehnholm, G. (2001). Use of multicoil arrays for separation of signal from multiple slices simultaneously excited. *J. Magn. Reson. Imaging*, 13(2):313–317.

Larkman, D. J. and Nunes, R. G. (2007). Parallel magnetic resonance imaging. *Phys. Med. Biol.*, 52(7):R15–R55.

Larsson, J. and Heeger, D. J. (2006). Two Retinotopic Visual Areas in Human Lateral Occipital Cortex. *J. Neurosci.*, 26(51):13128–13142.

Lee, S., Papanikolaou, A., Logothetis, N. K., Smirnakis, S. M., and Keliris, G. A. (2013). A new method for estimating population receptive field topography in visual cortex. *Neuroimage*, 81:144–157.

Levitt, H. (1970). Transformed UpDown Methods in Psychoacoustics. *J. Acoust. Soc. Am.*, 49(2B):467–477.

Lindquist, M. A., Meng Loh, J., Atlas, L. Y., and Wager, T. D. (2009). Modeling the hemodynamic response function in fMRI: efficiency, bias and mis-modeling. *Neuroimage*, 45(1 Suppl):S187–S198.

Lindquist, M. A. and Wager, T. D. (2007). Validity and Power in Hemodynamic Response Modeling: A Comparison Study and a New Approach. *Hum Brain Mapp*, 28(8):764–784.

Lloyd, S. P. (1982). Least Squares Quantitization in PCM. *IEEE Trans. Inf. Theory*, 28(2):129–137.

Logothetis, N. K. (2008). What we can do and what we cannot do with fMRI. *Nature*, 453(7197):869–878.

Logothetis, N. K., Pauls, J., Augath, M., Trinath, T., and Oeltermann, A. (2001). Neurophysiological investigation of the basis of the fMRI signal. *Nature*, 412(6843):150–157.

Lungu, C., Karp, B. I., Alter, K., Zolbrod, R., and Hallett, M. (2011). Long-term follow-up of botulinum toxin therapy for focal hand dystonia: Outcome at 10 years or more. *Mov. Disord.*, 26(4):750–753.

Maeda, Y., Kettner, N., Holden, J., Lee, J., Kim, J., Cina, S., Malatesta, C., Gerber, J., McManus, C., Im, J., Libby, A., Mezzacappa, P., Morse, L. R., Park, K., Audette, J., Tommerdahl, M., and Napadow, V. (2014). Functional deficits in carpal tunnel syndrome reflect reorganization of primary somatosensory cortex. *Brain*, 137(6):1741–1752.

Maldjian, J. a., Gottschalk, a., Patel, R. S., Detre, J. a., and Alsop, D. C. (1999). The sensory somatotopic map of the human hand demonstrated at 4 Tesla. *Neuroimage*, 10(1):55–62.

Mancini, F., Haggard, P., Iannetti, G. D., Longo, M. R., and Sereno, M. I. (2012). Fine-Grained Nociceptive Maps in Primary Somatosensory Cortex. *J. Neurosci.*, 32(48):17155–17162.

Mansfield, P. (1977). Multi-planar image formation using NMR spin echoes. *J. Phys. C Solid State Phys.*, 10(3):L55–L58.

Marquardt, D. W. (1963). An Algorithm for Least-Squares Estimation of Nonlinear Parameters.

Marshall, W. H., Woolsey, C. N., and Bard, P. (1937). Cortical Representation of Tactile Sensibility As Indicated By Cortical Potentials. *Science (80-.).*, 85(2207):388–390.

Martuzzi, R., van der Zwaag, W., Farthouat, J., Gruetter, R., and Blanke, O. (2014). Human finger somatotopy in areas 3b, 1, and 2: A 7T fMRI study using a natural stimulus. *Hum. Brain Mapp.*, 35(1):213–226.

Mathworks (2014). *MATLAB*. The Mathworks Inc., Natick, Massachusetts.

Merzenich, M. M., Kaas, J. H., Wall, J., Nelson, R. J., Sur, M., and Felleman, D. (1983). Topographic reorganization of somatosensory cortical areas 3b and 1 in adult monkeys following restricted deafferentation. *Neuroscience*, 8(1):33–55.

Merzenich, M. M., Nelson, R. J., Kaas, J. H., Stryker, M. P., Jenkins, W. M., Zook, J. M., Cynader, M. S., and Schoppmann, A. (1987). Variability in hand surface representations in areas 3b and 1 in adult owl and squirrel monkeys. *J. Comp. Neurol.*, 258(2):281–296.

Merzenich, M. M., Nelson, R. J., Stryker, M. P., Cynader, M. S., Schoppmann, A., and Zook, J. M. (1984). Somatosensory cortical map changes following digit amputation in adult monkeys. *J. Comp. Neurol.*, 224(4):591–605.

Moeller, S., Yacoub, E., Olman, C. A., Auerbach, E., Strupp, J., Harel, N., and Uurbil, K. (2010). Multiband multislice GE-EPI at 7 tesla, with 16-fold acceleration using partial parallel imaging with application to high spatial and temporal whole-brain FMRI. *Magn. Reson. Med.*, 63(5):1144–1153.

Molloy, F. M., Carr, T. D., Zeuner, K. E., Dambrosia, J. M., and Hallett, M. (2003). Abnormalities of spatial discrimination in focal and generalized dystonia. *Brain*, 126(10):2175–2182.

Mountcastle, V. B. (2011). Central Nervous Mechanisms in Mechanoreceptive Sensibility. *Compr. Physiol.*, pages 789–878.

Mugler, J. P. and Brookeman, J. R. (1990). Threedimensional magnetizationprepared rapid gradientecho imaging (3D MP RAGE). *Magn. Reson. Med.*, 15(1):152–157.

Mulderink, T. A., Gitelman, D. R., Mesulam, M.-M., and Parrish, T. B. (2002). On the Use of Caffeine as a Contrast Booster for BOLD fMRI Studies. *Neuroimage*, 15(1):37–44.

Napadow, V., Kettner, N., Ryan, A., Kwong, K. K., Audette, J., and Hui, K. K. S. (2006). Somatosensory cortical plasticity in carpal tunnel syndrome-a cross-sectional fMRI evaluation. *Neuroimage*, 31(2):520–530.

Naselaris, T., Kay, K. N., Nishimoto, S., and Gallant, J. L. (2011). Encoding and decoding in fMRI. *Neuroimage*, 56(2):400–410.

Nelder, J. A. and Mead, R. (1965). A Simplex Method for Function Minimization. *Comput. J.*, 7(4):308–313.

Nelson, A. J., Blake, D. T., and Chen, R. (2009). Digit-specific aberrations in the primary somatosensory cortex in writer's cramp. *Ann. Neurol.*, 66(2):146–154.

Nelson, A. J. and Chen, R. (2008). Digit somatotopy within cortical areas of the postcentral gyrus in humans. *Cereb. Cortex*, 18(10):2341–2351.

Nishimoto, S., Vu, A. T., Naselaris, T., Benjamini, Y., Yu, B., and Gallant, J. L. (2011). Reconstructing visual experiences from brain activity evoked by natural movies. *Curr. Biol.*, 21(19):1641–1646.

Noll, D. C. and Schneider, W. (1994). Theory, simulation, and compensation of physiological motion artifacts in functional MRI. *IEEE Int. Conf. Image Process.*, 3:40–44.

Ogawa, S., Lee, T. M., Kay, A. R., and Tank, D. W. (1990a). Brain magnetic resonance imaging with contrast dependent on blood oxygenation. *Proc. Natl. Acad. Sci. U. S. A.*, 87(24):9868–9872.

Ogawa, S., Lee, T. M., Nayak, A. S., and Glynn, P. (1990b). Oxygenation-sensitive contrast in magnetic resonance image of rodent brain at high magnetic fields. *Magn Reson Med*, 14(1):68–78.

Ogawa, S., Tank, D. W. W., Menon, R., Ellermann, J. M., Kim, S. G., Merkle, H., and Ugurbil, K. (1992). Intrinsic signal changes accompanying sensory stimulation: functional brain mapping with magnetic resonance imaging. *Proc. Natl. Acad. Sci.*, 89(13):5951–5955.

Overduin, S. A. and Servos, P. (2004). Distributed digit somatotopy in primary somatosensory cortex. *Neuroimage*, 23(2):462–472.

Papoulis, A. (1977). *Signal Analysis*. McGraw-Hill, New York.

Pauling, L. and Coryell, C. D. (1936). The Magnetic Properties and Structure of the Hemochromogens and Related Substances. *Proc. Natl. Acad. Sci. U. S. A.*, 22(3):159–163.

Penfield, W. and Boldrey, E. (1937). Somatic motor and sensory representation in the cerebral cortex of man as studied by electrical stimulation. *Brain*, 60(4):389–443.

Penfield, W. and Rasmussen, T. (1950). *The Cerebral Cortex of Man New York*. Macmillan, New York.

Peters, A. M., Brookes, M. J., Hoogenraad, F. G., Gowland, P. A., Francis, S. T., Morris, P. G., and Bowtell, R. (2007). T2* measurements in human brain at 1.5, 3 and 7 T. *Magn. Reson. Imaging*, 25(6):748–753.

Pruessmann, K. P., Weiger, M., Scheidegger, M. B., and Boesiger, P. (1999). SENSE: Sensitivity encoding for fast MRI. *Magn. Reson. Med.*, 42(5):952–962.

Ramirez-Castaneda, J. and Jankovic, J. (2013). Long-term efficacy and safety of botulinum toxin injections in dystonia. *Toxins (Basel).*, 5(2):249–266.

Rocchi, L., Casula, E., Tocco, P., Berardelli, A., and Rothwell, J. (2016). Somatosensory Temporal Discrimination Threshold Involves Inhibitory Mechanisms in the Primary Somatosensory Area. *J. Neurosci.*, 36(2):325–335.

Sanchez-Panchuelo, R. M., Besle, J., Beckett, A., Bowtell, R., Schluppeck, D., and Francis, S. (2012a). Within-Digit Functional Parcellation of Brodmann Areas of the Human Primary Somatosensory Cortex Using Functional Magnetic Resonance Imaging at 7 Tesla. *J. Neurosci.*, 32(45):15815–15822.

Sanchez-Panchuelo, R. M., Besle, J., Mougin, O., Gowland, P., Bowtell, R., Schluppeck, D., and Francis, S. (2014). Regional structural differences across functionally parcellated Brodmann areas of human primary somatosensory cortex. *Neuroimage*, 93:221–230.

Sanchez Panchuelo, R. M., Besle, J., Schluppeck, D., Humberstone, M., and Francis, S. (2018). Somatotopy in the Human Somatosensory System. *Front. Hum. Neurosci.*, 12(June):235.

Sanchez-Panchuelo, R. M., Francis, S., Bowtell, R., and Schluppeck, D. (2010). Mapping Human Somatosensory Cortex in Individual Subjects With 7T Functional MRI. *J. Neurophysiol.*, 103(5):2544–2556.

Sanchez-Panchuelo, R. M., Francis, S. T., Schluppeck, D., and Bowtell, R. W. (2012b). Correspondence of human visual areas identified using functional and anatomical MRI in vivo at 7 T. *J. Magn. Reson. Imaging*, 35(2):287–299.

Sanger, T. D., Tarsy, D., and Pascual-Leone, A. (2001). Abnormalities of spatial and temporal sensory discrimination in writer's cramp. *Mov. Disord.*, 16(1):94–99.

Sathian, K. and Zangaladze, A. (1996). Tactile spatial acuity at the human fingertip and lip: bilateral symmetry and interdigit variability. *Neurology*, 46(5):1464–1466.

Schellekens, W., Petridou, N., and Ramsey, N. (2017). Detailed somatotopy in primary motor and somatosensory cortex revealed by Gaussian population receptive fields. *Neuroimage, Press.*, 179(June):337–347.

Schick, F. (2005). Whole-body MRI at high field: Technical limits and clinical potential. *Eur. Radiol.*, 15(5):946–959.

Schweisfurth, M. A., Frahm, J., and Schweizer, R. (2014). Individual fMRI maps of all phalanges and digit bases of all fingers in human primary somatosensory cortex. *Front. Hum. Neurosci.*, 8(September):658.

Schweizer, R., Voit, D., and Frahm, J. (2008). Finger representations in human primary somatosensory cortex as revealed by high-resolution functional MRI of tactile stimulation. *Neuroimage*, 42(1):28–35.

Sengupta, A., Schluppeck, D., Barratt, E., Besle, J., Francis, S., and Sanchez-Panchuelo, R. (2018). A Probabilistic Atlas of Digit Somatotopy in the Human Primary Somatosensory Cortex. In *Proc Intl Soc Mag Reson Med*.

Sereno, M., Dale, A., Reppas, J., Kwong, K., Belliveau, J., Brady, T., Rosen, B., and Tootell, R. (1995). Borders of multiple visual areas in humans revealed by functional magnetic resonance imaging. *Science (80-.).*, 268(5212):889–893.

Servos, P., Zacks, J., Rumelhart, D. E., and Glover, G. H. (1998). Somatotopy of the human arm using fMRI. *Neuroreport*, 9(4):605–9.

Setsompop, K., Feinberg, D. A., and Polimeni, J. R. (2016). Rapid brain MRI acquisition techniques at ultra-high fields. *NMR Biomed.*, 29(9):1198–1221.

Setsompop, K., Gagoski, B. A., Polimeni, J. R., Witzel, T., Wedeen, V. J., and Wald, L. L. (2012). Blipped-controlled aliasing in parallel imaging for simultaneous multislice echo planar imaging with reduced g-factor penalty. *Magn. Reson. Med.*, 67(5):1210–1224.

Sokoloff, L. (1981). Localization of functional activity in the central nervous system by measurement of glucose utilization with radioactive deoxyglucose. *J. Cereb. Blood Flow Metab.*, 1(1):7–36.

Speck, O., Stadler, J., and Zaitsev, M. (2008). High resolution single-shot EPI at 7T. *Magn. Reson. Mater. Physics, Biol. Med.*, 21(1-2):73–86.

Stavrinou, M. L., Della Penna, S., Pizzella, V., Torquati, K., Cianflone, F., Franciotti, R., Bezerianos, A., Romani, G. L., and Rossini, P. M. (2007). Temporal dynamics of plastic changes in human primary somatosensory cortex after finger webbing. *Cereb. Cortex*, 17(9):2134–2142.

Steeves, T. D., Day, L., Dykeman, J., Jette, N., and Pringsheim, T. (2012). The prevalence of primary dystonia: A systematic review and meta-analysis. *Mov. Disord.*, 27(14):1789–1796.

Sterr, A., Müller, M. M., Elbert, T., Rockstroh, B., Pantev, C., and Taub, E. (1998). Perceptual correlates of changes in cortical representation of fingers in blind multifinger Braille readers. *J. Neurosci.*, 18(11):4417–23.

Stringer, E. A., Chen, L. M., Friedman, R. M., Gatenby, C., and Gore, J. C. (2011). Differentiation of somatosensory cortices by high-resolution fMRI at 7T. *Neuroimage*, 54(2):1012–1020.

Sur, M., Merzenich, M. M., and Kaas, J. H. (1980). Magnification, receptive-field area, and "hypercolumn" size in areas 3b and 1 of somatosensory cortex in owl monkeys. *J. Neurophysiol.*, 44(2):295–311.

The Dystonia Society (2014). Focal Hand Dystonia.

The Neurological Alliance (2004). Neuro numbers.

Thomas, J. M., Huber, E., Stecker, G. C., Boynton, G. M., Saenz, M., and Fine, I. (2015). Population receptive field estimates of human auditory cortex. *Neuroimage*, 105:428–439.

Tommerdahl, M. (2017). Brain Gauge.

Torres-Russotto, D. and Perlmutter, J. (2008). Focal Dystonias of the Hand and Upper Extremity. *J Hand Surg Am.*, 33(9):1657–1658.

Triantafyllou, C., Hoge, R. D., Krueger, G., Wiggins, C. J., Potthast, A., Wiggins, G. C., and Wald, L. L. (2005). Comparison of physiological noise at 1.5 T, 3 T and 7 T and optimization of fMRI acquisition parameters. *Neuroimage*, 26(1):243–250.

Ugurbil, K., Chen, W., Hu, X., Kim, S.-G., Zhu, X.-H., and Ogawa, S. (2007). Functional MRI at High Fields: Practice and Utility. *Encycl. Magn. Reson.*

Ugurbil, K., L, T., and DS, K. (2003). How accurate is magnetic resonance imaging of brain function? *Trends Neurosci.*, 26(2):108–114.

Vaidya, M., Collins, C. M., Sodickson, D. K., Brown, R., Wiggins, G. C., and Lattanzi, R. (2016). Dependence of B1+ and B1 Field Patterns of Surface Coils on the Electrical Properties of the Sample and the MR Operating Frequency. *Concepts Magn Reson Part B Magn Reson Eng*, 46(1):25–40.

van der Zwaag, W., Francis, S., Head, K., Peters, A., Gowland, P., Morris, P., and Bowtell, R. (2009). fMRI at 1.5, 3 and 7 T: Characterising BOLD signal changes. *Neuroimage*, 47(4):1425–1434.

van Westen, D., Fransson, P., Olsrud, J., Rosén, B., Lundborg, G., Larsson, E.-M., and Westen, D. V. (2004). Fingersomatotopy in area 3b: an fMRI-study. *BMC Neurosci.*, 5(28):28.

Victor, J. D., Purpura, K., Katz, E., and Mao, B. (1994). Population encoding of spatial frequency, orientation, and color in macaque V1. *J. Neurophysiol.*, 72(5):2151–66.

Wall, J. T., Kaas, J. H., Sur, M., Nelson, R. J., Felleman, D. J., and Merzenich, M. M. (1986). Functional reorganization in somatosensory cortical areas 3b and 1 of adult monkeys after median nerve repair: possible relationships to sensory recovery in humans. *J. Neurosci.*, 6(1):218–33.

Wandell, B., Winawer, J., and Kay, K. (2015). *Computational Modeling of Responses in Human Visual Cortex*, volume 1. Elsevier Inc.

Wandell, B. A. and Winawer, J. (2015). Computational neuroimaging and population receptive fields. *Trends Cogn. Sci.*, 19(6):349–357.

Warnking, J. (2002). fMRI Retinotopic MappingStep by Step. *Neuroimage*, 17(4):1665–1683.

Wiesinger, F., Van de Moortele, P.-F., Adriany, G., De Zanche, N., Ugurbil, K., and Pruessmann, K. P. (2004). Parallel imaging performance as a function of field strength–an experimental investigation using electrodynamic scaling. *Magn. Reson. Med.*, 52(5):953–64.

Worsley, K. (2001). Functional MRI: An introduction to methods. *Funct. MRI An Introd. to methods*, pages 251–270.

Worsley, K. and Friston, K. (1995). Analysis of fMRI Time-Series RevisitedAgain.

Wright, P. J., Mougin, O. E., Totman, J. J., Peters, A. M., Brookes, M. J., Coxon, R., Morris, P. E., Clemence, M., Francis, S. T., Bowtell, R. W., and Gowland, P. A. (2008). Water proton T1 measurements in brain tissue at 7, 3, and 1.5T using IR-EPI, IR-TSE, and MPRAGE: Results and optimization. *Magn. Reson. Mater. Physics, Biol. Med.*, 21(1-2):121–130.

Yacoub, E., Duong, T. Q., Van De Moortele, P.-F., Lindquist, M., Adriany, G., Kim, S.-G., Ugurbil, K., and Hu, X. (2003). Spin-echo fMRI in humans using high spatial resolutions and high magnetic fields. *Magn. Reson. Med.*, 49(4):655–664.

Yacoub, E., Shmuel, A., Pfeuffer, J., Van De Moortele, P. F., Adriany, G., Andersen, P., Vaughan, J. T., Merkle, H., Ugurbil, K., and Hu, X. (2001). Imaging brain function in humans at 7 Tesla. *Magn. Reson. Med.*, 45(4):588–94.

Yang, Q. X., Wang, J., Zhang, X., Collins, C. M., Smith, M. B., Liu, H., Zhu, X. H., Vaughan, J. T., Ugurbil, K., and Chen, W. (2002). Analysis of wave behavior in lossy dielectric samples at high field. *Magn. Reson. Med.*, 47(5):982–989.

Zeuner, K. E., Bara-Jimenez, W., Noguchi, P. S., Goldstein, S. R., Dambrosia, J. M., and Hallett, M. (2002). Sensory training for patients with focal hand dystonia. *Ann. Neurol.*, 51(5):593–598.

Zuiderbaan, W., Harvey, B. M., and Dumoulin, S. O. (2012). Modeling center surround configurations in population receptive fields using fMRI. *J. Vis.*, 12(3):1–15.

Zur, Y. (1991). Spoiling of transverse magnetization in steady-state sequences. *Magn. Reson. Med.*, 21:251–263.